COO-2250-4
MITNE-150

EVALUATION OF HIGH PERFORMANCE LMFBR BLANKET CONFIGURATIONS

by

G. J. Brown and M. J. Driscoll

May, 1974

Department of Nuclear Engineering
Massachusetts Institute of Technology
Cambridge, Massachusetts

AEC Research and Development
UC-34 Physics
Contract AT(11-1)-2250
U.S. Atomic Energy Commission

MASSACHUSETTS INSTITUTE OF TECHNOLOGY

DEPARTMENT OF NUCLEAR ENGINEERING

Cambridge, Massachusetts

EVALUATION OF HIGH PERFORMANCE LMFBR BLANKET CONFIGURATIONS

by

G.J. Brown and M.J. Driscoll

May, 1974

COO-2250-4

MITNE-150

AEC Research and Development

UC-34 Physics

Contract AT(11-1)-2250

U.S. Atomic Energy Commission

ABSTRACT

The economic performance of conventional and advanced radial blanket configurations for LMFBR power reactors has been analyzed considering both fuel cycle costs and the cost penalties associated with blanket overcooling. Simple models were developed to correlate total blanket heating rates and to relate mixed-mean coolant outlet temperatures to the cost of electric power. It was found, empirically, that the total blanket heating rate could be split into two terms: one proportional to local fission rate, and the other (independent of local fission rate) representing exponential attenuation of gamma and neutron leakage from the core. The economics of thermal-hydraulic design were quantified by relating changes in power-peaking factors to changes in mixed-mean coolant temperature, which were in turn related to cycle thermal efficiency and pumping power requirements, which determined the change in net electric power available for sale, and hence the incremental change in the cost of power.

A variety of blanket-reflector configurations were examined: one, two and three subassembly rows; depleted, natural and low-enrichment uranium fuel; steel and graphite reflectors; region-wide and row-by-row orificing. An individually orificed two-row depleted-uranium-fueled, graphite-reflected blanket was found to yield the largest savings ($\$1.4 \times 10^6$/yr) relative to the base-case three-row depleted-uranium-fueled steel-reflected, region-orificed blanket.

An experimental verification of the neutronic analysis of a graphite-reflected blanket was performed using the Blanket Test Facility at the M.I.T. Research Reactor. The results of this effort indicated that the nuclear design of graphite-reflected blankets can be accomplished at least as well as that of conventional steel-reflected blankets.

DISTRIBUTION

COO 2250 -4 MITNE -150

AEC Research and Development Contract

AT(11-1)-2250

UC-34 Physics

1-3. U. S. Atomic Energy Commission, Headquarters
Division of Reactor Development and Technology
Reactor Physics Branch

4,5. U. S. Atomic Energy Commission
Cambridge Office

6. Dr. Paul Greebler, Manager
Nuclear Energy Division
Breeder Reactor Department
General Electric Company
310 DeGuigne Drive
Sunnyvale, California 94086

7. Dr. Harry Morewitz, Manager
LMFBR Physics and Safety Projects
Atomics International
P. O. Box 309
Canoga Park, California 91305

8. Mr. Malcolm Dyos, Manager
Nuclear Development, LMFBR Project
Westinghouse Electric Corporation
Advanced Reactors Division
Waltz Mill Site
P. O. Box 158
Madison, Pennsylvania 15663

9. Dr. Robert Avery, Director
Reactor Physics Division
Argonne National Laboratory
9700 South Cass Avenue
Argonne, Illinois 60439

10. Dr. Charles A. Preskitt, Jr., Manager
Atomic and Nuclear Department
Gulf Radiation Technology
P. O. Box 608
San Diego, California 92112

ACKNOWLEDGMENTS

The work described in this report was performed primarily by the principal author, G.J. Brown, who has submitted substantially the same report in partial fulfillment of the requirements for the degree of Doctor of Philosophy at M.I.T.

Financial support from the U.S. Atomic Energy Commission as a research assistant on Contract AT(11-1)-2250 is gratefully acknowledged, as is the Traineeship provided the author by the National Science Foundation during his first year at M.I.T.

The assistance of Mr. A.T. Supple on the experimental work is gratefully acknowledged. Computer calculations for this work were performed at the Laboratory of Nuclear Science and at the M.I.T. Information Processing Center. D. Ferguson and V.A. Miethe supplied assistance in communicating with the computers and Esther Grande very ably handled the typing of this manuscript.

The principal author would like to acknowledge the motivation provided him by his family. And finally, a very special thanks is due the principal author's wife who so silently provided encouragement throughout the completion of this work.

TABLE OF CONTENTS

	Page
Abstract	2
Acknowledgments	3
Table of Contents	4
List of Figures	9
List of Tables	13
Chapter 1. Introduction	16
1.1 Foreword	16
1.2 Blanket-Reflector Design Considerations	17
1.2.1 Design Parameters	17
1.2.2 Previous Work	19
1.2.2.1 Blanket Fuel Management Schemes	19
1.2.2.2 Blanket Residence Time	24
1.2.2.3 Blanket Thickness and Reflector Composition	25
1.2.2.4 Initial Blanket Enrichment	27
1.2.2.5 Orificing Schemes	28
1.2.3 Objectives	30
1.2.4 Outline	30
Chapter 2. Blanket Heating Analysis	32
2.1 Introduction	32
2.2 Method of Analysis	33
2.2.1 Reactor Configuration	33
2.2.2 Tools of Analysis	37

Page

2.3 Fission Energy Distribution 39

2.3.1 Base Case – Three-Row Depleted Blanket 39

2.3.2 Enriched Blankets 43

2.3.2.1 Preface 43

2.3.2.2 Fission Heating Results 44

2.4 Gamma Heating Analysis 50

2.4.1 Gamma Energy Absorption Cross Sections 51

2.4.2 Gamma Heating Results 54

2.5 Neutron Heating Analysis 61

2.5.1 Mechanisms of Neutron Heating 64

2.5.2 Neutron Heating Results 66

2.6 Summary 76

Chapter 3. Evaluation of Blanket Configurations 81

3.1 Introduction 81

3.2 Burnup Analysis 82

3.2.1 Reactor Configurations 82

3.2.2 Cross-Section Preparation 85

3.2.2.1 Energy Group Structure 85

3.2.2.2 Variations with Blanket Enrichment 88

3.2.2.3 Variations with Reflector Composition 90

3.2.3 Method of Burnup 91

3.2.3.1 Introduction 91

3.2.3.2 Burnup Zones and Materials 92

3.2.3.3 Equilibrium Core 92

Page

3.2.3.3.1 Introduction 92

3.2.3.3.2 Calculations 99

3.2.3.4 Materials Included in the Burnup 103

3.2.4 Burnup Economics 105

3.3 Economics of Blanket Heating 109

3.3.1 Introduction 109

3.3.2 Economic Aspects of the Mixed-Mean Reactor Coolant Temperature 110

3.3.2.1 Thermal Efficiency Effects 110

3.3.2.2 Pumping Power Effects 113

3.3.3 Power Gradients and Temperature Relationships 115

3.3.3.1 Temporal and Spatial Gradients 115

3.3.3.2 Mixed-Mean Temperature and Radial Peaking Factors 119

3.3.4 Synthesis and Summary 122

3.4 Case Studies 123

3.4.1 Introduction 123

3.4.2 Base Case – Three-Row Depleted-Uranium Blanket 125

3.4.2.1 Burnup Results 125

3.4.2.2 Thermal-Hydraulic Results 129

3.4.3 Advanced Configurations 131

3.4.3.1 Design Variables 134

3.4.3.1.1 Thickness 134

3.4.3.1.2 Enrichment 134

3.4.3.1.3 Reflector Composition 135

Page

3.4.3.2 Burnup and Thermal-Hydraulic Results 136

3.4.4 Case Studies – Observations and Summary 143

3.5 Summary 148

Chapter 4. Blanket Mock-Up No. 3 152

4.1 Introduction 152

4.2 Description of Blanket Mock-Up No. 3 153

4.2.1 General Description 153

4.2.2 Blanket Subassembly Description 155

4.2.3 Description of the Graphite Reflector 161

4.3 Experimental Aspects 164

4.3.1 Introduction – Objectives 164

4.3.2 Experimental Procedure 167

4.3.2.1 Buckling Experiment 167

4.3.2.2 Axial Traverses 168

4.4 The Results 172

4.4.1 Analytical Predictions 172

4.4.1.1 Buckling 172

4.4.1.2 Axial Traverses 172

4.4.2 Experimental Results 173

4.4.2.1 Buckling 174

4.4.2.2 Axial Activation Traverses 174

4.4.3 Error Analysis 184

4.4.4 Discussion of Results 199

Page

4.4.4.1 Buckling Verification 199

4.4.4.2 Axial Traverses 200

4.5 Summary 205

Chapter 5. Summary and Conclusions 207

5.1 Introduction 207

5.2 Blanket Heating Analysis 209

5.2.1 Method of Analysis 209

5.2.2 Fission Heating Analysis 212

5.2.3 Gamma Heating Analysis 216

5.2.4 Neutron Heating Analysis 222

5.2.5 Summary of Heating Analysis 227

5.3 Evaluation of Blanket Configurations 229

5.3.1 Method of Burnup 229

5.3.2 Burnup Economic Model 230

5.3.3 Thermal-Hydraulic Economic Model 231

5.3.4 Results 236

5.4 Experimental Investigations 239

5.4.1 Description of the Experiment 239

5.4.2 Analysis of Experimental Results 240

5.5 Conclusions and Recommendations 245

References 249

LIST OF FIGURES

Fig. No.		Page
1.1	Power Swing in Radial Blankets for Various Fuel Management Schemes	22
2.1	1000 MWe Reference Reactor Configurations	34
2.2	Fission Density in a Three-Row Depleted-U Blanket	40
2.3	U-238 Capture Rate in a Depleted-U Blanket	42
2.4	Fission Density in a Three-Row Natural-U (0.71 w/o U-235 Blanket	45
2.5	Fission Rate as a Function of Enrichment at Various Positions in a Radial Blanket	46
2.6	U-235 Equivalent Enrichment of U-238 as a Function of Position in a Radial Blanket	48
2.7	Fission Density Distributions for Blankets of Various U-235 Enrichments	49
2.8	Gamma Energy Deposition Traverses for Variously Enriched Blankets	55
2.9	Ratio of Total Gamma to Fission Energy Deposition	56
2.10	Comparison between 40-Group and 26-Group Fission Density Calculations	58
2.11	Excess Gamma Energy Deposition in the Blanket	60
2.12	Ratio of Excess Gamma Energy (Due to Core Leakage) to Fission Energy in the Blanket	63
2.13	Neutron Heating Rates in the Blanket	68
2.14	Contributions to the Neutron Heating Rate	69
2.15	Ratio of Neutron Heating to Fission Heating	71
2.16	Effect of Enrichment on Neutron Heating	72
2.17	Contribution of the Core Leakage Neutrons to the Neutron Heating Rate in the Blanket	73
2.18	Contributions to the Total Blanket Heating Rate	78

Fig. No.		Page
3.1	1000 MW_e Reference Reactor Configuration	83
3.2	Schematic Elevation View of the Upper Right Quadrant of the Standard Reactor System with Burnup Zones Included	93
3.3	Unpoisoned Reactivity Swing	96
3.4	Poisoned Reactivity Swing	96
3.5	The Effect of Irradiation on System Effective Multiplication Factor, k_{eff}	101
3.6	The Effect of Core Fissile Loading on k_{eff}	102
3.7	The Effect of Boron-10 Concentration on k_{eff}	102
3.8	Comparison of Approximate and Exact Cycle Efficiency Relations	111
3.9	Overcooling Due to Temporal and Spatial Gradients	117
3.10	Power Cost Contribution from a Three-Row Depleted-U Blanket	126
3.11	Power Cost Contribution, by Row, from a Three-Row Depleted-U Blanket	128
3.12	Power Buildup in a Three-Row Depleted-U Blanket	130
3.13	Axial Power Distributions	132
4.1	Schematic View of Blanket Mock-Up No. 3 with Graphite Reflector	154
4.2	Overhead View of Blanket Mock-Up No. 3	156
4.3	Grid Plate for Blanket No. 3 Subassemblies	157
4.4	Blanket No. 3 Unit Cell	158
4.5	Schematic Cross-Section view of Blanket No. 3 Subassembly	160
4.6	Schematic View of Graphite Reflector Assembly	162
4.7	Graphite Reflector with Axial and Transverse Holder Rods Inserted	165

Fig. No.		Page
4.8	Thorium Foil Packet	169
4.9	Horizontal Activation Traverses in Blanket No. 3	177
4.10	Vertical Activation Traverses in Blanket No. 3	178
4.11	Spectral Index Traverse in Graphite Reflector of Mock-Up No. 3	179
4.12	Gold (n, γ) Axial Traverse	185
4.13	Sodium (n, γ) Axial Traverse	186
4.14	Chromium (n, γ) Axial Traverse	187
4.15	Ex-Rod U-238 (n, γ) Axial Traverse	188
4.16	U-238 (n, γ) Axial Traverse in Blanket	189
4.17	U-235 (n, f) Axial Traverse	190
4.18	Plutonium-239 (n, f) Axial Traverse	191
4.19	Manganese (n, γ) Axial Traverse	192
4.20	Molybdenum (n, γ) Axial Traverse	193
4.21	Indium (n, n') Axial Traverse	194
4.22	U-238 (n, f) Axial Traverse	195
4.23	In- and Ex-Rod U-238 (n, f) Axial Traverse	196
4.24	Thorium-232 (n, f) Axial Traverse	197
4.25	Neptunium (n, f) Axial Traverse	198
5.1	1000 MW_e Reference Reactor Configuration	208
5.2	Fission Density in a Three-Row Depleted-U Blanket at Beginning of Life	214
5.3	U-235 Equivalent Enrichment of U-238 as a Function of Position in a Radial Blanket	215
5.4	Gamma Energy Deposition Traverses for Variously Enriched Blankets	218

Fig. No.		Page
5.5	Excess Gamma Energy Deposition in the Blanket	220
5.6	Ratio of Excess Gamma Energy to Fission Energy Deposition in the Blanket	221
5.7	Effect of Enrichment on Neutron Heating	225
5.8	Contribution of the Excess Neutron Heating to the Total Neutron Heating Rate in the Blanket	226
5.9	Contributions to the Total Blanket Heating Rate	228
5.10	Overcooling Due to Temporal and Spatial Gradients	235
5.11	Overhead View of Blanket Mock-Up No. 3	241
5.12	U-238 (n-γ) Axial Traverse in Blanket	244

LIST OF TABLES

Table No.		Page
1.1	Comparison of Shuffling Schemes	21
2.1	Distribution of Energy Released in Fission	32
2.2	1-D Reference Reactor Parameters	36
2.3	Isotopic Number Densities for Reference Reactor	38
2.4	Effect of Mesh Interval on Calculations in a Depleted-Uranium Blanket	43
2.5	Peak-to-Minimum Fission Density Ratio for Various Blankets	50
2.6	Macroscopic Gamma Energy Absorption Cross Sections	53
2.7	Ratio of Excess Gamma Energy to Fission Energy	62
2.8	Summary of Microscopic Energy Absorption Cross Sections for Evaluation of Neutron Heating	67
2.9	Neutron Heating Due to Fissions in the Blanket	75
3.1	Reference Reactor Parameters	84
3.2	Comparison of Collapsed Group Structures	85
3.3	Ratio of 4-Group Calculations to 26-Group Calculations in a Depleted Blanket	87
3.4	Ratio of 4-Group Calculations to 26-Group Calculations in Different Blanket Configurations	89
3.5	Correspondence of Burnup Zones and Regions	94
3.6	Region-Collapsed Cross Sections by Burnup Zone	95
3.7	Isotopic Number Densities, Beginning-of-Life	100
3.8	"Equilibrium" Core and Axial Blanket Isotopic Number Densities	104
3.9	Economic Environment	108
3.10	Additional Input to the Economic Analysis	109

Table No.		Page
3.11	Parameter Values for Determination of Power Gradient Penalty	124
3.12	Power Cost Contribution from a Three-Row Depleted-Uranium Blanket	129
3.13	Energy Deposition Rates in a Three-Row Depleted-Uranium Blanket	133
3.14	Reflector Materials and Costs	136
3.15	Summary Performance of Various Blanket-Reflector Configurations	137
3.16	Thermal-Hydraulic-Economic Performance	140
3.17	Relative Blanket Economic Performance	142
3.18	Comparison of Blanket Economic Performance for Individually Orificed Blanket Rows	146
4.1	Subassembly Component Weights	159
4.2	Homogenized Atom Densities in Blanket No. 3	161
4.3	Activation Foils Used in B. T. F. Blanket No. 3	166
4.4	Typical Data Pertinent to Foil Counting	171
4.5	Activation Traverses for Vertical Buckling Determination	175
4.6	Activation Traverses for Horizontal Buckling Determination	176
4.7	Normalized Axial Reaction Rate Data	180
5.1	Reference Reactor Parameters	211
5.2	Distribution of Energy Released in Fission	213
5.3	Excess Gamma Energy Deposition	222
5.4	Summary of Microscopic Energy Absorption Cross Sections for Evaluation of Neutron Heating	224
5.5	Economic Environment	232

Table No.		Page
5.6	Definition of Parameters in the Thermal-Hydraulic Economic Model	233
5.7	Relative Savings Realized by Various Advanced Blanket Designs	237
5.8	Activation Foils Used in BTF No. 3	242

Chapter 1

INTRODUCTION

1.1 Foreword

The commercial development of breeder reactors has been the ultimate goal of the nuclear engineering community since the discovery of nuclear fission. The U.S. commitment to this end is clear; the Fast Test Reactor (FTR) is near completion, and contractual arrangements have recently been finalized for construction of a demonstration liquid-metal (sodium) cooled fast breeder reactor (LMFBR). Development of the LMFBR is also the major goal of nearly all other countries having a significant commitment to nuclear power; in particular, Britain with its Prototype Fast Reactor, France with its Phenix fast reactor, Russia with its operating BR-350 fast reactor; and Germany, Holland, Belgium, Italy and Japan, where fast reactor development is accelerating rapidly (B-1). It is conceded that the success of this program will insure a cheap source of nuclear power for centuries.

Achieving a high breeding ratio has long been recognized as critically important to the successful development of economically viable fast reactors. The blanket region of proposed 1000 MWe LMFBR's contributes about thirty percent of the breeding ratio, which is practically all of the breeding gain, and accounts for about seventy-five percent of the fertile inventory. Consequently optimization of the blanket region is an important subtask in the overall LMFBR development program; and the major theme of the work reported here.

Most of the reactor physics research applicable to fast reactors

has been to demonstrate criticality, safety and other physics characteristics of the core. Low power fast critical assemblies such as ZPR-3, ZPR-6, ZPPR, VERA, ZEBRA and SNEAK (A-1, W-1) have been used to explore these physics characteristics. Core behavior has been stressed and comparatively little has been done to develop an optimum blanket. Actually, most fast criticals have either no blanket or a blanket of unrealistic composition or configuration. It is precisely these circumstances which led to the creation of the M. I. T. Fast Reactor Blanket Research Project and, in particular, this study on improved designs for radial blankets for LMFBR's.

The remainder of this chapter discusses blanket-reflector design considerations, including a literature survey (Section 1.2.2), a statement of objectives (Section 1.2.3) and an outline of the report (Section 1.2.4).

1.2 Blanket-Reflector Design Considerations

1.2.1 Design Parameters

The blanket and reflector regions surrounding the core of an LMFBR serve many functions. Chief among these are fertile to fissile conversion, reflection of neutrons, power production and neutron and gamma shielding. It is clear that these functions are interrelated, and all must be analyzed in concert in designing the blanket region. However, for essentially all LMFBR designs of practical interest, the converter aspect of the blanket region is paramount.

There are two blanket regions, axial and radial, that collectively surround the core. Since the axial blanket fuel is contained in the same

fuel pins as the core, the axial blanket design is constrained by the core geometry in all respects except thickness, and this dimension is often set more by neutron shielding requirements than by strict economic performance. The radial blanket region is not constrained in this manner, except in terms of overall subassembly size. Consequently a great deal of freedom exists in its design.

Important design decisions intrinsic to the determination of the radial blanket configuration must be made with respect to:

a) fuel management scheme
b) residence time
c) blanket thickness
d) use of a moderating reflector
e) initial fissile concentration and distribution
f) orificing.

Various blanket-reflector configurations can be conceived of which vary in certain of the above parameters, as will be discussed in Chapter 3.

For this study, the ranking of alternative configurations will be according to economic criteria determined by evaluating the levelized fuel cycle cost contribution of the radial blanket region, taking into account not only fissile revenue and fabrication, reprocessing and carrying charges, but also economic penalties associated with power gradients across the region.

There are two distinct aspects to the power gradients, temporal and spatial, that occur during blanket irradiation. The temporal gradient is associated with the power swing over the irradiation lifetime. This comes about due to the fact that as plutonium is bred into the

blanket, the power production in the blanket increases. Since the blanket must be adequately cooled at maximum power conditions (at the end of life), the blanket is overcooled even if the power density is uniform spatially. The spatial gradient occurs because of the sharp neutron flux attenuation through the blanket, resulting in a skewed power distribution across the blanket. Since the hottest fuel pin in the blanket must be cooled sufficiently, the non-uniform power shape will result in overcooling of the other fuel pins.

Overcooling the blanket results in a degradation in the mixed mean reactor outlet temperature and decreased thermal efficiency. This can be translated into an economic penalty (Section 3.3) which must be analyzed in determining overall blanket economics.

The remainder of this section will discuss in general terms the aforementioned six aspects of radial blanket design, citing relevant studies where appropriate, and indicating the approach taken in the present work.

1.2.2 Previous Work

1.2.2.1 Blanket Fuel Management Schemes

There are two basic ways to manage the blanket fuel: leave it in one place during its irradiation lifetime (batch or region scatter, sometimes called roundelay, schemes) or move it to different positions (out-in or in-out shuffle: in the latter fresh fuel is placed closest to the core and moved outward until discharge; in-out is the reverse of out-in). Each of these options offers unique advantages which deserve further discussion.

Barthold, in a paper on blanket fuel shuffling (B-2) analyzes in-out, out-in and batch schemes with respect to fissile production and power distribution. He concludes that each scheme produces essentially the same amount of fissile plutonium, but that in-out management produces the flattest radial power and out-in the most skewed. The reason for this last result is clear, since the fissile build-up rate is greatest near the core. Thus, moving irradiation-enriched fuel outwards into a low flux region, and inserting fresh blanket fuel, with hardly any enrichment into the high flux region near the core creates a relatively flat radial power profile.

Wood has also looked at the differences in blanket management schemes (W-5) and reaches the same conclusions as Barthold.

Another report (W-2) also compares out-in, in-out and no blanket shuffling. The conclusions here are identical to the prior studies. Table 1.1 summarizes these latter results, and Fig. 1.1 depicts the assembly power swing during irradiation. Residence time in all cases was five years.

Out-in fuel management has also been studied for blanket fuel management and found to be economically desirable (E-1, E-2, H-1). However, these studies did not take into account the power gradient penalty associated with this scheme. Even more fundamentally, the economic analysis used in obtaining these conclusions about low blanket fuel cycle cost is open to question – specifically the handling of revenue from the sale of fissile isotopes. There are two methods of accounting for this revenue: capitalization or non-capitalization. Capitalization means that the blanket fuel is depreciated over its lifetime,

TABLE 1.1 Comparison of Shuffling Schemes (W-2)

Fuel Management Scheme	Assembly Avg. Discharge Pu-239 (kg)	Lifetime Min-Max Power (MW_T)		
		Row 1	Row 2	Row 3
Batch	2.5	0.44-0.98	0.16-0.40	0.07-0.18
Out-in	2.7	0.66-0.87	0.20-0.32	0.07-0.10
In-out	2.7	0.44-0.68	0.33-0.44	0.25-0.26

Figure 1.1 Power Swing in Radial Blankets for Various Fuel Management Schemes

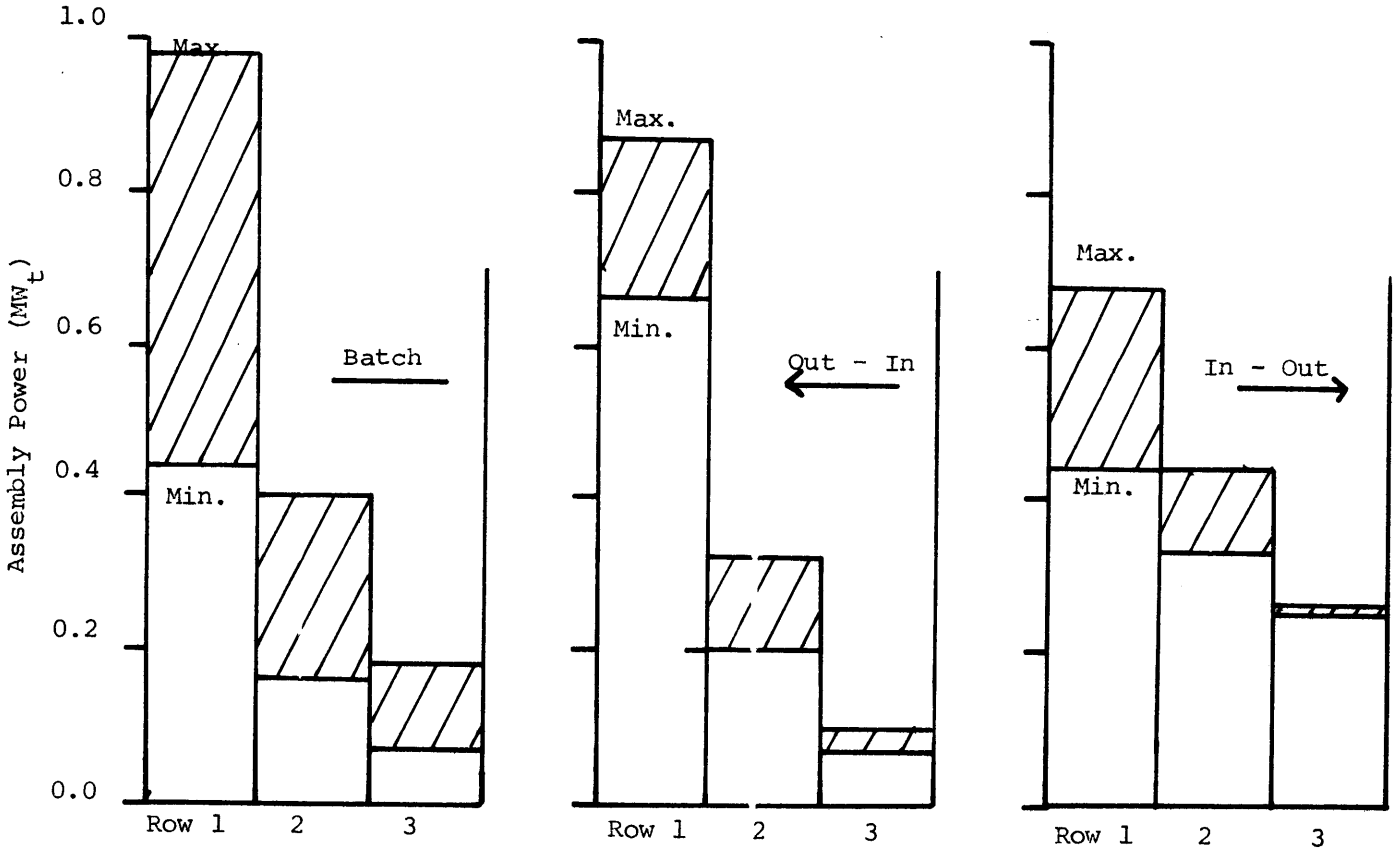

receiving a tax depreciation credit. This is the way thermal reactor fuel is treated and since the salvage value is always less than the initial cost this method is proper. Fast reactor blanket fuel, on the other hand, appreciates in value, i.e., has a salvage value greater than the initial costs. Hence capitalization is inappropriate, since for tax purposes appreciation is not the opposite of depreciation.

The non-capitalization method used in the present work in the form described by Brewer (B-3), treats the salvage value of fuel (fissile value less reprecessing costs) as ordinary income, paying taxes on the net value in the year it is received. This version of the cash flow method (CFM) seems to be most appropriate in the case of an LMFBR where the ordinary and designated product is both electricity and fissile material (N-1).

Now then, if the second approach is utilized, non-capitalization, there can be no economic distinction between different time histories for accumulation of fissile material so long as the same integral amount of product is sold at the end of a given time interval. Penalizing the in-out management scheme, where most of the fissile material in a given subassembly is bred near the beginning of in-reactor residence time while the subassembly is in the inner high flux blanket region does not appear appropriate. All schemes producing the same amount of fissile material from the same number of subassemblies over the same time interval should have the same fuel cycle economics, as is the case for the CFM accounting used in the present work.

Batch management also produces approximately the same amount of plutonium, and its radial power peaking factor is between that for

out-in and in-out management. Its main advantage over the shuffling schemes derives from its simplicity. Fuel elements see only one position in the reactor. The downtime devoted to refueling and reshuffling the blanket is thereby minimized. Considering that every added day of shutdown represents about $100,000 of lost revenue to the utility, this feature can become controlling. According to Pellaud (P-1) the extra benefits achieved from a shuffled blanket are insufficient to justify the additional operational complexity.

The rotation of fuel elements has also been studied (F-1, P-1, W-2, W-3) as a means of improving the operating characteristics of radial blankets by achieving more uniform subassembly fissile production, resulting in a power flattening of about 10-20%. However, this scheme and the other shuffling schemes discussed previously is considered by some (V-1) to be of little interest at this time in view of handling problems.

Taking all of the above considerations into account, batch managed blankets have been selected for analysis in the present work.

1.2.2.2 Blanket Residence Time

The optimum residence time for a blanket element to remain in the reactor is determined mainly by economic considerations. Previout studies (B-2, W-2) indicate an optimum irradiation time of about 4-10 years. This is ascertained by evaluating the time when material credits less material purchase, fabrication, reprocessing and carrying charges are maximized. An optimum exists, since as time increases the blanket produces fissile material but at a decreasing rate

and the effect of reprocessing, fabrication and material purchase decreases, while carrying charges increase.

It is also necessary to take into account the long irradiation times required, making sure that design limits are not violated. Such items as neutron-induced swelling, bowing, fuel melting, development of clad hotspots, clad strain and creep, corrosion, et al., have been identified in a Westinghouse report on blanket design (W-2). It is outside the scope of the present study to go into this aspect of blanket design, except in the important area of evaluating radial power peaking factors and assessing the effect this has on blanket economics. The design limit of maximum clad temperature will be utilized, assuming other design constraints are consequently met.

1.2.2.3 Blanket Thickness and Reflector Composition

The thickness of the radial blanket region has been addressed in previous studies (A-2, B-3, G-1, G-2, H-1). The consistent conclusion in each is that economic considerations are the determining factor. When the value of plutonium becomes high, thicker blankets become desirable. The range of reported thicknesses are from no rows to three rows (45 cm) for radial blankets; and from 30-50 cm for axial blankets.

Investigations by Brewer (B-3) and Tzanos (T-1) indicate that reducing the blanket thickness by replacing one or two rows of blanket and the conventional stainless steel reflector with a high-albedo and moderating reflector such as graphite or beryllium, can improve the blanket economics substantially. The concept of using moderators in

LMFBR blankets, reflectors and cores is not new, and many reports have analyzed the use of such materials as beryllium, beryllium oxide, graphite, aluminum, aluminum oxide, zirconium hydride, nickel, copper, and water. (A-3, A-4, B-3, B-4, C-1, D-1, E-1, E-2, F-2, G-2, H-1, H-2, M-1, S-1, T-1.) [See Brewer's work (B-3) for a more detailed discussion of these references.] In summary, the qualitative effects on radial blanket neutronic and economic performance of reducing the blanket thickness and changing to a high-albedo radial reflector material are:

(a) Fabrication and reprocessing costs for the blanket region eliminated (typically one blanket row) are saved.

(b) The plutonium which would have been bred in the region eliminated is not totally forfeited since breeding performance of the remaining radial blanket is improved by bringing the high-albedo reflector closer to the high flux regions of the blanket.

(c) The albedo effect is primarily responsible for the increased U^{238} captures (T-1), although the moderating effect tends to soften the spectrum and increase the resonance captures.

(d) The total flux is more uniform across the radial blanket, hence the power generated from Pu^{239} fissions and the associated mixed mean outlet temperature is more uniform, resulting in an improved thermal efficiency and in an economic savings.

(e) A more uniform mixed mean outlet temperature implies that the pumping power requirements for a given reactor power output are decreased.

(f) Material purchase and fabrication cost (both initial and re-

placement) of the high albedo reflector will add expenses if these subassemblies are more expensive than the steel reflector subassemblies they replace.

(g) The shielding performance of a high-albedo reflector could translate into an economic savings (or penalty).

(h) The thinner blanket and more uniform power profile could result in less fuel handling during refueling, which could decrease the reactor down-time, resulting in an economic savings.

1.2.2.4 Initial Blanket Enrichment

Flattening of the radial power distribution, resulting in improved mixed mean outlet temperature is a long recognized design objective for achieving optimum reactor core performance. This objective is typically obtained by use of several enrichment zones, with the lowest enrichment in the center of the core, by fuel management, and by use of an effective peripheral reflector. An LMFBR blanket should also have as flat a radial power distribution as possible – hence the motivation for the analysis of blanket reflectors and different enrichment zones.

This last item, sometimes called blanket seeding, can be achieved using either U-235 or Pu-239. The utilization of plutonium enriched fuel fabricated solely for blanket usage is deemed undesirable due to increased fabrication costs. However, various enrichments of UO_2 are easily obtained. Two obvious choices are depleted (~0.2-0.3% enriched) and natural (0.71% enriched). Other enrichments can be

obtained from spent LWR fuel (~1% enriched), and of any specification from the A.E.C. gaseous diffusion enrichment plant.

An early study of breeder reactors by Avery (A-4) proposed use of depleted and natural uranium in the radial blanket region: an inner natural row followed by a row of beryllium and then an outer row of depleted uranium. Another more recent paper (B-5) analyzed the economic potential of different uranium in LMFBR's. concentrating mainly on the core, concluding that natural uranium might be desirable under certain economic conditions.

1.2.2.5 Orificing Schemes

The preceding section discussed in some detail five different design considerations for radial blankets: fuel management schemes, residence time, blanket thickness, moderator usage, and seeding. Blanket fuel cycle economics, neglecting overcooling effects due to radial power gradients, is essentially independent of the fuel management scheme chosen (D-3). Therefore for the remainder of this report batch blanket burnup will be utilized when analyzing the blanket fuel cycle economics. However, the economics of power flattening will be discussed in Chapter 3 so that the results of the various fuel cycle schemes can be discussed from this point of view.

The effect of blanket management schemes on power distribution has been alluded to previously in Section 1.2.2.1. The task of matching cooling requirements to power production has been variously approached. Early fast reactors such as EBR II and Fermi, accommodated the radial power gradient by supplying a separate controllable

coolant supply to a radial blanket inlet plenum (Y-1). However, the cooling concept chosen for subsequent fast breeder reactors, such as Rapsodie, PFR, and the 1000 MWe design plants (W-1) employs a fixed orificing system inside the vessel to control the flow by maintaining a constant ratio of core coolant flow to blanket coolant flow. The amount of flow is determined by the maximum power conditions that will exist in each assembly. To allow for fuel management schemes other than batch refueling the orifice for each row must be individually selected, otherwise sufficient cooling might not be supplied. The ideal orifice would continuously vary (as in the GCFR demonstration plant) during a cycle to cope with the changing power level in the blanket assembly (B-6, P-1). Continuously variable orificing can be accomplished either by external adjustment, as in the GCFR, or by an incorporation of a self-adjusting internal thermostatic device, as suggested in Ref. (W-1). However, a device to achieve this latter feat has not yet been developed, and according to some, even external adjustment will not be practical since it adds undue complexity to the design (W-2, L-1).

Another advanced scheme (W-4) which has been proposed makes use of perforated subassemblies in the blanket region. This permits some degree of cross-flow which tends to reduce hot channel factors resulting in some degree of "self-orificing." A similar effect, on a subassembly basis, could be achieved using cross-flow baffles.

For this study, the fixed orificing scheme, designed to accommodate end-of-cycle power, will be employed in evaluating the amount of overcooling in the batch managed blanket since none of the other

options have been subjected to in-core proof-testing.

1.2.3 Objectives

The specific objectives of the present work are as follows. First, a method to analyze the total heating rate in the blanket will be developed. This will comprise an evaluation of the fission, gamma and neutron heating rates including the effect of the leakage of neutrons and gamma rays from the core into the blanket.

Next, an advanced, high performance configuration of the radial blanket region of an LMFBR will be defined. This will encompass determination of an optimum thickness and residence time; also whether to use a moderating reflector (graphite) or fissile seeding of the blanket. An economic model, describing the effect of power flattening in the blanket will be developed and utilized in evaluation of the advanced blanket configuration.

Another objective of this report is experimental verification of the methods and cross-sections used in achieving the aforementioned objectives. The Blanket Test Facility (BTF) (F-3) provides the means to accomplish this goal. Conventional, steel-reflected blankets have been studied by Leung (L-2). However, it remains for this study to substantiate the results obtained with high-albedo and moderating reflectors surrounding the blanket.

1.2.4 Outline

The main body of this report consists of three chapters. Chapter 2 contains a detailed blanket heating analysis, necessary for

determining blanket radial power profiles. First the method of analysis will be discussed (Section 2.2), then the various heating components will be studied – fertile and fissile fissions (Section 2.3), gamma (Section 2.4), and neutron (Section 2.5) heating.

Chapter 3 treats the economics of the various case studies examined, to sort out the various options having the best combination of design parameters mentioned in Section 1.2.1. The burnup economics model will be summarized in Section 3.2 and the economics of power flattening will be developed in Section 3.3. In Section 3.4 a variety of cases will be studied.

An experimental verfication of the analytical tools and cross sections utilized in the previous chapters is included in Chapter 4. A description of the blanket mock-up (Section 4.2) is followed by a discussion of the experiment (Section 4.3), and then the experimental results (Section 4.4).

Chapter 5 summarizes this investigation, reiterating the main conclusions, and suggesting areas that need further work.

Chapter 2

BLANKET HEATING ANALYSIS

2.1 Introduction

There are approximately 200 million electron volts (1 Mev = 1.60×10^{-10} kW/sec) of recoverable energy released per fission reaction. This includes (E-3, L-3) not only the kinetic energy of the fission fragments, but also the prompt fission gammas and delayed beta particles and gamma rays from the decaying fission products, capture gammas from non-fission events and neutron kinetic energy deposited as the fission neutrons slow down in the reactor (including gamma production via inelastic scattering). Table 2.1 summarizes the energy contributions from the various events.

TABLE 2.1 Distribution of Energy Released in Fission

Type	Recoverable Energy (Mev)
Fission Fragments	167
Fission Product Decay	
β rays	7
γ rays	7
(neutrinos)	(11; not recoverable)
Prompt γ rays	7
Fission Neutrons (including inelastic scatter γ's)	5
Capture γ rays	7 (varies with reactor composition)
TOTAL	200

In the blanket region of an LMFBR, however, one cannot assume that all the energy deposited at a point is due to local fission events. This is because the blanket acts as a shield for leakage of core neutrons and gamma rays, which creates a net energy flow into the blanket. It will be shown in this chapter that adequate estimates of the radial power density can be simply obtained by superposition of local and leakage effects for each of the major contributions; namely,

(a) Fission heating rate

(b) Gamma ray heating rate

(c) Neutron heating rate.

The purpose of this chapter is to analyze in detail these various contributions to the radial power density distribution in the blanket region of an LMFBR for various fissile enrichments. The results obtained here will facilitate the subsequent thermal-hydraulic analysis of blankets as they are irradiated in the reactor and their fissile content changes.

Section 2.2 discusses the method of analysis including the reactor model, computer program and cross sections utilized. Sections 2.3, 2.4 and 2.5 analyze the three main contributions to the heating rate: fissions, gamma rays and neutrons. A summary is included in Section 2.6.

2.2 Method of Analysis

2.2.1 Reactor Configuration

In order to analyze the three contributions to the heating rate in the radial blanket region the LMFBR configuration shown in Fig. 2.1 was

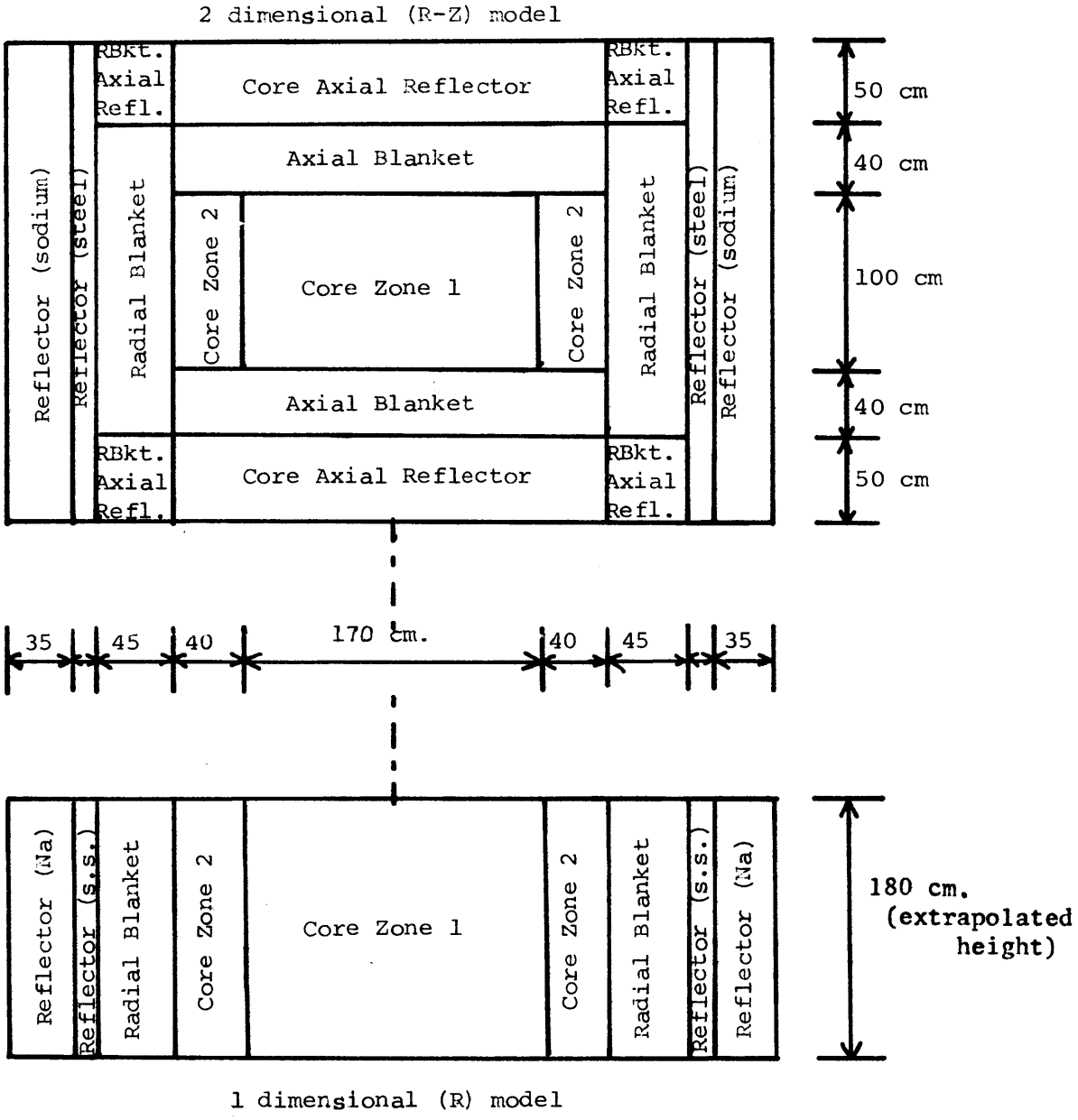

Fig. 2.1 1000MWe Reference Reactor Configurations

employed. The dimensions closely resemble the reference LMFBR used for the MIT Blanket Test Facility design calculations (F-3), and other 1000 MWe LMFBR blanket studies (B-3, W-5). The main features to note in this cylindrically symmetric configuration are two approximately equal-volume core enrichment zones, three radial blanket rows, each fifteen centimeters thick, and a core height-to-diameter (H/D) of 0.4. A more detailed discussion of the two-dimensional reference reactor is found in Section 3.2. A radial one-dimensional version of this two-dimensional reference reactor was devised to facilitate the analysis performed in this chapter (again see Fig. 2.1). Table 2.2 lists pertinent data for the one-dimensional reference configuration used henceforth.

The equivalent core height for this one-dimensional mock-up was found by evaluating the reflector savings of the axial blanket. The reflector savings, δ, is given by Eq. 2.1 (L-3):

$$\delta = \frac{\bar{D}_c}{\bar{D}_r} L_r, \tag{2.1}$$

where $\bar{D}$ is the diffusion coefficient (cm), L is the diffusion length (cm), and the subscripts c and r refer to the core and axial reflector (i.e., axial blanket), respectively. Expressions for D and L in terms of macroscopic cross sections for absorption, Σ_a, and transport, Σ_T are:

$$D = \frac{1}{3\Sigma_T} \qquad \text{and} \qquad L = \sqrt{\frac{1}{\Sigma_a - \nu\Sigma_F}}. \tag{2.2}$$

The macroscopic cross section, Σ_x, is derived for each reactor zone by the summation:

TABLE 2.2 1-D Reference Reactor Parameters

Core

Radial extent = 125 cm

Equivalent number of assemblies* = 245

Volume fractions:

Fuel (oxide, 85% T.D.) = 30 v/o

Structure (S.S.) = 20 v/o

Coolant (Na) = 50 v/o

Radial Blanket

Radial thickness = 45 cm

Equivalent number of assemblies*

Row 1 = 63

Row 2 = 70

Row 3 = 77

Volume fractions:

Fuel (oxide, 95% T.D.) = 50 v/o

Structure (S.S.) = 20 v/o

Coolant (Na) = 30 v/o

Steel Reflector

Radial thickness = 15 cm

Equivalent number of assemblies* = 84

Volume fractions:

Structure (S.S.) = 80 v/o

Coolant (Na) = 20 v/o

Na Reflector

Radial thickness = 35 cm

Equivalent number of assemblies* = 222

Volume fraction:

Sodium = 100 v/o

*Assume hexagonal assembly 15 cm across the flats.

$$\Sigma_x = \sum_j N_j \sigma_j^x, \tag{2.3}$$

where N_j is the number density of the j^{th} material in the zone and σ_j^x is the microscopic cross section for reaction x, material j. Using typical one-group fast reactor cross sections (D-2) and the number densities in Table 2.3, the value for δ is found to be

$$\delta = 25 \text{ cm.}$$

2.2.2 Tools of Analysis

The methods of analysis employed in determining the power distributions for the three contributions to the heating rates are all similar. A criticality calculation was made with the ANISN transport code (E-4), S-8 option (which was shown sufficient by Leung (L-2)). This yielded multigroup fluxes of both neutrons and gamma rays which were then used to calculate the volumetric energy deposition rates, E, for the various heating contributions in the blanket by the following equation:

$$E(r) = \sum_{i,j} N_j(r)\, \sigma_{ij}^E \phi_i(r), \tag{2.4}$$

where

$N_j(r)$ is the j^{th} material number density (atoms/barns-cm), at a particular radius, r (cm),

σ_{ij}^E is the microscopic energy absorption cross section for material j, energy group i (Mev-barns), and

$\phi_i(r)$ is the radial flux in energy group i, at a particular radius r (particles/cm^2 sec).

Two multigroup cross-section sets were employed to analyze the

TABLE 2.3 Isotopic Number Densities for Reference Reactor (atoms/barn-cm)

Material	Core Zone 1	Core Zone 2	Radial Blanket
U-238	0.005324	0.004825	0.01155
Pu-239	0.0005769	0.0008916	0.0
Pu-240	0.0001930	0.0003113	0.0
Pu-241	0.0001099	0.0001698	0.0
Pu-242	0.00002748	0.00004245	0.0
U-235	0.0	0.0	0.00008271
O-16	0.01248	0.01248	0.02326
Na	0.0110	0.0110	0.00660
Cr	0.00300	0.00300	0.00300
Fe	0.0126	0.0126	0.0126
Ni	0.00140	0.00140	0.00140

Material	Steel Reflector	Na Reflector
Na	0.0044	0.0220
Cr	0.0120	0.0
Fe	0.0504	0.0
Ni	0.0056	0.0

three contributions to the total heating rate. A twenty-six group neutron cross section set developed from the so-called "Russian" or "ABBN" set (A-6) was utilized to acquire fission heating rates and neutron heating rates. A forty-group coupled neutron-gamma cross-section set developed at ORNL (M-2) was used to determine the amount of gamma energy absorption. This will be described further in Section 2.4.1.

The remainder of this chapter discusses the determination of energy deposition rates in the blanket for various blanket enrichments. The emphasis is placed on development of the capability for predicting the heating rates using uniform enrichment in the blanket, for later application to the more practical case involving varied enrichments.

2.3 Fission Energy Distribution

The fission energy distribution in the blanket region was evaluated using a 26-group neutron cross-section set with self-shielding corrections appropriate for fast reactor calculations (A-6, B-3). The microscopic energy absorption cross section is given simply by the microscopic fission cross section times the average energy released per fission quoted in Section 2.1, namely 200 Mev. As previously noted, this will yield "conventional" heating rates corresponding to the assumption that all energy is deposited locally. The results will be used as the bases for evaluating the importance of the other heating contributions from gamma rays and neutrons.

2.3.1 Base Case – Three-Row Depleted Blanket

Figure 2.2 shows the relative fission power density as a function of radius for the base case, three-row depleted uranium radial blanket.

Fig. 2.2
Fission Density in a Three Row Depleted-U Blanket, at Beginning of Life

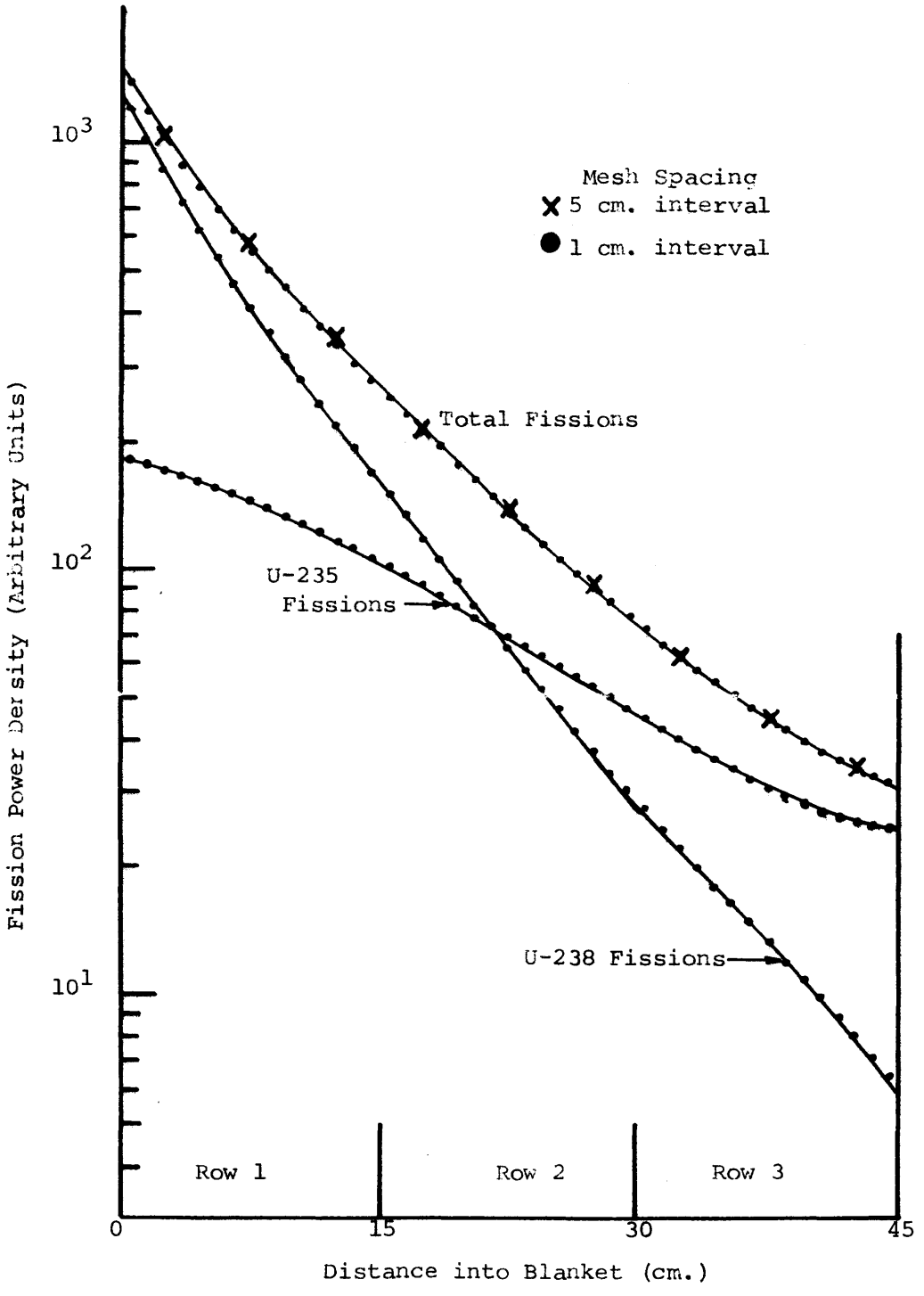

It is significant to note that the fission power density drops off by a factor of approximately 50, with the most severe decrease occurring in the innermost row.

This case corresponds to the beginning of life of a depleted-uranium-fueled radial blanket. Analysis of the fission power distribution, with respect to fertile (U-238) and fissile (U-235) fissions yields the interesting result that fast fissions in the fertile isotope uranium-238 dominate the total fission rate in the first half of the blanket, whereas the fissile isotope, uranium-235 fissions, dominate in the latter half of the blanket. This result, depicted in Fig. 2.2, indicates the importance of considering the presence of uranium-235 even in the very small quantities occurring in depleted uranium ($0.2\,^{w}/_{o}$).

One further analysis is depicted in Fig. 2.2, namely the insensitivity of the results to the mesh spacing used in the ANISN computer code. Since it is important for this (and future) analyses to determine, among other things, peak-to-minimum power ratios, it is necessary to be able to draw smooth curves through the data points with some degree of confidence. Figure 2.2 indicates the close fit between the smooth curve drawn through the data points determined with a five-centimeter mesh (3 points per blanket row) and a one-centimeter mesh (15 points per blanket row). Figure 2.3 shows this same insensitivity to mesh spacing for the important U-238 capture reaction. The coarser mesh represents a cost savings in computer operations by a factor of slightly less than five. Table 2.4 lists the percent difference between the results obtained from the two cases at 5.0 centimeter intervals. The largest difference in the total fission rate distribution occurs in the first row

Fig. 2.3
U-238 Capture Rate in a Depleted-U Blanket

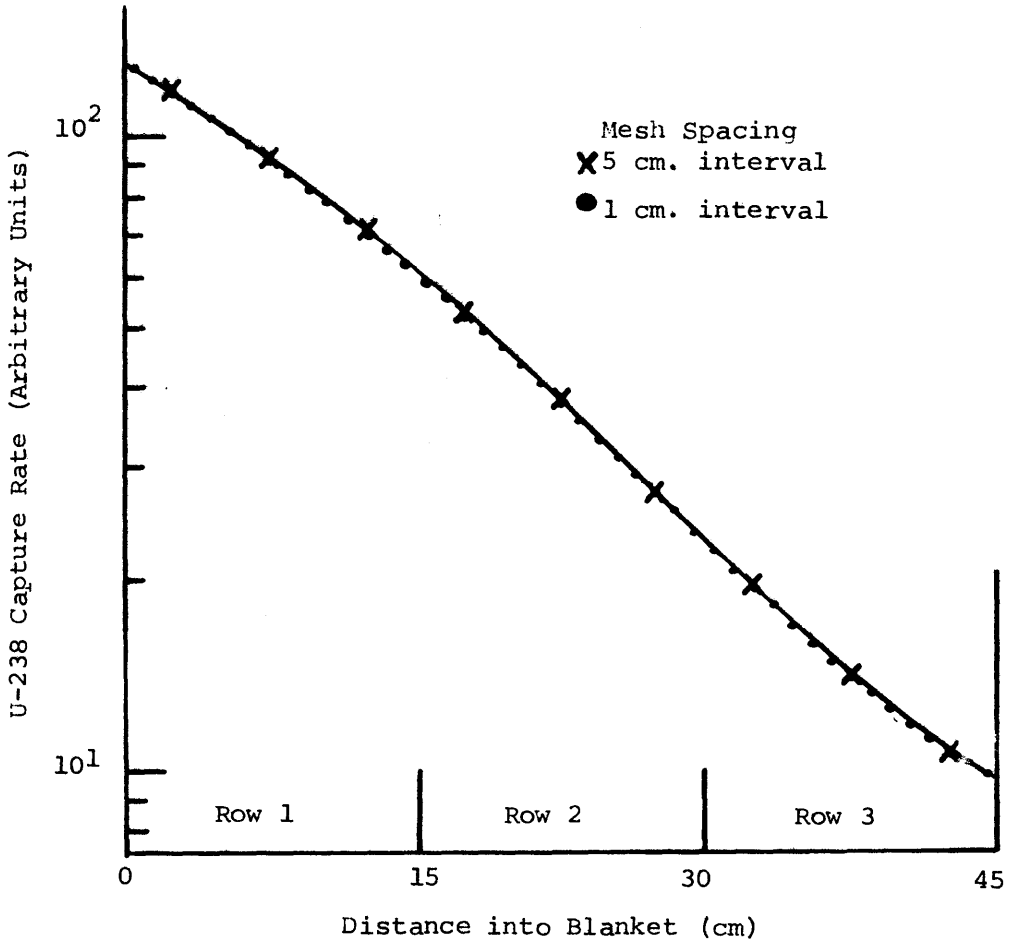

TABLE 2.4 Effect of Mesh Interval on Calculations in a Depleted Uranium Blanket

Distance into Blanket (cm)	Difference between Coarse and Fine Mesh (%)	
	Fission Rate U-238 + U-235	Capture in U-238
2.5	2.3	0.1
7.5	3.9	0.7
12.5	4.1	1.0
17.5	1.2	1.1
22.5	0.1	0.9
27.5	-0.9	0.7
32.5	-1.2	0.3
37.b	-1.3	-0.5
42.5	-1.2	-0.4

and is only about 4 percent, which is negligible when compared to the factor of 5.7 attenuation across the first row. The largest difference in the U-238 capture rate is 1.1%, which, considering the cost savings, is deemed acceptable. The multiplication factors in both cases are also identical. These results were to be expected since five centimeters is on the order of one mean free path for neutrons in a fast reactor.

2.3.2 Enriched Blankets

2.3.2.1 Preface

Different blankets of various fissile (U-235) enrichment are analyzed in this section. The enrichments considered are: 0.2 weight percent ($^{w}/_{o}$)

U-235 (presented in Section 2.3.1); 0.71 $^{w}/_{o}$ or natural uranium, 1.2 $^{w}/_{o}$ U-235, 2.0 $^{w}/_{o}$ U-235, 2.5 $^{w}/_{o}$ U-235 and two other blankets with different enrichments in each row, i.e., 0.71/1.2/2.0 and 2.0/1.2/0.71. These cases run a wide gamut of available enrichments, as might be considered for blanket seeding. Furthermore, these fissile uranium enrichments (especially the mixed enrichment cases) roughly simulate the fissile plutonium enrichment that might be experienced in a radial blanket after irradiation or after out-in or in-out fuel management.

It should be noted at this point that only the generation of thermal energy in the radial blanket will be analyzed here; the economic savings (or penalty) associated with either plutonium production or power gradients will be addressed in Chapter 3.

2.3.2.2 Fission Heating Results

Figure 2.4 depicts the results of the fission heating analysis for a natural uranium three-row blanket. The figure shows the contributions from fertile and fissile fissions to the total fission rate. Here the U-238 and U-235 fission rates are equal at about six centimeters into the blanket, compared to 21 centimeters in the depleted blanket (Fig. 2.2). As would be expected, as the enrichment in the blanket increases, the importance of the fertile fissions becomes less dominant, although non-negligible.

Another way to determine the contribution of fertile fissions in the blanket region is demonstrated by Fig. 2.5, a linear plot of the fission rate versus initial fissile enrichment at the same point in the different blankets. The positive intercept on the ordinate indicates that at zero

Fig. 2.4 Fission Density in a Three Row Natural-U (0.71% U-235) Blanket

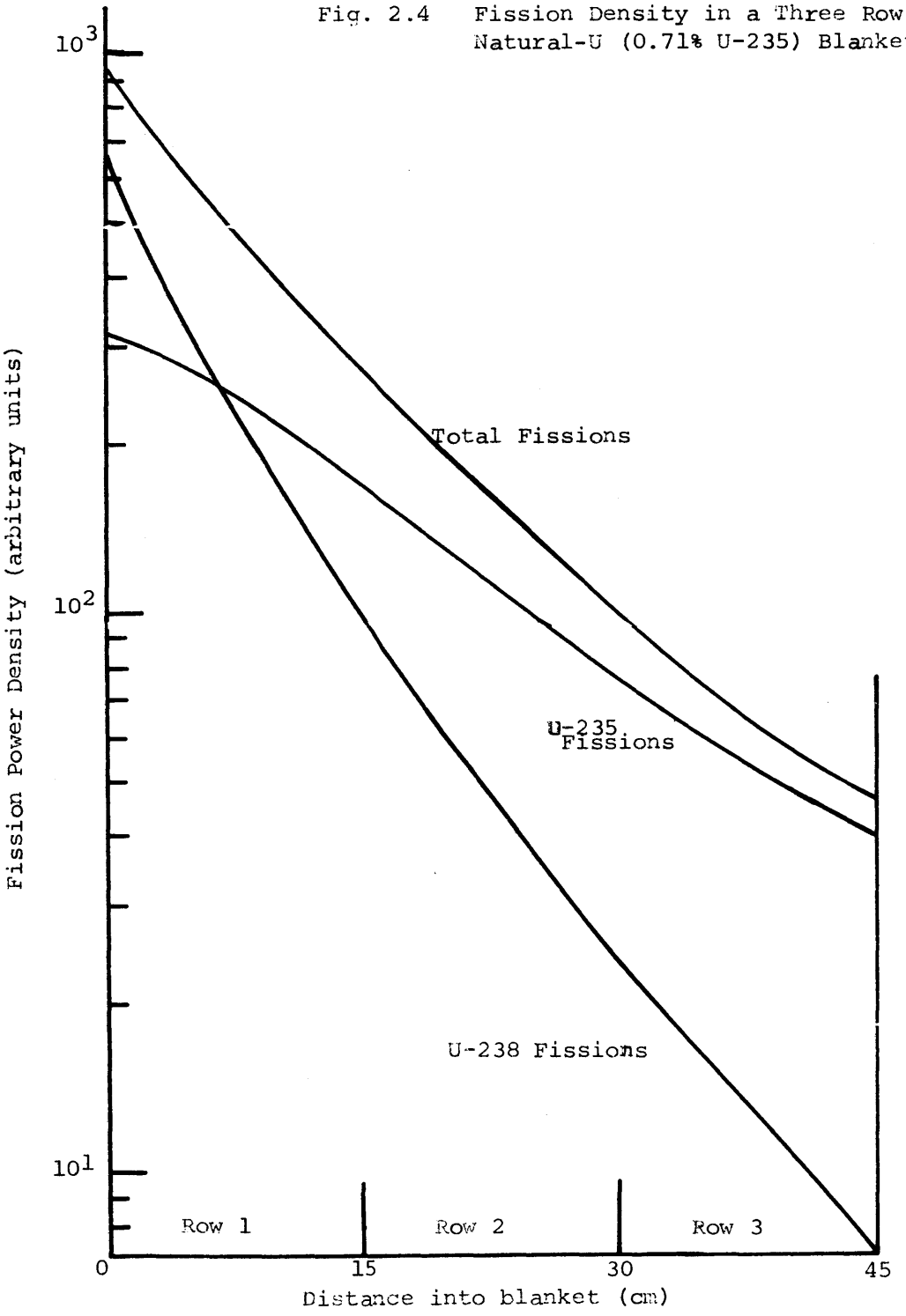

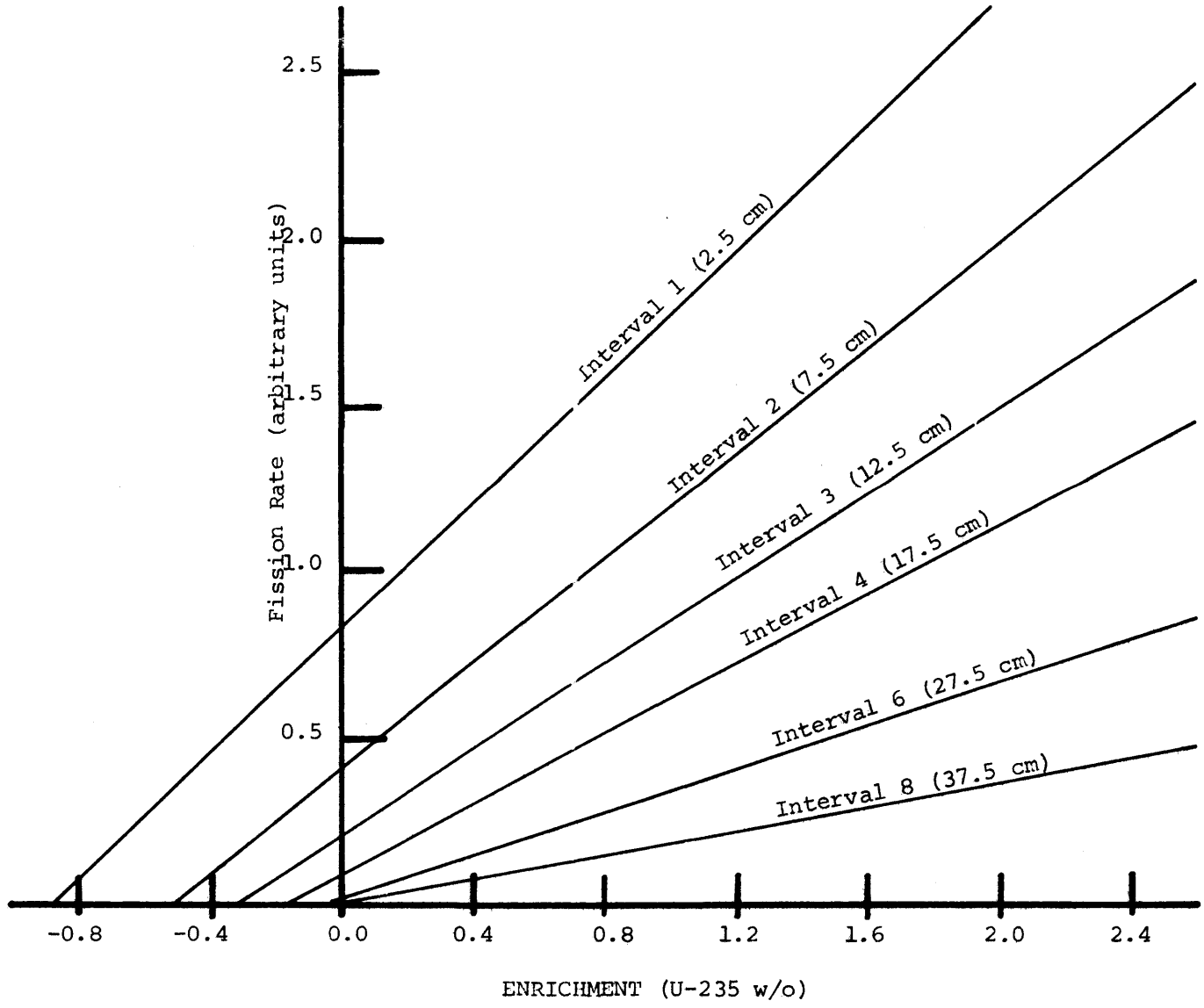

Figure 2.5 Fission Rate as a Function of Enrichment at Various Positions in a Radial Blanket

enrichment there are still fissions which must be due to the presence of U-238. The negative intercept on the abscissa is interpreted as the effective (U-235 equivalent) enrichment of U-238. As expected this "equivalent enrichment" decreases (approaches zero) with distance into the blanket. These results are plotted in Fig. 2.6, yielding a straight line on the semilog scale. This exponential relationship can be explained by noting that the fast flux also falls off exponentially in the blanket, as shown by the U-238 fission rates in Figs. 2.2 and 2.4.

Figure 2.7 shows the results for the total fission rate in all blankets considered. Since the entire reactor system in each case is normalized to the same total fission rate, the more highly enriched blankets, with their higher fission rates, indicate a reduction in core fission rate. This effect will be discussed further in Chapter 3 when the economics of power flattening is discussed. This phenomenon will not affect the relative degree of power flattening achieved in the different blankets.

Also shown in Fig. 2.7 are the fission density distributions for the mixed enrichment cases. The fission rate in the inner row of the 0.71/1.2/2.0 enriched blanket is about five percent greater than the corresponding fission rate in the 0.71 uniformly enriched blanket. However, the fission rate in the outer row is about ten percent less than the corresponding fission rate in the 2.0 uniform enrichment case. In the mixed enrichment blanket, 2.0/1.2/0.71, the fission rate is greater by about ten percent than in the corresponding 0.71 uniform enriched case.

Table 2.5 summarizes the degree of power flattening achieved in the various blankets presented in Fig. 2.7. As anticipated, the degree of flattening achieved increases with enrichment. However, as indicated

Fig. 2.6 U-235 Equivalent Enrichment of U-238 as a Function of Position in a Radial Blanket

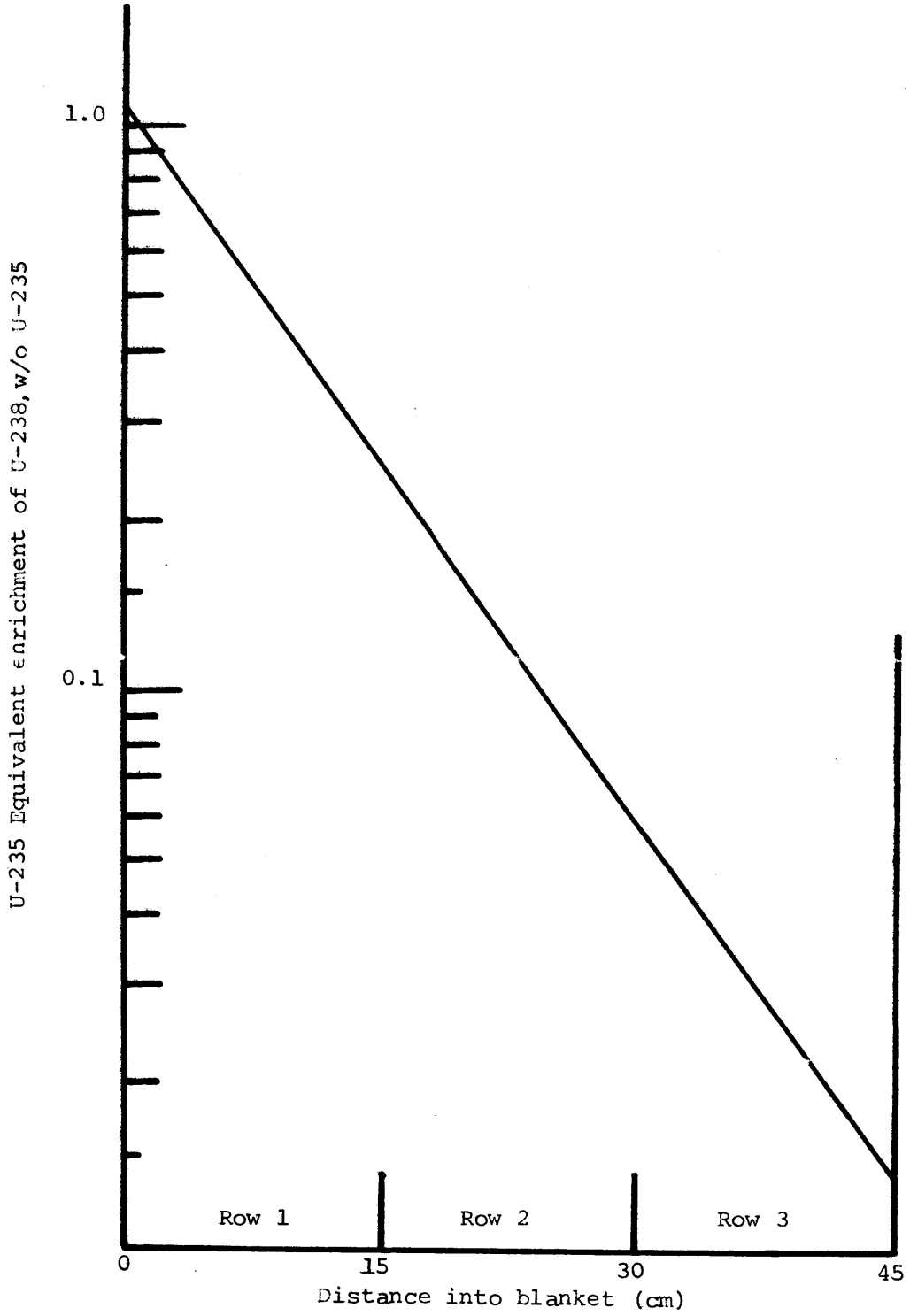

Fig. 2.7 Fission Density Distributions for Blankets of Various U-235 Enrichments

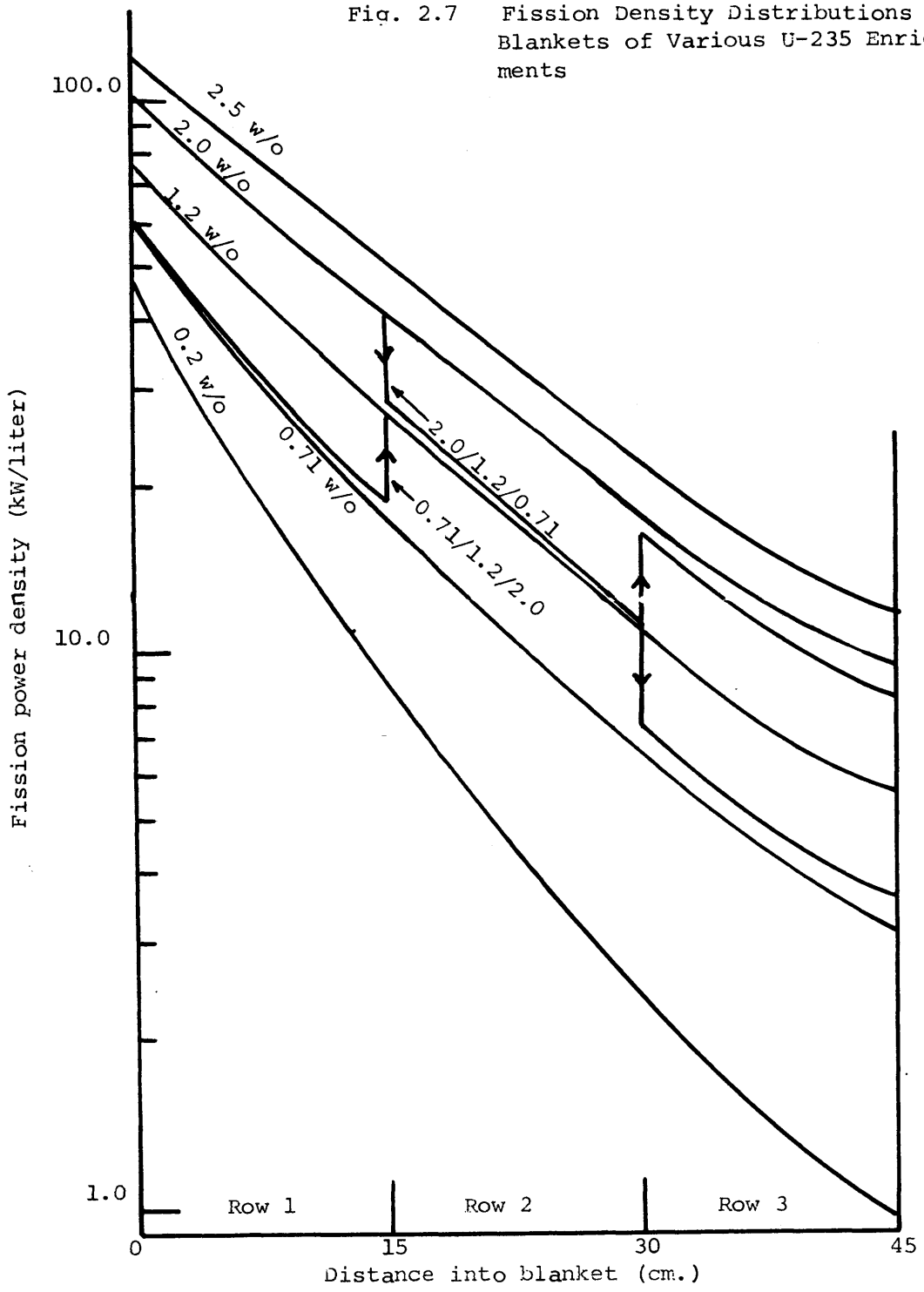

in Table 2.5 the incremental gain in power flattening decreases after about 1.2 $^{w}/_{o}$. It should be pointed out that the multiply enriched blankets offer little change in the individual row peaking factors, except for the case where row two is more highly enriched than row one.

TABLE 2.5 Peak-to-Minimum Fission Density Ratio for Various Blankets

Blanket Enrichment	Entire Blanket	Row 1	Row 2	Row 3
0.20 $^{w}/_{o}$ U-235	50	5.7	3.5	2.5
0.71 $^{w}/_{o}$ "	21	3.7	2.7	2.1
1.2 $^{w}/_{o}$ "	14	2.8	2.5	2.0
2.0 $^{w}/_{o}$ "	11	2.5	2.35	1.9
2.5 $^{w}/_{o}$ "	10	2.4	2.3	1.85
0.71/1.2/2.0	7.5	3.3	2.5	2.0
2.0/1.2/0.71	30	2.5	2.5	2.1

The results of this section pertain only to fission heating analysis. To complete the blanket heating analysis gamma and neutron heating due to leakage from the core must also be analyzed. Sections 2.4 and 2.5 address gamma and neutron heating, respectively.

2.4 Gamma Heating Analysis

As shown in Table 2.1, gamma rays form about twelve percent (25 Mev) of the total energy recoverable from a fission event. However, in the blanket region of an LMFBR one cannot assume that local fissions are the only source of local energy deposition. This is because the blanket acts as a shield for leakage of core neutrons and gamma rays,

which creates a net energy flow into the blanket. Looked at in this respect, the blanket produces heat from fission events, gamma ray absorption and neutron attenuation, with the latter two originating both locally and from the core. This section will deal with blanket heating from gamma ray absorption.

2.4.1 Gamma Energy Absorption Cross Sections

A forty-group coupled neutron (22 groups)-gamma (18 groups) cross-section set developed at the Oak Ridge National Laboratory (M-2) was used for gamma heating analysis. The production of gamma rays is treated by appropriate downscatter from the upper 22 neutron groups into the lower 18 gamma groups; and one multigroup S_n solution suffices for both neutron and gamma ray distributions. Use of coupled neutron-gamma cross sections is considerably more convenient than running successive neutronic and photonic calculations, as is sometimes done (e.g., Ref. M-3).

Gamma rays are produced by:

1. Nuclear fission
2. Fission product decay
3. Neutron capture product decay
4. Inelastic scatter of neutrons
5. Annihilation of positrons.

They lose energy to their surroundings by:

1. Pair production
2. Compton scattering
3. Photoelectric effect.

The three absorption events cover the range of important gamma interactions (E-5). Pair production, which is important at high energies (>1.02 Mev) creates a positron-electron pair. When the positron annihilates, new gamma rays are formed at lower energies than the original gamma ray. This event is accounted for by a formulation similar to inelastic scattering of neutrons in the cross-section set.

Compton scattering is important in the 0.1 to 2.0 Mev range. These events reduce the gamma energy, but without extinction of the gamma ray itself. Again this is a scattering event that is accounted for by downscatter terms in the 18 gamma ray groups.

The final event, dominant at low energies (< 100 kev) is the photoelectric effect. Here, the gamma is absorbed, depositing all of its energy locally.

Microscopic gamma energy absorption cross sections in units of Mev-barns were conveniently included in the cross-section set so that the calculation of the volumetric energy deposition rate (Eq. 2.4) could be straightforwardly performed. Table 2.6 lists the region-wise multigroup macroscopic gamma energy absorption cross sections (in units of Mev/cm) which were input into the ANISN code as "foil materials," so that when activation rates were calculated the proper summation (Eq. 2.4) was performed yielding the distribution of gamma energy deposition rates in units of Mev/sec-cm^3. (Note: Since there was no significant difference between the uranium and plutonium microscopic gamma absorption cross sections, regions with the same volume percents of fuel, structural material and coolant have the same macroscopic cross section.) It is also interesting to note that the steel reflector is a much better energy

TABLE 2.6 Macroscopic Gamma Energy Absorption Cross Sections (Mev/cm)

Group Number	Upper E Mev	Core	Blanket	Steel Reflector	Na Reflector
23	10.0	1.3452	2.1422	1.3200	0.14081
24	8.0	1.0382	1.5852	1.1332	0.11521
25	6.5	0.7473	1.1732	0.87524	0.09500
26	5.0	0.5555	0.86391	0.67267	0.07820
27	4.0	0.4148	0.6369	0.52784	0.064625
28	3.0	0.32103	0.4901	0.42265	0.054275
29	2.5	0.26782	0.4053	0.35684	0.04700
30	2.0	0.23023	0.3500	0.30304	0.040525
31	1.66	0.20591	0.3159	0.25953	0.03500
32	1.33	0.18856	0.2672	0.21447	0.028875
33	1.00	0.17960	0.2839	0.17464	0.023383
34	0.80	0.18216	0.29930	0.14151	0.018728
35	0.60	0.21095	0.3634	0.10637	0.013583
36	0.40	0.28586	0.5088	0.080994	0.00940
37	0.30	0.44020	0.79716	0.070356	0.006488
38	0.20	0.82181	1.5006	0.094285	0.00375
39	0.10	0.7766	1.3828	0.29545	0.00313
40	0.05	3.252	5.5012	2.72288	0.02625

absorber than a pure sodium reflector.

2.4.2 Gamma Heating Results

The results of the gamma heating analysis using the methods outlined in the previous section is given in Fig. 2.8. For clarity, only the 0.2, 1.2 and 2.5 enriched blankets are plotted. The other cases, including the mixed enrichment blankets, are similar to, and within the bounds of the 0.2 and 2.5$^{w}/_{o}$ blankets. A few pertinent observations can be made.

Most noticeable is the characteristic exponential attenuation of the gamma-deposited energy for all blanket enrichments. The lines on this semilog plot are almost parallel showing an e-folding distance of 13 centimeters for the depleted blanket and 15 centimeters for the 2.5% blanket. The other blankets have an e-folding distance between 13 and 15 cm. Other general features are the nonlinearity of the curves at both extremes of the blanket, which is attributed to the discontinuities in material composition (indicated in Table 2.6) at the core blanket and blanket-reflector interfaces.

To show the relative effect of gamma attenuation in the blanket, a plot of the ratio of the local gamma ray energy deposition to fission energy deposition (assuming 200 Mev per fission event) is given in Fig. 2.9. The results indicate that gamma rays are relatively more important deeper in the blanket and in the lower enrichment blankets where the fission rate is smaller.

However, it must be noted at this point that the fission rates used in evaluating these ratios were those obtained from the coupled neutron gamma cross-section set. This set underpredicts the fission rate in

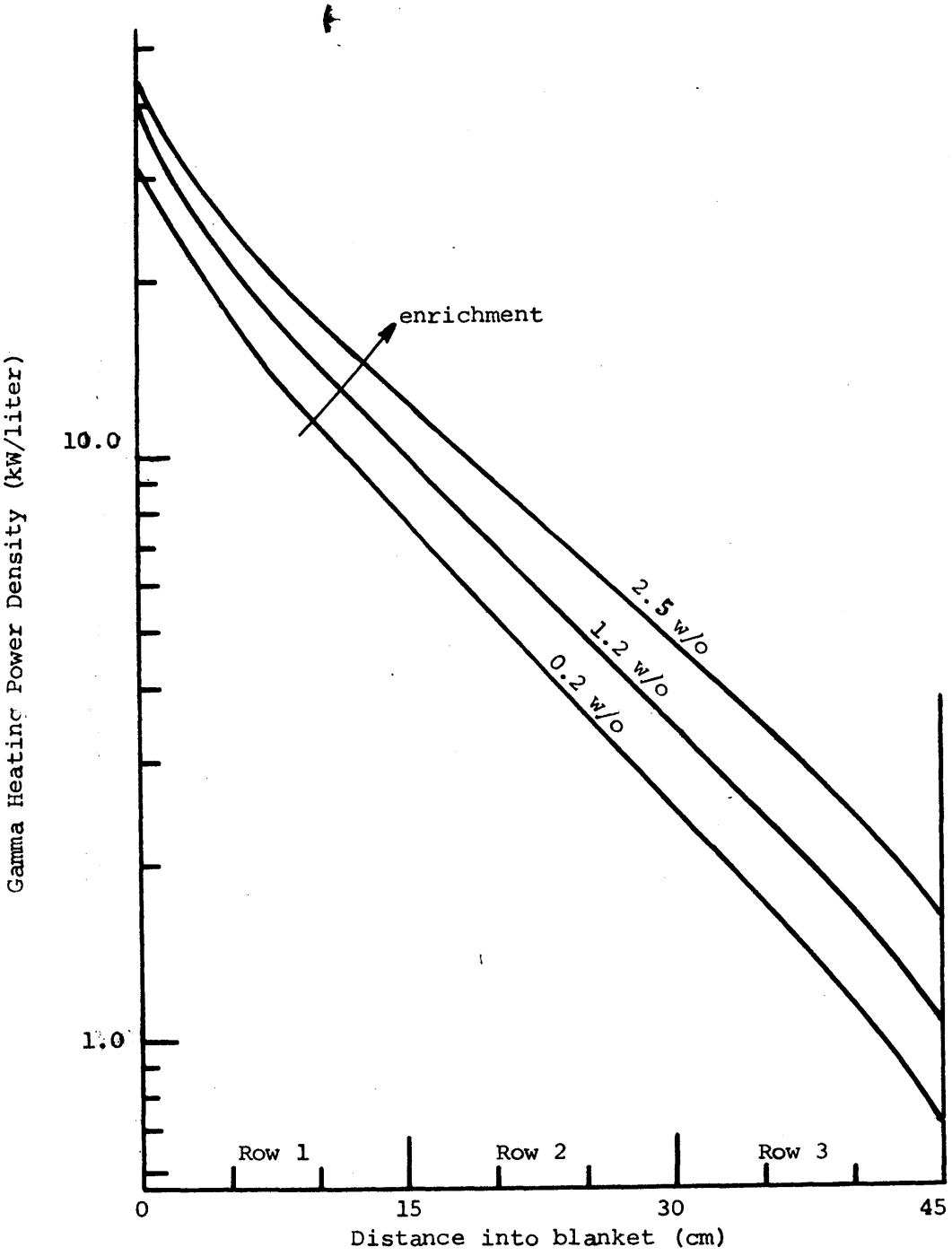

Fig. 2.8 Gamma Energy Deposition Traverses for Variously Enriched Blankets

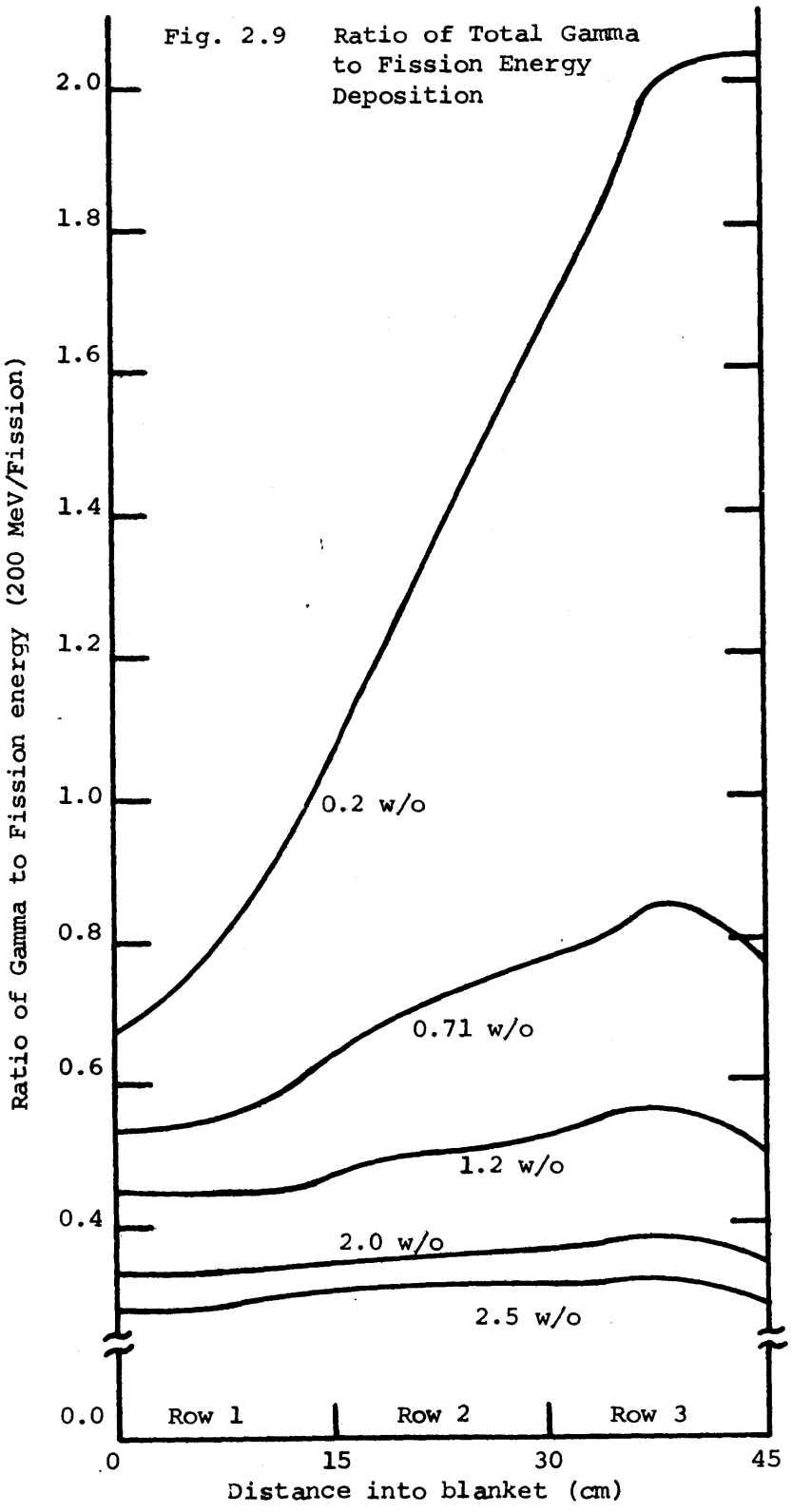

Fig. 2.9 Ratio of Total Gamma to Fission Energy Deposition

the blanket with respect to those evaluated with the 26-group neutron cross section used in Section 2.3.2. The 26-group cross-section set is deemed more accurate than the 40-group coupled neutron-gamma set for calculating fission distributions since the 26-group set has been especially prepared for fast reactor calculations, including self-shielding of the U-238 capture cross section. Also the 26-group set has many more groups below 100 kev, whereas the coupled set has more neutron energy groups above 1 Mev, which is more suitable for shielding calculations.

A comparison of the fission rates calculated with the two different cross-section sets is shown in Fig. 2.10. Normalizing the two fission rates at the innermost point in the blanket shows that fairly good agreement is attained in the core, with a maximum underprediction by the 40-group set of about 14% at the core center. However, in the blanket the 40-group set underpredicts the blanket fission rate throughout, with a maximum underprediction of more than a factor of two at the blanket-reflector interface. Thus one would prefer to use the 26-group fission data, and the 22/18-group gamma data. To evaluate the effect of the core gamma rays leaking into the blanket, the effect of blanket-fission-produced gammas, given by the 22/18-group calculation, was decoupled from the total production of gamma rays. This was achieved by making the assumption that gamma rays produced by fission events were absorbed locally. As previously noted, this is the usual "infinite medium" or "zero gradient" assumption made when calculating energy deposition rates from fission rates in reactors (L-3), used here as a matter of expediency. Thus 25 Mev (Table 2.1) per local fission event (22/18-

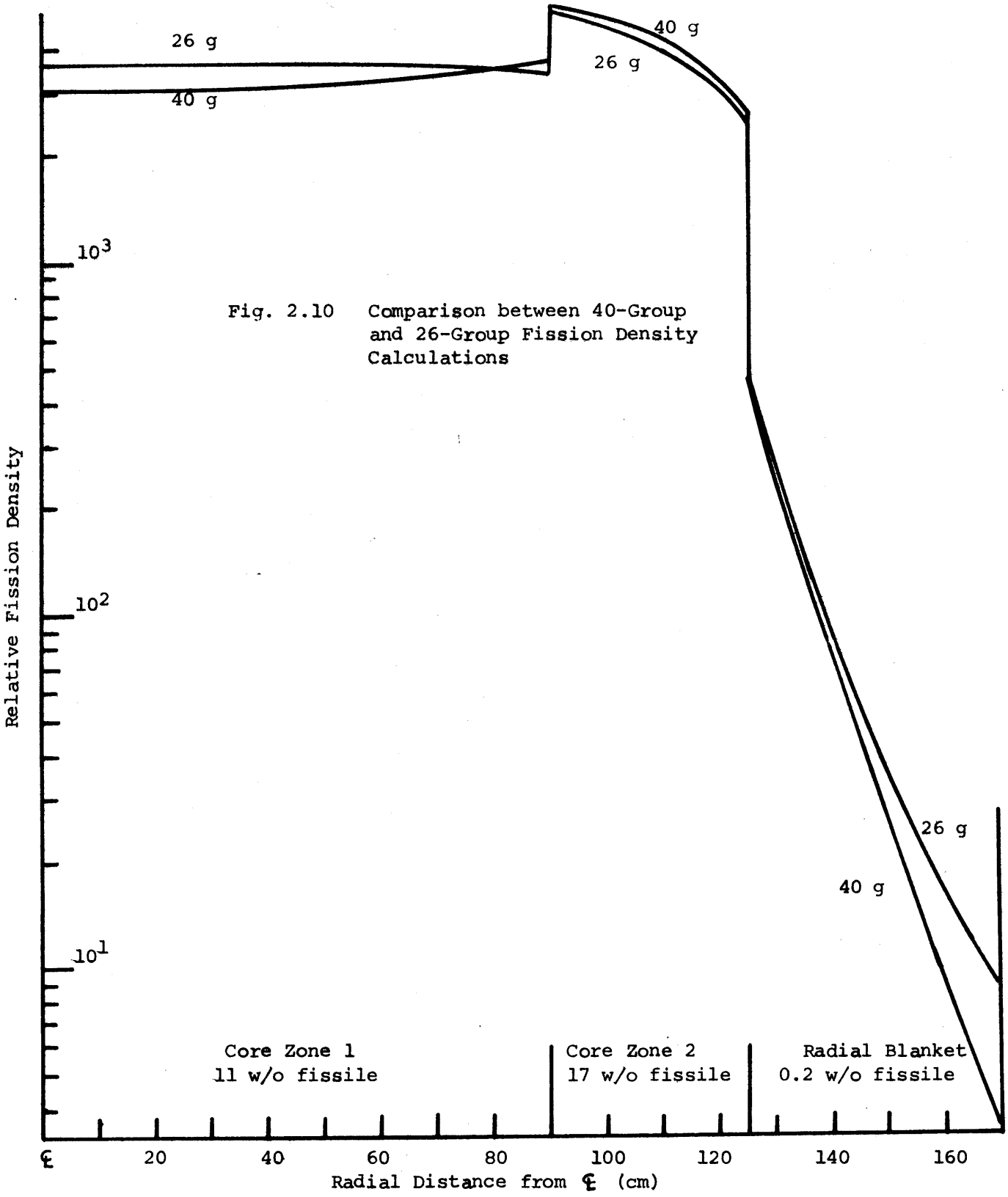

Fig. 2.10 Comparison between 40-Group and 26-Group Fission Density Calculations

group calculation) was subtracted from the calculated local gamma energy deposition, leaving the excess gamma energy, i.e., that gamma energy not attributable to local fissions, but rather due to leakage of core gamma rays. Figure 2.11 shows the excess gamma energy as a function of enrichment and distance into the blanket. The mixed enrichment blankets are not shown in Fig. 2.11 for simplicity, since the data falls within the data already plotted. Basically this plot shows the gamma energy deposition rate in the blanket; treating the blanket as if it were just a neutron and gamma shield, for the core.

The major consequence of Fig. 2.11 follows from the closeness of the curves for the different enrichments, especially in the first 15 centimeters where the variation is less than 8 percent. This figure implies that the excess gamma heating is essentially independent of enrichment, and therefore independent of blanket fission rate. This result is important since it permits inclusion of gamma rays in the heating analysis by simply adding a component, independent of the local fission heating rate to the local fission heating rate. This component is a function only of distance from the core, x cm, and can be represented by the following equation:

$$E_\gamma = 21.6\ e^{-0.0715x}\ \text{kW/liter} \tag{2.5}$$

It should be noted that the factor 21.6 depends only on the reactor power (2500 MW_T) for a given reactor configuration. Hence, to make Eq. 2.5 more general, it is rewritten as

$$E_\gamma = P\ (0.864)\ e^{-0.0715x}, \tag{2.6}$$

Fig. 2.11 Excess Gamma Energy Deposition in the Blanket

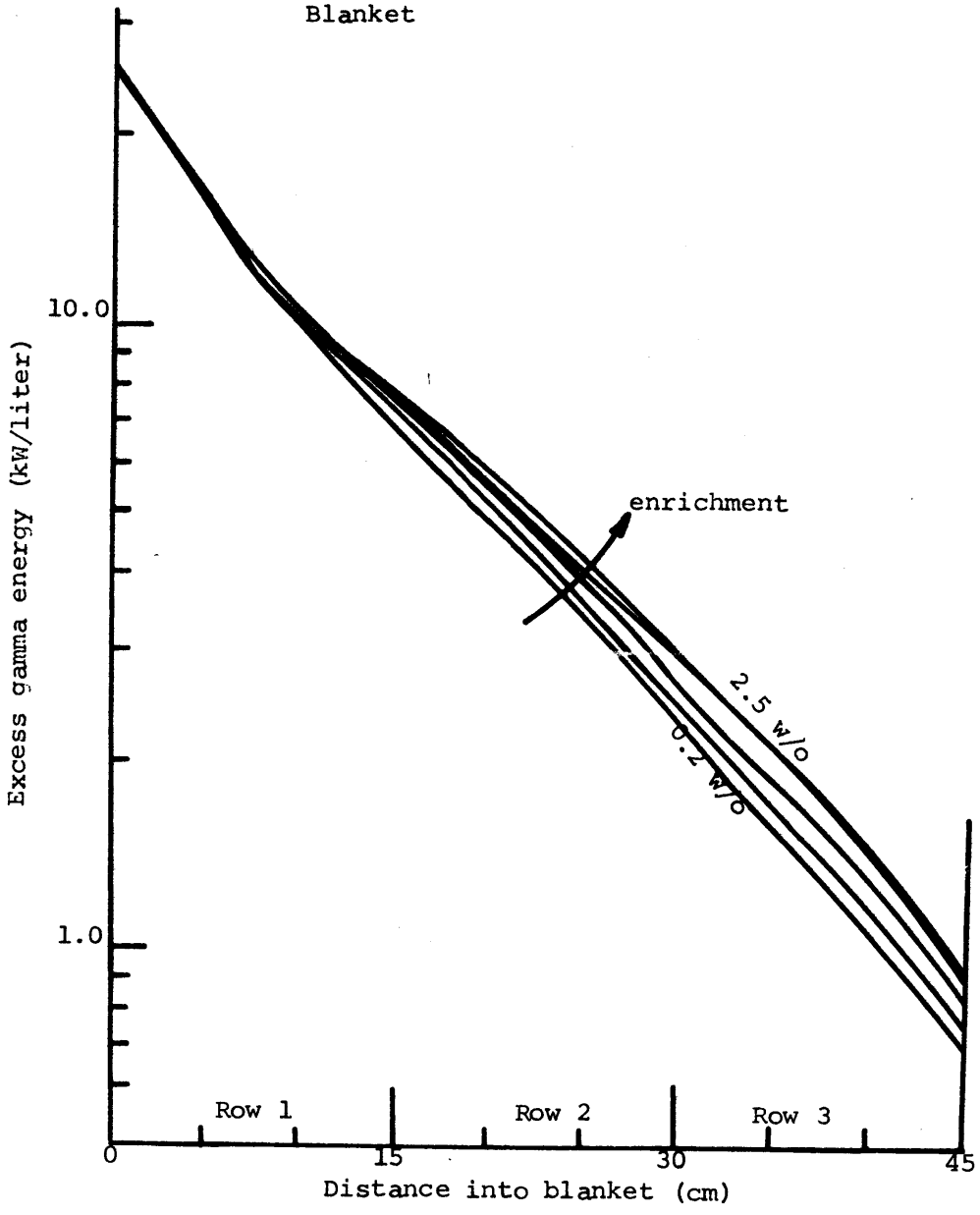

where P is the reactor power in units of 100 MW_T.

Utilizing Eq. 2.6 the maximum discrepancy, at the core-blanket interface would be about twelve percent, and since the relative gamma heating at that point ranges from about twenty to fifty percent of the fission energy, the absolute discrepancy in heating rates is only about two to six percent.

Table 2.7 shows the ratio of the average excess gamma energy (given by Eq. 2.5) to the local fission heating rate (26-group calculation). This ratio is depicted in Fig. 2.12, and indicates the importance of including gamma heating in a heating analysis of the blanket. As can be seen, the ratio at a given point decreases with enrichment.

Except for the depleted blanket which has a ratio of about 1.0, the ratio is less than 0.5 decreasing to about 8 percent. Thus even a difference of up to 20 percent, which is more than the maximum deviation between Eq. 2.6 and the data presented in Fig. 2.11 and listed in Table 2.7, typically creates less than ten percent error in the total heating rate. It should be emphasized that this is a general result, since the mixed enrichment cases, which constitute a severe test of this development, conform to within the maximum deviations listed in Table 2.7.

2.5 Neutron Heating Analysis

The previous two sections have discussed the blanket heating effects due to fission events and gamma absorptions. To complete the heating analysis the contribution of neutron heating to the total heating rate will be presented in this section.

TABLE 2.7 Ratio of Excess Gamma Energy (Eq. 2.6) to Fission Energy as a Function of Enrichment and Position

Depth into Blanket (cm)	Ratio of Excess Gamma Energy to Fission Energy							Excess γ Energy (Eq. 2.6) (kW/liter)	Maximum Deviation* (%)
	Blanket Enrichment (w/o U-235)								
	0.2	0.71	1.2	2.0	2.5	0.71/1.2/2.0	2.0/1.2/0.71		
2.5	0.5397	0.3814	0.2832	0.2065	0.1768	0.4202	0.2065	18.06	12.8
7.5	0.6774	0.4134	0.2873	0.1996	0.1675	0.3804	0.2003	12.64	8.96
12.5	0.7901	0.4328	0.2805	0.1852	0.1529	0.3978	0.1868	8.837	5.94
17.5	0.9055	0.4350	0.2669	0.1718	0.1405	0.2672	0.2588	6.181	10.7
22.5	0.9861	0.4144	0.2535	0.1598	0.1294	0.2537	0.2468	4.323	10.9
27.5	1.0428	0.3938	0.2403	0.1490	0.1197	0.2475	0.2338	3.024	11.8
32.5	1.0644	0.3821	0.2261	0.1380	0.1100	0.1368	0.3327	2.115	16.5
37.5	1.0464	0.3501	0.2069	0.1244	0.0985	0.1018	0.3094	1.479	18.9
42.5	0.9582	0.3109	0.1766	0.1042	0.0817	0.1017	0.2672	1.044	17.9

*Absolute percent difference between excess gamma energy predicted by Eq. 2.6 and the excess gamma energy plotted in Fig. 2.11.

Fig. 2.12 Ratio of Excess Gamma Energy (Due to Core Leakage) to Fission Energy in the Blanket

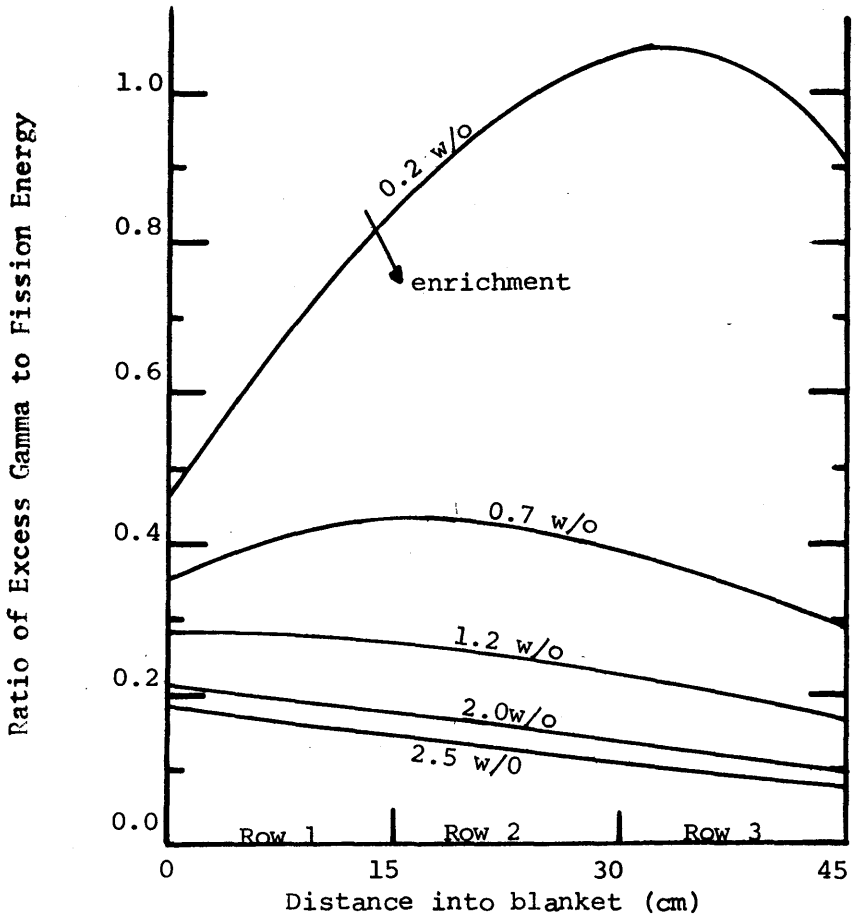

2.5.1 Mechanisms of Neutron Heating

Three different events are considered to contribute to the neutron heating rate. They are:

a. neutron elastic scattering

b. neutron inelastic scattering

c. neutron capture.

Actually, these three events are similar in the sense that the energy associated with each is a recoil energy determined by the law of conservation of momentum. Thus the microscopic energy absorption cross section, ${}_x\sigma^E_{ij}$ is determined by simply multiplying the mean energy loss per event (ΔE_{ij}) times the microscopic cross section for event x, ${}_x\sigma_{ij}$:

$$ {}_x\sigma^E_{ij} = ({}_x\sigma_{ij})(\Delta E_{ij}), \tag{2.7} $$

where ${}_x\sigma^E_{ij}$ is the microscopic energy absorption cross section for material j, energy group i, defined for use in Eq. 2.4.

The following paragraphs will briefly describe the derivation of ${}_x\sigma^E_{ij}$ for the three events listed above. A more detailed development is presented by Wood (W-5).

The average energy lost per elastic scatter can be defined as (L-3)

$$ ({}_a\overline{\Delta E_{ij}}) = \overline{E}_i(1 - e^{-\xi}), \tag{2.8} $$

where

$\overline{E_i}$ is the mean energy of energy group i, bound by energies E_i and E_{i+1}

$\overline{E}_i = (E_i - E_{i+1})/\ln (E_i/E_{i+1})$

ξ is the average increase in lethargy per collision

$\xi = 1 + (\alpha/(1-\alpha)) \ln \alpha$, with $\alpha = (A-1/A+1)^2$.

The microscopic elastic scattering cross section ${}_a\sigma_{ij}$ is contained in the 26-group cross-section set (A-6).

The average recoil energy lost per inelastic scattering can be approximated by assuming that the recoil energy from the incident neutron is totally deposited before the neutron is reemitted. Then for inelastic scattering with a nucleus of atomic weight A the recoil energies are:

$$ {}_bE_I = \frac{1}{A+1} E_i \tag{2.9} $$

$$ {}_bE_R = \frac{1}{A} E_n, \tag{2.10} $$

where E_i and E_n are the incident and reemitted neutron energies.* The microscopic inelastic scattering cross section, ${}_b\sigma_{ij}$, and inelastic downscatter cross section, ${}_b\sigma_{i\rightarrow n,j}$, are in the form of an inelastic downscatter matrix contained in the 26-group cross section set (A-6).

Capture events lead to the formation of a compound nucleus, as do

---

*Actually, the compound nucleus reemits a neutron before it dissipates its energy. The total recoil energy of an inelastic scatter event where the compound nucleus has energy, ${}_bE_I$, before reemission (as opposed to zero energy assumed above) is a function of the direction of the reemitted neutron with respect to the initial neutron direction. If all directions are equally probable, then the total recoil energy of the nucleus can be shown to be equal to $(E_i + E_n)/A$ which is identical to the sum of Eqs. 2.9 and 2.10, but with $A+1 \approx A$ in Eq. 2.9, an excellent approximation for the heavy metals which are involved in most of the inelastic scattering.

inelastic scattering events. Hence the same recoil energy is imparted to the compound nucleus, ${}_cE_I$, as given in Eq. 2.9. Also, after a compound nucleus is formed by a neutron capture event, there is a recoil energy imparted by the emission of a gamma ray of energy E_γ given by

$$ {}_cE_R = \frac{1}{A} \frac{E_\gamma^2}{2m_o c^2}, \qquad (2.11) $$

where $m_o c^2$ = 931 Mev, the mass energy equivalent of one nucleon. A conservative estimate (i.e., leading to an overprediction) of E_γ can be determined by assuming that only one gamma ray of energy equal to the binding energy of the last nucleon (E-5) is emitted immediately after capture. The microscopic cross section for this event is given by the appropriate cross section in the 26-group neutron cross-section set (A-6).

A summary of the energy absorption cross sections for the three neutron heating mechanisms is contained in Table 2.8. To get the heating rates presented in the next section the procedure outlined by Eq. 2.4 is followed; namely, the cross sections are homogenized for the constituent materials in the different reactor zones, and multiplied by the multigroup flux determined by an ANISN calculation.

2.5.2 Neutron Heating Results

The results of the neutron heating analysis for the variously enriched blankets are shown in Fig. 2.13. The total heating rate plotted in Fig. 2.14 shows the contributions of the mechanisms discussed in Section 2.5.1 to the total neutron heating rate. Figure 2.14 is for the depleted blanket; the results for the other blankets are similar. As can

TABLE 2.8 Summary of Microscopic Energy Absorption Cross Sections for Evaluation of Neutron Heating

Mechanism	Energy per Event ($\Delta\bar{E}_{ij}$)	Microscopic Cross Section ($_x\sigma_{ij}$)	Equation Number
Elastic Scattering	$\bar{E}_i(1 - e^{-\xi})$	$_{el}\sigma_{i,j}$	2.8
Inelastic Scattering Recoil			
due to incident neutron, $\bar{E}_i$	$\left(\frac{1}{A+1}\right)\bar{E}_i$	$_{in}\sigma_{i,j}$	2.9
due to re-emitted neutron, $\bar{E}_n$	$\left(\frac{1}{A}\right)\bar{E}_n$	$_{in}\sigma_{i\rightarrow n,j}$	2.10
due to de-excitation gamma, E_γ	$\frac{1}{A}\left(\frac{E_\gamma^2}{2m_oc^2}\right)$	$_{in}\sigma_{i\rightarrow n,j}$	2.11
Neutron Capture Recoil			
due to incident neutron, $\bar{E}_i$	$\left(\frac{1}{A+1}\right)\bar{E}_i$	$_c\sigma_{i,j}$	2.9
due to gamma, E_γ	$\frac{1}{A}\left(\frac{E_\gamma^2}{2m_oc^2}\right)$	$_c\sigma_{i,j}$	2.11

Total microscopic energy absorption cross section for neutron heating:

$$\sigma_{ij}^E = \bar{E}_i(1 - e^{-\xi})({}_{el}\sigma_{i,j}) + \left(\frac{\bar{E}_i}{A+1}\right)({}_{in}\sigma_{i,j}) + \left(\frac{\bar{E}_n}{A} + \frac{E_\gamma^2}{2m_oc^2A}\right)({}_{in}\sigma_{i\rightarrow n,j}) + \left(\frac{\bar{E}_i}{A+1} + \frac{E_\gamma^2}{2m_oc^2A}\right)({}_c\sigma_{i,j}).$$

Fig. 2.13 Neutron Heating Rates in the Blanket

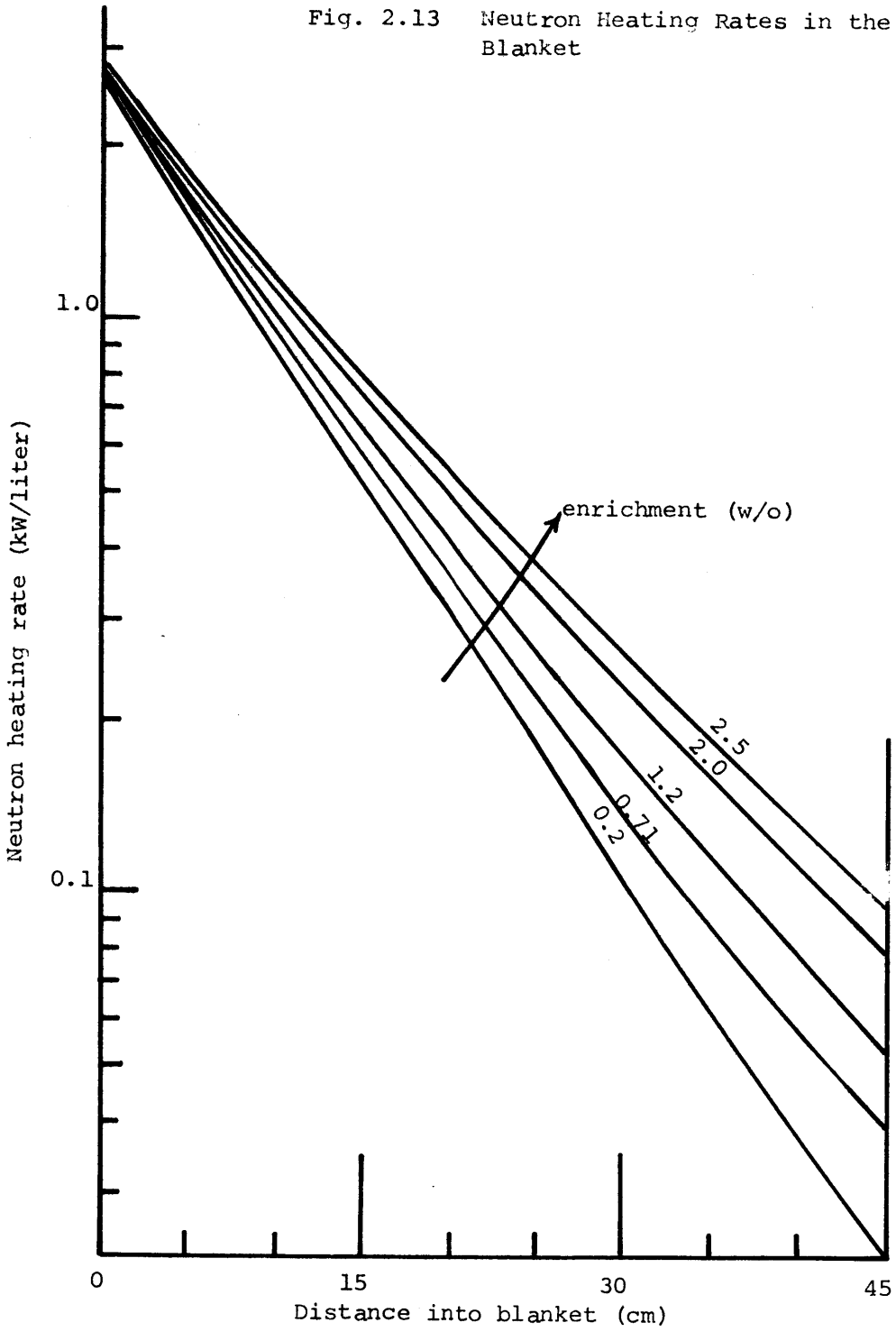

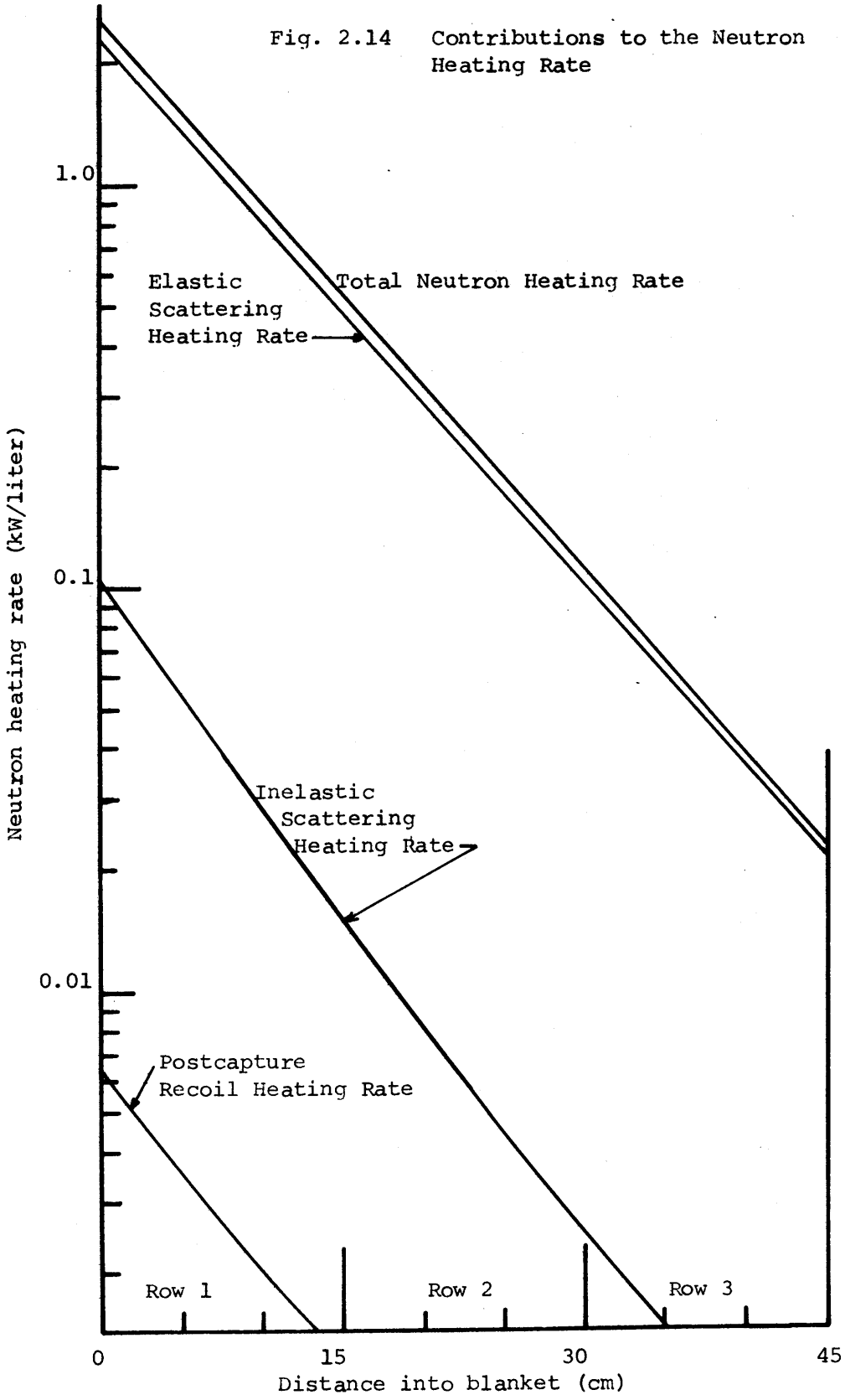

Fig. 2.14 Contributions to the Neutron Heating Rate

be seen, elastic scattering accounts for practically all of the neutron heating, with the recoil energy due to neutron capture practically negligible. Hence, the assumptions made with respect to calculating recoil energy are shown here to have a negligible effect.

To show the relative effect of neutron heating in the blanket, a plot of the ratio of the local neutron heating rate to the local fission energy deposition rate (200 Mev per fission) is presented in Fig. 2.15. It should be noted here, as with the gamma heating analysis, that the relative contribution of neutron heating increases with decreasing enrichment. However, in comparison to the gamma heating ratio, the neutron heating to fission heating ratio is small.

Figure 2.16 shows the neutron heating at various positions in the blanket as a function of enrichment. To deduce the effect of the core on the total neutron heating rate the contribution to the neutron heating rate due to neutrons produced by fissions in the blanket was determined by extrapolating the lines in Fig. 2.16 to the appropriate negative enrichment where the fission rate is zero (as determined in Fig. 2.6). The portion of the neutron heating due to neutrons originating in the core, or excess neutron heating, is found to be independent of enrichment, depending only on the distance from the core, as shown in Fig. 2.17. This general result, isolating the excess neutron heating (due to core neutrons) parallels the result obtained in Section 2.3.2 which isolated the excess gamma heating in the blanket caused by gammas leaking from the core. Equation 2.12 summarizes the excess neutron heating, E_n, in the blanket caused by neutrons originating in the core.

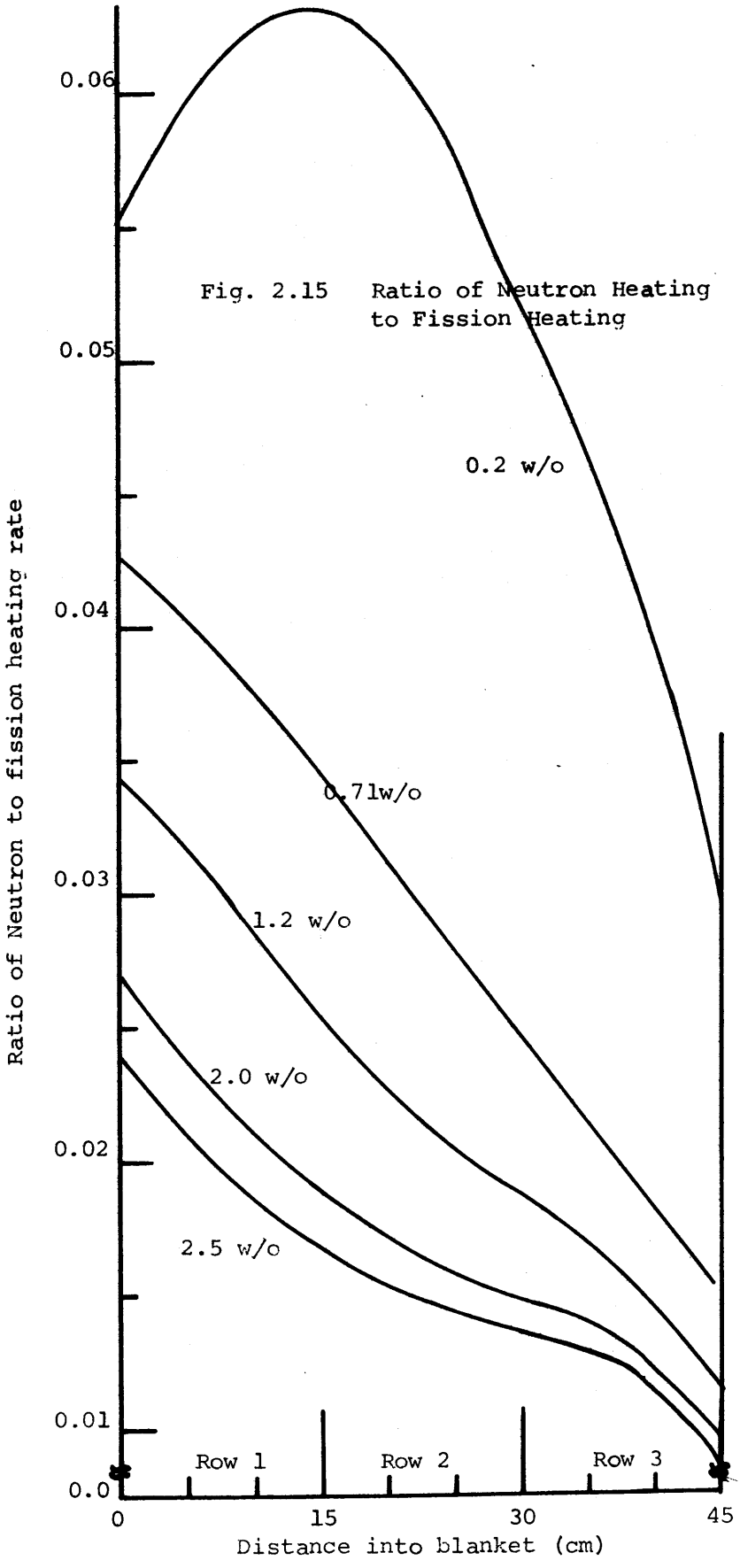

Fig. 2.15 Ratio of Neutron Heating to Fission Heating

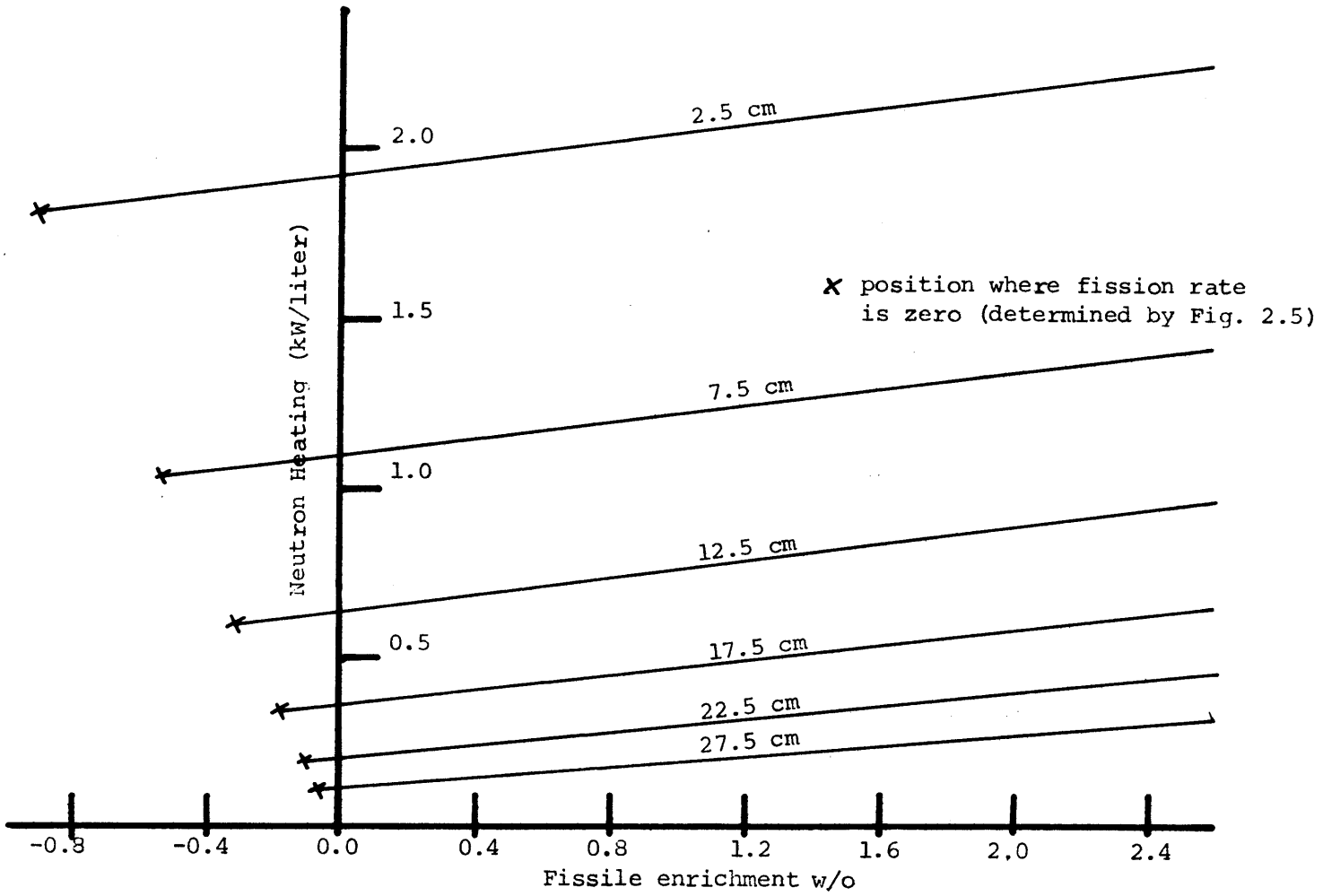

Fig. 2.16 Effect of Enrichment on Neutron Heating

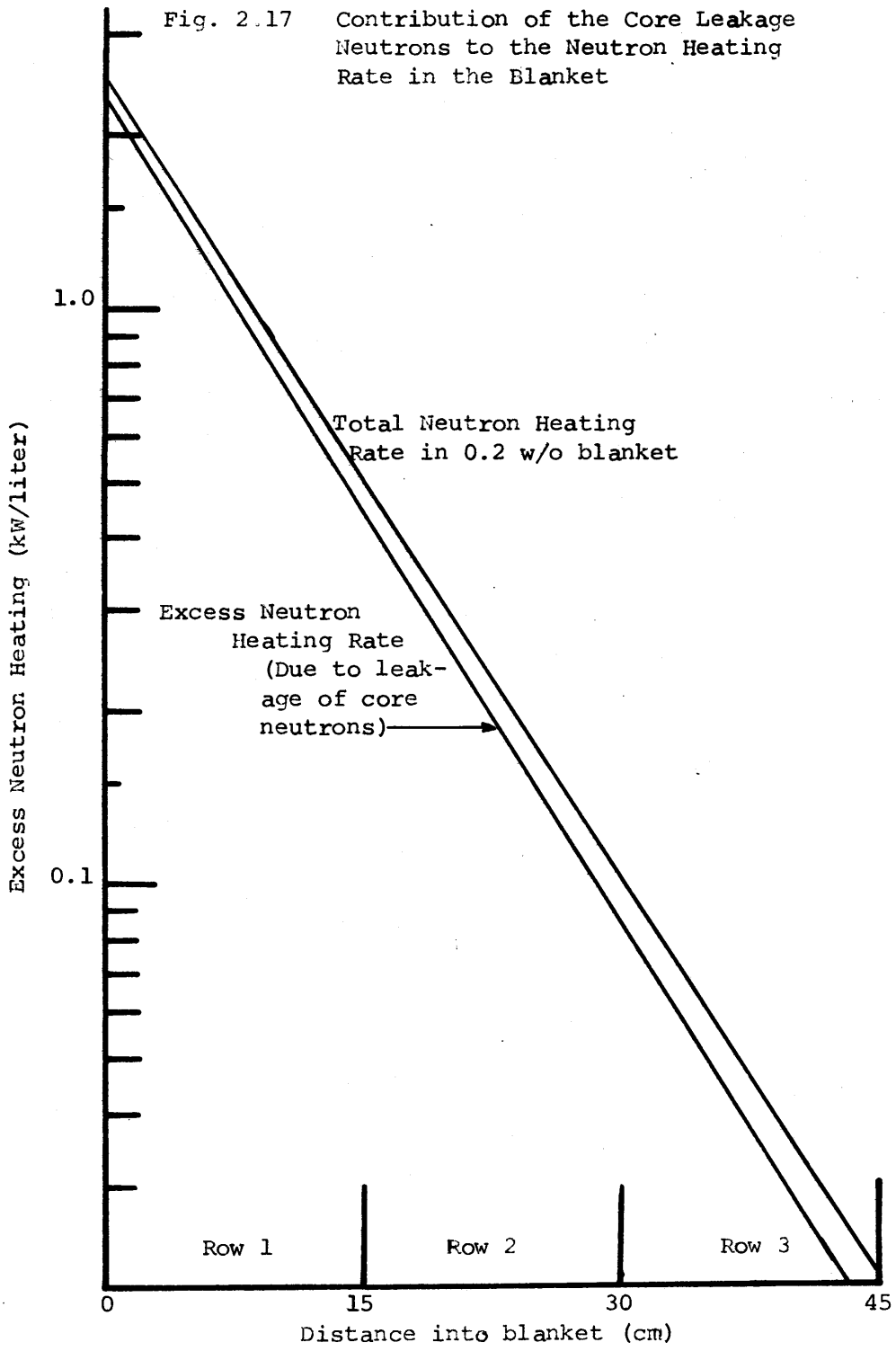

Fig. 2.17 Contribution of the Core Leakage Neutrons to the Neutron Heating Rate in the Blanket

$$E_N = 2.4\ e^{-0.1098x\,(cm)}\ (kW/liter) \qquad (2.12)$$

The factor 2.4 is a function of the reactor power, in this case 2500 MW_T, and otherwise depends only on the given reactor configuration. To make Eq. 2.12 more general it is rewritten as

$$E_n = P(0.096)\ e^{-0.1098x}, \qquad (2.13)$$

where P is the reactor power in units of 100 MW_T.

Table 2.9 lists the neutron heating in the blanket caused by neutrons originating in the blanket at the midpoint of each blanket row. As can be seen the excess blanket neutron heating, i.e., due to the leakage of core neutrons, is the predominant contribution to the total heating rate in all of row one. Deeper in the blanket (where Eq. 2.12 decreases rapidly) and in the more highly enriched blankets (where the fission rates are high) the relative effect of the core on neutron heating diminishes.

The difference between the total neutron heating rate and the excess neutron heating is the neutron heating due to neutrons produced by fissions in the blanket. Table 2.9 lists the absolute and relative effect of this heating by locally produced neutrons, in the blanket. As can be seen the ratio of neutron heating due to fissions in the blanket to fission heating is very small, and practically the same (~0.6%) for all enrichments. The nominal infinite medium result (Table 2.1) would be 5/202 ~ 0.025 which indicates that only about 1 of the 5 Mev is deposited as neutron kinetic energy, the rest converted to gamma rays through inelastic scatter. This is the same conclusion reached by Wood (W-5).

TABLE 2.9 Neutron Heating Due to Fissions in the Blanket for Various Enrichments (0.2-2.5 w/o).

Neutron Heating Due to Neutrons Produced in the Blanket (kW/liter)						
Distance from Core (cm)	Blanket Enrichment (w/o U-235)					Excess Neutron Heating (Eq. 2.12)
	0.2	0.71	1.2	2.0	2.5	
7.5	0.0720	0.149	0.209	0.298	0.359	1.053
22.5	0.0256	0.0729	0.118	0.193	0.242	0.2026
37.5	0.00913	0.0319	0.0543	0.0926	0.118	0.0389

Ratio of Blanket-Produced Neutron Heating to Fission Heating					
Distance from Core (cm)	Blanket Enrichment (w/o U-235)				
	0.2	0.71	1.2	2.0	2.5
7.5	0.00386	0.00239	0.00475	0.00471	0.00476
22.5	0.00584	0.00699	0.00692	0.00714	0.00724
37.5	0.00646	0.00755	0.00760	0.00779	0.00786

2.6 Summary

The purpose of this chapter was to analyze the various contributions to the radial power distribution in the radial blanket region of an LMFBR. Since the blanket acts as a shield for the copious leakage of gamma rays and neutrons from the core, it is not sufficient to determine blanket power production by simply multiplying the local fission rate by the constant, 200 Mev/fission. For example, in a blanket fueled with 0.2% U-235 roughly 85 percent of the total neutron heating and gamma heating is due to the leakage of neutrons and gamma rays from the core. In a 2.5% U-235 enriched blanket, the core is responsible for about 50 percent of the blanket gamma and neutron heating.

Furthermore, since the fission rate in the blanket changes as the fissile enrichment changes, it is apparent that the relative effect of the core leakage on the blanket heating will also change, hence any simple multiplicative factor used to convert fission rate to power must also change. Lastly, the relative effect of the core leakage will vary with distance, and if a multiplier is used it must be a function of distance, as well as time.

The approach presented in this chapter bypasses these problems. Careful analysis of the three main contributions to the total blanket heating rate – fission heating, gamma heating, and neutron heating – has led to the development of equations to determine the total blanket heating rate, in a manner which separates in-leakage from local contributions. The total blanket heating rate (BHR) was approximated as the sum of the blanket fission heating rate (FHR) treated as a local source at

200 Mev/fission, and an effective blanket shield heating rate (SHR), to take into account the effect of neutron and gamma leakage from the core:

$$BHR = FHR + SHR, \tag{2.14}$$

and

$$SHR = GHR + NHR, \tag{2.15}$$

where the shield heating rate is given by the sum of the gamma heating rate (GHR) and neutron heating rate (NHR). Equations 2.6 and 2.13, repeated here in combined form give the SHR.

$$SHR = P[0.864\ e^{-0.0715x} + 0.096\ e^{-0.1098x}]\ kW/liter, \tag{2.16}$$

where x is the distance into the blanket in centimeters, and P is the reactor power in units of 100 MW_T.

The first term is the contribution of gamma heating; the second is the contribution of neutron heating, as discussed in Sections 2.3 and 2.4, respectively. It is clear that the effect of gamma heating is dominant, becoming an order of magnitude greater than neutron heating at only 2.7 cm into the blanket, and increasing with depth into the blanket, so that at 45 cm the ratio of gamma to neutron heating is 50:1. This effect is depicted in Fig. 2.18.

Figure 2.18 also shows the contributions to the total heating rate for the 0.2% and 2.5% U-235 enriched blankets discussed previously. It is clear that neglecting the contribution of the shield heating rate can lead to substantial underprediction of the total blanket heating rate. In the 0.2% blanket, the THR would be underpredicted by 50 to 100 percent, whereas in the 2.5% blanket the THR would be underpredicted

Fig. 2.18 Contributions to the Total Blanket Heating Rate

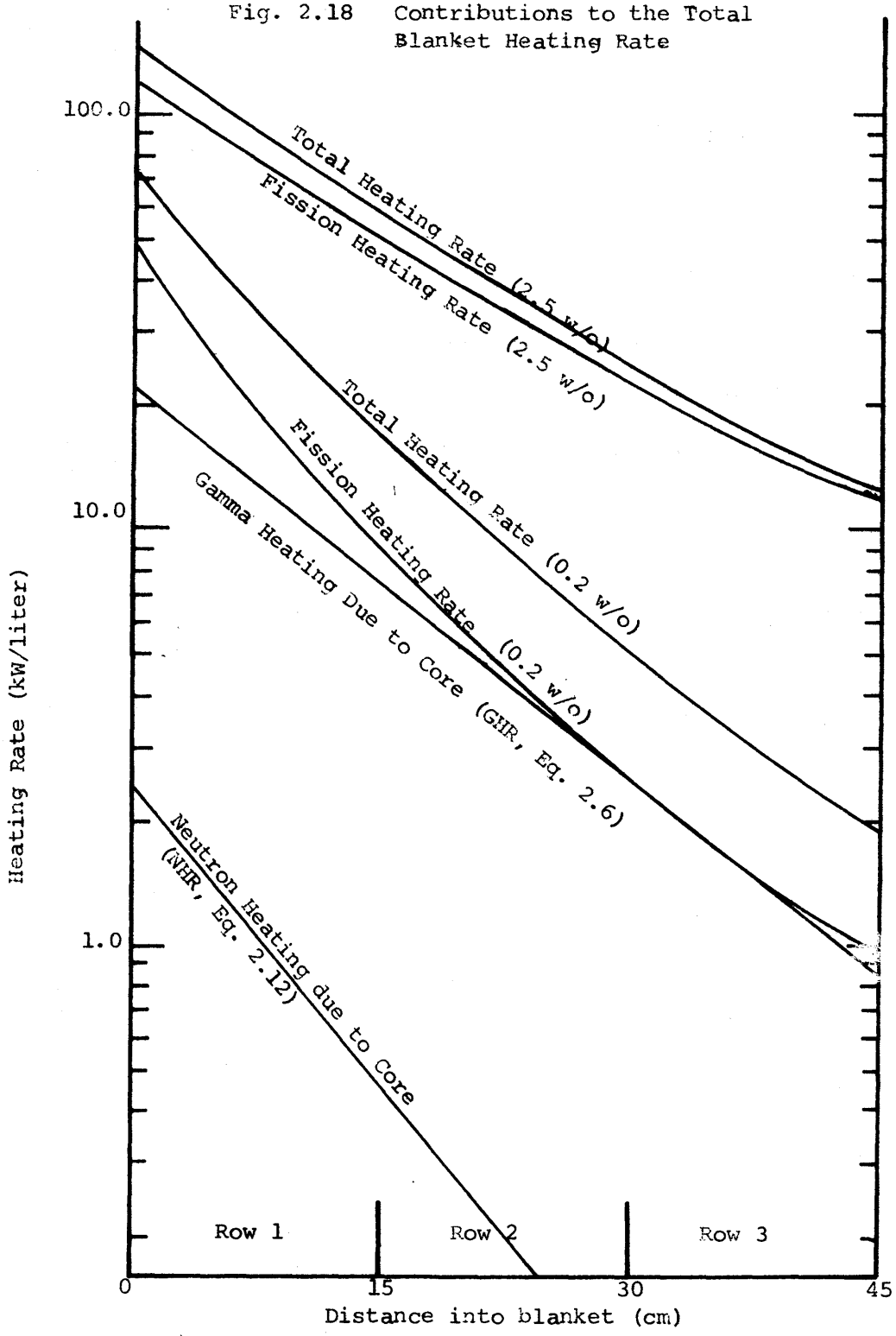

by about 10 percent. The smaller underprediction of the more highly enriched blanket would be expected since the fission rate is higher than for a lower enrichment blanket, and the shield heating rate becomes correspondingly less important.

One final point to be observed in Fig. 2.18 is the effect of the shield heating rate on the evaluation of power peaks in the blanket. Qualitatively speaking, inclusion of the shield heating rate will tend to flatten the power peak determined solely by the fission density if the fission density distribution decreases more sharply than the shield heating rate. This is the case for the 0.2% blanket where the ratio of maximum-to-minimum total power is 39, which is over twenty percent less than the factor of 50 determined from the ratio of maximum-to-minimum fission heating. However, the reverse is true for the 2.5% blanket where the ratio of maximum-to-minimum total power is 12, twenty percent greater than the ratio evaluated solely from the fission density.

In conclusion, it should be emphasized that the results presented in this chapter are not only applicable to beginning-of-life distributions (uniform enrichment blankets) but also to end-of-life distributions (mixed enrichment blankets). Furthermore, the results are applicable to seeded blankets, with variable or uniform enrichment; in-out managed blankets (represented by the 0.71/1.2/2.0 mixed enrichment case); and out-in managed blankets (represented by the 2.0/1.2/0.71 mixed enrichment case).

Chapter 3 will next analyze the economics of various blanket configurations, taking into account not only the fuel cycle economics but

also the economics of power flattening, utilizing the formalism for determining power depositions presented in this chapter.

Chapter 3

EVALUATION OF BLANKET CONFIGURATIONS

3.1 Introduction

The objective of the work reported in this chapter is the evaluation of the relative performance of various blanket configurations considering both blanket burnup and thermal-hydraulic contributions to the total power cost. In the latter assessment the results presented in Chapter 2 will be used to evaluate the effects of radial power gradients in the blanket on the reactor mixed-mean outlet temperature and ascertain the resultant changes in reactor thermal efficiency and pumping power.

This chapter is divided into three main sections. The first two describe in detail the methods employed to examine the various blanket-reflector configurations reported on in the third section. More specifically, Section 3.2 describes the burnup analysis; the reference reactor configuration is specified in Section 3.2.1 followed by a discussion of the preparation of a four-group cross-section set (Section 3.2.2). Section 3.2.3 cites the method of burnup employed, and Section 3.2.4 describes the burnup-economics model. Then, Section 3.3 develops the thermal-hydraulic-economics model.

Power and temperature relationships are utilized to derive equations expressing the economic penalty associated with the degradation of the mixed-mean outlet temperature (Section 3.3.2.1), and increased pumping power (Section 3.3.2.2) caused by power gradients in the blanket (Section 3.3.4).

Section 3.4 applies the methods set forth in Sections 3.2 and 3.3 to

a variety of blanket-reflector configurations. These case studies will consider variations in thickness, enrichment (seeding) and reflector composition.

A summary of Chapter 3 is included as Section 3.5.

3.2 Burnup Analysis

3.2.1 Reactor Configuration

The reactor configuration utilized in performing burnup studies is identical to the two-dimensional configuration mentioned in Section 2.2.1 and depicted in Fig. 2.1, repeated here as Fig. 3.1. The general features to note in this 1000 MWe, cylindrically-symmetric configuration are two approximately equal core enrichment zones, a core height-to-diameter ratio of 0.4, a forty centimeter thick axial blanket and a forty five centimeter thick (three row) radial blanket. The blanket regions are surrounded by reflectors: fifty centimeters of steel in the axial direction, and fifteen centimeters of steel followed by thirty-five centimeters of sodium in the radial direction. Table 2.2 in the previous chapter lists the corresponding data for the 1-D reference reactor configuration; the only additional data needed to complete the 2-D description is that for the axial blanket and reflector, both of which have the same coolant volume percent (50 ^{v}/o) as the core. The axial blanket is 30 ^{v}/o fuel (uranium dioxide at 95 percent of theoretical density), the stainless steel structure occupies 20 ^{v}/o of the blanket and the axial reflector is 50 ^{v}/o stainless steel. Table 3.1 summarizes the dimensions and compositions of the various regions in the reference geometry.

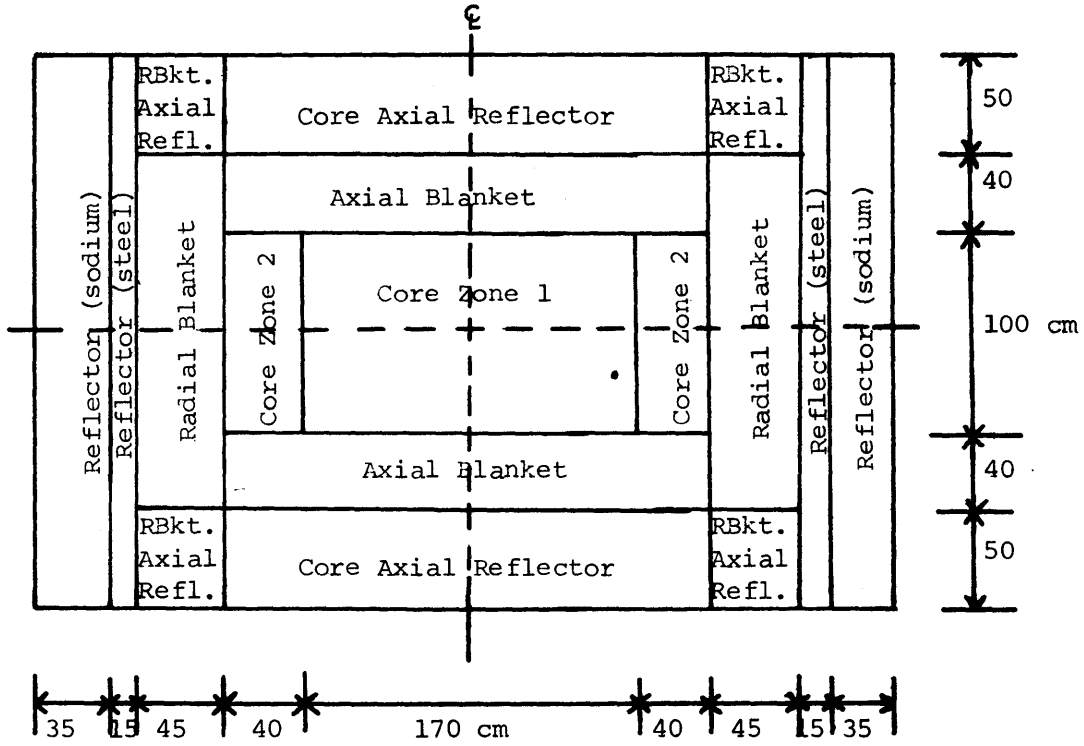

Fig. 3.1 1000 MW_e Reference Reactor Configuration

TABLE 3.1 Reference Reactor Parameters

	Ht. (cm)	Rad. Thick. (cm)	No. of Equiv. Assems.[b]	Percent by Volume		
				Fuel[c]	Coolant[d]	Structure[e]
Core						
Zone 1	100	85	127	30 (85% t.d.)	50	20
Zone 2	100	40	118	30 (85% t.d.)	50	20
Axial Blanket[a]	80	125	245	30 (85% t.d.)	50	20
Radial Blanket						
Row 1	180	15	63	50 (95% t.d.)	30	20
Row 2	180	15	70	50 (95% t.d.)	30	20
Row 3	180	15	77	50 (95% t.d.)	30	20
Axial Reflector[a]						
For axial blanket	50	125	245	—	50	50
For radial blanket	50	45	210	—	30	70
Radial Reflector						
Inner	140	15	84	—	20	80
Outer	140	35	222	—	100	—

[a]Axial blanket and reflector heights refer to thickness above or below core.

[b]Assumes hexagonal assemblies 15 cm across the flats.

[c]Fuel consists of mixed uranium and plutonium dioxide in the core and uranium dioxide in the blanket. The 100 v/o, 100% t.d. molecular density is taken as 0.02447 atoms/barn-cm. Plutonium is assumed to be typical light water reactor discharge Pu at 30,000 MWD/T: 63% Pu-239/22% Pu-240/12% Pu-241/3% Pu-242 (B-9).

[d]Coolant is sodium at ~900°F having a (100 v/o) density = 0.0220 atoms/barn-cm.

[e]Structure is stainless steel with 17.7% chromium/8.3% nickel/74.0% iron having a (100 v/o) density = 0.0850 atoms/barn-cm.

3.2.2 Cross-Section Preparation

The burnup analyses were performed using the two-dimensional diffusion theory code, 2DB (L-4) with 4-group cross sections prepared by collapsing the 26-group ABBN cross-section set (A-6) over spectra appropriate to the various reactor regions, using the one-dimensional ANISN program (E-4). Separate 4-group cross-section sets were obtained for the seven radial regions depicted in the 1-D model shown in Fig. 2.1.

3.2.2.1 Energy Group Structure

The energy group structure of the collapsed cross sections is specified in Table 3.2, together with values used by other investigators. As shown, the energy group structure is similar to the others, except that the last two groups of the set used by Hoover and Menley (H-3) have been combined into one, and to get more detail in the higher end of the neutron energy spectrum, Fuller's (F-5) second group cutoff was incorporated.

TABLE 3.2 Comparison of Collapsed Group Structures

Upper Neutron Energy (E-1)				
Group Number	This Study	Hoover and Menley (H-3)	Fuller (F-5)	Wood (W-5)
1	10.0×10^6	10.0×10^6	10.0×10^6	10.5×10^6
2	1.35×10^6	0.498×10^6	1.35×10^6	0.80×10^6
3	111.0×10^3	24.8×10^3	40.9×10^3	46.5×10^3
4	24.8×10^3	3.36×10^3	1.13×10^3	1.00×10^3

To check the accuracy of these 4-group cross sections and to justify the use of the proposed energy group collapsing scheme, the U-238 capture and fission reaction rates in a depleted three-row blanket were calculated with two 4-group sets and the 26-group set using the ANISN code (E-4), in the k-mode, normalized to constant power. The two different 4-group energy structures compared were the one selected for this study, and the one suggested by Hoover and Menley (H-3) (see Table 3.2). Table 3.3 lists the ratio of the 4-group calculated value divided by the corresponding value from the 26-group calculation, here taken to be the "exact" value. As can be seen, both 4-group sets slightly overpredicted k, but by less than half a percent. The U-238 capture reaction in blanket row 1 is predicted to within 2 percent with the chosen 4-group collapsing scheme; the discrepancy increased to approximately 6.5 percent in the outer blanket row. The other 4-group set predicts the U-238 capture slightly less accurately.

Lastly, Table 3.3 shows the comparison between the U-238 fission reaction rates. In this case the selected 4-group collapsed cross sections predict the U-238 fission rate in blanket row 1 to within 1 percent; the accuracy decreasing to approximately 5 percent in the outermost part of the blanket. The other 4-group collapsed cross sections are less accurate, with a maximum discrepancy of over 9 percent. These discrepancies are in agreement with those found by Wood (W-5) in a similar analysis.

TABLE 3.3 Ratio of 4-Group Calculations to 26-Group Calculations in a Depleted Blanket

Comparison	4G Energy Structure	
	This Study	Hoover and Menley
k (entire system)	1.004144	1.004936
U-238 Capture		
Row 1		
2.5 cm*	1.01284	1.01823
7.5	0.99635	0.99336
12.5	0.98011	0.97338
Row 2		
17.5	0.99241	0.98691
22.5	0.97745	0.97062
27.5	0.96324	0.95519
Row 3		
32.5	0.98481	0.97132
37.5	0.96786	0.95706
42.5	0.94341	0.93701
U-238 Fission		
Row 1		
2.5 cm*	0.99109	0.96669
7.5	0.99658	1.00115
12.5	0.99453	1.06454
Row 2		
17.5	1.00874	0.93755
22.5	0.96243	0.95775
27.5	0.98481	0.96255
Row 3		
32.5	0.96596	0.93355
37.5	0.96399	0.91028
42.5	0.94803	0.91391

* Distance into blanket.

3.2.2.2 Variations with Blanket Enrichment

Also of come concern was the application of region-wide collapsed cross sections, derived from a blanket with beginning-of-life depleted uranium fissile concentration (0.2 $^{w}/_{o}$), in blankets where the fissile enrichment has increased (due to initial loading or irradiation-buildup). To check this, ANISN k-calculations, normalized to constant power, were performed, and the calculated blanket U-238 fission and capture rates were compared, using 26 groups and the 4-group set previously derived, for two blanket enrichments: one with three rows of 2.5 $^{w}/o$ U-235, the other with 2.0, 1.2 and 0.7 $^{w}/o$ U-235 in Rows 1, 2, and 3, respectively. The ratios of the 4-group to the 26-group calculations are shown in Table 3.4. As can be seen, the 4-group results are in close agreement with the 26-group calculations, to within 5 percent, except for the U-238 fission in the outer region of the 2.5 $^{w}/o$ enrichment blanket, where the discrepancy increases to 11 percent. Nonetheless, the 4-group calculations summarized in Tables 3.3 and 3.4 agree sufficiently well with the 26-group calculations that one set of 4-group, region-wide collapsed cross sections will be used in the blanket burnup analyses.

It should also be pointed out that Hoover and Menley (H-3) have made quantitative comparisons between a 13-group set and a region-wide 4-group collapsed set. Their results show that the percent error in discharge Pu-239 and Pu-241 from the blanket of a 1000 MWe (GE advanced design) LMFBR is less than 0.1 percent. This result further justifies the use of region-wide 4-group collapsed cross sections for burnup analysis, particularly since it has been shown (B-5) that the inner row,

TABLE 3.4 Ratio of 4-Group Calculations to 26-Group Calculations in Different Blanket Configurations

Comparison	Blanket Configuration*		
	2.5/2.5/2.5	2.0/1.2/0.71	0.2/0.2/C†
k (entire system)	1.00449	1.00434	1.00421
U-238 Fission			
2.5 cm‡	1.00193	1.00573	0.98978
7.5	1.00397	0.98621	0.99667
12.5	1.01894	1.00609	1.00572
17.5	1.02869	0.99635	1.00431
22.5	1.04750	1.00708	0.98189
27.5	1.06337	0.99877	0.92058
32.5	1.09811	1.00668	–
37.5	1.11154	1.00604	–
42.5	1.09917	0.99352	–
U-238 Capture			
2.5 cm‡	1.01345	1.01548	1.01145
7.5	1.00262	1.00166	0.99276
12.5	0.99314	0.99000	0.97112
17.5	1.00937	1.00288	1.03476
22.5	1.00159	0.99039	0.99431
27.5	0.99313	0.97620	0.90492
32.5	1.01712	0.99567	–
37.5	1.00839	0.97826	–
42.5	0.99568	0.95483	–

*Values shown in heading are Row 1/2/3 enrichments.

†Third row is graphite reflector.

‡Distance into blanket.

which contributes most of the blanket plutonium production, is in the best agreement with 26-group calculations.

3.2.2.3 Variations with Reflector Composition

One of the main conclusions that will be made from the analysis presented in this chapter will be the use of a graphite reflector in place of steel (see Section 3.4.3). Consequently the validity of using region-wide collapsed cross sections must be checked for this type of advanced blanket-reflector configuration. To this end, ANISN k-calculations, normalized to constant power were performed and the calculated blanket U-238 fission and capture rates were compared, using 26-groups and the 4-group set previously derived. The ratios of the 4-group to the 26-group calculations are shown in the last column of Table 3.4. As can be seen the 4-group calculations agree sufficiently well with the 26-group calculations (less than 10 percent discrepancy in the outermost blanket region, and less than 3 percent discrepancy elsewhere), justifying the use of 4-group, region-wide collapsed cross sections for burnup studies of advanced blanket-reflector configurations.

3.2.3 Method of Burnup

3.2.3.1 Introduction

The purpose of this section is to describe the manner in which the reactor burnup was simulated. Burnup analysis was performed with the two-dimensional diffusion-theory code 2DB (L-4). Since diffusion theory calculations will be performed, it is desirable to compare diffusion theory to the more accurate transport theory calculations. This has been done by Wood (W-5) and by others (R-1). Utilizing ANISN (E-4) in the diffusion and transport modes, and a spherical reactor core (4850 liters) with a 40-centimeter thick blanket, Wood (W-5) found that there was excellent agreement between diffusion theory and transport theory in the core. In the blanket, the U-238 capture rate exhibited on the order of one percent discrepancy, while only fair agreement (errors as large as 20 percent) existed between the diffusion and transport theory calculation of U-238 fission rate. For the purpose of burnup studies, the capture rate in the fertile U-238 is most important; whereas for the fertile fissions in the blanket, even a twenty percent error is tolerable, especially when the fissile concentration increases (see Section 2.3).

The remainder of this section deals with the definition of burnup zones, and burnup materials. Then a method for dealing with reactivity changes in the core will be presented, leading to the definition of an "equilibrium" core and axial blanket around which the radial blanket is irradiated.

3.2.3.2 Burnup Zones and Materials

The 2DB code places a limit of 99 on the sum of the number of burnup zones and cross-section sets. It also treats each burnup zone as a homogeneous mixture during irradiation. Thus, after irradiation each burnup zone has uniform material concentrations, leading to the desirability of having many separate burnup zones in regions of the reactor where the spatial distribution of bred isotopes is important.

Figure 3.2 shows the arrangement of burnup zones for the 2DB analysis. Table 3.5 shows the correspondence between burnup zones and regions in the reactor (as shown in Fig. 3.1). Of the 43 burnup zones used in this analysis, only 4 are core zones, 8 are axial blanket zones and 27 are radial blanket zones, where the most detail is desired. The remaining 4 zones were required only to allow specification of the different types of reflector shielding materials used in the standard reactor.

Fourteen different elements and isotopes appear in the various reactor regions. Since the maximum number of remaining cross-section sets available for use in the computer code is 56 (i.e., 99 burnup zones and cross-section sets less 43 burnup zones), not every element could be individually described by a region-wide collapsed cross-section set in every region. Table 3.6 contains a summary of the cross-section sets that were individually collapsed for each reactor region.

3.2.3.3 Equilibrium Core

3.2.3.3.1 Introduction

The purpose of this section is to discuss, first qualitatively, then quantitatively, the formation of an "equilibrium" core and axial blanket

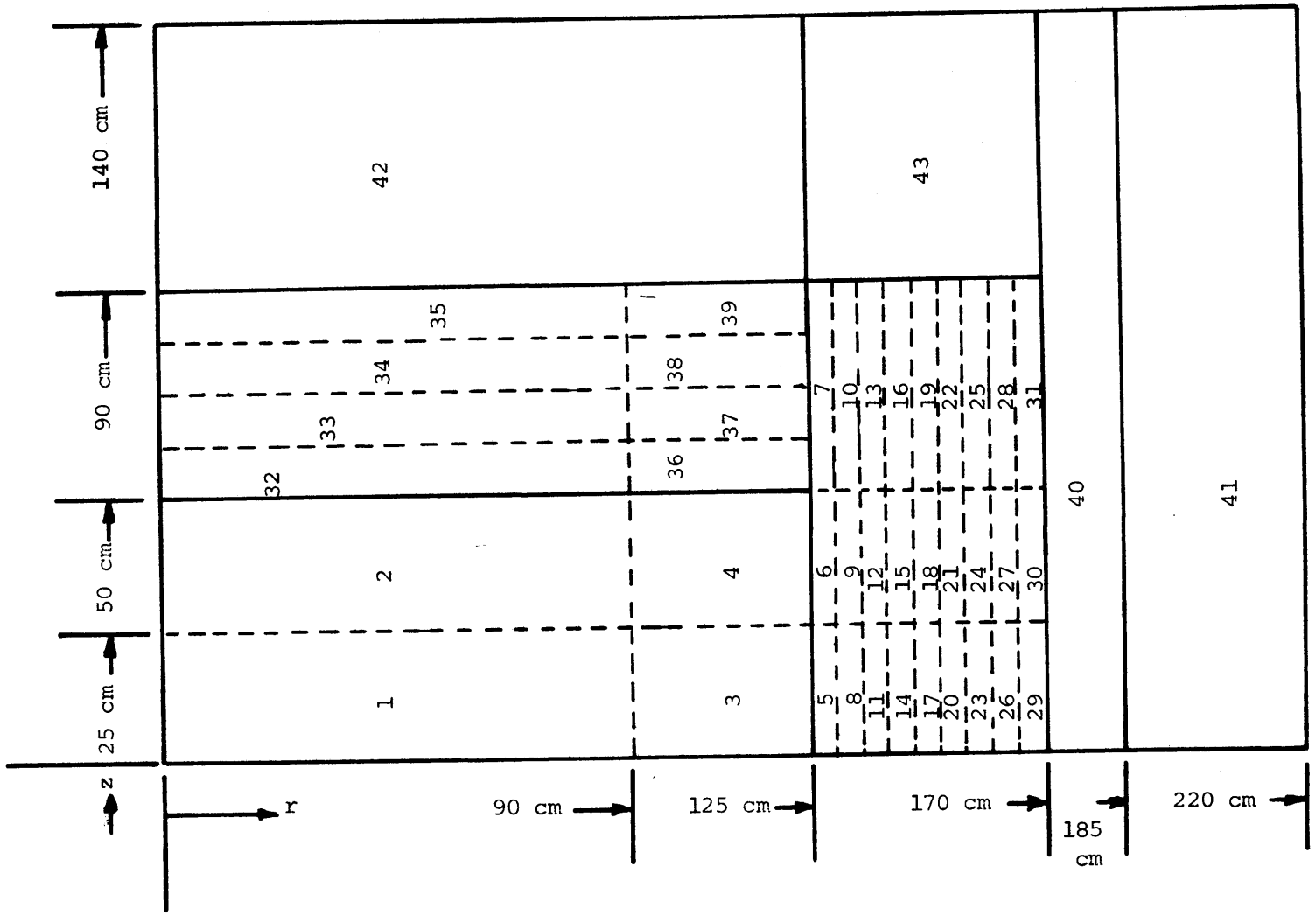

Fig. 3.2 Schematic Elevation View of the Upper Right Quadrant of the Standard Reactor System with Burnup Zones Included

TABLE 3.5 Correspondence of Burnup Zones and Regions*

Burnup Zone	Region
1 and 2	Core Zone 1
3 and 4	Core Zone 2
5 → 13	Radial Blanket Row 1
14 → 22	Radial Blanket Row 2
23 → 31	Radial Blanket Row 3
32 → 39	Axial Blanket
40	Radial Reflector (Steel)
41	Radial Reflector (Sodium)
42	Core Axial Reflector
43	Radial Blanket Axial Reflector

*See Figs. 3.1 and 3.2 and Table 3.1 for further details.

that will remain fixed in time as the irradiation of the radial blanket progresses. The motivation for adopting this procedure lies in the fact that typical radial blanket irradiations are long (on the order of six years) with respect to core refueling intervals (one year). Thus the radial blanket surrounds a core and axial blanket that will have gone through quite a few refuelings, and the subsequent control poison variations required to keep the reactor just critical.

Figure 3.3 shows a schematic of the unpoisoned reactivity swing of a batch managed core with a one-year refueling interval. It should be noted that, k', the initial, unpoisoned, effective multiplication factor (k_{eff}) is chosen such that at each refueling k_{eff} is just equal to unity.

Table 3.6. Region-Collapsed Cross Sections by Burnup Zone.
(each letter signifies a unique cross-section set)

Burnup Zones / Nuclide	Core		Radial Blanket			Axial Blanket				Reflector
	1, 4	2, 3	5-13	14-22	23-31	32, 36	33, 37	34, 38	38, 39	40-43
U-238	A	B	C	D	E	F	G	H	H	
Pu-239	A	B	C	D	E	F	G	H	H	
Pu-240	A	A	B	C	C	D	D	D	D	
Pu-241	A	A	B	B	B	C	C	C	C	
Pu-242	A	A	B	B	B	B	B	B	B	
U-235	A	A	B	C	D	E	F	F	F	
U-236	A	A	B	B	C	A	A	A	A	
F.P.	A	A	B	C	C	D	D	D	D	
Na	A	A	B	B	B	B	B	B	B	C
Cr	A	A	B	B	B	B	B	B	B	B
Fe	A	A	B	B	B	B	B	B	B	C
Ni	A	A	B	B	B	B	B	B	B	B
O	A	A	A	A	A	B	B	B	B	C
B-10	A	A				B	B	B	B	

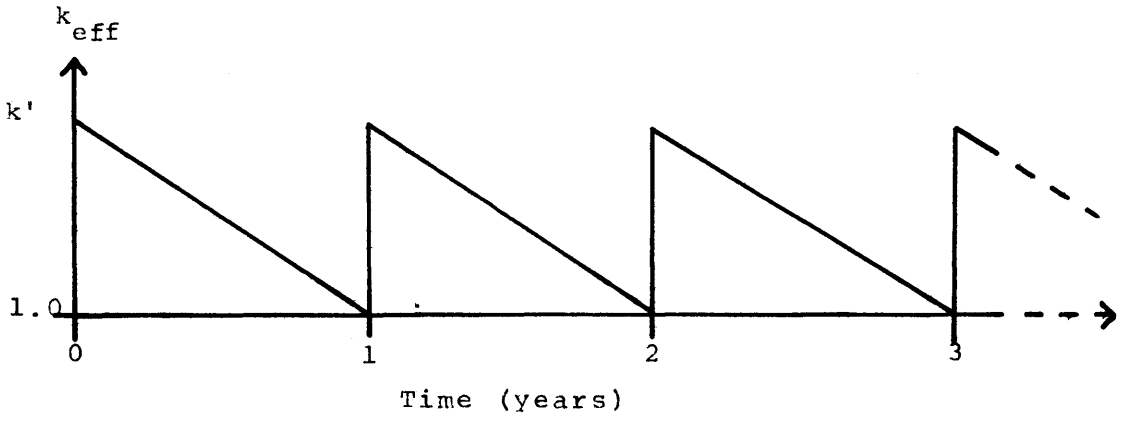

Fig. 3.3 Unpoisoned Reactivity Swing

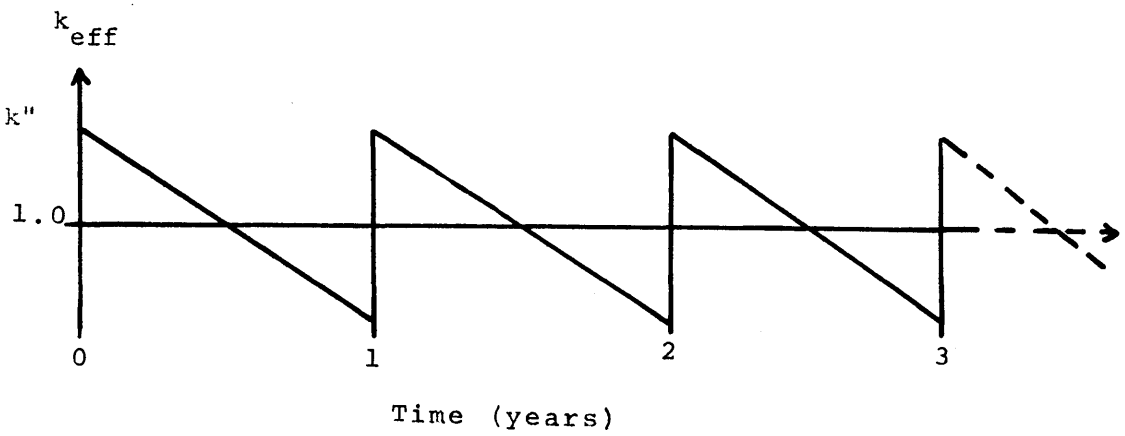

Fig. 3.4 Poisoned Reactivity Swing

In actual operation, it is necessary to maintain the system k_{eff} at unity throughout the operating cycle. This is accomplished through the use of movable control rods which are progressively withdrawn from the core.

For the purposes of this study it was necessary to simulate the actual operating sequency of the reactor, since the 2DB code does not have the capability for handling movable control rods. This simulation was made by adding Boron-10 control poison in a concentration such that its reactivity worth was equal to the (linearized) time averaged excess reactivity $\left(\frac{k'_{eff} - 1}{2}\right)$ during the refueling interval. Figure 3.4 shows a schematic of the reactivity swing of a core poisoned in this manner. The "equilibrium" core occurs at the point where the poisoned k_{eff} is equal to unity. Since the axial blanket is an integral part of the core, an "equilibrium" axial blanket is also determined at the point where the poisoned k_{eff} is equivalent to unity. It should be noted that the poison concentration in the axial blanket will be an average of 2.3 times greater than that in the core because of the continuous presence of control and safety rods in that region. The factor of 2.3 is determined by the following observations and assumptions:

1. The safety system is composed of rods which are always in the ready position in the upper axial blanket with their lower ends at the interface between the axial blanket and the core.
2. The safety system has 50% more poison material than the control system.
3. The reference reactor refueling cycle is one refueling every year. During that year the control rods are uniformly withdrawn from the fully inserted position (at the lower core/blanket inter-

face) to the fully withdrawn position (at the upper core/blanket interface).

4. The control system has sufficient worth (on a time-average basis) to make the system k_{eff} equal to 1.0 after one-half year of operation.
5. For the reactor analyzed here (which was assumed symmetric about the center plane), it is assumed that the poison concentration in the axial blanket is half the poison concentration expected in the upper axial blanket.
6. For the burnup analysis it is assumed that the poison is distributed uniformly throughout the core at the appropriate concentration, and uniformly throughout the axial blanket at the (higher) appropriate concentration.
7. As previously noted, for the burnup analysis the poison concentration is held constant at the time-averaged value throughout the life of the system.

Although considerable care has been placed on definition of a realistic core composition, it should be noted that other investigators (B-5, H-4, W-5) have looked into the effect of different core management methods on radial blanket economics, and have concluded that there is an insignificant effect on the results. Furthermore, since the same core treatment will be used for all cases studied, any systematic bias (however small) should cancel out so long as relative comparisons are employed.

3.2.3.3.2 Calculations

The preceding paragraphs have outlined the approach employed in evaluating the equilibrium core and axial blanket. The calculation of the required nuclide concentrations, using the 2DB burnup code (L-4) with the 4-group cross sections (Section 3.2.2) previously derived, proceeded as follows:

1. The initial fissile loading in the inner and outer core regions was taken to be 14.6 and 18.6 weight percent ($^{w}/_{o}$), respectively. Nuclide concentrations for the base reactor, consistent with Table 3.1 are given in Table 3.7.

2. The variation of the system effective multiplication factor, k_{eff}, was determined for a one-year period (which is equivalent to 300 full power days: 365 days at 82% load factor). This result is plotted in Fig. 3.5 (top line). As is shown, $k_{eff} = 1.0266$ at the end of one year. Also, the linearity of k_{eff} with time, as postulated by Fig. 3.3 is shown to be a rather good assumption.

3. The next step was to determine the change in initial fissile loading so that k_{eff} would equal unity at the end of one year. To accomplish this, 2DB snapshot physics calculations were made for different core fissile loadings. Figure 3.6 shows these results. The appropriate fissile loading now became 13.6 $^{w}/_{o}$ and 17.3 $^{w}/_{o}$ in the inner and outer core. A one-year burnup of this new unpoisoned core is also depicted in Fig. 3.5 and is shown to have the desired k_{eff} of unity at the end of one year.

4. The last step was to determine the time-averaged mean boron-10 poison concentration as indicated in Fig. 3.4. First the effect of boron-10

TABLE 3.7 Isotopic Number Densities, Beginning of Life
(in Units of nuclei/barn-cm)

FUEL MATERIALS				
Material	Inner Core	Outer Core	Axial Blanket	Radial Blanket
U-238	5.043×10^{-3}	4.688×10^{-3}	6.930×10^{-4}	1.155×10^{-3}
Pu-239	7.546×10^{-4}	9.718×10^{-4}	0.0	0.0
Pu-240	2.523×10^{-4}	3.394×10^{-4}	0.0	0.0
Pu-241	1.437×10^{-4}	1.851×10^{-4}	0.0	0.0
Pu-242	3.594×10^{-5}	4.627×10^{-5}	0.0	0.0
U-235	1.011×10^{-5}	9.400×10^{-6}	4.963×10^{-6}	8.271×10^{-6}
U-236	0.0	0.0	0.0	0.0
F.P.	0.0	0.0	0.0	0.0

NON-FUEL MATERIALS							
Material	Core	Axial Blanket	Radial Blanket	Core Axial Ref.	Radial Blanket Axial Ref.	Steel Radial Ref.	Na Radial Ref.
O	0.01248	0.01396	0.02326	0.0	0.0	0.0	0.0
Na	0.0110	0.0110	0.0066	0.0110	0.0066	0.0044	0.022
Cr	0.0030	0.0030	0.0030	0.0075	0.0105	0.0120	0.0
Fe	0.0126	0.0126	0.0126	0.0315	0.0441	0.0504	0.0
Ni	0.0140	0.0140	0.0140	0.0350	0.0490	0.0560	0.0
B-10	0.0	0.0	0.0	0.0	0.0	0.0	0.0

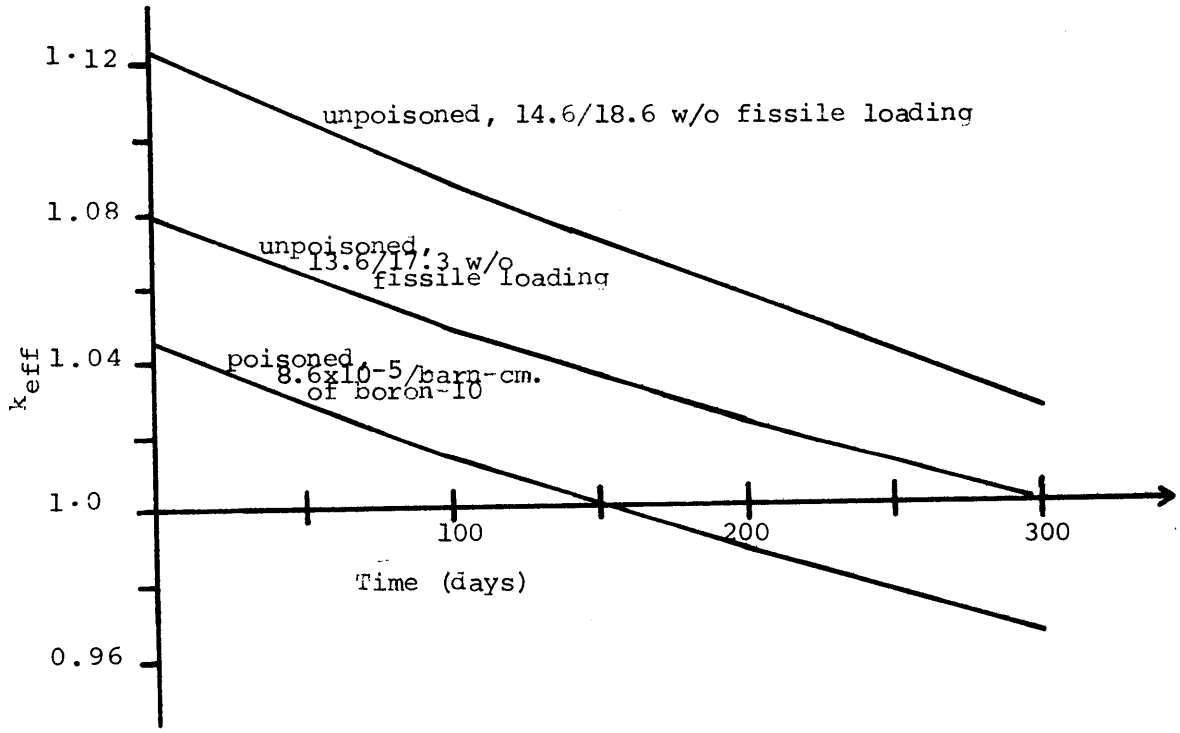

Fig. 3.5 The Effect of Irradiation on System Effective Multiplication Factor, K_{eff}

Fig. 3.6 The Effect of Core Fissile Loading on K_{eff}

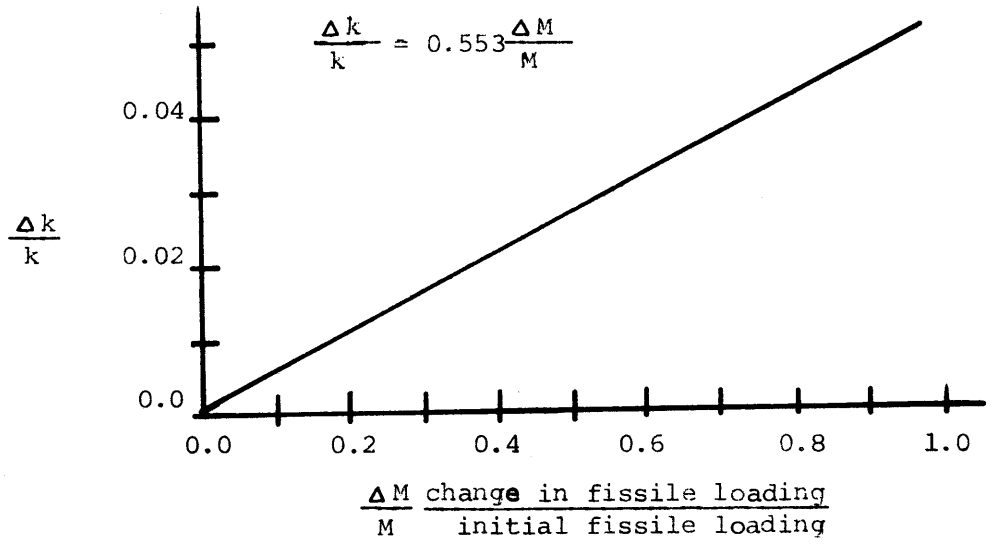

Fig. 3.7 The Effect of Boron-10 Concentration on K_{eff}

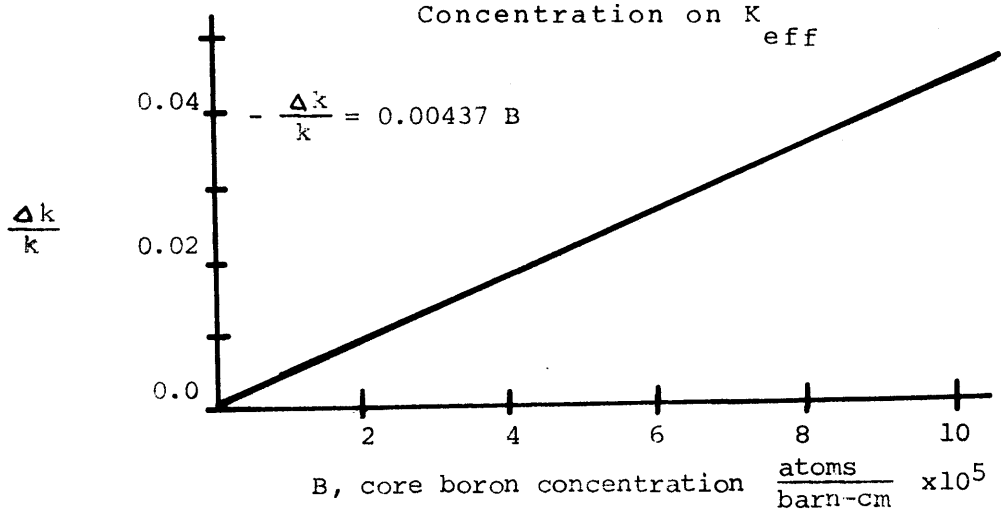

concentration on k_{eff} was determined. This was achieved using 2DB to perform several snapshot physics calculations in which the boron-10 concentration was varied. In all cases the ratio of boron concentration in the core to that in the blanket was 1.0 to 2.3 as previously specified. Figure 3.6 shows these results. The uniform boron-10 concentration was thus determined to be 8.6×10^{-5} atoms/barn-cm in the core. A one-year burnup of the 13.6/17.3 enriched core including the aforementioned uniform boron-10 concentration is given in Fig. 3.5, where it is shown that k_{eff} equals unity at 150 days. The "equilibrium" core and axial blanket are defined to consist of the compositions achieved at this $k_{eff} = 1.0$, 150-day point. Table 3.8 lists the nuclide concentrations in the four core zones and eight axial blanket zones (see Fig. 3.2) obtained in this manner.

3.2.3.4 Materials Included in the Burnup

In the burnup analysis performed by 2DB (L-4), materials whose concentration changed as a function of irradiation time were specified, together with the precursor isotope and the reaction which produced the isotope of interest.

The fissioning of the following heavy metals contributed to the creation of fission products: Pu-239, Pu-240, Pu-241, Pu-242, U-235, U-236, U-238.

The buildup of heavy isotopes was assumed to occur by the following neutron capture reactions:

Pu-239 (n, γ) Pu-240

Pu-240 (n, γ) Pu-241

TABLE 3.8 "Equilibrium" Core and Axial Blanket Isotopic Number Densities (nuclei/barn-cm)

Zone Number	U-238 (10^{-3})	Pu-239 (10^{-4})	Pu-240 (10^{-6})	Pu-241 (10^{-7})	Pu-242 (10^{-8})	U-235 (10^{-5})	U-236 (10^{-6})	Fission Prod. (10^{-5})	B-10 (10^{-4})
Core									
1	4.970	6.943	218.3	1080.0	3632.0	0.808	0.484	16.85	0.860
2	5.015	6.993	242.7	1148.0	3571.0	0.865	0.366	11.83	0.860
3	4.704	8.703	322.3	1504.0	4544.0	0.828	0.294	13.43	0.860
4	4.730	8.804	305.9	1558.0	4487.0	0.865	0.216	9.471	0.860
Axial Blanket									
32	6.714	1.768	6.029	1.318	0.209	3.508	3.676	4.238	1.978
33	6.787	1.246	3.411	0.711	0.098	3.810	3.216	2.228	1.978
34	6.839	0.825	1.667	0.280	0.025	4.100	2.544	1.219	1.978
35	6.869	0.569	0.928	0.110	0.007	4.259	2.242	0.777	1.978
36	6.795	1.151	2.387	0.327	0.032	4.009	2.458	2.362	1.978
37	6.842	0.793	1.323	0.172	0.014	4.223	2.099	1.214	1.978
38	6.875	0.513	0.629	0.065	0.004	4.421	1.620	0.668	1.978
39	6.893	0.348	0.340	0.024	0.001	4.528	1.398	0.430	1.978

Pu-241 (n, γ) Pu-242

U-235 (n, γ) U-236

U-238 (n, γ) Pu-239

As shown, neutron capture in U-238 is assumed to lead directly to the production of Pu-239, neglecting the formation of Np-239 (and its precursor U-239) which would beta decay with a half-life of 2.35 days into Pu-239. Neglecting the possibility of neutron captures in Np-239 will lead to a very slight overprediction in the formation rate of Pu-239 (B-5).

These burnup reactions will be limited to the radial blanket region for the remainder of the report. In determining the equilibrium core and axial blanket these burnup reactions were previously employed for the core and blankets. However, as discussed in Section 3.2.3.3, the equilibrium core and axial blanket then remain fixed in time as the irradiation of the radial blanket progresses.

3.2.4 Burnup Economics

In this work the burnup-economics analysis was performed utilizing the cash flow method contained in the computer code BRECON, developed by Brewer (B-5), and modified by Wood (W-5) to permit direct use of 2DB burnup results.

Levelized fuel cycle costs (in mills/kW-hr) were calculated according to the following general expression:

$$e = \frac{1000}{E} M^0_{HM} \left[\frac{C_{fiss} \epsilon_0 F^{mp}(T)}{T} \right.$$ material purchase cost component

$$+ \frac{C_{fab} F^{fab}(T)}{T}$$ fabrication cost component

$$+ \frac{C_{repr} F^{repr}(T)}{T}$$ reprocessing cost component

$$\left. - \frac{C_{fiss} \epsilon(T) F^{mc}(T)}{T} \right]$$ material credit cost component (3.1)

where e is the local levelized fuel component of the energy cost (mills/kW-hr), E is the electrical energy produced by the reactor in one year (kwhe/yr), T is the local irradiation time (yr), C_{fab} and C_{repr} are the unit fabrication and reprocessing costs ($/kgHM), C_{fiss} is the fissile (uranium and/or plutonium) price ($/kg), ϵ_0 is the initial (uranium and/or plutonium) enrichment, $\epsilon(T)$ is the discharge (uranium or plutonium) enrichment (kg fissile discharged per kg of heavy metal loaded), $F^q(T)$ is the carrying charge factor for cost component q, and M^0_{HM} is the mass of heavy metal loaded.

The carrying charge factors, $F^q(T)$, are given by

$$F^q(T) = \frac{1}{1 - \tau} \left[\frac{1}{(1+x)^{Tq}} - \tau \right]$$ for capitalized costs or revenues

$$= \frac{1}{(1+x)^{Tq}}$$ for noncapitalized costs or revenues (expensed cost or taxed revenue)

(3.2)

where

$$x = (1 - \tau)r_b f_b + r_s f_s = \text{"discount rate"} \qquad (3.3)$$

and where τ is the income tax rate, f_b and f_s are the debt and equity fractions, r_b and r_s are the debt and equity rates of return, and T^q is the time between the cash flow transaction q and the irradiation mid-point.

All the results quoted here were computed using an accounting method, suggested by Brewer (B-5), in which material purchases and fabrication charges were capitalized and consequently depreciated for tax purposes; whereas reprocessing charges and material credit were treated as an expensed cost and taxable revenue, respectively. (See Section 1.2.2.1 for further discussion on accounting methods.)

It should be noted that Eq. 3.1 can be applied to an entire region (e.g., radial blanket) or subregion (e.g., radial blanket row) under fixed element (batch) management. This feature of Eq. 3.1 facilitates the determination of the minimum fuel cycle cost contribution (i.e., the optimum irradiation time) for a blanket row or for the entire blanket.

Table 3.9 lists the basic economic parameters used in this study of radial blanket burnup fuel economics. These conditions (except for fissile U-235) are the same as those presented by Brewer (B-5) and Wood (W-5) and are within the range projected for the mature U.S. nuclear fuel cycle economy (W-6). The range of values for fissile U-235 ($/kg) is based in $38.50 per kilogram of separative work (F-6). Other information necessary to evaluate fuel cycle costs is given in Table 3.10.

In summary, this section presents the basic burnup economics model that will be used to evaluate radial blanket performance. This is the

TABLE 3.9 Economic Environment

Financial Parameters	
Income Tax Rate, τ	0.5
Capital Structure	
Bond (debt) fraction, f_b	0.5
Stock (equity) fraction, f_s	0.5
Rates of Return	
Bonds, r_b	0.07
Stocks, r_s	0.125
Discount Rate, x	0.08
Unit Blanket Fuel Processing Costs ($/kg HM)	
Fabrication, C_{fab}	69
Reprocessing, C_{repr}	50
Isotopic Market Value ($/kg)	
Pu-239, C_{Pu}	10,000
Pu-241, C_{Pu}	10,000
Pu-240	0
Pu-242	0
U-238	0
U-235 (F-6), C_U	
0.2 $^{w}/_{o}$	1,500
0.711	3,300
1.00	5,140
1.50	7,130
2.00	8,360
3.00	9,190
98.00	15,190

TABLE 3.10 Additional Input to the Economic Analysis

Time prior to beginning of irradiation when:	
Fabrication cash flow occurs	0.5 yr
Material purchase cash flow occurs	0.5 yr
Time after end of irradiation when:	
Reprocessing cash flow occurs	0.5 yr
Material credit occurs	0.5 yr
Load factor (fraction of time at full power)	0.82

same method used by other investigators (e.g., B-5, W-5). The next section will set forth an economic model to deal with the thermal-hydraulic aspects of radial blanket configurations.

3.3 Economics of Blanket Heating

3.3.1 Introduction

Overcooling of the radial blanket region due to spatial and temporal power gradients leads to decreased thermal efficiency and increased pumping power. These gradients also cause undesirable temperature gradients in the upper reactor internals, and complicate the problem of providing core radial restraint due to nonuniform assembly expansion. Due to the large number of assemblies (a three-row blanket has almost as many assemblies as the core), the radial blanket accounts for a large fraction of the total reactor flow (up to 30 percent (P-2)). Consequently, conservation of flow, by reducing power gradients, can lead to significant economic advantages between different blanket configurations.

The objective of this section is the development of an economic

model to treat the effects of power gradients in the blanket so that economic comparisons between various configurations and design options can be easily made. In Section 3.3.2 changes in mixed-mean reactor outlet temperature are related to changes in fuel cycle costs. In Section 3.3.3 the relationship between radial power peaking factors and mixed-mean temperature rise is derived.

3.3.2 Economic Aspects of the Mixed-Mean Reactor Coolant Temperature

3.3.2.1 Thermal Efficiency Effects

The economic effect of changes in mixed-mean outlet temperature can be derived from two basic assumptions relating to the overall plant efficiency:

(a) The cost of electricity, e, varies inversely with the thermal efficiency, η, of the reactor plant (B-8).

$$e = \frac{k}{\eta}, \tag{3.4}$$

where k is a constant of proportionality.

(b) The thermal efficiency is directly proportional to the Carnot efficiency, η_c, of the reactor plant (A-8) determined by its mixed-mean core outlet temperature and condensing temperature:

$$\eta = f\eta_c, \tag{3.5}$$

where the constant or proportionality, f, is approximately 0.62 for a well-designed system. The validity of Eq. 3.5 is demonstrated in Fig. 3.8 which compares Eq. 3.5 to a plot of thermal efficiencies

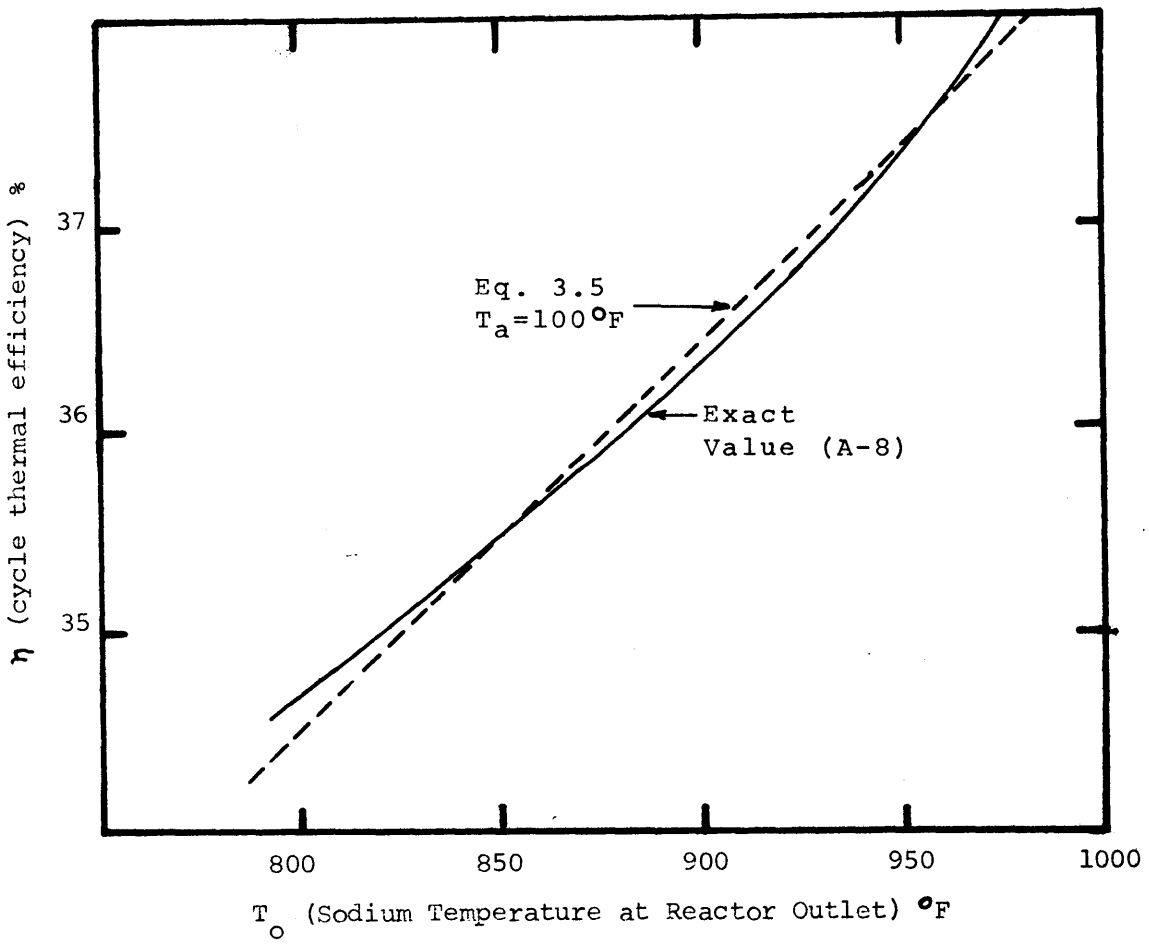

Fig. 3.8 Comparison of Approximate and Exact Cycle Efficiency Relations

versus mean reactor outlet temperature taken from an LMFBR design study (B-8) which re-optimized the LMFBR plant design and Rankine cycle parameters for each reactor outlet temperature.

The Carnot efficiency is defined by

$$\eta_c = \frac{T_o - T_a}{T_o}, \tag{3.6}$$

where T_o is the mixed-mean reactor outlet temperature (°R), and T_a is the condenser temperature of the plant (°R).

Equation 3.4 can now be written as

$$e = \frac{k}{f\eta_c} = \frac{k}{f}\left(\frac{T_o}{T_o - T_a}\right), \tag{3.7}$$

where the only variable on the right side of the equation is T_o, the outlet temperature. Differentiating Eq. 3.7 with respect to T_o, and rearranging the result yields the following expression:

$$\frac{\delta e}{e} = -\frac{f - \eta}{\eta}\,\frac{\delta T_o}{T_o}. \tag{3.8}$$

The minus sign indicates that a decrease in outlet temperature represents an increase in the cost of electricity, an economic penalty. The reactor outlet temperature can be written in terms of the mean reactor temperature rise, ΔT_r:

$$T_o = \Delta T_r + T_i, \tag{3.9}$$

where T_i is the reactor inlet temperature (°R). Equation 3.8 can now be written in terms of changes in the mixed-mean reactor coolant temperature rise:

$$\frac{\delta e}{e} = -\left(\frac{f - \eta}{\eta}\right)\left(\frac{1}{1 + T_i/\Delta T_r}\right)\frac{\delta \Delta T_r}{\Delta T_r}. \qquad (3.10)$$

In Section 3.3.3.2 an expression relating the radial power peaking in the blanket to mixed-mean reactor coolant temperature rise is derived. Section 3.3.4, completing this analysis, describes the combination of these steps into an expression linking variations in radial power peaking factors to changes in the cost of the electric power produced.

3.3.2.2 Pumping Power Effects

Another consequence of overcooling the blanket region is an increase in the pumping power expended. The degradation of the mixed-mean outlet temperature due to the radial power distribution is a direct consequence of the fact that excess sodium is pumped through the reactor.

A general expression for the pumping power requirements, P_p, of a reactor system can be written in terms of the reactor mass flow rate, ω_r, the coolant density, ρ, and the system pressure drop, Δp (E-6):

$$P_p = \frac{\omega_r}{\rho}\,\Delta p. \qquad (3.11)$$

The total reactor thermal power, P_r, is also directly proportional to the reactor mass flow rate:

$$P_r = \omega_r C(\Delta T_r), \qquad (3.12)$$

where C is the specific heat of the sodium coolant, and ΔT_r is the reactor mixed-mean temperature rise. Thus, an expression for the pumping power can be written in terms of ΔT_r by combining Eqs. 3.11 and 3.12:

$$P_p = \frac{\Delta p}{C\rho} \frac{P_r}{\Delta T_r}. \tag{3.13}$$

In order to determine how a change in the mixed-mean reactor temperature affects the pumping power when the reactor is to supply approximately constant thermal power, Eq. 3.12 is differentiated:

$$\frac{\delta P_p}{P_p} = - \frac{\delta(\Delta T_r)}{\Delta T_r}. \tag{3.14}$$

The system pressure drop and coolant material properties are also assumed to be constant with respect to these changes in pumping power and temperature. The negative sign implies that a decrease in temperature requires an increase in pumping power.

An increase in pumping power delivered to the coolant means that more electrical power must be expended to drive the coolant pumps. However, the pumps also return power to the primary loop, hence not all of the extra pumping power is lost to the system. The total energy balance on the plant is

$$(P_r + P_p)\eta = P_e + P_p, \tag{3.15}$$

where P_e is the electrical output of the plant, i.e., the power available for sale, which is directly proportional to income. The net change in power available for sale as a function of the change in pumping power can be determined by differentiating Eq. 3.15:

$$\frac{\delta P_p}{P_e} = - \frac{(1 - \eta)\delta P_p}{P_e} = - \frac{\delta e}{e} \tag{3.16}$$

Combining Eqs. 3.13 through 3.16 yields the pumping power penalty:

$$\frac{\delta e}{e} = -(1 - \eta) \frac{P_p}{P_e} \frac{\delta \Delta T_r}{\Delta T_r}, \qquad (3.17)$$

which is analogous to the thermal efficiency penalty given by Eq. 3.10.

In Section 3.3.3.2 an expression relating changes in the radial power peaking in the blanket to changes in the mixed-mean reactor coolant temperature rise, $\frac{\delta \Delta T_r}{\Delta T_r}$, is derived. Completing this analysis, Section 3.3.4 contains an expression relating variations in radial power peaking factors to their economic consequences.

3.3.3 Power Gradients and Temperature Relationships

The objective of this section is the determination of the variation in the mean reactor temperature rise as a function of the degree of flattening of the radial blanket power distribution. This result, when coupled with Eqs. 3.9 and 3.16 will complete the analysis of the economic aspects of power flattening in the radial blanket.

3.3.3.1 Temporal and Spatial Gradients

Before proceeding further it is desirable to draw a distinction between temporal and spatial power gradients, and to discuss the thermal-hydraulic design consequences of these power gradients in the radial blanket.

The temporal power gradient, R(t), is defined as the ratio of the blanket average power at a given time, P(t), to the beginning-of-life (BOL) average blanket power (e.g., at the end-of-life (EOL), $R_{EOL} = P_{EOL}/P_{BOL}$). Case studies to be discussed later show that the temporal gradient increases linearly with time to a very good approximation

(see Fig. 3.12).

The spatial gradient, F, is the peak-to-average radial power density ratio. While this spatial gradient factor is also a function of time, only the EOL value is of interest in determining blanket cooling requirements.

Figure 3.9 is a schematic plot of the average blanket power as a function of time. Since the entire blanket is (identically) orificed to insure that the maximum power at end-of-life is accommodated without exceeding the coolant temperature limit, a considerable degree of overcooling is experienced. This can be demonstrated in a convenient manner on Fig. 3.9. Since a channel's coolant temperature rise is directly proportional to channel power (at constant coolant flow), the ordinate can also be labelled "temperature rise."

Given this insight, the average power line can be seen to correspond to the mixed-mean temperature rise, and the peak power line to the peak channel's EOL temperature rise (ΔT^*). The degradation in outlet temperature is then proportional to the distance between the function line and the horizontal benchmark at the top of the graph, which corresponds to peak power at EOL and a channel outlet coolant temperature of 1050°F, the maximum allowable. The average loss in outlet temperature over lifetime, here defined as the "overcooling," is proportional to the area traced out by this distance as time advances. One can define "spatial overcooling" and "temporal overcooling" effects, which, in turn, can be identified with the cross-hatched areas shown on Fig. 3.9. Evidently:

Fig. 3.9 Overcooling Due to Temporal and Spatial Gradients

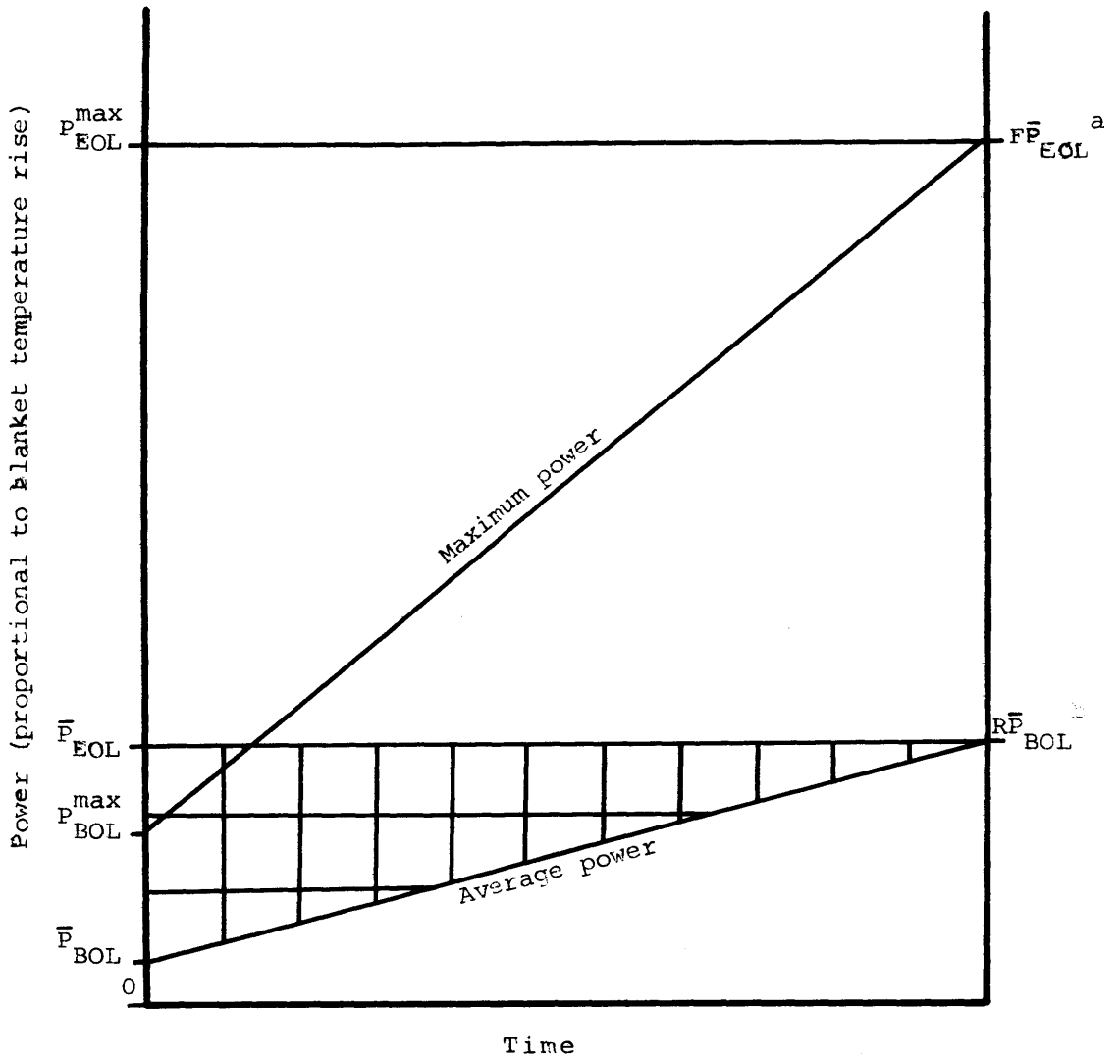

[a] F: Spatial peak-to- average radial power gradient

[b] R: Temporal power gradient, end-of-life average power divided by beginning-of-life power

$$\frac{\text{spatial overcooling}}{\text{temporal cooling}} = \frac{t(FR\bar{P}_{BOL} - R\bar{P}_{BOL})}{\frac{1}{2}t(R\bar{P}_{BOL} - \bar{P}_{BOL})}$$

$$= \frac{2R(F-1)}{R-1} . \qquad (3.18)$$

Several interesting observations follow:

1. The temporal allowance is the dominant cause of blanket overcooling at BOL; later spatial effects dominate.

2. In the limiting case of a large temporal power increase ($R \to \infty$) the ratio of spatial to temporal overcooling becomes $2(F-1)$ and spatial effects dominate for $F \gtrsim 1.5$.

3. Clearly, when $R = 1$ there is no temporal effect, and all overcooling is spatially generated. This would also be the case under ideal time-varying zone-orificing (as discussed in Section 1.2.2.5).

4. In practice, it can be shown that the spatial effects dominate. For example, in the base case blanket (3 rows of depleted uranium fuel) $R \sim 6.9$ and $F \sim 3.4$; thus from Eq. 3.18 the EOL spatial effect accounts for over 80% of the blanket overcooling during its lifetime. Thus the primary objective of blanket design should be to flatten end-of-life power.

Although the above analysis is for the case of a batch-managed blanket, the general approach can be extended to more complicated management schemes, albeit with the introduction of considerable complexity. The batch system with uniform orificing will remain the focus of the present work, however, because this constitutes the maximum overcooling case and the results will yield the maximum overcooling penalty.

We are now ready to proceed with the analysis.

3.3.3.2 Mixed-Mean Temperature and Radial Peaking Factors

The relationship between power generation, P, and mixed-mean outlet temperature can be developed from the basic heat transport equation, given previously as Eq. 3.12:

$$P = \omega C \Delta T, \tag{3.12}$$

where

ω is the total coolant mass flow rate

C is the mean coolant heat capacity (BTU/lb°F) (here assumed to be independent of temperature)

ΔT is the mixed-mean coolant temperature increase (°F); the mixed-mean outlet minus the inlet: $(T_o - T_i)$°F.

Equation 3.12 applies to the core and blanket separately or in conjunction, according to the choice of parameters.

The inlet temperature, T_i, is fixed during reactor operation so that ΔT becomes a function only of the outlet temperature, T_o. The operation of the reactor is assumed to be outlet temperature limited due to material property constraints placed on the cladding. At maximum power production this temperature rise limit is applied to the hottest channel in the reactor. This constraint holds not only for the core, but also for the blanket.

Another way of writing ΔT is in terms of ΔT^*, the maximum allowable temperature increase, and the maximum-to-average radial power peaking factor, F:

$$\Delta T = \frac{\Delta T^*}{F} . \tag{3.19}$$

Blanket orificing, as discussed in Section 1.2.2.5, is designed to set the coolant flow rate in the blanket, so that at maximum power production (at the end-of-life (EOL) of a batch-managed blanket) the blanket mixed-mean outlet temperature is ΔT^* divided by the blanket peaking factor, F_b.

$$\Delta T_b = \Delta T^*/F_b, \tag{3.20}$$

where the subscript b refers to the blanket.

If the flow to the blanket region is maintained, so that the maximum temperature increase is achieved (i.e., time-varying orificing (see Section 1.2.2.5)), then F_b will only pertain to spatial effects, and Eq. 3.20 will then be valid for all time. (See previous section.)

A similar expression exists for the core temperature rise:

$$\Delta T_c = \Delta T^*/F_c, \tag{3.21}$$

where the subscript c refers to the core. Since the core is refueled frequently with respect to the blanket (1 year versus about 6 years) and has an internal conversion ratio approaching unity, it is permissible to assume that the core peaking factor does not change appreciably during the blanket lifetime, and thus can be replaced by an average value. This result is also implicit in our use of an equilibrium core.

It should be noted that an inherent assumption in Eq. 3.21 is that the core power remains constant with time, even as the blanket power increases, implying that the total reactor power increases. This will

probably not be the actual case, instead the entire system power will remain constant resulting in the lowering of the core power contribution (which can be accounted for by an increase in F_c) as the blanket power increases. However, for the sake of simplifying this thermal-hydraulic analysis, the assumption of an invariant core peaking factor will be made. Since only blanket thermal-hydraulic performance is being analyzed, and the blanket power increase is correctly accounted for, the method developed here will be adequate for comparing the various blanket schemes.

The total reactor power is the sum of the power produced by the core, P_c, and by the blanket, P_b:

$$P_r = P_b + P_c. \tag{3.22}$$

Equation 3.12 can be used to define an expression for the mean reactor temperature rise:

$$\Delta T_r = \frac{\omega_c \Delta T_c + \omega_b \Delta T_b}{\omega_r}, \tag{3.23}$$

where the mean coolant heat capacities cancel, because they are assumed to vary negligibly with ΔT.

The ratio of blanket coolant flow to core coolant flow is a fixed quantity determined by the orificing condition established to satisfy sufficient cooling in the core and blanket. Denoting this ratio by W, it is defined as

$$W = \frac{\omega_b}{\omega_c} = \frac{P_b F_b}{P_c F_c} = \frac{P_b^{max}}{P_c^{max}}. \tag{3.24}$$

Thus, noting that ω_r is the sum of ω_b and ω_c, Eq. 3.24 can be rewritten as:

$$\Delta T_r = \frac{\Delta T_c + W\Delta T_b}{1 + W} . \tag{3.25}$$

Utilizing Eq. 3.19, this now becomes

$$\Delta T_r = \Delta T^* \left(\frac{1}{F_c} + \frac{W}{F_b} \right) / (1 + W). \tag{3.26}$$

The immediate objective of this analysis is the determination of the variation in the mean reactor temperature rise as a function of the degree of flattening attained for the radial blanket power distribution. Taking the partial derivative of Eq. 3.26 with respect to F_b, manipulating the results, and replacing the differential by the difference yields the desired result:

$$\frac{\delta(\Delta T_r)}{(\Delta T_r)} = -\left(\frac{W}{W+1} \right) \frac{\delta F_b}{F_b} . \tag{3.27}$$

The minus sign indicates that a decrease in the radial peaking power represents an increase in the reactor mean outlet temperature.

3.3.4 Synthesis and Summary

The purpose of Section 3.3 was to develop an economic model to treat the effects of power gradients in the radial blanket. Two effects were analyzed: a decrease in thermal efficiency and an increase in pumping power. The results of this analysis are embodied in Eqs. 3.10, 3.17, and 3.27, and are given here in consolidated form:

Thermal efficiency effect*:

$$\frac{\delta e}{e} = \left(\frac{1-\eta_c}{\eta_c}\right)\left(\frac{1}{1 + T_i/\Delta T_r}\right)\left(\frac{W}{W+1}\right)\frac{\delta F_b}{F_b} \qquad (3.28)$$

Pumping power effect*:

$$\frac{\delta e}{e} = (1-\eta)\ \frac{P_p}{P_e}\ \left(\frac{W}{W+1}\right)\frac{\delta F_b}{F_b}. \qquad (3.29)$$

Table 3.11 contains typical values for the various parameters in Eqs. 3.28 and 3.29. The peaking factor will be discussed further in Section 3.4 when the different blanket configurations are considered. However, one result is immediately apparent from the given data: The economic penalty due to thermal efficiency effects is an order of magnitude greater than the economic penalty due to increased pumping power. In Section 3.4 this economic penalty will be further quantified.

3.4 Case Studies

3.4.1 Introduction

The objective of the work reported in this section was the identification of the characteristics of an advanced high-performance configuration for the radial blanket region. To this end, the methods described in Sections 3.2 and 3.3 were applied to a variety of radial blanket configurations. These configurations varied in initial enrichment, thickness (i.e., number of rows), and radial reflector material.

The 2DB code (L-4) was used to determine the burnup behavior of the radial blanket, thereby supplying the necessary data to do the burnup-

*Finite difference versions of these equations, accurate for large changes in F, are given on page 139.

TABLE 3.11 Parameter Values for Determination of Power Gradient Penalty

Parameter	Value	Remarks
T_o	1050°F (1510°R)	Typical full power value for recent plant designs (A-2)
T_i	750°F (1210°R)	
ΔT_r	300°F (560°R)	Eq. 3.9
T_a	100°F	Typical condenser temperature
η_c	0.63	Eq. 3.6
η	0.40	Eq. 3.5
Δp	100 psi	Typical core pressure drop (P-2)
ρ	52 lb_m/ft^3	(E-6)
ω_r	10^8 lb/hr	(P-2)
P_p	10.5 MW	Eq. 3.11
P_e	1000 MW	Design value
F_c	1.6	(P-2)

These values yield

for Eq. 3.28: $$\left(\frac{\delta e}{e}\right)_{\text{thermal}} = 0.113 \left(\frac{W}{1+W}\right) \frac{\delta F_b}{F_b}$$

for Eq. 3.29: $$\left(\frac{\delta e}{e}\right)_{\text{pump}} = 0.007 \left(\frac{W}{1+W}\right) \frac{\delta F_b}{F_b}.$$

economic analysis (described in Section 3.2.4).

The 2DB fission power distribution results were also used in conjunction with the gamma and neutron heating results presented in Chapter 2, to determine total blanket heating rates. Power peaking factors could then be determined and employed in the thermal-hydraulic-economic evaluation described in Section 3.3.

3.4.2 Base Case-3-Row Depleted Blanket

The reference (3-row, depleted uranium-fueled) radial blanket configuration discussed in Section 3.2 (see Table 3.1) will be analyzed in this section. The burnup and thermal-hydraulic-economic performance results will serve as reference values against which other blanket configurations will be judged.

3.4.2.1 Burnup Results

The burnup economic performance for a batch-managed, steel-reflected 3-row blanket fueled with depleted uranium is shown in Fig. 3.10 (see Sections 3.2.3 and 3.24 for a discussion of the burnup method and burnup economics model employed). The ordinate of Fig. 3.10 represents the power cost contribution of the blanket region in units of mills/kW-hr and the abscissa represents the blanket residence time in units of years. (Note that 300 full power days equals 1 year.) The reference economic environment given in Table 3.9 was used. Curve b of Fig. 3.10 shows the effect of neglecting the value of U-235 on the blanket economics, a common practice in blanket studies (e.g., B-5, W-5). As expected, including the value of U-235 decreases the economic performance (i.e.,

Fig. 3.10 Power Cost Contribution from a Three-Row Depleted-U Blanket (Batch Irradiation)

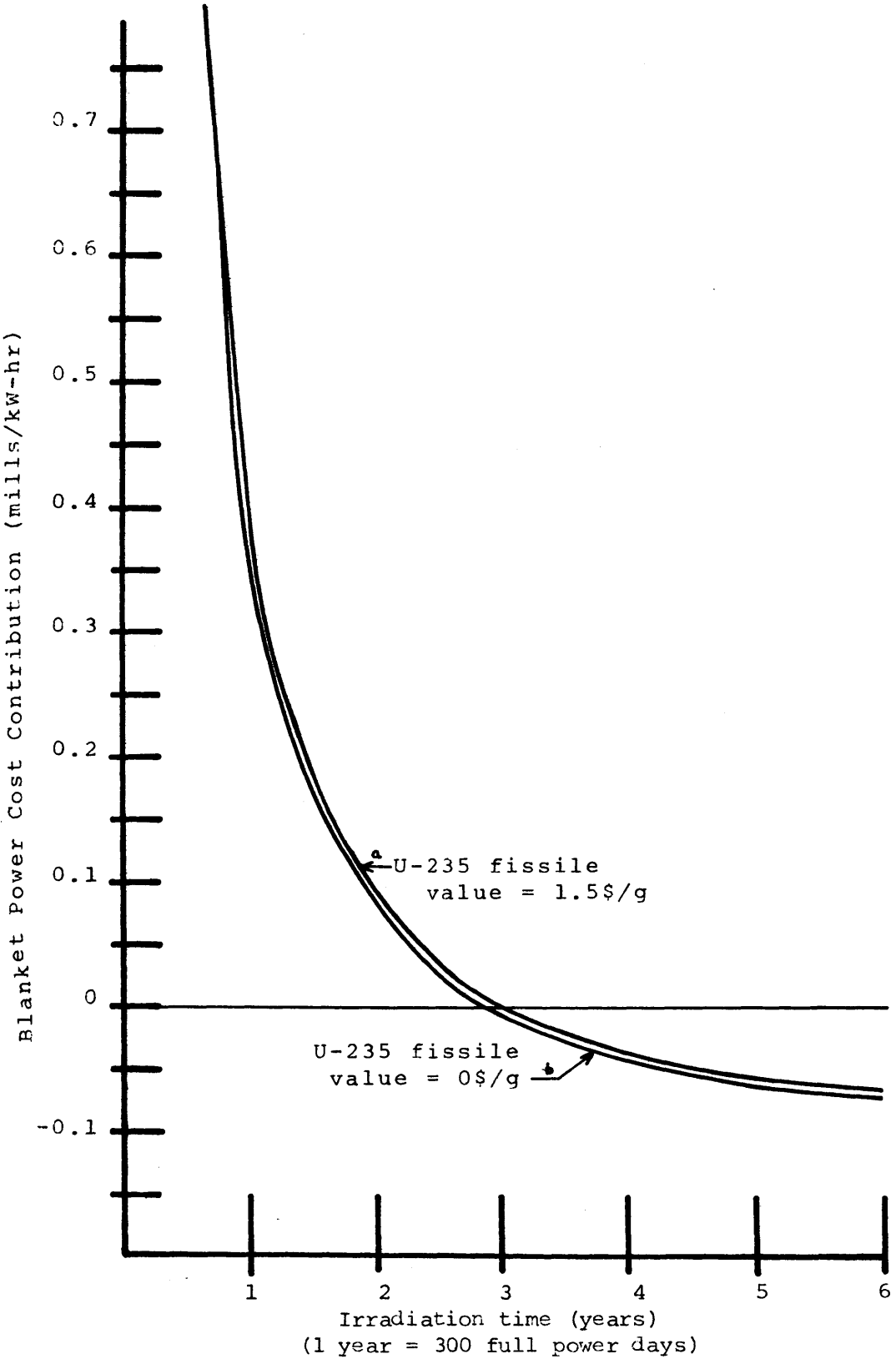

adds a positive increment to the power cost) of the blanket. The absolute economic effect, while less than 0.006 mills/kW-hr, represents about a 10 percent decrease in the fuel cycle savings contributed by the radial blanket. Consequently, for the remainder of this analysis, and for all other blankets analyzed, the value of U-235 will be included.

Further insight into the blanket economic performance can be gleaned from Fig. 3.11, which compares the individual economic performance of rows 1, 2, and 3 of a batch-irradiated uranium radial blanket in the reference economic environment. As shown, the blanket rows nearer to the core have a more negative cost contribution. Also, during the 6-year irradiation period only row 1 exhibits an optimum power cost contribution, whereas row 2, row 3, and the blanket taken as a whole do not reach an optimum; row 3, in fact, does not reach break-even.

From this last observation it might be expected that in some economic environments an engineering limit (e.g., clad embrittlement, accumulated clad strain, or duct deformation) might be reached by the blanket prior to attaining an optimum. Since the scope of the present work does not include determination of specific engineering limits, it will be somewhat arbitrarily assumed that 6 years of irradiation is the maximum allowed for any radial blanket assembly.

Table 3.12 summarizes the economic performance of the radial blanket, corresponding to the minimum blanket power cost contribution.

Again note that the power cost contribution of row 3 is positive, thereby adding to the cost of electricity, and indicating that not enough power and plutonium are delivered by the outermost row to compensate

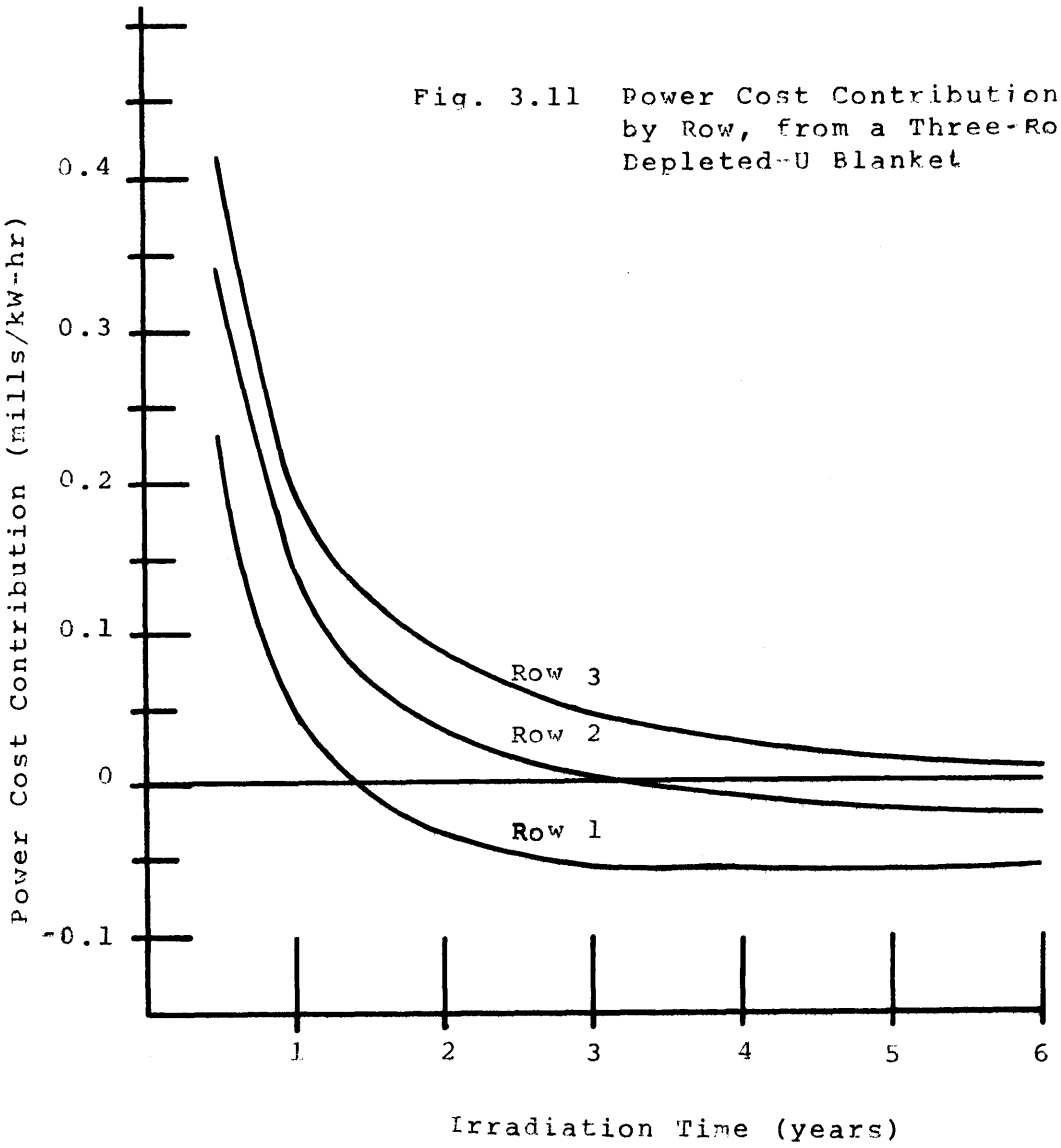

Fig. 3.11 Power Cost Contribution, by Row, from a Three-Row Depleted-U Blanket

TABLE 3.12 Power Cost Contribution from a Three-Row Depleted Uranium Blanket

	e (mill/kW-hr)	Irradiation Time (yrs)
Entire Blanket	-0.0659	6
Row 1	-0.0594	4.5
Row 2	-0.0210	6
Row 3	+0.0100	6

for the expenses it incurs. Two-row and one-row variations of this reference blanket are analyzed in Section 3.4.3.

3.4.2.2 Thermal-Hydraulic Results

In order to analyze the thermal-hydraulic performance of blankets the total heating rate must be known. The burnup analysis performed by 2DB (L-4) yields (among other things) the time history of the power produced by fissions in the blanket. Figure 3.12 shows the buildup in blanket thermal power due to fissions, as a function of time, for the 3-row depleted uranium blanket.

However, the contribution of gamma and neutron heating in the blanket due to leakage from the core must be included. This effect is given by the Shield-Heating Rate (SHR) derived in Chapter 2:

$$SHR = P(0.864\, e^{-0.0715\, r} + 0.096\, e^{-0.1098\, r}) \frac{kW}{liter}, \qquad (3.30)$$

where P is total reactor power (due to fissions) in units of 100 MW (in this case P = 25), and r is the distance from the core-blanket interface in centimeters.

Fig. 3.12

Power Buildup in a 3-Row depleted-uranium radial blanket

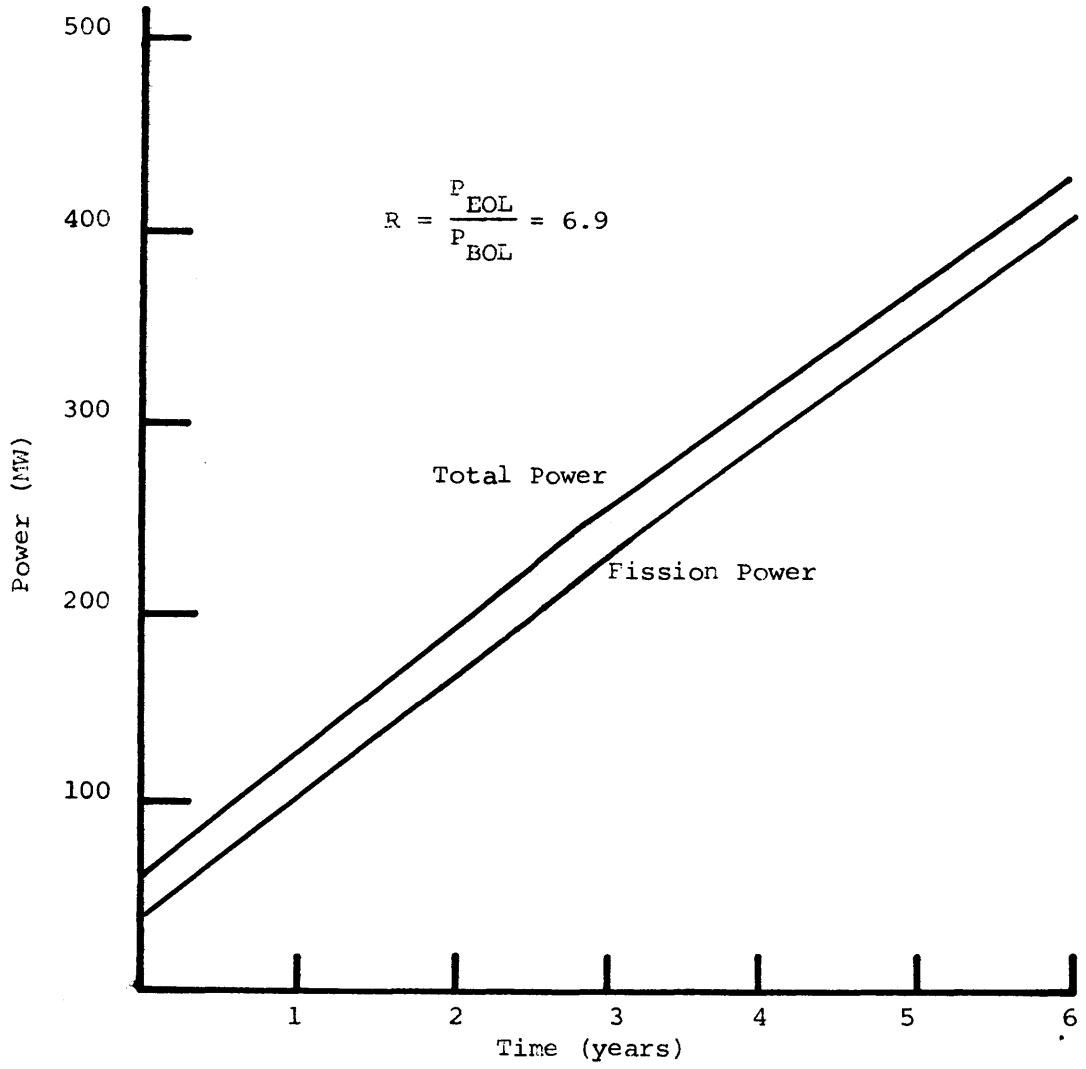

It should be noted that Eq. 3.30 applies along the reactor midplane, and must be integrated over the radial and axial dimensions in order to determine the power generated in the entire blanket volume. The integration is performed straightforwardly with the aid of Fig. 3.13, which shows the axial distribution of the core and axial blanket power density. As shown, the core power density exhibits a chopped cosine distribution whose effective height is about 150 cm (corresponding to a reflector savings of 25 cm) whereas the axial blanket power density, which is an order of magnitude lower than the core power density at the interface, falls off exponentially.

Integrating over this axial distribution yields an added blanket power contribution attributable to core leakage neutron and gamma heating of 24 MW. This result is included in Fig. 3.12, where it is combined with the fission power to give an EOL-BOL power ratio, R = 6.9.

Table 3.13 summarizes these blanket heating results, showing not only the total average power generated in each row, but also the average and maximum power density. The radial peaking factor in Table 3.13 is the radial peak-to-average power density.

3.4.3 Advanced Configurations

Variations in three key blanket-reflector design parameters: blanket thickness, initial blanket enrichment and reflector composition will be analyzed in this section. Section 3.4.3.1 will discuss the effect of these three parameters qualitatively, and Section 3.4.3.2 will present the results of the burnup and thermal-hydraulic analysis for the various configurations.

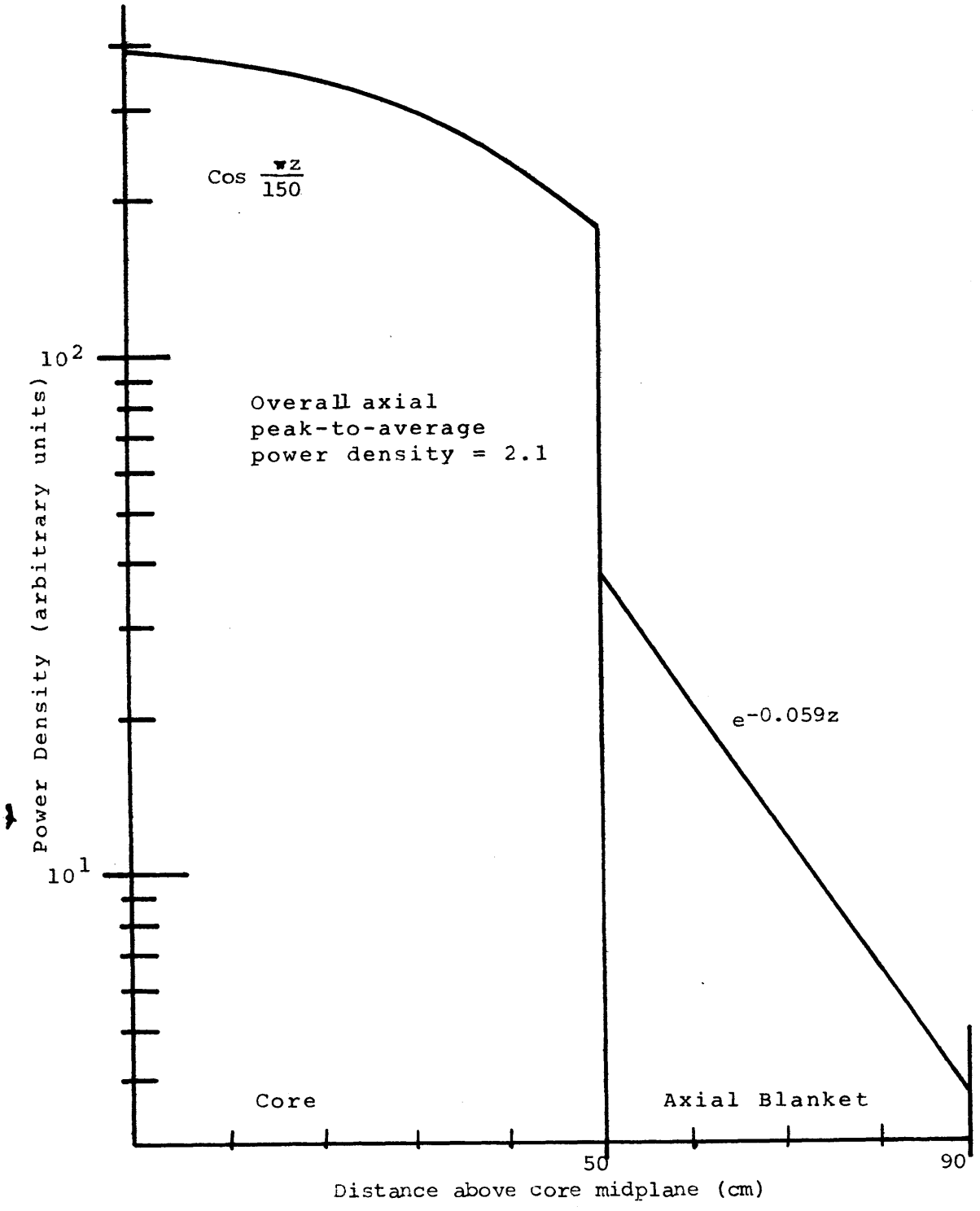

Table 3.13 Axial Power Distributions

TABLE 3.13 Energy Deposition Rates in a 3-Row Depleted Uranium Blanket

	Row 1	Row 2	Row 3	Entire Blanket
Volume (Liters)	2248	2502	2757	7507
Power* (MW)				
Fission	260	109	36	405
γ and n†	15	5.6	2.1	23
Total	275	115	38	428
Power Density*				
q''' (kW/ℓ)	122	46.0	13.8	57.0
q'''_{max} (kW/ℓ)	193	84.2	27.3	193
Peaking Factor*				
Spatial, F	1.58	1.83	1.98	3.40
Temporal, R	6.22	8.48	7.90	6.69

*End-of-life (6-year irradiation).

†γ-n heating is independent of time.

3.4.3.1 Design Variables

3.4.3.1.1 Thickness

The results shown in Fig. 3.11 indicate that the burnup economic performance of the blanket deteriorates with distance from the core. This result is consistent with the findings of other investigators (B-5, W-5). The reason for this behavior is that the local production of plutonium (and power) decreases with decreasing neutron flux, which itself decreases with distance from the core. Consequently expenses due to fabrication and reprocessing become dominant over revenue received from the sale of power and plutonium; and, as shown in Fig. 3.11, can create a situation in the outermost regions of the blanket where the net local power cost contribution is positive.

Furthermore, the individual row power peaking factors (Table 3.13) increase with distance from the core, implying that the thermal-hydraulic-economic performance also deteriorates with distance from the core.

For these reasons, blankets thinner than 45 cm are included in the case studies presented in Section 3.4.3.2.

3.4.3.1.2 Enrichment

The main advantage of using enriched fuel in the radial blanket is improved blanket thermal-hydraulic performance. As the fissile content in the fuel increases, the power distribution tends to flatten. However, any thermal-hydraulic gain realized by using enriched blankets must be offset by the cost (carrying charges) of the U-235 (or other fissile species). In Section 3.4.3.2 variously enriched blankets are

analyzed assuming U-235 values as given in Table 3.9.

3.4.3.1.3 Reflector Composition

A radial reflector region surrounds the radial blanket. (See Fig. 3.1.) In the base case, the reflector composition consists of steel cooled by sodium; however, other materials have been suggested in place of steel (see Section 1.2.2.3).

In a comparative study (B-10) of four candidate reflector materials – beryllium oxide, graphite, nickel, and iron – blanket performance was measured in terms of the integral U-238 capture rate achieved in the blanket. Graphite was shown to perform slightly better than beryllium oxide and significantly better than nickel and iron. The study also showed that there was no significant increase in blanket performance for graphite reflectors thicker than 15 centimeters (i.e., one subassembly row).

However, any burnup-economic gain achieved must be diminished by the increased cost (if any) of utilizing an improved reflector. Table 3.14 shows the quantity and the cost of reflector material needed to supply a 15-cm thick radial reflector. The last line gives the calculated power cost contribution (in mills/kW-hr) for the reflector material, conservatively assuming a 6-year reflector lifetime (the same as a blanket fuel element).

Based upon the economic comparison presented in Table 3.14, and the nuclear performance shown in Ref. B-10, graphite was selected to be the advanced reflector material to be included in the case studies analyzed in Section 3.4.3.2. Furthermore, envisioning similarly-fabricated reflector subassembies consisting of an array of stainless steel

clad reflector rods, the added cost of replacing steel reflector assemblies by graphite reflector assemblies was deemed sufficiently small (less than 10^{-4} mills/kW-hr) that it could be neglected in the studies which follow.

TABLE 3.14 Reflector Material Costs

	Graphite	Be	BeO	Steel
Amount (lb)	5000	6000	8400	23,000
Unit Price ($/lb)	7[a]	102[b]	25[c]	0.60[d]
Initial Cost (10^3)	35.0	612.0	210	13.8
Power Cost[e] (mils/kwh)	11×10^{-5}	190×10^{-5}	65×10^{-5}	4.3×10^{-5}

[a]From Ref. (W-7)
[b]From Ref. (E-8)
[c]From Ref. (E-7)
[d]From Ref. (C-3)
[e]Assuming 7×10^9 kwh/yr and 6-yr reflector lifetime.

3.4.3.2 Burnup and Thermal Hydraulic Results

Table 3.15 presents the results of the burnup analysis of various blanket-reflector configurations. These configurations were determined by varying three design variables: blanket thickness, initial blanket enrichment, and reflector composition; with the constraint that the new blanket and reflector fit within the 45-cm thick radial annulus taken up by the 3-row reference blanket (see Fig. 3.1), and that only whole rows

TABLE 3.15 Summary Performance of Various Blanket-Reflector Configuration

Case No.*	e_{opt} (mills/kW-hr)	T_{opt} (yrs)	F, Spatial Power Peaking Factor	R, Temporal Power Peaking Factor
3DS	-0.066	6.0	3.40	6.87
2DS	-0.083	5.3	2.36	6.48
2NS	-0.078	5.2	2.32	4.34
2MS	-0.082	5.4	2.35	5.64
2ES	+0.026	5.8	2.00	2.35
2DC	-0.085	5.3	2.18	5.34
1DS	-0.070	3.9	1.60	5.50
1DC	-0.079	3.7	1.42	5.84

*Key: 3DS

- Reflector composition: steel (S) or graphite (C).
- Fuel: depleted (D), natural (N), enriched (E) or mixed (M).
- Number of rows.

(15 cm) could be manipulated. All other reference parameters previously identified, e.g., the "equilibrium" core, remained unchanged.

In Table 3.15 the first column designates the particular blanket-reflector configuration studied. The first digit designates the number of blanket rows (1, 2 or 3) and the following two letters designate the initial enrichment of the blanket fuel, and the reflector material, respectively. The uranium enrichments studied were: depleted, 0.2 $^{w}/_{o}$ U-235 (D), natural, 0.71 $^{w}/_{o}$ U-235 (N), 2.5 $^{w}/_{o}$ enriched (E), and a 2-row mixed case having an inner row depleted and an outer row natural (M). The reflector compositions were either steel (S) or graphite (C).

The second column, e_{opt}, is the entire blanket's minimum burnup fuel cycle cost contribution to the total power cost and the third column, T_{opt}, is irradiation time to achieve e_{opt}. The last two columns represent the spatial, F, and temporal, R, blanket peaking factors, respectively.

Burnup related economics depicts only part of the total blanket economic performance. The economic penalty due to blanket overcooling must also be considered. The thermal-hydraulic economic results are obtained utilizing the methods developed in Sections 3.2 and 3.3. All comparisons were made relative to the base case (3-row depleted uranium) blanket. It should be noted that in most cases, since the changes in F are large (between 30 and 60% $\delta F/F$), Eqs. 3.28 and 3.29 must be used in an integral form (or $\frac{\delta e}{e}$ will be underestimated by up to 20%) as follows:

$$\frac{e_2 - e_1}{e_1} = \left(\frac{f - \eta_2}{\eta_2}\right)\left(\frac{W_2}{1 + W_2}\right)\left(\frac{1}{1 + \frac{T_i}{\Delta T_{r'}}}\right)\frac{F_{b_2} - F_{b_1}}{F_{b_2}} \qquad (3.28')$$

$$\frac{e_2 - e_1}{e_1} = \frac{P_p}{P_E}(1 - \eta_1)\left(\frac{W_2}{1 + W_2}\right)\frac{F_{b_2} - F_{b_1}}{F_{b_2}}, \qquad (3.29')$$

where the subscripts 1 and 2 refer to the two cases being analyzed: in each instance case 1 is 3 DS. The other parameters are as defined previously in Section 3.3 and Table 3.11.

Table 3.16 lists the thermal-hydraulic economic results for the various cases studied, showing the cost increment relative to the base case. The first column designates the particular blanket-reflector configuration analyzed. The next column, $\delta e/e_1$, lists the relative economic penalty due to changes in the spatial peaking factor in the blanket (see Table 3.15) determined by summing the results of Eqs. 3.28' and 3.29'. It should be emphasized that a smaller $\delta e/e_1$ (i.e., more negative) is desirable since δe is defined by subtracting e_1, the fuel cycle cost for the base case from the particular case of interest. Note also that e_1 is the <u>total</u> cost of electricity, not just the local power cost contribution of the blanket.

As discussed in Section 3.3.3.1 there are two contributions to the total overcooling of the radial blanket: spatial and temporal. Column two accounts for the spatial contribution only. However, making use of Eq. 3.18 and the data in Table 3.15, the ratio of total blanket overcooling (TOC) to spatial overcooling (SOC) can be easily calculated. This ratio is listed in column 3 of Table 3.16. As shown, the ratio varies from

TABLE 3.16 Thermal-Hydraulic-Economic Performance

Case Number (see key on Table 3.15)	$\delta e/e_1$ (Eq. 3.28' plus Eq. 3.29')	TOC/SOC (total to spatial overcooling)	$\delta e_{oc}/e_1$ (total overcooling economic effect)	δe_{oc} (mills/kW-hr)	E_{oc} (10^3 \$/yr)
3DS	–	1.18	–	–	–
2DS	-0.0124	1.31	-0.0108	-0.108	-756
2NS	-0.0129	1.29	-0.0115	-0.115	-805
2MS	-0.0125	1.30	-0.0110	-0.110	-770
2ES	-0.0170	1.29	-0.0151	-0.151	-1057
2DC	-0.0148	1.35	-0.0123	-0.123	-861
1DS	-0.0225	1.68	-0.0113	-0.113	-791
1DC	-0.0252	1.98	-0.0052	-0.052	-336

1.18 to 1.98 which supports the conclusion stated at the end of Section 3.3.3.1, that the spatial effects dominate the temporal effects of overcooling. In order to incorporate this result into the economics of power flattening, $\delta e/e_1$ is adjusted by the ratio of total to spatial overcooling. (For example, case 2DS has 13% more overcooling than the base case, 3DS (1.31 - 1.18 = 0.13). Therefore, column 3, $\delta e/e_1$, is to be increased by 13% in order to compensate for the relatively larger amount of temporal overcooling in case 2DS relative to case 3DS.) Column 4 lists the result of this adjustment: the relative economic penalty due to both temporal and spatial effects, $\delta e_{oc}/e_1$.

The next column, δe_{oc}, is determined by multiplying $\delta e_{oc}/e_1$ by e_1, the base case cost of electricity, here taken to be 10 mills/kW-hr.

The last column in the table, E_{oc}, gives the difference in dollars per year (assuming 7×10^9 kW-hr/yr), due to thermal-hydraulic effects, between the base case and the particular case of interest.

Table 3.17 combines the burnup-economic results presented in Table 3.15 with the thermal-hydraulic-economic results presented in Table 3.16 to determine the total blanket economic performance. The first column designates the particular blanket-reflector configuration analyzed. The next column, E_{opt}, is derived utilizing the results listed in column 2 of Table 3.15. E_{opt} is the absolute difference in dollars per year (assuming 7×10^9 kW-hr/yr of electricity) between the base case burnup economics and the particular case of interest. Column 3, E_{oc}, is reproduced from the last column of Table 3.16 and is the absolute difference in dollars per year between the base case thermal-hydraulic-economics and the particular case of interest. The last column,

E_{net}, is the sum of E_{oc} and E_{opt} and represents the total economic difference between the base case and the particular case of interest. Note again, that a minus sign indicates a cost savings in going to an advanced blanket-reflector configuration.

TABLE 3.17 Relative Blanket Economic Performance*

Case Number†	E_{opt} (10^5 \$/yr)	E_{oc} (10^5 \$/yr)	E_{net} (10^5 \$/yr)
3DS	–	–	–
2DS	-1.14	-7.56	-8.70
2NS	-0.84	-8.05	-8.89
2MS	-1.06	-7.71	-8.77
2ES	+6.44	-10.57	-4.13
2DC	-1.36	-8.61	-9.97
1DS	-0.23	-7.91	-8.14
1DC	-0.93	-3.36	-4.29

*Uniformly orificed; relative to 3DS, the base case.
†See key on Table 3.15.

From the results presented in Table 3.17, for the given economic environment, and batch irradiation, it is apparent that the two-row depleted-uranium-fueled, graphite-reflected, blanket-reflector configuration offers the largest economic improvement, relative to the base case. The savings is almost one million dollars per year, a value more than one-hundred thousand dollars per year better than the next best configuration.

Section 3.3.4 will comment further on the results presented in this section.

3.4.4 Case Studies – Observations and Summary

This section will summarize and draw conclusions from the data presented in Sections 3.4.1 through 3.4.3. First, conclusions will be made considering only burnup-economic aspects of blanket-reflector configurations. Then a set of conclusions will be presented considering only the thermal-hydraulic economic effects. Lastly, the two effects will be analyzed in concert, with particular emphasis on how changes in the assumed operating conditions affect blanket performance.

From a strict burnup-economic point of view the following statements can be made:

1. Enrichment is undesirable due to the added cost of fissile U-235.

2. Two-row blankets are preferable in the economic environment specified. Even considering the added cost of replacing the third blanket row with a steel reflector (calculated to be $2.8\ 10^{-3}$ mills/kW-hr, using a 6-year reflector lifetime and the blanket fabrication cost as an upper limit of the steel reflector fabrication cost), the third row exerts a net positive cost contribution (see Table 3.12), warranting its removal. The second row is a negative contributor to the fuel cycle cost and should therefore be retained.

3. Use of graphite reflectors in place of steel reflectors improves overall blanket economics. In particular, since the reflector predominantly affects the adjacent blanket row, the economic performance of thinner blankets is improved more than that of thicker blankets. Thus one would not expect to see an appreciable gain in blanket performance for a 3-row blanket surrounded by a graphite reflector. This conclusion

concurs with Brewers analysis (B-5).

4. The improved economic performance of a graphite-reflected 1-row blanket can not compensate for the lost revenue due to the removal of blanket row 2.

In summary, then, considering only burnup economics, the best blanket-reflector configuration would be case 2DC, a 2-row depleted uranium-fueled blanket surrounded by a graphite reflector.

Considering only thermal-hydraulic performance the following statements can be made:

1. Graphite reflectors reduce blanket spatial power peaking factors.

2. Increased blanket enrichment reduces blanket spatial power peaking factors.

3. Total blanket overcooling is dominated by spatial effects as opposed to temporal effects, e.g., over 50% of the total is due to spatial effects in a 1-row blanket, increasing to over 80% in a 3-row blanket (entire blanket uniformly orificed).

4. Thin blankets are superior to thick blankets. This effect is accentuated due to the selection of one fixed orifice setting for the entire blanket in these case studies.

In summary, then, considering only thermal-hydraulic economic considerations, the best blanket-reflector configuration would be case 2ES, a 2-row enriched (2.5 $^{w}/_{o}$) uranium-fueled blanket surrounded by a steel reflector.

However, in order to select an optimum blanket-reflector configuration both burnup and thermal-hydraulic economic considerations must be analyzed. In this case the optimum configuration is the

two-row depleted uranium-fueled blanket surrounded by a graphite reflector, as shown in the last column of Table 3.17.

It should be emphasized that these conclusions are based upon the environment characterized in Tables 3.9, 3.10 and 3.11, and the fuel-management scheme of batch irradiation and fixed orificing. To see how changes in these assumptions affect the results, the following points are made:

1. The operating conditions of the reactor (Table 3.11) are not expected to vary.

2. Changes in the orificing scheme can greatly improve the thermal-hydraulic performance of the radial blanket. In particular, using the methods presented in previous sections, it is calculated that individual row orificing offers the chance to save about $\$8.2 \times 10^5$/year for <u>any</u> 3-row blanket and about $\$4.2 \times 10^5$/year for <u>any</u> 2-row blanket. (One-row blankets are, by definition, individually orificed.) Table 3.18 lists the absolute difference in dollars per year between the base case configuration, individually (row-by-row) orificed and the particular case of interest, also individually orificed. Note that the burnup economic performance does not change in going from a uniform to an individually orificed blanket.

Comparing this list to the last column in Table 3.17 it is apparent that that the magnitude of the relative economic gain of individually orificed blankets is reduced. Nonetheless, the optimum configuration is still the 2-row depleted uranium blanket with graphite reflector. Since individual (row-by-row) orificing is the likely design choice (e.g., the Phoenix Fast Reactor (P-3) makes use of baffles in the

TABLE 3.18 Comparison of Blanket Economic Performance for Individually Orificed Blanket Rows

Case Number	E_{net} (10^5 \$/year)*
3DS (Base Case)†	–
2DS	-5.56
2NS	-5.61
2MS	-5.55
2ES	-1.94
2DC	-7.14
1DS	-6.97
1DC	-4.18

*10^5 \$/yr ~ 0.014 mills/kW-hr (assuming 7×10^9 kW-hr/yr).
†All other numbers are relative to this case.

inlet plenum to control the flow to different regions of the reactor), this case is also the most interesting of those studied.

3. The economic conditions stated in Tables 3.9 and 3.10 may change. In general, an increase in plutonium value would imply that thicker blankets would be desired from a burnup-economic point of view. This would have to be weighed against the degradation of thermal-hydraulic performance. An increase in fabrication or reprocessing costs would suggest the use of thinner blankets. A more detailed analysis of the effects of changes in the economic environment on fuel cycle costs can be found in reference W-5.

4. Different blanket fuel management schemes can affect the burnup and thermal-hydraulic-economic performance of the radial blanket. However, schemes other than batch-managed blankets increase the complexity

of, and time needed for refueling. For example, it has been suggested that periodic rotation of the blanket elements decreases the blanket spatial gradient factor, F, by about 10% (F-1). This corresponds to a savings of about \$300,000/year ($\sim 4 \times 10^{-2}$ mills/kW-hr) using the methods set forth by Eqs. 3.28 and 3.29. However, the added fuel handling may extend reactor down-time, which involves a penalty of about \$100,000 per day (T-2). Assuming it takes one hour to move one assembly (V-1) and assuming only one blanket row is moved per year (~70 assemblies), then the economic penalty is about \$300,000/year, thereby negating the thermal-hydraulic benefits. Thus blanket element rotation will be attractive only if fuel shuffling is not the limiting item governing the shutdown duration; or if other advantages, such as equalization of radiation-induced bowing are important.

5. Schemes to reduce the spatial power gradient offer larger potential savings for a given blanket-reflector configuration than schemes which would reduce the effect of the temporal gradient. For example, if it were possible to achieve "perfect" orificing, both spatially and temporally, the maximum thermal-hydraulic economic gain to be achieved for the base-case configuration would be about 2.5 million dollars per year representing a present value of about 11 million dollars over the 6-year blanket lifetime, of which over 80% can be attributed to the "perfect" spatial orifice. This amount of savings is rather significant, however, when considering the fact that the total fabrication cost of the blanket is only 3 million dollars!

It should be emphasized that reduction of the effects of the temporal gradient considers only schemes, such as time-varying orificing, that

control the coolant flow to accommodate the average blanket power. Fuel-management schemes that actually reduce the EOL-to-BOL average power ratio (R), in a given row have not been addressed as such here, although increased initial blanket enrichment, which reduces R, was shown not to have a very large effect on improving the thermal-hydraulic-economic performance.

In summary, it must be reemphasized that the blanket burnup performance should not be the sole criterion in the design of the radial blanket reflector configuration. Other effects such as thermal-hydraulic performance (the main thrust of this section), mechanical limitations, increased complexity, and fuel handling associated with fuel-management schemes, etc. should be carefully analyzed before making a final selection of an optimum blanket-reflector configuration.

3.5 Summary

The main objective of the work reported in this chapter was evaluation of the performance of various blanket-reflector configurations. To this end a reference reactor configuration was identified and a burnup method was defined. Neutronic calculations were made with the two-dimensional, diffusion theory, burnup code 2DB (L-4). Four-group cross sections were used in 2DB. These cross sections were obtained with the ANISN code (E-4), which was used to perform a regionwide collapse of the 26-group ABBN cross-section set (A-6). An "equilibrium" core and axial blanket were then defined so that radial blanket burnup studies (up to 6 years in length) could be performed independent of the core. The results obtained from this blanket burnup analysis were

material inventories and fission rates as a function of blanket position and irradiation time. These results were then used as input into the burnup-economic and thermal-hydraulic-economic models.

The burnup economic analysis was performed utilizing the cash flow method contained in the computer code BRECON, developed by Brewer (B-5) and modified by Wood (W-5) to permit direct use of the 2DB burn-up results.

The thermal-hydraulic economic analysis, developed in Section 3.3, relates changes in power-peaking factors to changes in fuel cycle costs. Two types of blanket power-peaking factors were discussed – spatial and temporal. The former is the ratio of peak power density to average power density; whereas the later is the ratio of end-of-life power (P_{EOL}) to beginning-of-life power (P_{BOL}). It was shown that the spatial effects dominate the temporal effects, accounting for over 75% of the detrimental effects of blanket overcooling due to non-uniform power.

Equations 3.28 and 3.29 summarize the method of dealing with the economic effect of blanket thermal-hydraulics. These equations were derived by relating changes in power-peaking factors to changes in mixed-mean reactor coolant temperature rise (ΔT_r). Changes in ΔT_r were then associated with changes in reactor thermal efficiency and pumping power requirements. These last two phenomena were then related to changes in available electric power and ultimately to relative changes in the cost of power.

The fission heating rates determined by the 2DB analysis, in conjunction with the excess gamma and neutron heating rates in the blanket (due to core leakage gamma rays and neutrons) determined in Chapter 2,

were used to perform the thermal-hydraulic analysis. It should be noted that the beginning-of-life power will be underpredicted substantially (up to 50%) if the gamma-neutron heating effect is neglected, giving rise to an overestimate of the temporal power-peaking factor. The effect of neglecting the gamma-neutron heating on the spatial gradient is smaller (a few percent) since the end-of-life spatial peaking factor is the proper one to be used in the analysis, and the local fission heating accounts for practically all of the blanket heating at this time.

A series of blanket-reflector configurations differing in blanket thickness, initial enrichment and reflector composition were then studied. The results of these case studies is given in Table 3.16 for uniformly orificed blankets under the economic and operating conditions given in Tables 3.9, 3.10 and 3.11.

The basic conclusions to be made are:

1. Two-row blankets are preferable to 3-row blankets in the reference economic condition.

2. Initial enrichment of the blanket is undesirable.

3. Graphite reflectors are to be preferred to steel reflectors.

4. Individual row orificing in place of uniform orificing improves the thermal-hydraulic performance of multirow blankets (~0.118 mills/kW-hr for a 3-row blanket and ~0.060 mills/kW-hr for a 2-row blanket).

5. Schemes to reduce spatial power gradients (e.g., rapid subassembly rotation, effective coolant cross-flow mixing) offer larger potential savings for a given blanket-reflector configuration than schemes

which would reduce the effect of the temporal power gradient (e.g., time-varying orificing).

6. An optimum blanket-reflector configuration can only be selected by considering both the burnup performance and the thermal-hydraulic performance.

Since it has been concluded that graphite-reflected blankets can substantially outperform steel-reflected blankets, it is both timely and essential to verify the underlying neutronic analysis against experimental data. This task is the subject of the next chapter.

Chapter 4

BLANKET MOCK-UP NUMBER 3

4.1 Introduction

In the analysis of reactor core performance, the adequacy of the calculational methods and cross sections employed is always of paramount concern. In the present case, where a high-albedo moderating reflector is involved, it was not clear that methods and cross-section sets previously proven adequate for core calculations (by comparison with critical assembly data) would prove adequate. The severe spectral degradation of the flux and consequent accentuation of resonance self-shielding effects in U-238 were of particular concern. For this reason it was considered essential to acquire experimental verification on a mock-up of a blanket using the Blanket Test Facility (BTF) at the M.I.T. Research Reactor.

A detailed description of the design and construction of the BTF is presented in reference (F-3). For present purposes the only point requiring reiteration is that the BTF converter assembly provides neutrons closely simulating the leakage spectrum from an LMFBR core, which can be used to drive blanket mock-ups.

To date four blankets have been irradiated. The first contained no uranium and was used only to evaluate facility performance. Blankets No. 2 and No. 4, however, were accurate mock-ups of a typical three-subassembly-row, steel reflected blanket; No. 2 was driven by a simulated 1000 MWe reactor core, and No. 4 by a harder spectrum simulating a smaller demonstration plant core. The results of these experi-

ments have been documented in a series of reports (F-2, F-4, K-1, L-2, O-1, W-5). Blanket No. 3, the present subject, was designed to incorporate a graphite reflector region in place of the third row of fuel in Blanket No. 2; otherwise all important characteristics were kept the same. Section 4.2 reviews the design and construction of Blanket No. 3; Section 4.3 discusses the experimental program, whose results are presented and analyzed in Section 4.4. Conclusions and comments are outlined in Section 4.5.

4.2 Description of Blanket Mock-Up No. 3

4.2.1 General Description

Figure 4.1 shows a schematic view of the BTF Blanket Mock-Up No. 3 assembly on its cart, including the uranium subassemblies, and the graphite and steel reflectors. The support structure for the assembly consists of two pieces of 1 inch by 60 inches by 39 inches and one piece of 1 inch by 62-7/16 inches by 58-1/4 inches hot-rolled, mild steel plates, welded to make an H-frame. The H-frame support structure and cart for this mock-up are identical to those used for Blanket Mock-Up No. 2 except for an additional steel plate, 0.5 inch by 23 inches by 61 inches, welded to the bottom of the cart, providing the necessary overhang to support the uranium subassemblies and graphite reflector on the front half of the H-frame.

There are 19 full subassemblies (5-13/16 inches by 5-13/16 inches by 60 inches) arranged in two rows. The full-size subassemblies are filled with steel-clad uranium rods and sodium chromate. The two half-size peripheral subassemblies, used to provide a staggered array,

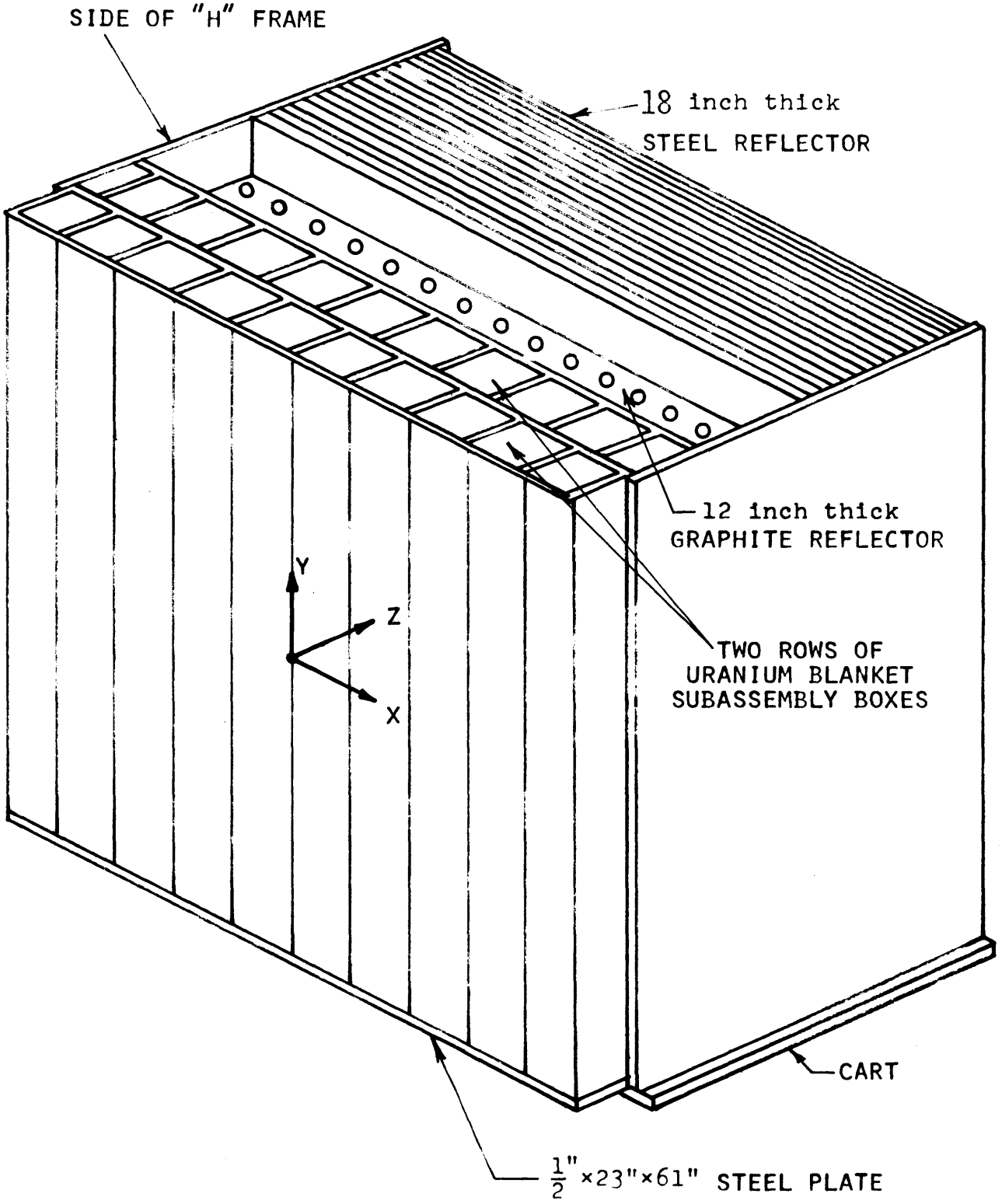

FIG 4.1 SCHEMATIC VIEW OF BLANKET MOCK-UP NO. 3
WITH GRAPHITE REFLECTOR

are filled with a mixture of iron and borax, shown to be a good representation of a fueled assembly in the work on Blanket No. 1 (F-3).

Forty-three foil tubes are provided for the irradiation of various foils in the blanket and reflector in the axial and transverse directions, as depicted in Fig. 4.2. The foil tubes are mild steel tubing of 7/16-inch outside diameter, 0.028 inch thick and 58 inches long, and are held in place by the top and bottom grid plates in each subassembly.

4.2.2 Blanket Subassembly Description

The subassemblies for Blanket Mock-Up No. 3 are identical to those used in Blanket Mock-Up No. 2. A detailed description of these subassemblies is given in reference (L-2) and is included here for completeness.

Each subassembly box has a wall thickness of approximately 3/32 inch and a seal-welded bottom closure plate. It contains 121 fuel rods arranged in an 11 by 11 square lattice whose pitch is 0.511 inch (Figs 4.3 and 4.4). The uranium metal rods are 0.250 inch in diameter and 48 inches in length. Sixty of the rods have a U-235 enrichment of 1.016%, and sixty-one have a U-235 enrichment of 1.134%; the two enrichments are loaded in a checkerboard pattern within the subassembly box. The uranium metal rods are clad in low-carbon, mild steel tubing. The clad tubing dimensions are 5/16-inch O.D., 0.018-inch wall thickness and 50 inches in length. Each end of the tube is closed by a press-fitted steel plug, 1/2 inch long by 9/32 inch O.D. This arrangement leaves a 1-inch free space in the tube to allow for dimensional variations and fuel expansion. The fuel rods are held in place by aluminum bottom

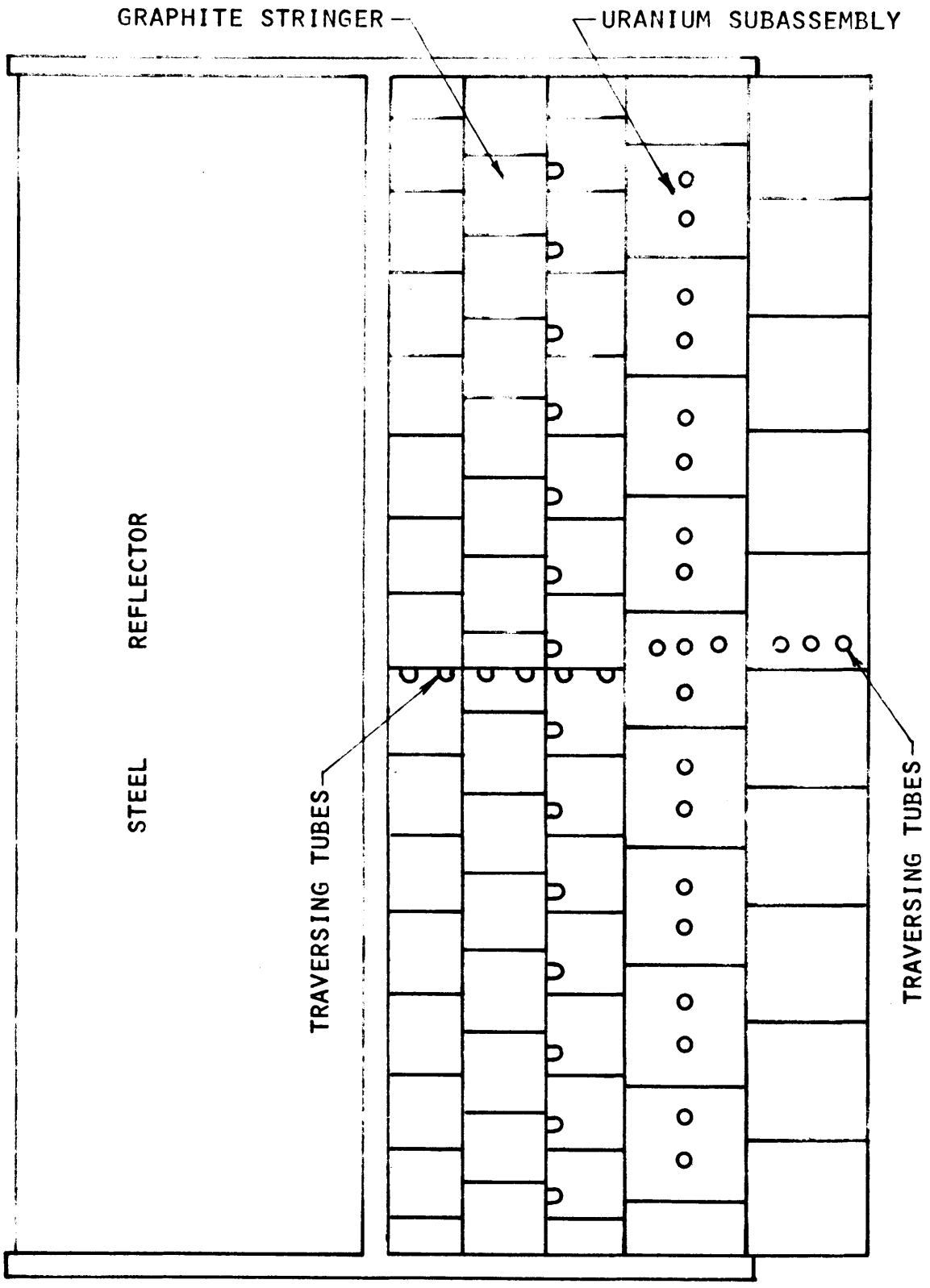

FIG. 4.2 OVERHEAD VIEW OF BLANKET MOCK-UP NO. 3

FIG. 4.3 GRID PLATE FOR BLANKET NO. 3 SUBASSEMBLIES

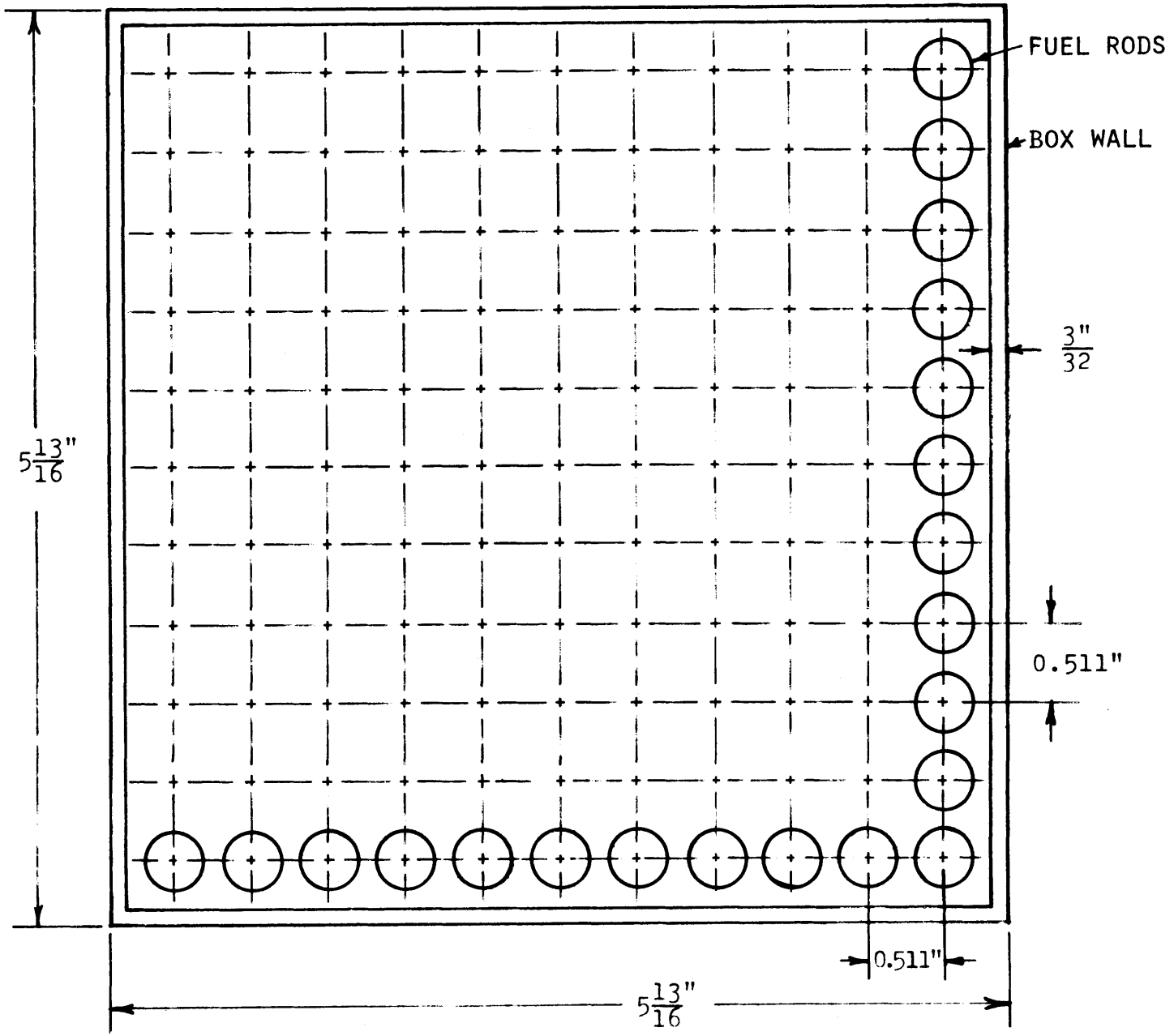

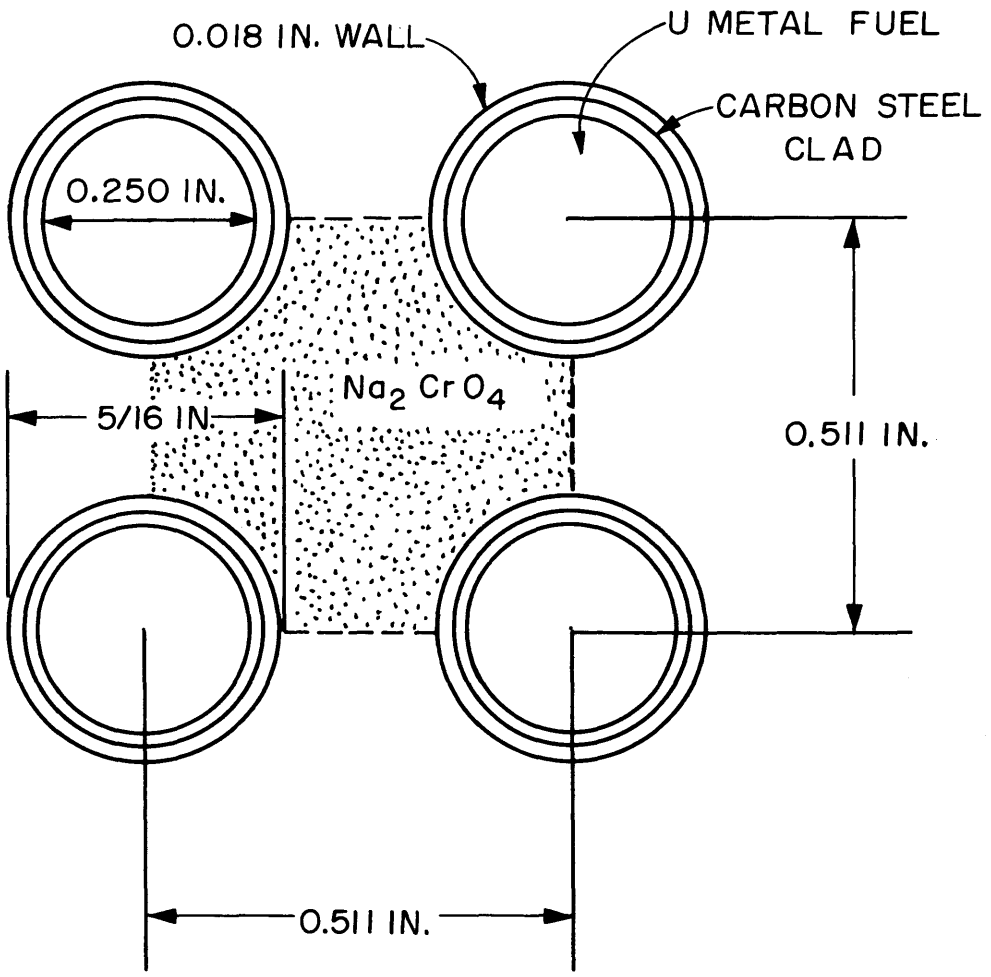

FIG. 4.4 BLANKET NO. 3 UNIT CELL

and top grid plates, 1/4 inch in thickness.

Technical grade anhydrous sodium chromate powder, Na_2CrO_4, baked at 400°F to decrease the water content to less than 0.1%, and ground into a uniform powder, occupies the inter-rod volume. Each subassembly is sealed by a 0.035-inch-thick steel top plate, epoxied in place to make the subassembly air- and water-tight. Figure 4.5 shows the cross-sectional view of the blanket subassembly.

A breakdown of the average subassembly weight is given in Table 4.1 (as reported in reference (L-2)).

TABLE 4.1 Subassembly Component Weights

Uranium metal	89.30 kg
Na_2CrO_4	31.11 kg
Cladding	13.00 kg
Subassembly box	26.55 kg
Grid plate support tubes	0.91 kg
Grid plates	0.36 kg
Total	161.23 kg

The homogenized subassembly atom densities in Blanket No. 3 are given in Table 4.2. They represent the nuclide densities in the central portions of the assembly. Table 4.2 also includes the atom densities for an "equivalent realistic blanket" composed of 37 v/o depleted UO_2 (at 90% t.d.), 20.7 ^{v}/o Type 316 stainless steel (71.2 ^{w}/o Fe, 20.0 ^{w}/o Cr, 8.8 ^{w}/o Ni), 32 ^{v}/o sodium and 10.3 ^{v}/o void. Nuclide densities for the graphite and steel reflectors are also listed in

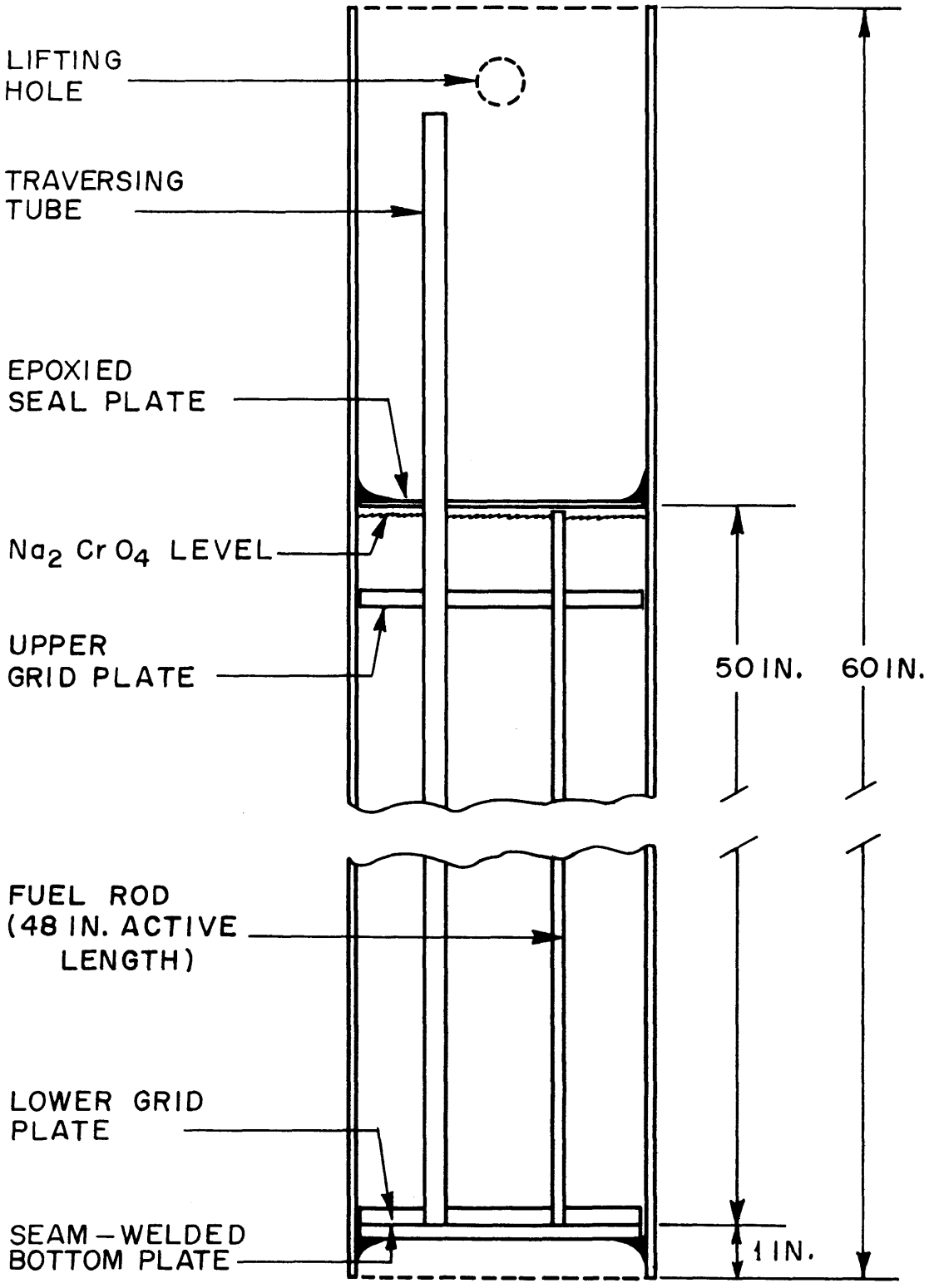

FIG. 4.5 SCHEMATIC CROSS SECTION VIEW OF BLANKET NO. 3 SUBASSEMBLY

TABLE 4.2

Homogenized Atom Densities in Blanket No. 3

(Atoms/barn-cm)

Nuclide	Blanket No. 3		Equivalent Realistic Blanket*	
U^{235}	0.000088		0.000016	
U^{238}	0.008108		0.008131	
O	0.016293		0.016293	
Na	0.008128		0.008128	
Cr	0.004064	0.017814	0.003728	0.017814
Fe	0.013750		0.012611	
Ni	0.000000		0.001475	
H	0.000073		0.000000	
C	0.000096		0.000082	
Nuclide	**Graphite Reflector**			
C	0.083245			
H	0.000298			
Nuclide	**Steel Reflector**			
C	0.000590			
Fe	0.084570			

* Composed of 37.0 v/o depleted UO_2 (at 90% of the theoretical density), 20.7 v/o Type 316 stainless steel, 32.0 v/o sodium and 10.3 v/o void.

Table 4.2. It is evident that Blanket No. 3 provides a realistic blanket composition.

4.2.3 Description of the Graphite Reflector

Figure 4.6 shows a schematic view of the graphite reflector assembly. It consists of a bottom graphite layer acting as the lower

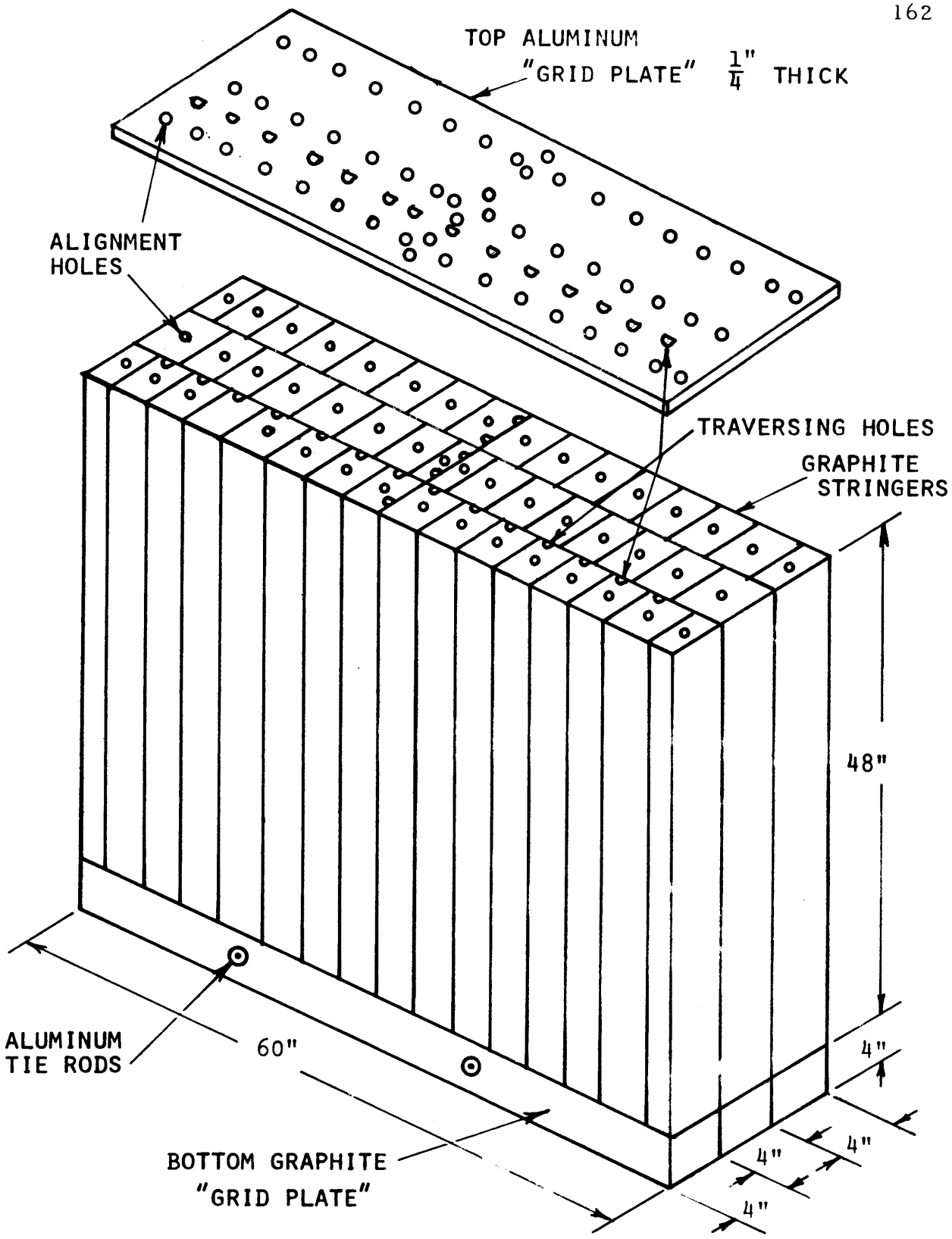

FIG. 4.6 SCHEMATIC VIEW OF GRAPHITE REFLECTOR ASSEMBLY

grid plate, the graphite reflector, and an aluminum top grid plate, forming a parallelepiped 52-1/4 inches high, 12 inches thick (i.e., two fuel subassemblies) and 60 inches wide. From a neutronic standpoint, 12 inches of graphite are effectively infinite in the present application.

The bottom grid plate was made from three 60-inch pieces of 4-inch-square graphite stringers placed side-by-side, forming a slab 4 inches by 12 inches by 60 inches.

These three stringers are held together by two aluminum rods which fit into 1/2-inch-diameter holes drilled through the stringers 15 inches from each end. The rods are threaded at each end and recess-bolted to clamp the grid plate together. Holes were then drilled into the top face of the plate to align the vertical stringers which make up the reflector. These holes are 1/4 inch in diameter and 3/4 inch deep and seat aluminum pins 1-1/2 inches long. The reflector consists of 48 graphite stringers 48 inches high. Four of the outside stringers are half pieces, 4 inches by 2 inches instead of 4 inches by 4 inches to permit formation of a staggered array. Also, the two stringers in the center of the assembly are half pieces, making 6 half stringers in all.

In each of these 48 stringers, 1/4-inch-diameter holes, 3/4-inch deep, were drilled in the top and bottom ends to fit over the aluminum pins set in the bottom grid plate, and to house pins which in turn align with the positioning holes in the top 1/4-inch-thick aluminum grid plate.

In order to permit foil activation traverses in the reflector assembly, twenty 3/8-inch-square vertical slots were milled into the

faces of selected graphite stringers comprising the reflector. These slots house the holder rods for foil samples, as can be seen in Fig. 4.7. There are 6 slots which can be used to determine axial traverses and 14 slots for the transverse measurements.

In the experiments which follow, positions within the blanket and reflector are described in terms of a Cartesian coordinate system whose origin is at the center of the front face of the blanket (i.e., the converter-blanket interface): the $\pm X$ and $\pm Y$ axes delineate the horizontal and vertical directions, respectively, while the $+Z$ axis (corresponding to the radial direction in a cylindrical core and blanket) designates the depth into the blanket (see Fig. 4.2).

4.3 Experimental Aspects

4.3.1 Introduction – Objectives

The objective of the present experiments was to obtain the necessary data to evaluate the transverse buckling and axial reaction rates for various foil materials in Blanket No. 3. The foil materials employed are listed in Table 4.3 along with the reactions of interest.

Buckling measurements in the X and Y directions are important because, in order to validate the one-dimensional calculational model, the leakage must be characterized by a buckling formulation. If this is the case, the neutron flux can be separated in space according to the relation:

$$\phi(X, Y, Z, E) = \cos\left(\frac{\pi X}{W}\right) \cos\left(\frac{\pi Y}{H}\right) \phi(Z, E), \qquad (4.1)$$

where the buckling is given by

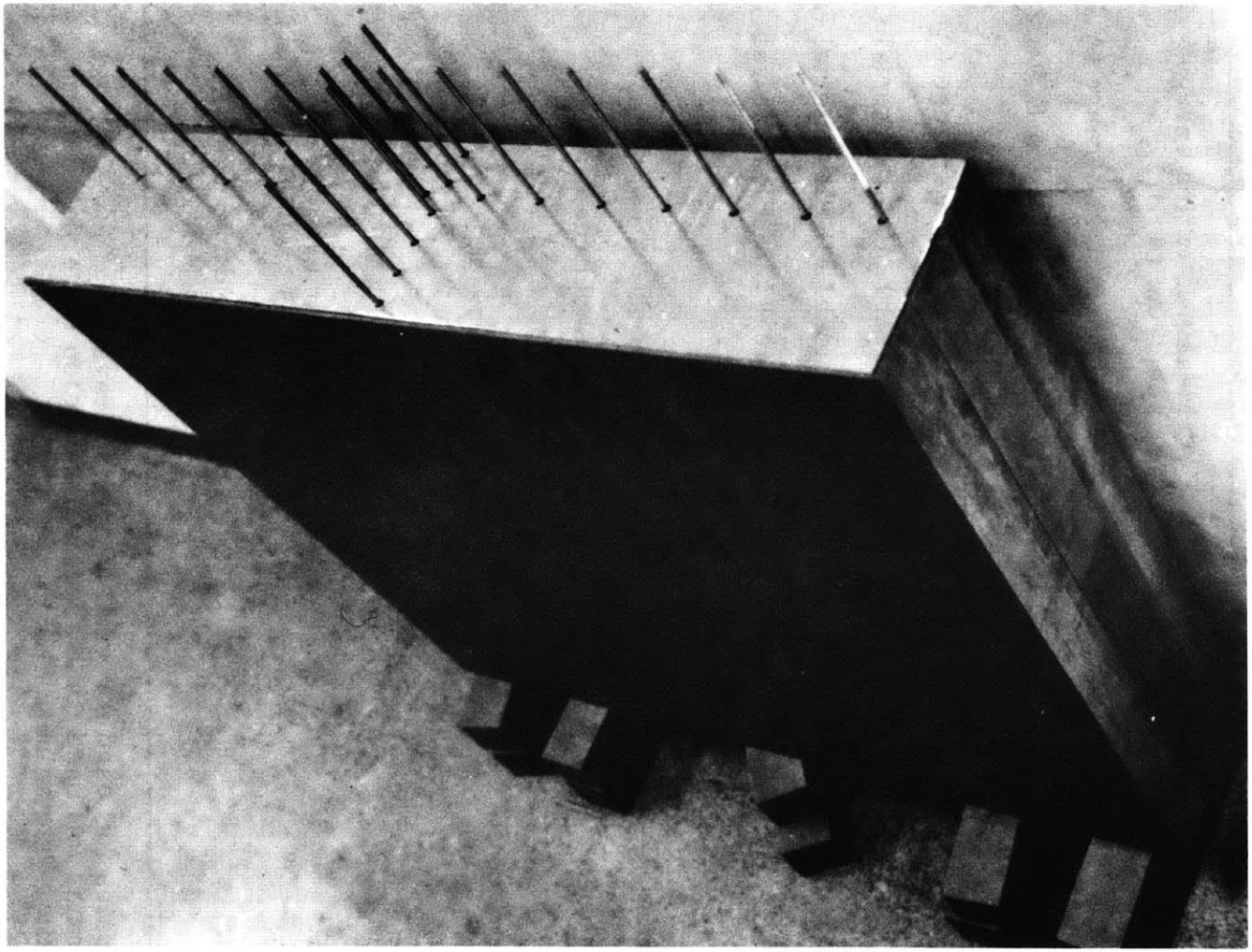

FIG. 4.7 GRAPHITE REFLECTOR WITH AXIAL AND TRANSVERSE HOLDER RODS INSERTED

TABLE 4.3

Activation Foils Used in BTF No. 3

Foil	Reaction	Remarks
Gold	$Au^{197}(n,\gamma)Au^{198}$	Measures entire energy spectrum (A,B)*
Molybdenum	$Mo^{98}(n,\gamma)Mo^{99}$	Emphasizes keV range (A,B)
Indium	$In^{115}(n,n')\ In^{115m}$	Threshold reaction E > 0.2 MeV (A,B)
Manganese†	$Mn^{55}(n,\gamma)Mn^{56}$	Emphasizes keV range (A)
Sodium	$Na^{23}(n,\gamma)Na^{24}$	Typical LMFBR material (A)
Chromium	$Cr^{50}(n,\gamma)Cr^{51}$	Typical LMFBR material (A)
Uranium	—	Typical LMFBR material
-238 in-rod	$U^{238}(n,\gamma)$	(A)
-238 ex-rod	$U^{238}(n,\gamma)$	(A,B)
-238 in-rod	$U^{238}(n,f)$	Threshold reaction E > 1.0 MeV (A)
-238 ex-rod	$U^{238}(n,f)$	(A,B)
-235	$U^{235}(n,f)$	(A)
Plutonium-239	$Pu^{239}(n,f)$	Typical LMFBR material (A)
Thorium†	$Th^{232}(n,f)$	Threshold reaction E > 1.75 MeV (A,B)
Neptunium†	$Np^{237}(n,f)$	Threshold reaction E > 0.75 MeV (A)

* A indicates foil used for axial activation traverse.
B indicates foil used for transverse activation traverse (i.e., buckling determination).

† New materials, not used in BTF No. 2.

$$B^2 = BX^2 + BY^2 = \left(\frac{\pi}{W}\right)^2 + \left(\frac{\pi}{H}\right)^2 \qquad (4.2)$$

and where W and H are experimentally determined values of the extrapolated width and height, respectively. The system was designed to achieve this result and the experiments on Blanket No. 2 have confirmed that this desired cosine dependence is attained (L-2). In the present work, therefore, less emphasis was placed on transverse buckling determinations than previously, and measurements were made just to confirm that the values of W and H in the graphite reflector are consistent with those previously determined in the blanket region of Blanket No. 2. The necessity for high precision in these measurements has been further reduced by the observation that calculated Z traverses are not sensitive to the transverse buckling; even setting $B^2 = 0$ results in negligible changes in the calculated results.

4.3.2 Experimental Procedure

The experimental technique is rather conventional and practically identical to that used in the analysis of BTF No. 2 (L-2). Thus, only a brief description, primarily noting changes in the experimental procedure, will be presented.

4.3.2.1 Buckling Experiment

Transverse buckling measurements were made in the graphite reflector utilizing various foil materials. Gold, molybdenum and thorium foils were utilized for horizontal measurements. Gold and thorium foils were utilized in the vertical measurements. The thorium foils were used

to detect fast neutrons by counting fission products produced in the threshold fission reaction. The experimental techniques were similar to those used in Blanket No. 2.

Aluminum rods containing milled axial depressions were used to position the foils vertically and, when inserted in the respective transverse traversing rods, provided the desired lateral positioning (see Fig. 4.7). Aluminum holders were used in the graphite instead of the standard steel holders employed for the blanket to avoid absorption of low-energy neutrons moderated by the graphite.

For vertical measurements, one rod holding 10 equispaced foils (3-inch spacing) was inserted in the central transverse slot. The horizontal measurements utilized all 14 slots (4-inch spacing) with foils held in place at locations along the midline (Y-axis) of the graphite.

The counting procedure used to obtain the raw data was identical to that used with BTF No. 2, as were foil weight, background and decay time corrections (where necessary) (L-2). The only procedural innovation involved the thorium foils, which were not used previously. In order to achieve useful counting statistics, a sandwich arrangement of three aluminum fission product catcher foils and two thorium foils held together with Mylar tape was used (Fig. 4.8). By counting the fission products recoiled into the catcher foils, instead of those in the thorium itself, the high thorium background activity did not compromise the fission product counting.

4.3.2.2 Axial Traverses

Axial traverses were made in the blanket and graphite reflector

FIG. 4.8 THORIUM FOIL PACKET

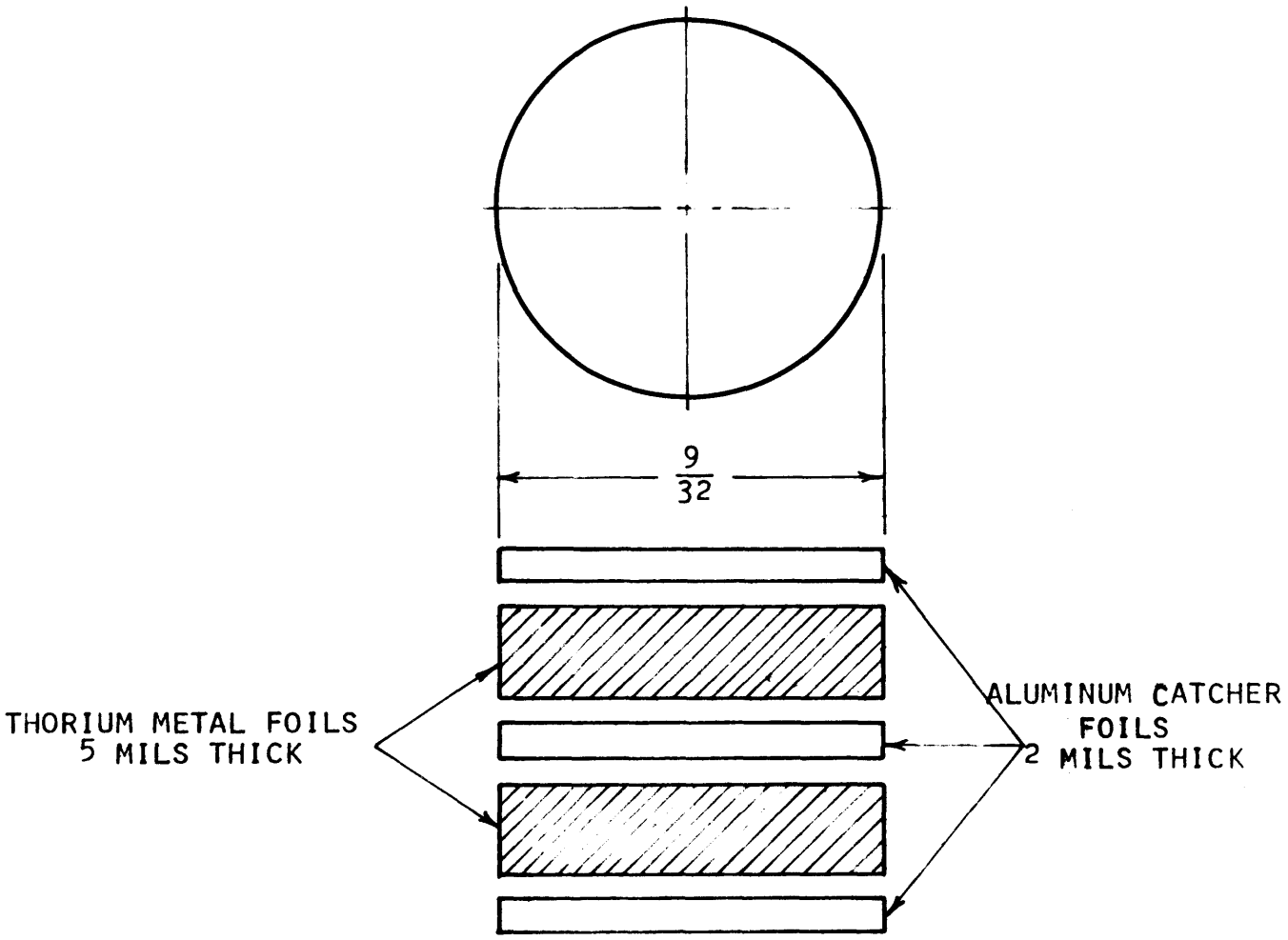

assemblies. Simulating traverses in the radial direction in cylindrical geometry, twelve axial traversing slots are provided, six each in the blanket and graphite. Steel foil-holder rods were used in the blanket region and aluminum rods were used in the graphite region. The foils irradiated in this phase of the experiment are listed in Table 4.3. Along with thorium, which was discussed in Section 4.3.2.1, neptunium and manganese represent the only foil materials not irradiated previously in Blanket No. 2.

The manganese, in powder form, was encapsulated in poly vials in a manner similar to that used for the sodium foils. The neptunium compound, a nitrate of undetermined composition, was loaded in 1/4-inch-diameter by 1-inch-long aluminum capsules and taped to the foil-holder rods. The relative neptunium content of the individual capsules was determined by background activity measurements.

The counting procedure used to obtain the raw data was identical to that used in Blanket No. 2, as were corrections for foil weights, background and decay time. The only additional modification involved determination of the relative weights of the plutonium samples, where background activity was used to determine the relative plutonium content instead of direct weighing or thermal activation calibration.

Table 4.4 summarizes the counting characteristics of the thorium, neptunium and manganese foils used in the reaction rate measurements. Similar data for the other foil materials are found in reference (L-2).

TABLE 4.4

Typical Data Pertinent to Foil Counting

Parameter	Thorium Foil	Neptunium Foil	Manganese Foil
Reaction	$Th^{232}(n,f)$	$Np^{237}(n,f)$	$Mn^{55}(n,\gamma)$
Product nuclide	Fission products	Fission products	Mn^{56}
Half life	~2.5 hours	~2.5 hours	2.58 hours
Eγ (MeV)	≥ 0.5	≥ 0.5	0.84
Eγ detected (MeV)	0.72-∞	1.28-∞	0.72-∞
Discriminator setting			
E_{min} (volts)	1.54*	2.80*	1.90†
E_{max} (volts)	∞	∞	∞
Typical counts (less bkg.)	500	2,000	30,000
Counting time (minutes)	10	5	2
Irradiation time (hours)	12	12	16

* Calibration approximately 0.46 MeV per volt

† Calibration approximately 0.38 MeV per volt

4.4 The Results

4.4.1 Analytical Predictions

4.4.1.1 Buckling

As previously mentioned, the transverse fluxes in Blanket No. 2 were found to follow the anticipated cosine shape. Hence, the buckling in Blanket No. 3 should also conform to this result:

$$A(X) = A(o) \cos\left(\frac{\pi X}{W}\right)$$

and (4.3)

$$A(Y) = A(o) \cos\left(\frac{\pi Y}{H}\right),$$

where the extrapolated width and height, W and H, are best determined by curve-fitting the experimental data, and A(o) is the maximum amplitude. The values of W and H obtained in Blanket No. 2 were 74 inches and 60 inches, respectively; the corresponding assembly width and active fuel height are 58 inches and 48 inches. No significant change is to be expected for Blanket No. 3, since the graphite was sized to have approximately the same theoretical extrapolated peripheral dimensions as the rest of the assembly, which is otherwise identical to Blanket No. 2 in the X and Y directions.

4.4.1.2 Axial Traverses

Axial reaction rates were computed by means of the one-dimensional transport theory code, ANISN (E-4) in the S_8 option, using the 26-group Russian ABBN cross-section set (A-6) for all but four materials. The

effect of U-238 self-shielding in the converter plate and blanket fuel rods has been taken into account. Broad group cross sections for U-238, which account for resonance self-shielding, have been generated with the MIDI code (F-2). These cross sections were then incorporated into the 26-group ABBN set.

Au-197 capture, In-115(n,n') and Np-237 fission cross-section data were developed from the SAND-II Library (M-4) by collapsing over the ABBN weighting spectrum. It should be noted that the cross-section data used to evaluate the foil activities were not self-shielded, except for in-rod U-238 capture; i.e., the calculated ex-rod U-238 reaction rate is for infinite dilution cross sections.

Plots of these data are found in the figures referred to in the next section, where they are compared with experimental results.

4.4.2 Experimental Results

The data reported in this section are normalized activities corrected for counter dead time, background activity, foil weight, and sample decay time. To facilitate comparison, the experimental data were normalized to coincide with the calculated results at a convenient point. Thus, for example, the experimental axial results were made to coincide with the calculated results at approximately 12.7 centimeters from the converter-blanket interface, which is a little less than halfway into the blanket. The only exception occurs in Fig. 4.16, where the correct experimental ratio between in-rod and ex-rod U-238 captures is maintained.

Error brackets are shown on the graphs when the experimental

point itself is not large enough to cover the experimental error. Typically, over 10,000 counts were accumulated to ensure statistical precision of better than ± 1%. At deep penetrations and where background activity was a substantial portion of the counts, ± 1%, statistical error in the relative activity was sometimes exceeded. The errors shown in Tables 4.5 and 4.6 and 4.7 show either the uncertainty in counting statistics or the experimental standard deviation corrected for small sample statistics, whichever is applicable. A more detailed discussion of experimental error is included in Section 4.4.3.

4.4.2.1 Buckling

Tables 4.5 and 4.6 show the normalized vertical and horizontal buckling traverse data as a function of distance from the origin of coordinates. Figures 4.9 and 4.10 show representative plots of these data for the Au, Mo and Th horizontal and Au and Th vertical data, respectively. The cosine distributions conform to Eq. 4.1 with W = 74 inches and H = 60 inches, the Blanket No. 2 values.

To ensure that spectral equilibrium is achieved in the central region of the graphite, the ratio of U-238 to gold captures was plotted in Fig. 4.11. The flat region, approximately 16 inches wide, confirms the result found in Blanket No. 2 and ensures that the central reflector region has achieved spectral equilibrium.

4.4.2.2 Axial Activation Traverses

Table 4.7 lists the normalized data for the axial traverses of the various foils as a function of the distance from the converter-blanket

TABLE 4.5

Activation Traverses for Vertical Buckling Determination

Foil Position	Distance from $\mathcal{L}$ (inches)	Normalized Data Au (n,γ)	Normalized Data Th (n,f)
1	-21	0.419 ± 0.001*	0.466 ± 0.087*
2	-18	0.546 ± 0.001	0.556 ± 0.081
3	-15		0.671 ± 0.083
4	-12	0.787 ± 0.001	0.765 ± 0.086
5	-9	0.881 ± 0.001	0.901 ± 0.084
6	-6	0.950 ± 0.001	0.830 ± 0.082
7	-3	0.988 ± 0.001	0.792 ± 0.089
8	0	1.000 ± 0.001	1.000 ± 0.087
9	3	0.994 ± 0.001	0.971 ± 0.089
10	6	0.952 ± 0.001	0.405 ± 0.087
11	9	0.896 ± 0.001	0.970 ± 0.085
12	12	0.839 ± 0.001	0.887 ± 0.087
13	15	0.740 ± 0.001	0.752 ± 0.086
14	18	0.621 ± 0.001	0.647 ± 0.087
15	21	0.472 ± 0.001	0.515 ± 0.086

* Statistical uncertainty, ±σ.
See section 4.4.3 for discussion of errors.

TABLE 4.6

Activation Traverses for Horizontal Buckling Determination

Foil Position	Distance from $\mathbb{C}_L$ (inches)	Normalized Data Au (n,γ)	Normalized Data Mo (n,γ)	Normalized Data Th (n,γ)
1	-26	0.400 ± 0.001*	0.403 ± 0.028*	
2	-22	0.574 ± 0.001	0.554 ± 0.028	0.711 ± 0.109*
3	-18	0.730 ± 0.001	0.706 ± 0.035	1.132 ± 0.113
4	-14	0.838 ± 0.001	0.855 ± 0.034	1.209 ± 0.118
5	-10	0.934 ± 0.001	0.908 ± 0.036	1.468 ± 0.113
6	-6	0.991 ± 0.001	0.912 ± 0.036	1.294 ± 0.112
7	-2	0.999 ± 0.001	1.000 ± 0.040	1.450 ± 0.121
8	2	1.000 ± 0.001	0.925 ± 0.037	1.500 ± 0.118
9	6	0.986 ± 0.001	1.139 ± 0.044	1.337 ± 0.121
10	10	0.938 ± 0.001	0.917 ± 0.037	1.290 ± 0.120
11	14	0.856 ± 0.001	0.779 ± 0.031	1.115 ± 0.115
12	18	0.718 ± 0.001	0.744 ± 0.031	1.183 ± 0.117
13	22	0.559 ± 0.001	0.612 ± 0.035	0.910 ± 0.115
14	26	0.364 ± 0.001	0.436 ± 0.026	

* Statistical uncertainty, ±σ.
See section 4.4.3 for discussion of errors.

FIG. 4.9 HORIZONTAL ACTIVATION TRAVERSES IN BLANKET NO. 3

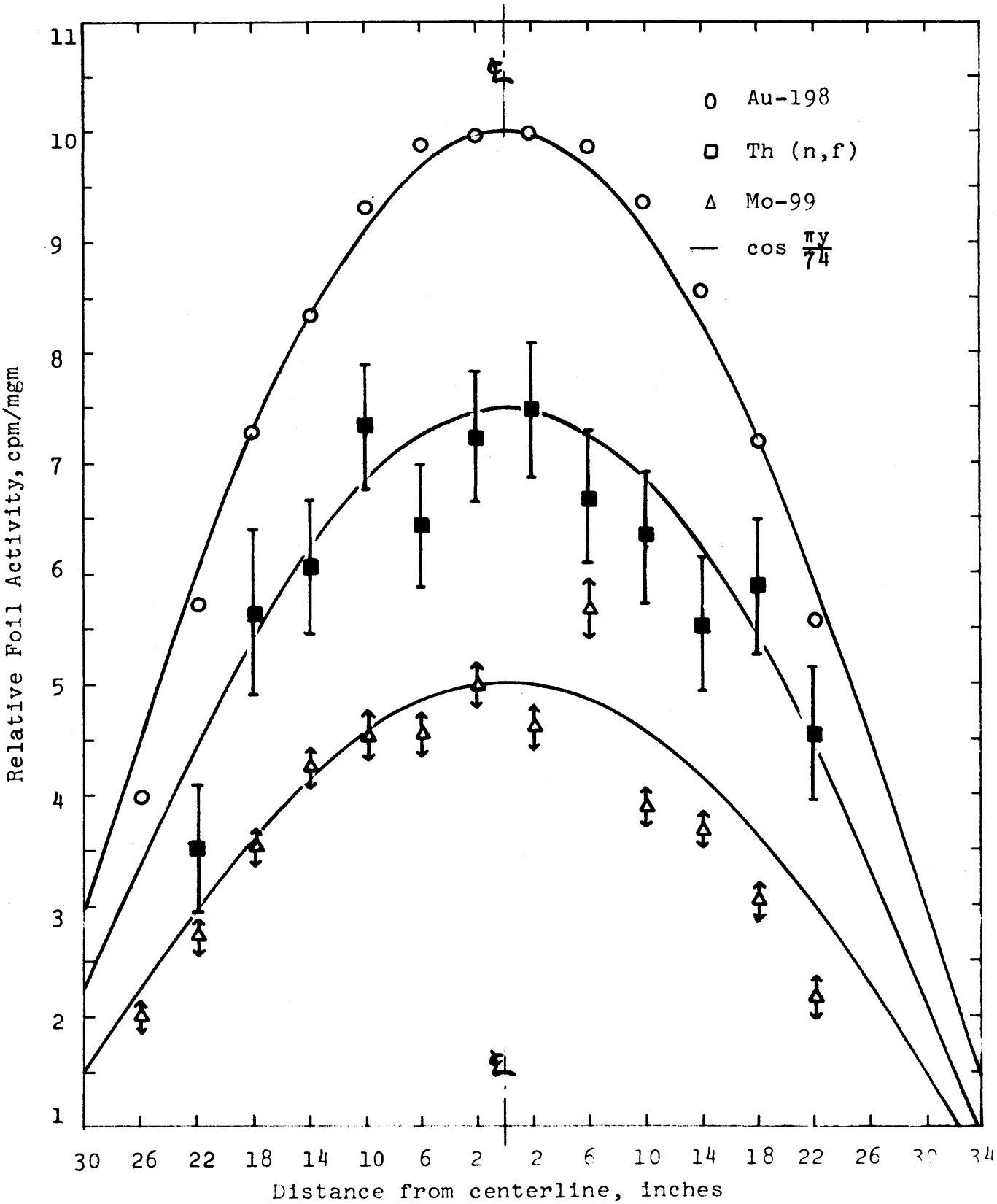

FIG. 4.10 VERTICAL ACTIVATION TRAVERSES IN BLANKET NO. 3

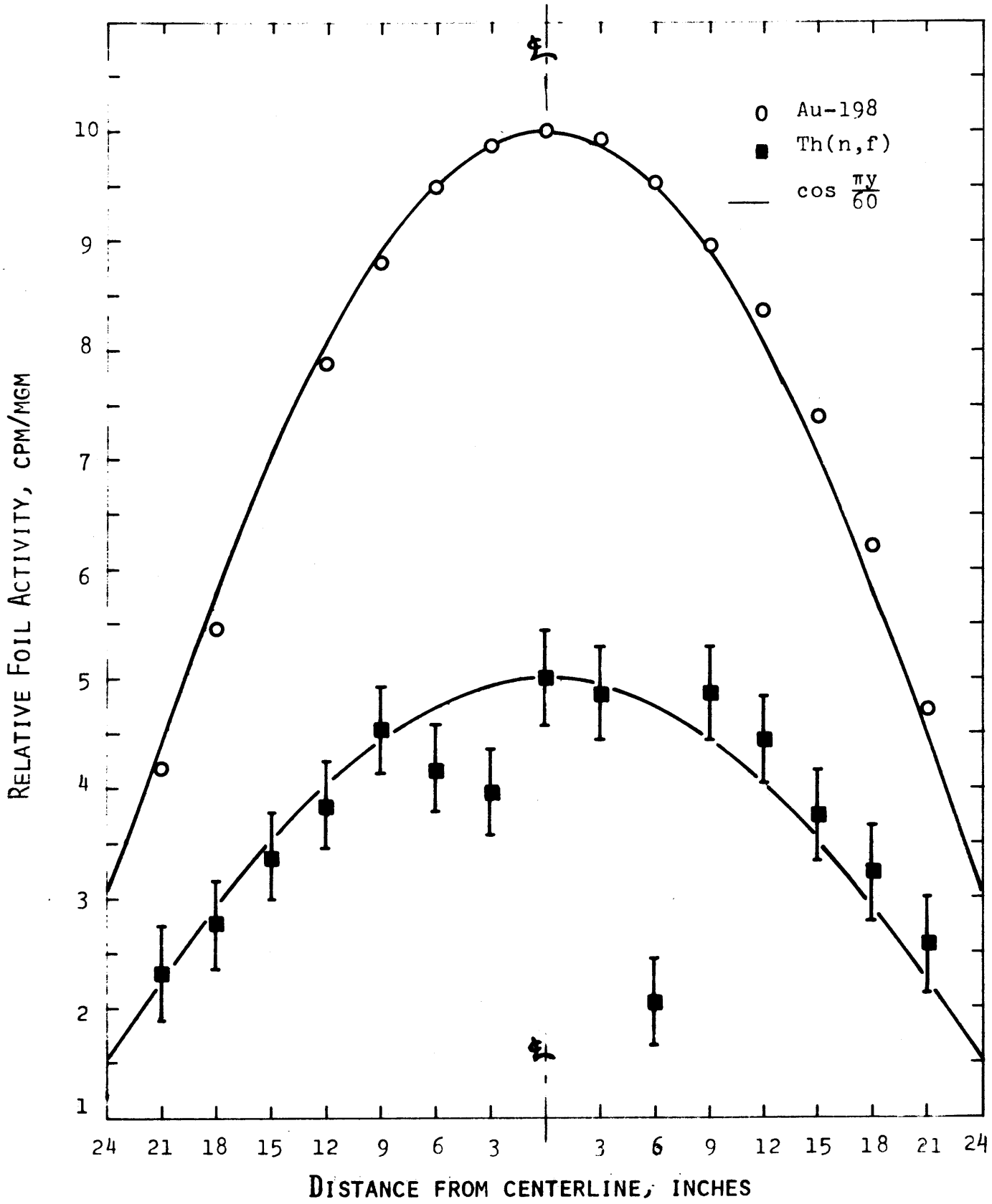

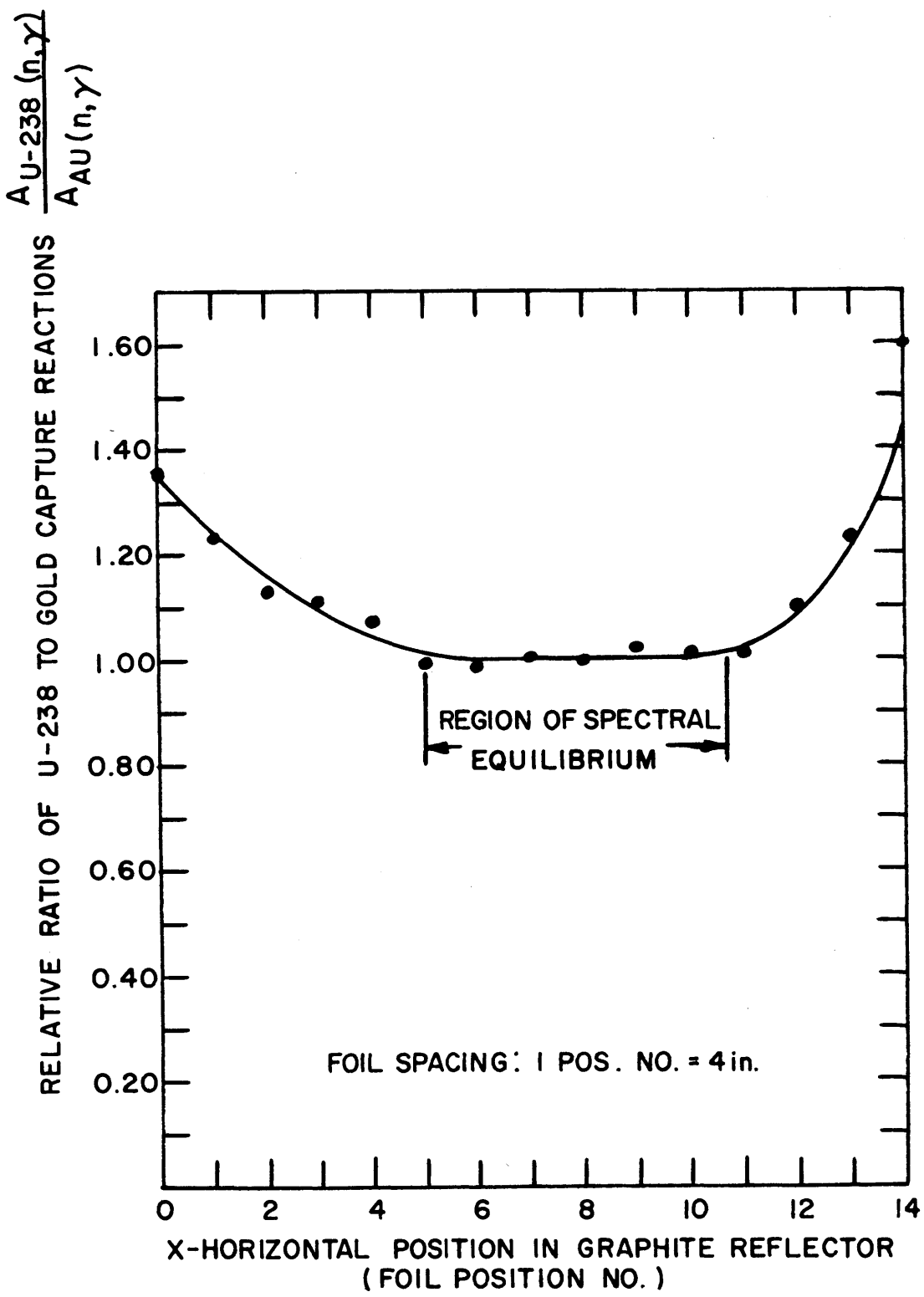

FIG. 4.11 SPECTRAL INDEX TRAVERSE IN GRAPHITE REFLECTOR OF MOCKUP NO. 3

TABLE 4.7. Normalized Axial Reaction Rate Data

Distance From Converter (cm)	Au (n,γ)	Au (n,γ), Dilute	In (n,n')	Mo (n,γ)
2.34	0.1798 ± 0.0105*	0.1617 ± 0.0062*	13.10 ± 0.300*	3.088 ± 0.025*
2.50	0.1624 ± 0.0079	0.1515 ± 0.0130	9.254 ± 0.015	2.764 ± 0.033
12.70	0.1475 ± 0.0000	0.1475 ± 0.0000	6.748 ± 0.004	2.500 ± 0.047
17.40	0.1439 ± 0.0021	0.1634 ± 0.0212	5.280 ± 0.360	2.118 ± 0.010
22.60	0.1663 ± 0.0102	0.2364 ± 0.0045	4.487 ± 0.227	1.856 ± 0.014
27.80	0.2501 ± 0.0076	0.4359 ± 0.0130	4.073 ± 0.210	1.755 ± 0.018
32.87	0.6423 ± 0.0443	1.1786 ± 0.1397	3.096 ± 0.273	1.917 ± 0.000
37.95	0.8941 ± 0.0512	1.4690 ± 0.0590	2.391 ± 0.358	1.707 ± 0.038
43.03	0.9692 ± 0.0588	1.5777 ± 0.0961	2.089 ± 0.208	1.367 ± 0.031
48.11	0.8993 ± 0.0427	1.2353 ± 0.0630	1.674 ± 0.283	1.004 ± 0.016
53.19	0.7278 ± 0.0455	1.0117 ± 0.2322	1.432 ± 0.255	0.6871 ± 0.0051
58.27	0.4923 ± 0.0324	0.7577 ± 0.0893	1.201 ± 0.330	0.4365 ± 0.0027

(Continued)

TABLE 4.7. Normalized Axial Reaction Rate Data (continued)

Distance From Converter (cm)	Mn (n,γ)	Na (n,γ)	Cr (n,γ)	U^{238} (n,f)
2.34	2.255 ± < 0.01*	2.968 ± 0.034*	1.115 ± 0.079*	16.12 ± 0.73*
2.50	2.123 ± < 0.01	2.475 ± 0.103	0.977 ± 0.048	11.83 ± 0.55
12.70	1.950 ± < 0.01	2.205 ± 0.000	0.894 ± 0.053	9.350 ± 0.000
17.40	2.528 ± < 0.01	2.190 ± 0.085	0.938 ± 0.037	7.511 ± 0.410
22.60	2.065 ± < 0.01	2.789 ± 0.139	1.262 ± 0.017	6.969 ± 0.794
27.80	3.334 ± < 0.01	5.249 ± 0.159	2.504 ± 0.137	6.295 ± 0.051
32.87	8.467 ± < 0.01	15.98 ± 0.63	7.937 ± 0.000	5.112 ± 0.967
37.95	12.302 ± < 0.01	23.96 ± 1.27	11.89 ± 0.565	4.576 ± 0.382
43.03	13.847 ± < 0.01	27.36 ± 0.89	13.63 ± 0.731	4.349 ± 1.069
48.11	13.250 ± < 0.01	26.58 ± 1.20	13.25 ± 0.741	4.112 ± 1.215
53.19	10.574 ± < 0.01	21.60 ± 0.82	10.93 ± 0.584	3.875 ± 1.078
58.27	6.859 ± < 0.01	13.57 ± 0.34	6.889 ± 0.479	3.606 ± 0.930

(Continued)

TABLE 4.7. Normalized Axial Reaction Rate Data (Continued)

Distance From Converter (cm)	U^{238} (n,γ) Ex-Rod	U^{235} (n,f)	Th (n,f)	Np (n,f)
2.34	10.10 ± 0.48*	2.719 ± 0.029*	10.41 ± 0.10†	9.138 ± 0.147†
2.50	8.71 ± 0.35	2.477 ± 0.056	6.417 ± 0.094	7.420 ± 0.142
12.70	8.10 ± 0.00	2.208 ± 0.000	4.544 ± 0.092	5.500 ± 0.145
17.40	7.50 ± 0.39	2.194 ± 0.069	3.624 ± 0.093	4.367 ± 0.114
22.60	7.26 ± 0.73	2.533 ± 0.223	2.931 ± 0.092	4.383 ± 0.116
27.80	8.46 ± 0.44	4.676 ± 0.146	2.687 ± 0.092	4.746 ± 0.114
32.87	18.83 ± 0.35	15.90 ± 0.45	1.671 ± 0.091	7.134 ± 0.146
37.95	20.74 ± 0.17	25.47 ± 1.10	0.864 ± 0.090	11.985 ± 0.157
43.03	19.40 ± 1.72	29.62 ± 0.54	0.579 ± 0.090	11.501 ± 0.164
48.11	15.59 ± 0.88	28.71 ± 0.83	0.128 ± 0.090	10.675 ± 0.152
53.19	11.38 ± 0.96	23.81 ± 0.66	0.246 ± 0.090	7.772 ± 0.136
58.27	7.85 ± 0.70	14.70 ± 0.55	0.149 ± 0.090	4.417 ± 0.111

(Continued)

TABLE 4.7. Normalized Axial Reaction Rate Data (Concluded)

Distance From Converter (cm)	U^{238} (n,γ) In-Rod	U^{238} (n,γ) Ex-Rod‡	U^{238} (n,f) In-Rod	Pu (n,f)
2.34	3.052 ± 0.034*	3.30 ± 0.16*	16.02 ± 0.50	2.81 ± 0.42*
2.50	2.618 ± 0.010	2.85 ± 0.11	11.45 ± 0.81	2.34 ± 0.19
12.70	2.230 ± 0.020	2.65 ± 0.00	9.25 ± 0.00	2.10 ± 0.00
17.40	1.920 ± 0.069	2.45 ± 0.13	8.02 ± 0.09	1.93 ± 0.12
22.60	1.690 ± 0.010	2.37 ± 0.24	7.11 ± 0.53	2.22 ± 0.12
27.80	1.818 ± 0.056	2.77 ± 0.14	6.88 ± 1.49	3.36 ± 0.11
32.87				10.00 ± 1.29
37.95				13.78 ± 1.73
43.03				15.24 ± 4.56
48.11				16.12 ± 1.01
53.19				12.13 ± 1.74
58.27				7.34 ± 0.24

* This standard deviation includes Student's t-Factor. See section 4.4.3.

† Statistical error only. See section 4.4.3.

‡ Normalized to U^{238} (n,γ) in-rod experimental data.

interface. Figures 4.12 through 4.25 show these data plotted on the same graph as the numerical predictions. For the sake of comparison, it is found convenient to normalize both the experimental and calculated results to the same value at approximately the midpoint of the blanket, i.e., at 12.7 cm from the converter.

These results are discussed further in Section 4.4.4.

4.4.3 Error Analysis

In general, the experimental error associated with the data reported here is the standard deviation from the mean (SDM) computed from duplicate runs, with allowance made for the small sample size by incorporation of Student's t-factor (M-5). It is a measure of the overall reproducibility of the data. The governing relations are:

$$SDM = \sum_{i=1}^{N} \left[(Am-Ai)^2/(N-1) \right]^{1/2} \qquad (4.4)$$

where

Am = arithmetic mean value of the N different individual repetitions, Ai.

The reported error, $\pm\sigma$ (the "one-sigma" value – namely, the range about the reported value into which 68% of further repetitions would be expected to fall), is then obtained from:

$$\sigma = t \cdot SDM, \qquad (4.5)$$

where t is Student's t-factor which accounts for the fact that a small sample does not constitute a normal population. For example, t = 1.84

FIG. 4.12 GOLD (n,γ) AXIAL TRAVERSE

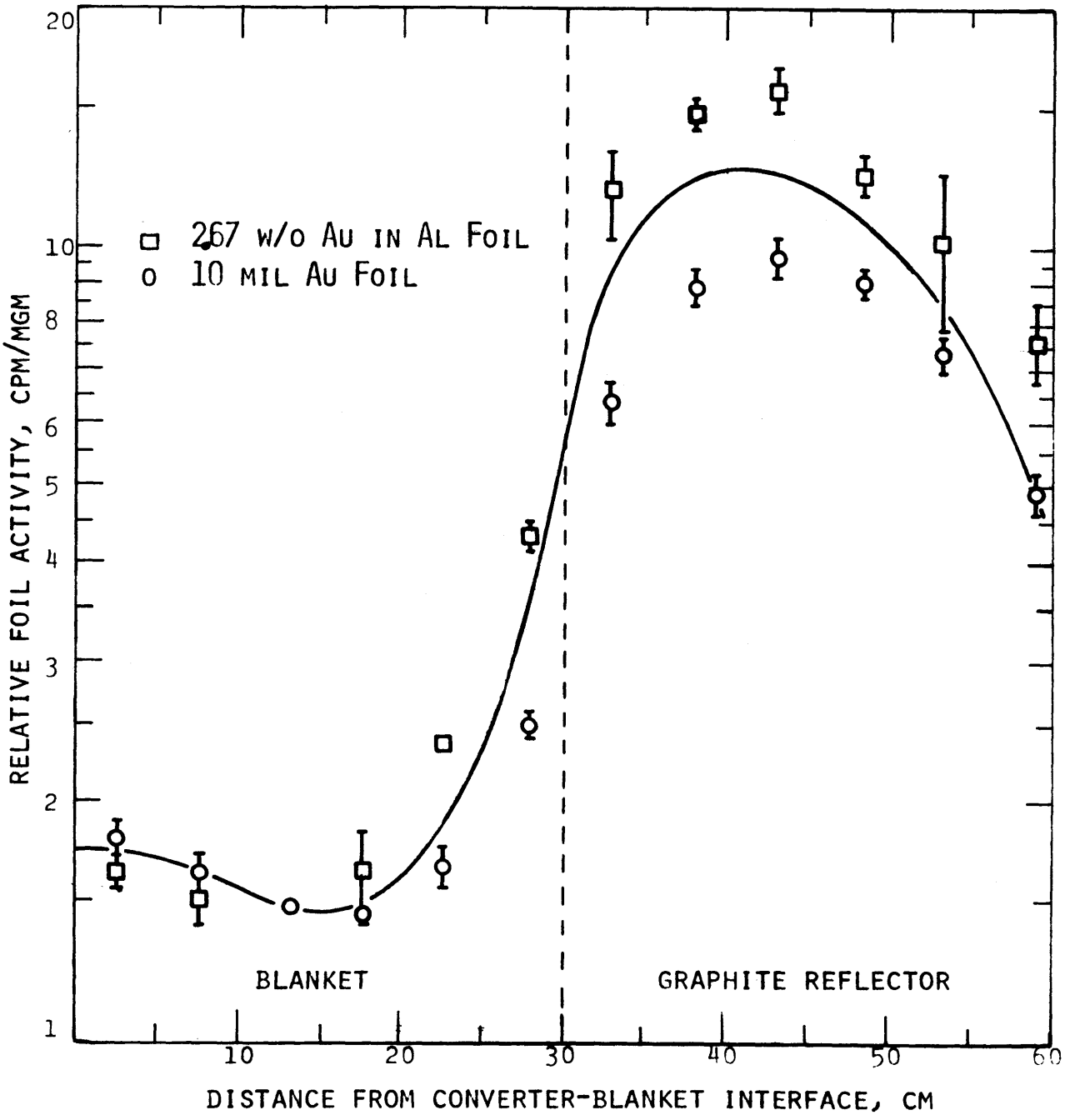

FIG. 4.13 SODIUM (n,γ) AXIAL TRAVERSE

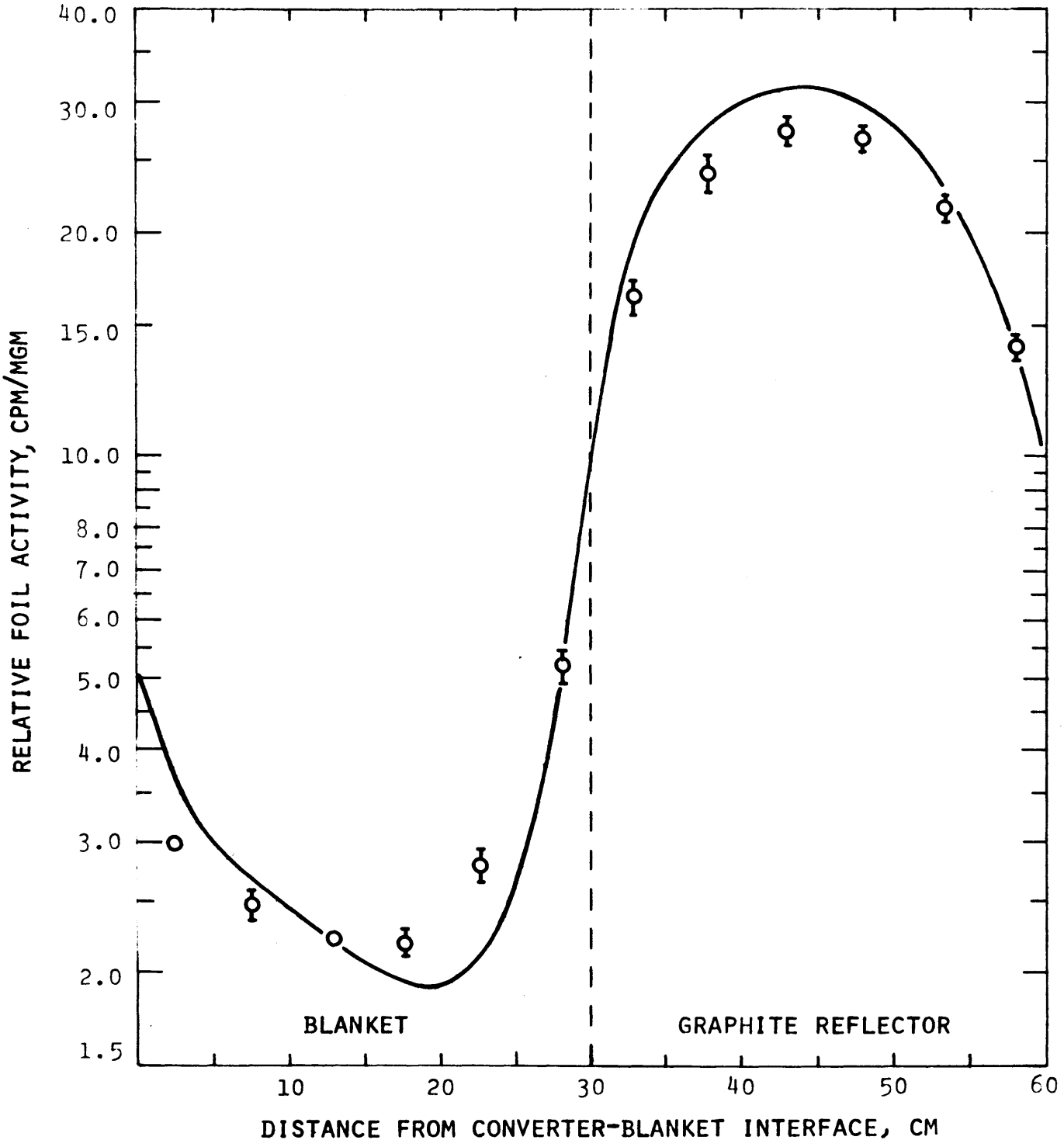

FIG. 4.14 CHROMIUM (n,γ) AXIAL TRAVERSE

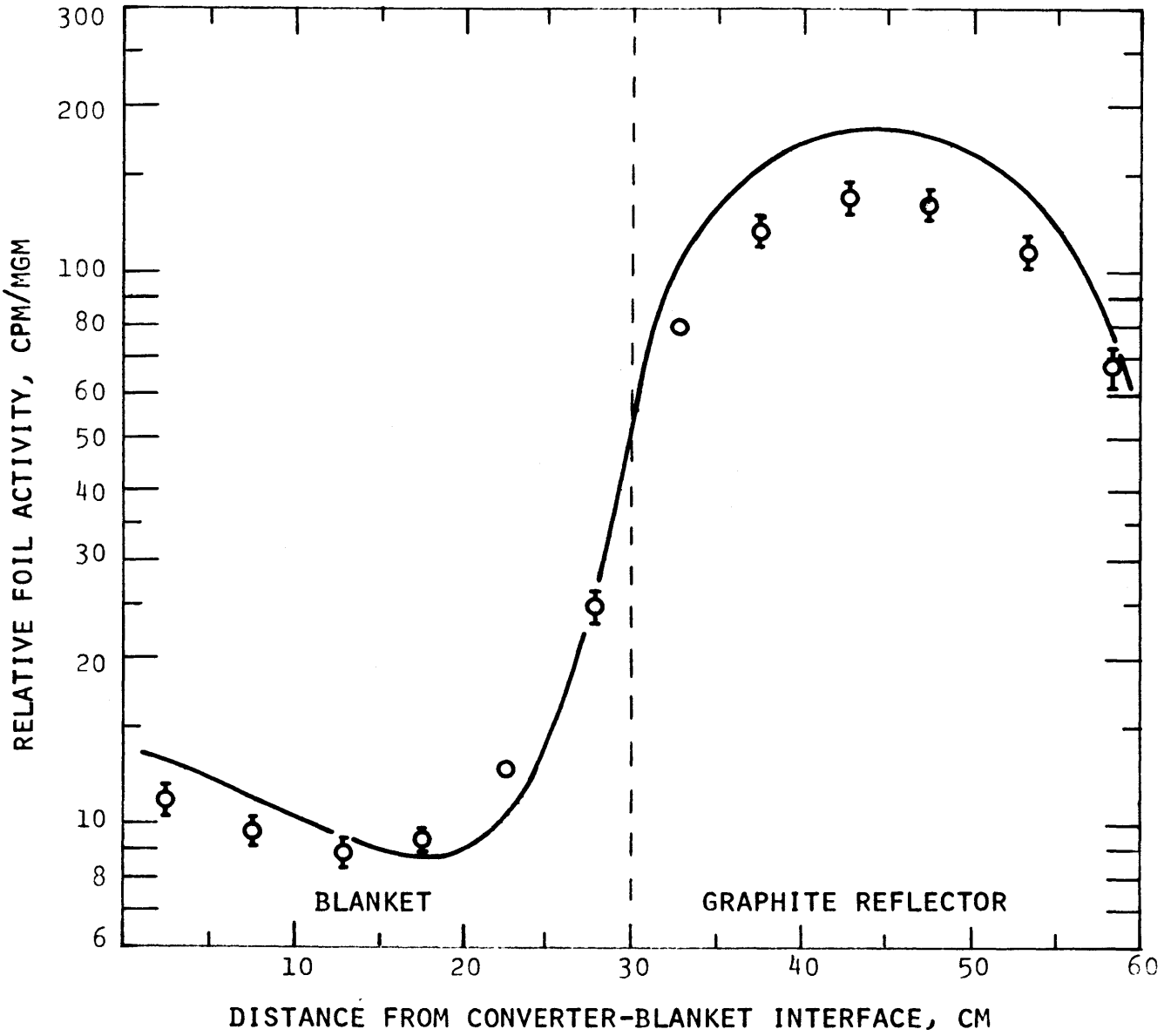

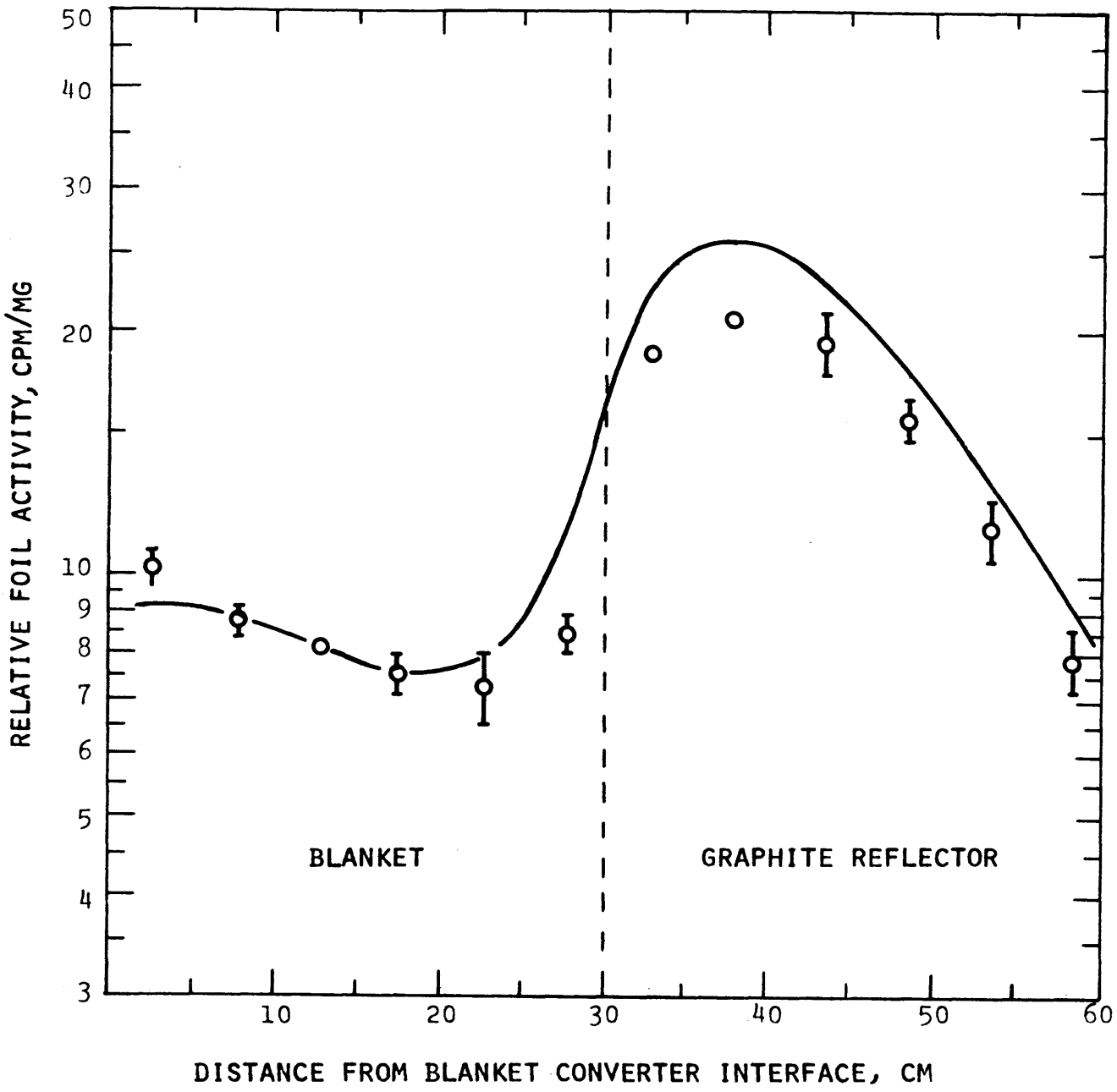

FIG. 4.15 EX-ROD U-238 (n,γ) AXIAL TRAVERSE

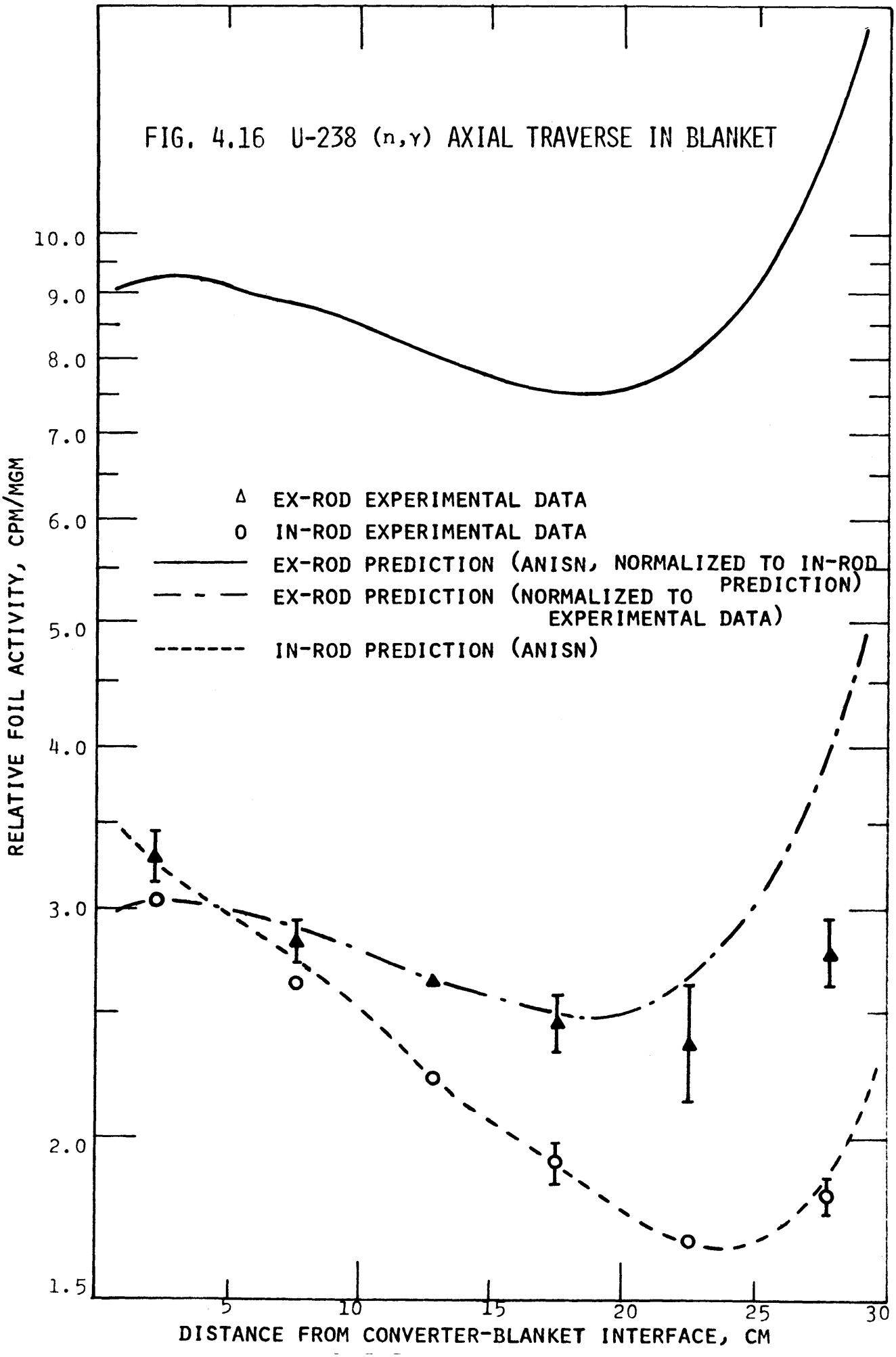
FIG. 4.16 U-238 (n,γ) AXIAL TRAVERSE IN BLANKET
RELATIVE FOIL ACTIVITY, CPM/MGM
10.0
9.0
8.0
7.0
6.0
5.0
4.0
3.0
2.0
1.5
Δ EX-ROD EXPERIMENTAL DATA
O IN-ROD EXPERIMENTAL DATA
EX-ROD PREDICTION (ANISN, NORMALIZED TO IN-ROD PREDICTION)
EX-ROD PREDICTION (NORMALIZED TO EXPERIMENTAL DATA)
IN-ROD PREDICTION (ANISN)
5
10
15
20
25
30
DISTANCE FROM CONVERTER-BLANKET INTERFACE, CM

FIG. 4.17 U-235 (n,f) AXIAL TRAVERSE

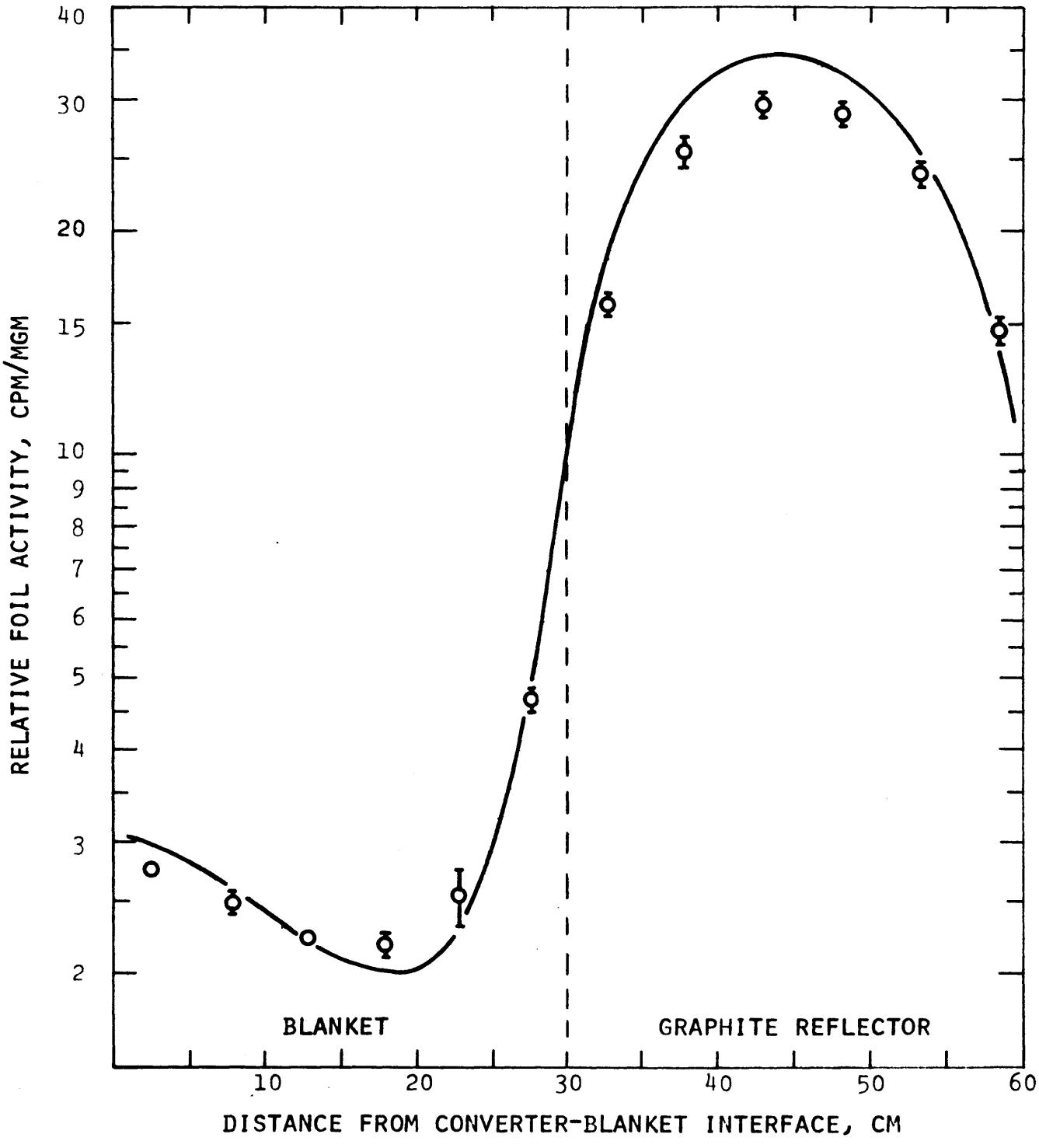

FIG. 4.18 PLUTONIUM-239 (n,f) AXIAL TRAVERSE

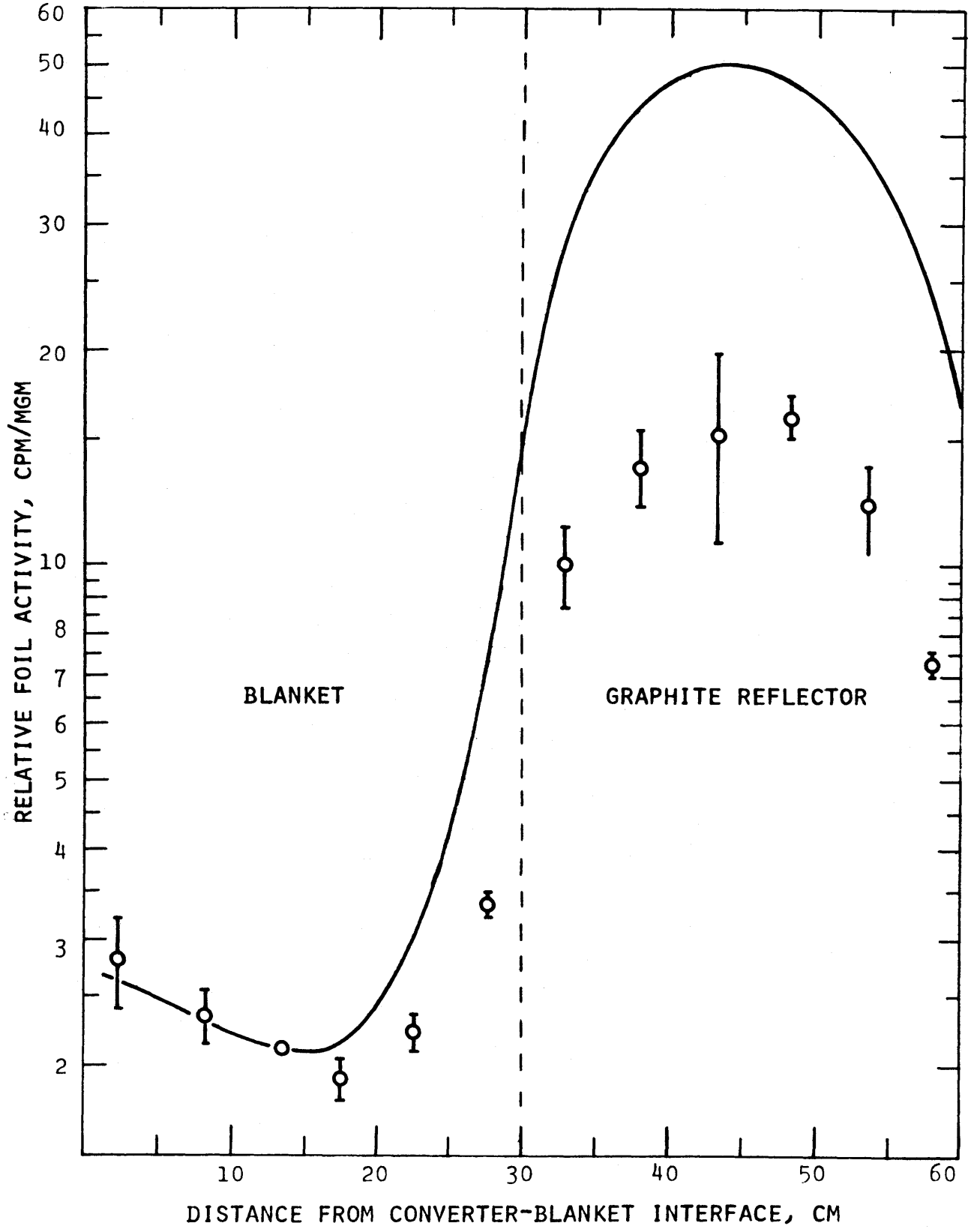

FIG. 4.19 MANGANESE (n,γ) AXIAL TRAVERSE

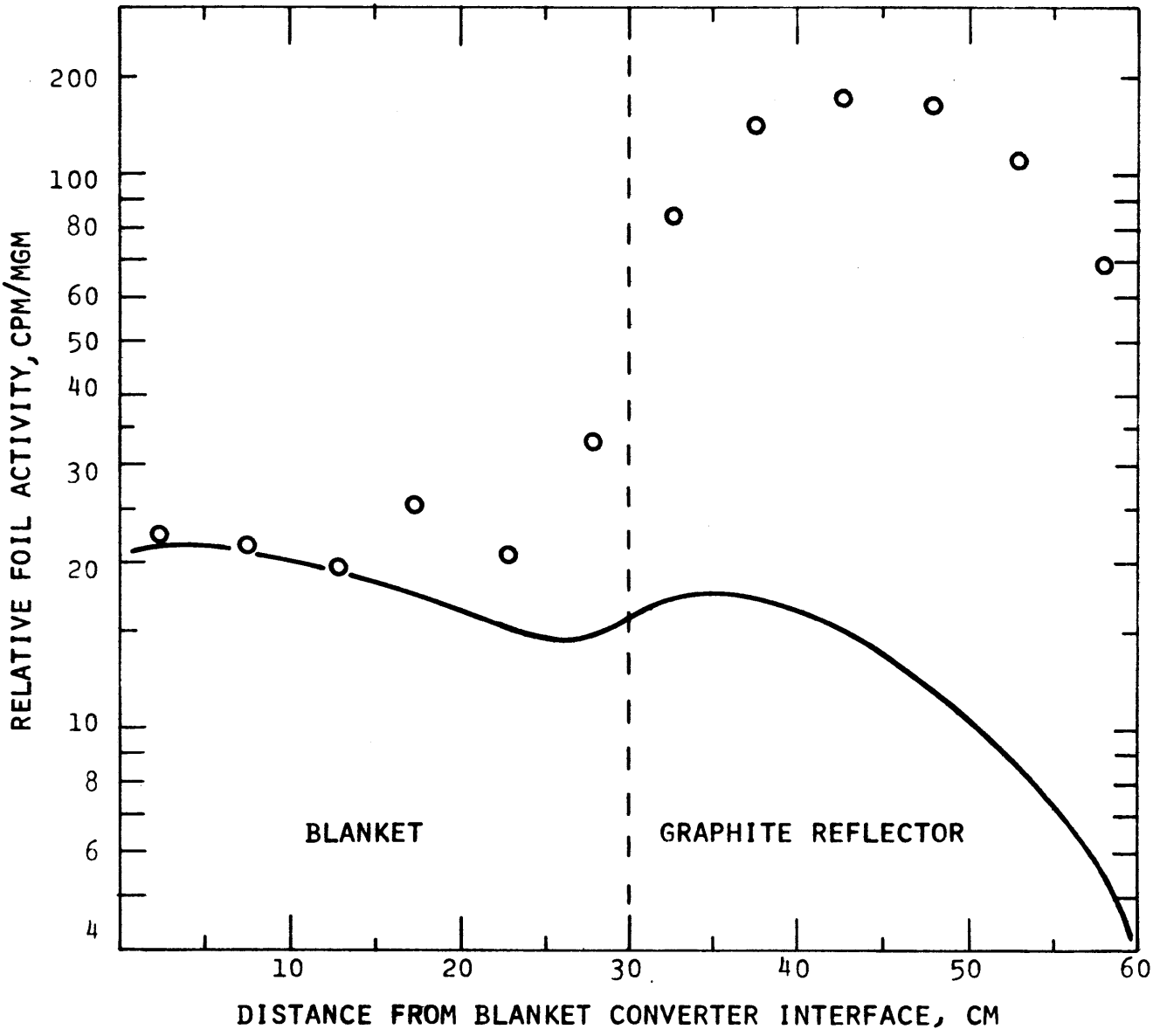

FIG. 4.20 MOLYBDENUM (n,γ) AXIAL TRAVERSE

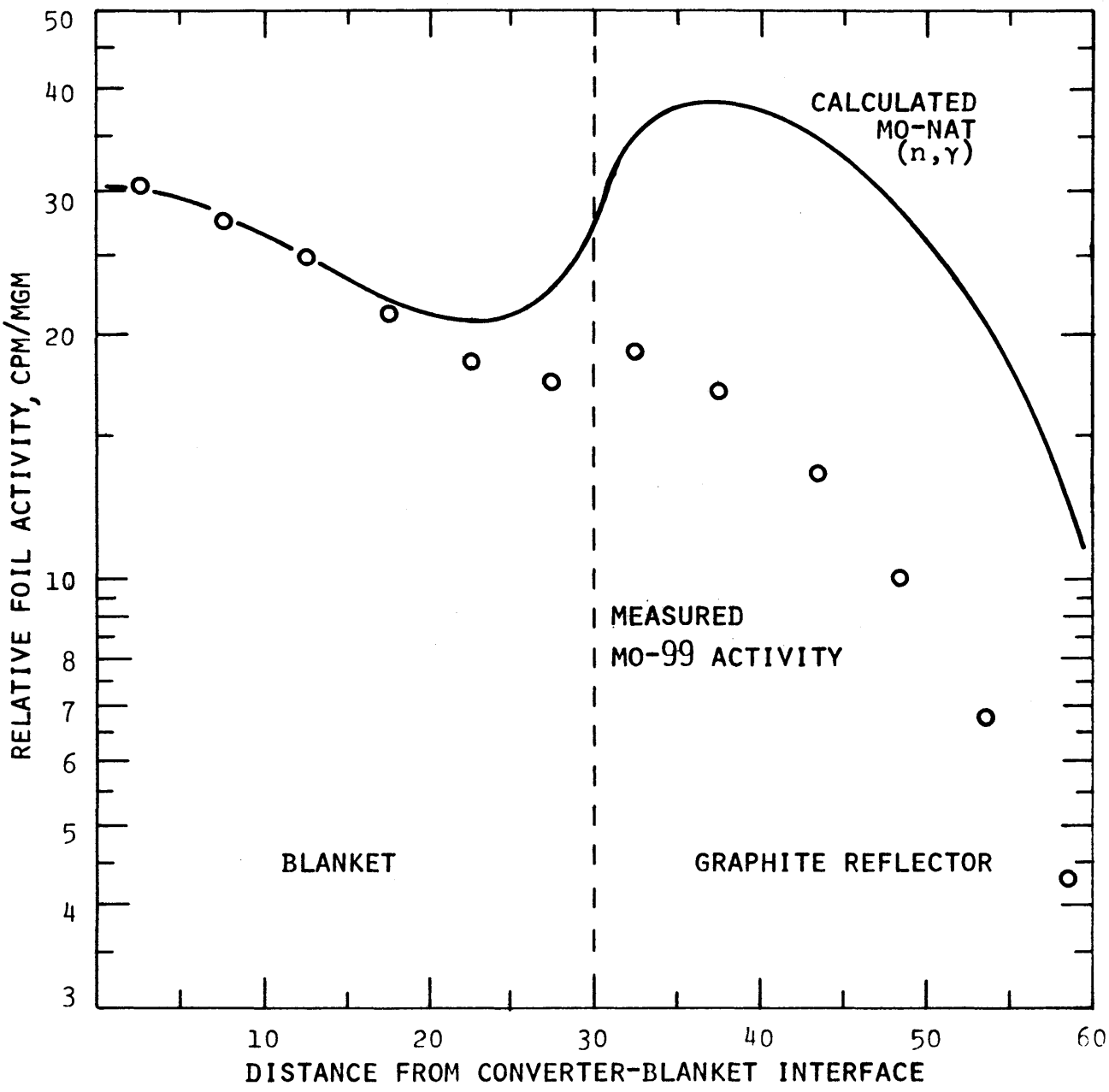

FIG. 4.21 INDIUM (n,n') AXIAL TRAVERSE

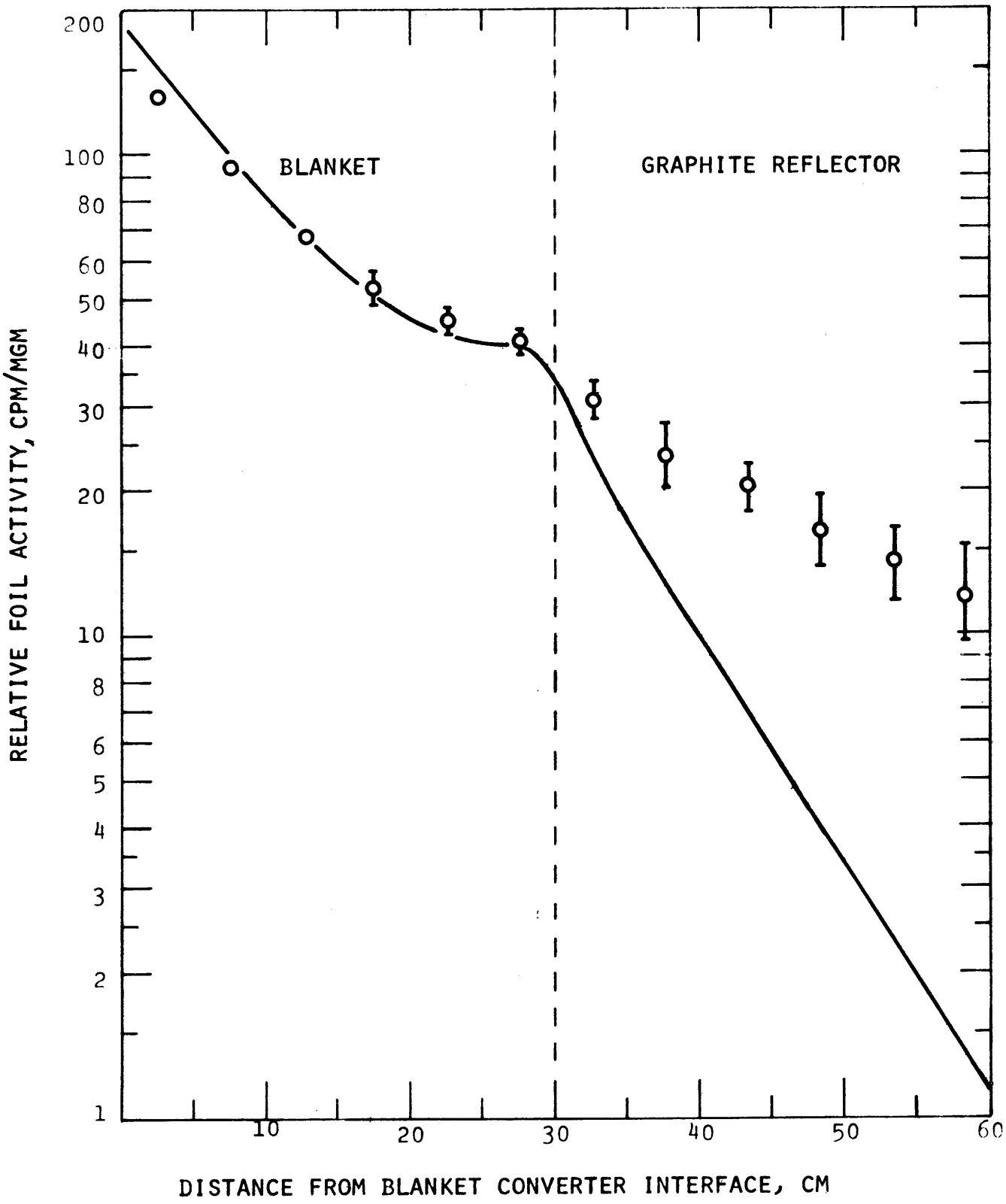

FIG. 4.22 U-238 (n,f) AXIAL TRAVERSE

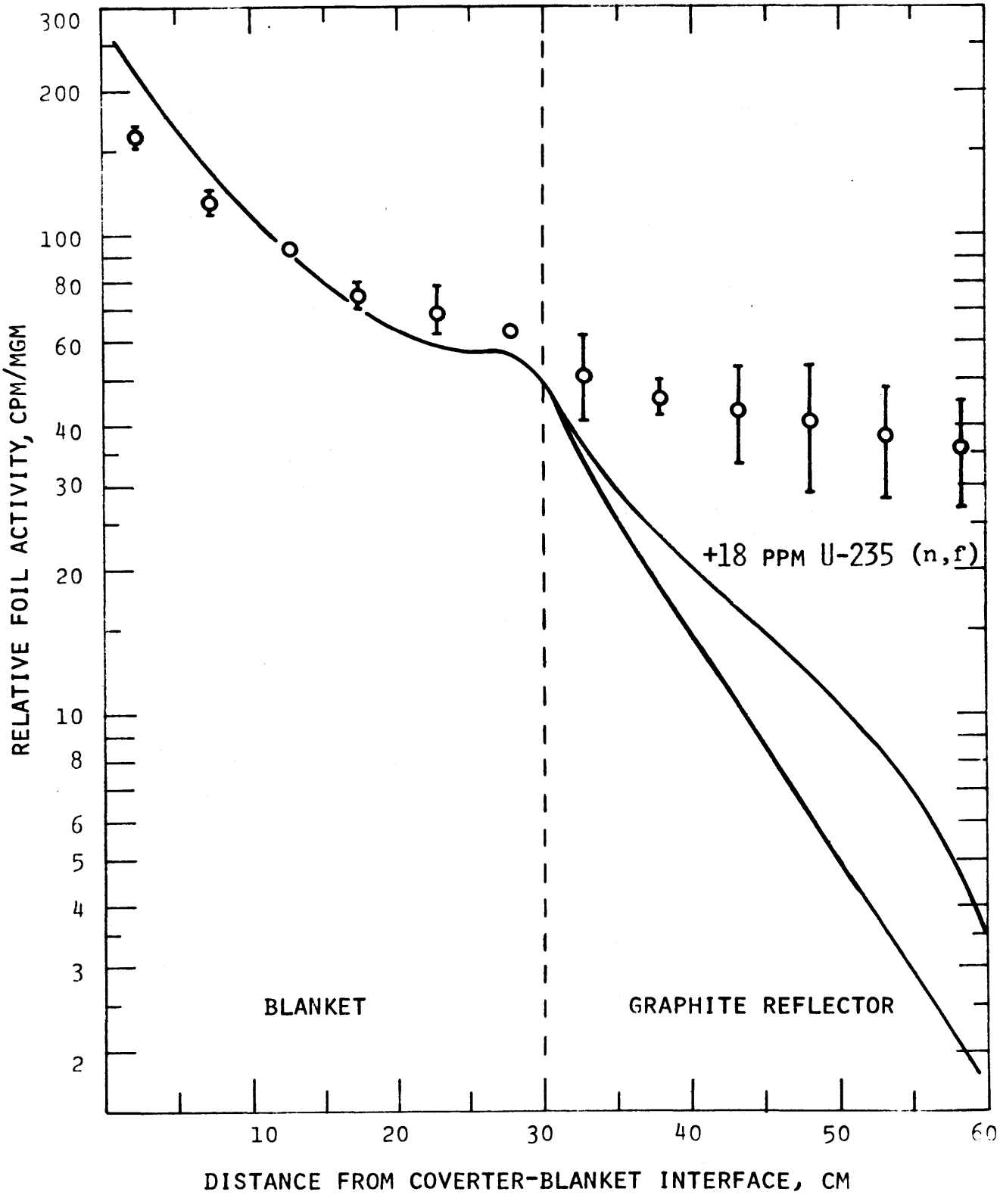

FIG. 4.23 IN AND EX ROD U-238 (n,f) AXIAL TRAVERSE

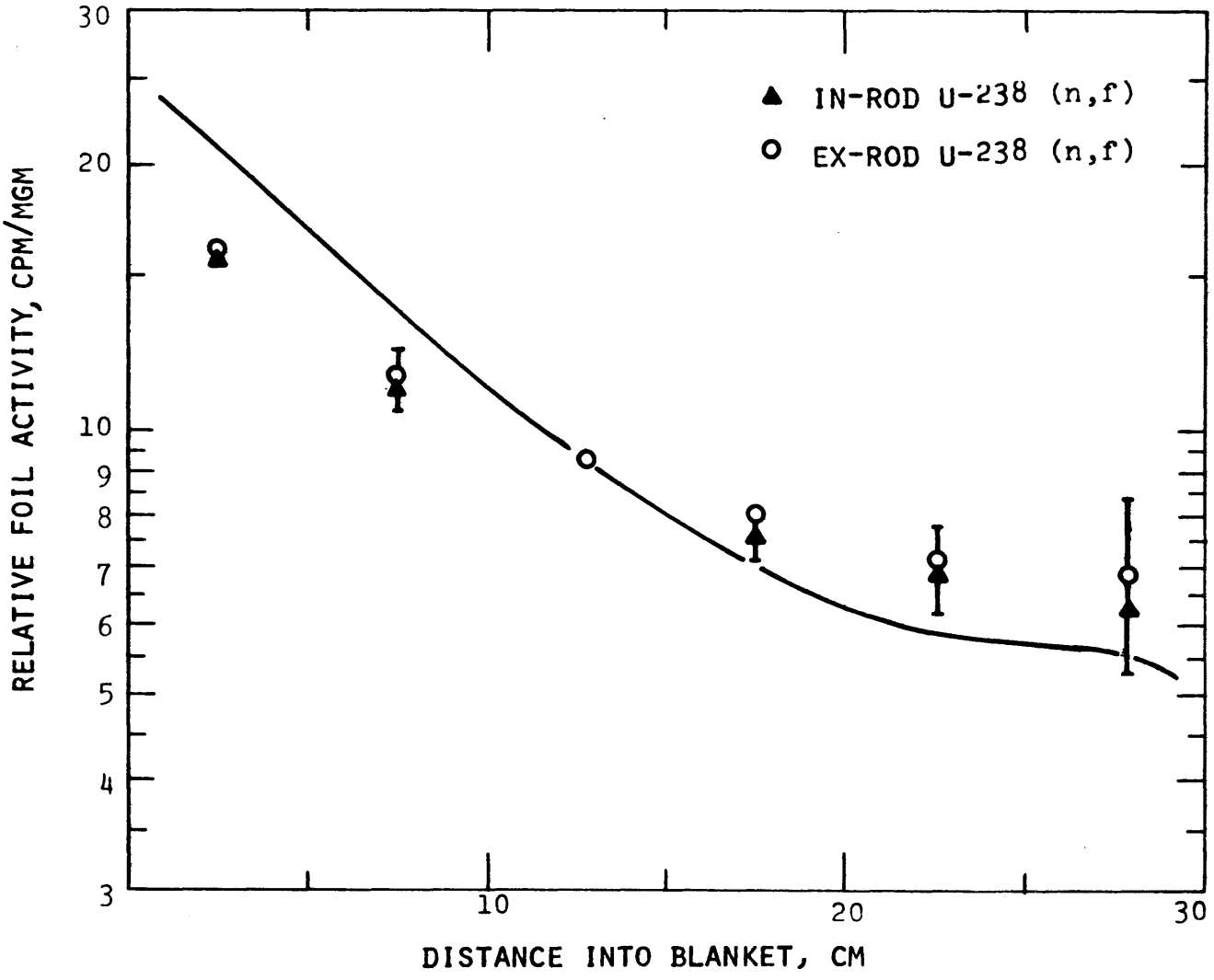

FIG. 4.24 Th^{232} (n,f) AXIAL TRAVERSE

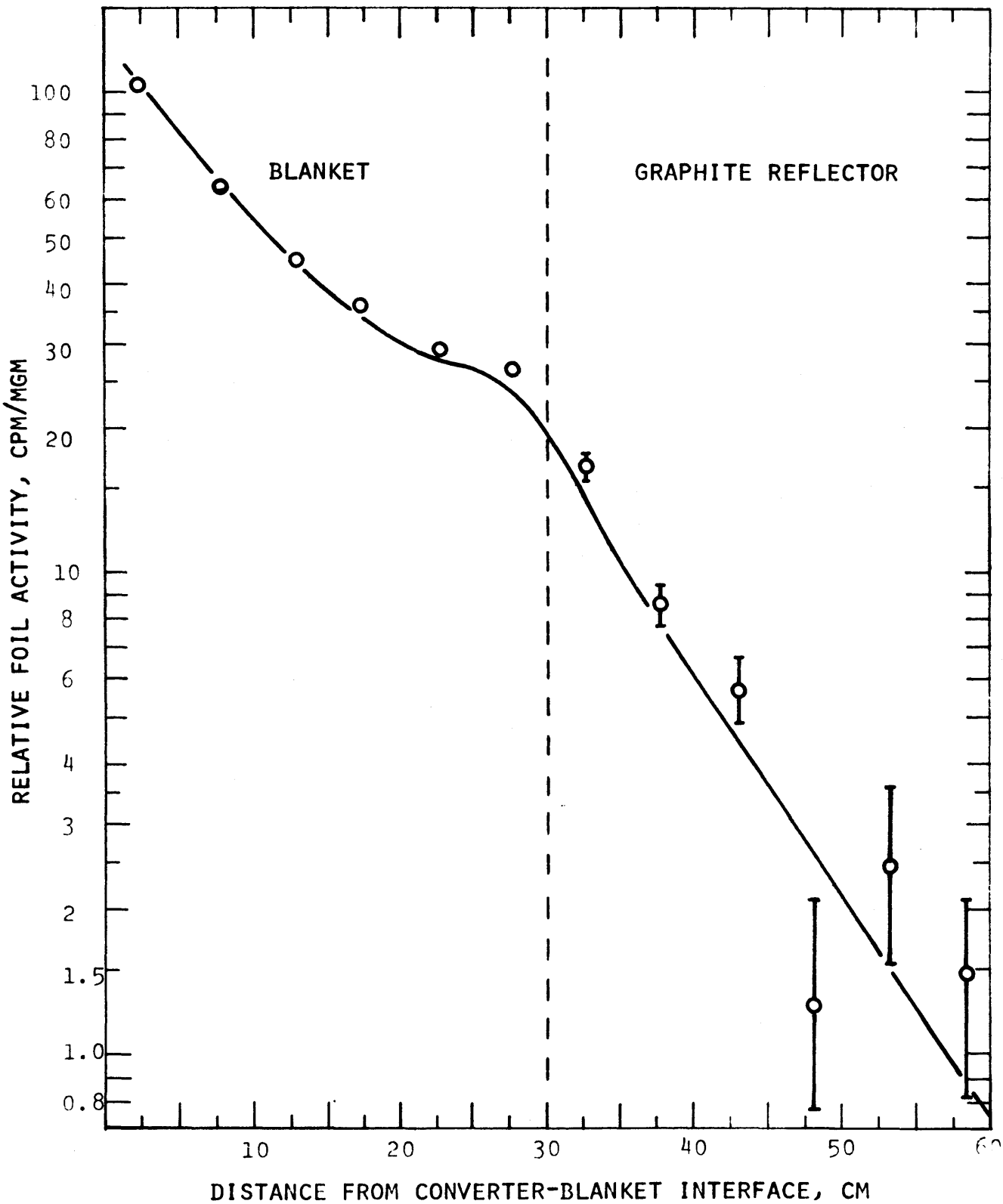

FIG. 4.25 NEPTUNIUM (n,f) AXIAL TRAVERSE

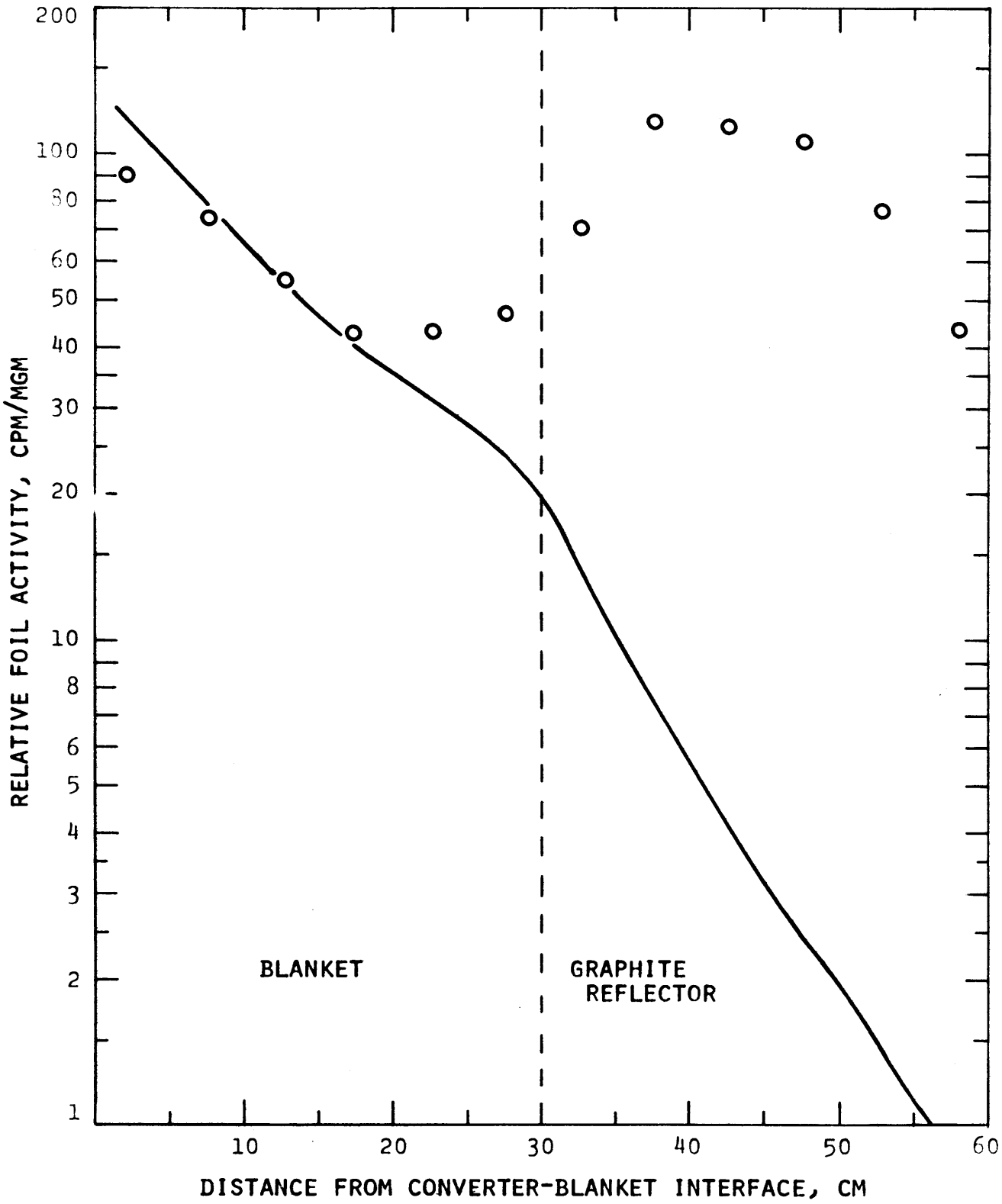

for a two-sample population and approaches 1.0 for a large number of samples.

Leung (L-2) has discussed the various identifiable contributions to the error, including counting statistics, foil weights, time interval determination and the like, and concludes that counting statistics represent the most important factor. In the present work, thorium runs being the main exception, a minimum of 10,000 counts was usually collected on each foil, implying an uncertainty of less than ± 1% from this source.

In those few runs, noted in Tables 4.5 through 4.7, where only one set of data was obtained, the error reported is the counting statistic uncertainty:

$$\sigma_C = \sqrt{C}, \tag{4.6}$$

where C is the total number of counts accumulated. Experience would suggest a SDM of ± 1 or 2% for this type of measurement, if repeated.

In all cases, errors have been combined in the usual fashion: for example, in correcting data by background subtraction.

4.4.4 Discussion of Results

4.4.4.1 Buckling Verification

As shown in Fig. 4.9, the buckling in the graphite reflector has the desired cosine distribution. Superposition of the cosine distributions determined for Blanket No. 2 on the experimental data for the graphite reflector of Blanket No. 3 indicates that the horizontal and vertical extrapolated dimensions are again approximately 74 and 60 inches,

respectively. It has been shown that the calculated axial reaction rates in the blanket are insensitive to changes in buckling since the transverse leakage is small (L-2); thus, the transverse buckling value for Blanket No. 3 was set at the value identical to that for Blanket No. 2, and Eq. 4.2 becomes $B^2 = BX^2 + BY^2 = 0.000704\ cm^{-2}$.

The major problem encountered in measuring the buckling in the graphite reflector involved the determination of the spatial shape of the high-energy region of the neutron energy spectrum. The threshold reactions In-115(n, n') and U-238(n, f) proved unsuitable, owing to poor counting statistics, interference from capture products and, in the case of U-238 fission, due to fission in the small amount of U-235 present, which was enhanced by the highly moderated spectrum. However, it was possible to acquire usable data using the Th-232(n, f) reaction, albeit with large relative counting errors.

4.4.4.2 Axial Traverses

The general features of each reaction rate axial traverse will first be discussed, followed by discussion of the discrepancies between the experimental and theoretical results.

Data from two types of gold foils are plotted along with the predicted traverse in Fig. 4.12. In general, and especially in the blanket region, the shape of each is consistent with the prediction. The upper set of experimental points is for the infinitely dilute 2.67 $^{w}/_{o}$ gold dispersed in aluminum foil. The lower set of data points is for the standard 10-mil-thick foil. The difference between the two, evident in the graphite reflector, is what one would expect – the "infinitely dilute" foil showing higher

activation rates than the standard foil. The predicted activation rate, falling between the two experimentally determined rates, indicates that the gold cross sections used in the ANISN calculations may not correspond to a truly infinitely dilute value. The lack of allowance for self-shielding is also characteristic of the other foil traverses and is a major contribution to the discrepancies noted in the graphite region. In general, however, the behavior in the blanket region is of greater concern, since it is there that the important reactions take place.

Figures 4.12 through 4.18 depict axial traverses for reactions having similarly shaped profiles. In each case – gold, sodium, chromium, U-238 captures, U-235 and Pu-239 fissions – the cross section increases, and also displays more prominent resonances with decreasing neutron energy, which accounts for the large peak in the graphite where the flux is much softer than in the blanket, and also for the observation that the unshielded predicted traverse lies above the experimental traverse.

It should be emphasized that in the present work, agreement in the blanket region between experiment and prediction was of primary interest. However, should it become a matter of some practical importance to match the reflector traverses more closely, then the effort must be invested to develop multigroup self-shielding corrections for all of the candidate foil materials. This objective was assigned a low priority for this study.

On the other hand, self-shielding of U-238 in the blanket region is clearly of considerable interest.

Figure 4.16 displays plots of the measured in-rod and ex-rod U-238 capture data. As expected, the ex-rod foils are more active, being

shielded only by neighboring fuel and not by the host fuel rod. Also shown are the calculated in-rod traverse (normalized to the experimental data) and a comparable traverse calculated using infinitely-dilute U-238 cross sections (solid line at top of graph) correctly normalized relative to the in-rod traverse. The same traverse is also shown renormalized to the ex-rod data (dot-dash line). While it is clear that the ex-rod activities are less shielded than those in-rod, they are far from being in an infinitely dilute environment. Even so, the shape of the infinitely dilute calculated traverse is in fair agreement with that of the ex-rod measured traverse. It should also be noted that Leung (L-2) shows a comparable plot for Blanket No. 2 in which only the infinitely dilute U-238 calculations normalized to the ex-rod data are shown, and which may therefore give the false impression that the ex-rod foils can be correctly represented as infinitely dilute.

The results shown in Fig. 4.16 display the expected effects of spectral softening near the graphite reflector: the in-rod flux depression is enhanced and the spread between the in-rod and ex-rod traverses widens.

The manganese data of Fig. 4.19 show extremely poor agreement with the predicted traverse, leaving in doubt the validity of the manganese cross section, or the experiment, or both. No plausible explanation can be offered at the present time.

Molybdenum (Fig. 4.20) shows only slightly better agreement between experiment and prediction. In the first row of blanket, adequate agreement is found (due, in part, to the normalization); however, deeper in the blanket and in the graphite reflector, the prediction is too high by a factor of almost 2.5. As before, this is probably due in part

to the spectral shift in the blanket and the inability of the cross sections used by this "keV range" absorber to properly reflect the self-shielding. A further obvious source of discrepancy is that natural molybdenum cross sections were employed, whereas the measured Mo-99 activity is produced from isotope Mo-98, which is only 24% abundant.

The last set of graphs, Figs. 4.21 through 4.25, depict threshold reactions: inelastic scattering by indium (E_t = 0.3 MeV) and fast fission in uranium-238 (E_t = 1.0 MeV), thorium-232 (E_t = 1.75 MeV), and neptunium (E_t = 0.75 MeV). The predicted axial traverses have practically identical shapes for all of these reactions, implying that the fast reactions (above 300-keV indium threshold) behave similarly.

The experimental data agree quite well with the predictions in the blanket region. This is in agreement with similar results reported for U-238 fission data by Leung (L-2) in Blanket No. 2, and the U-238 and Th-232 fission data collected by Wood (W-5) in Blanket No. 4. However, in the graphite, the situation is different. Within the experimental error, the thorium data and prediction agree; the other three sets of data do not. The neptunium data exhibit a peak in the reflector region, similar in shape to the nonthreshold reactions discussed previously. This would indicate that Np-237 capture products (Np-238, T 1/2 = 2.1 d) and not fission products were actually being counted in the experiment. This was undoubtedly the case, since it was found necessary in the counting procedure to use a baseline setting above the Np-238 1.03-MeV gamma peak to count the fission products. However, the observed Np-238 contribution was so strong that this effect was probably not entirely eliminated. Another potential cause for the discrepancy is subthreshold

fission. However, activation rates calculated using subthreshold fission cross sections developed from data measured at LASL (B-7) and data measured by Gavrilov (G-3) showed a maximum increase in fission rate of only seventy percent at the outer edge of the graphite reflector, still an order of magnitude below the experimental observation, and also failing to reproduce the observed peak in the reflector region.

The uranium and indium data deep in the reflector are an order of magnitude higher than calculated. It is important to note that this same problem was observed in the steel reflector of Blankets No. 2 and No. 4. Choong (C-2) has explained this anomaly for the U-238 fission traverse in the steel reflector of Blanket No. 4 by including U-235 background fission events (U-235 contamination is 18 parts per million in the U-238 foils), by adjusting the iron cross-section weighting scheme and by including subthreshold fissions in U-238, and by adjusting the near-threshold cross-section value. However, in the graphite reflector of Blanket No. 3, inclusion of subthreshold fissions using the data reported by Choong (C-2) led to an increase of less than one percent in the calculated fission rate at the outer edge of the graphite reflector. The addition of 18-ppm U-235 increases the fission rate by a factor of two, leaving the predicted fission rate an order of magnitude below the experimental value at the edge of the graphite reflector.

Choong (C-2) has also looked at the indium data in the reflector of Blanket No. 4. He has determined, by use of B-10 shielded foils that subthreshold excitation of the indium (n, n') reaction has little effect. He also shows, by both experiment and calculation, that gamma excitation could not explain these results, even though Swedish researchers (A-7)

have attributed similar discrepancies to this effect in water shielding studies.

One further attempt to explain similar discrepancies was made by Wood (W-5). His concern was with the elastic downscatter cross section, and the 1/E intra-group spectrum weighting employed in the Russian cross-section set (A-6). However, the 1/E spectrum is much more appropriate for a graphite reflected blanket than a steel reflected blanket, and therefore this concern was not pursued further here.

4.5 Summary

Blanket No. 3, incorporating a moderating, high-albedo graphite reflector has been designed, built and studied. The work presented in Chapter 3 has indicated economic advantages for this blanket-reflector combination, motivating this experimental study in order to reinforce the confidence placed in the analytical results, particularly in view of the severe spectral changes in the blanket-reflector region which made it questionable whether the codes and cross sections available could adequately describe this configuration.

The general conclusion that can be drawn from this effort is that the analytical methods adequately describe the neutronic behavior of the graphite-reflected blanket, for present purposes, and at least as well as they do conventional, steel-reflected blankets. In particular, the important uranium-238 capture event is adequately calculated, in agreement with similar observations reported by Leung (L-2) and Wood (W-5) in Blankets No. 2 and No. 4, respectively.

However, threshold-detector activities in the reflector are not being

predicted well, as was the case in the steel reflector used with Blankets No. 2 and No. 4. Serious questions with respect to fast neutron shielding can thereby arise. Choong (C-2) has looked into this problem and showed some improvement in the U-238 data by including subthreshold fission events, by accounting for U-235 contamination, and by adjusting the iron cross section. In the future, Blanket No. 5, with a special steel reflector designed to permit more detailed and more precise measurements, will be studied, so that further experimental information can be acquired to aid in the resolution of this problem, and also in the improvement of U-238 self-shielding factors near the blanket-reflector interface.

Finally, the other and lesser unresolved experimental and computational discrepancies noted in this chapter are also the objects of continuing scrutiny as part of the ongoing research at the Blanket Test Facility, as is the general subject of evolving improved blanket neutronic calculations.

Chapter 5

SUMMARY AND CONCLUSIONS

5.1 Introduction

The blanket and reflector regions surrounding the core of an LMFBR serve many functions. Chief among these are fertile-to-fissile conversion, reflection of neutrons, power production, and neutron and gamma shielding. It is clear that these functions are interrelated, and all must be analyzed in concert in designing the blanket region.

The purpose of the research summarized here has been to identify and evaluate the performance of an advanced radial blanket-reflector configuration, including experimental verification of the neutronic analysis. To accomplish this latter task the Blanket Test Facility at the M.I.T. Research Reactor was utilized (see Section 5.4). In the overall evaluation design decisions were made with respect to a) blanket thickness, b) initial blanket fissile enrichment (seeding), c) reflector composition, and d) orificing scheme. Various blanket-reflector configurations differing in certain of the above parameters were studied using state-of-the-art computer methods.

Figure 5.1 depicts the major material subdivisions used to describe the 1000 MW_e LMFBR chosen as the subject for this study. Included are both a two-dimensional configuration used in the burnup studies and a one-dimensional configuration used in the blanket-heating analysis (developed from the two-dimensional results by determining a 25 cm reflector savings).

The main features to note in this cylindrically symmetric layout

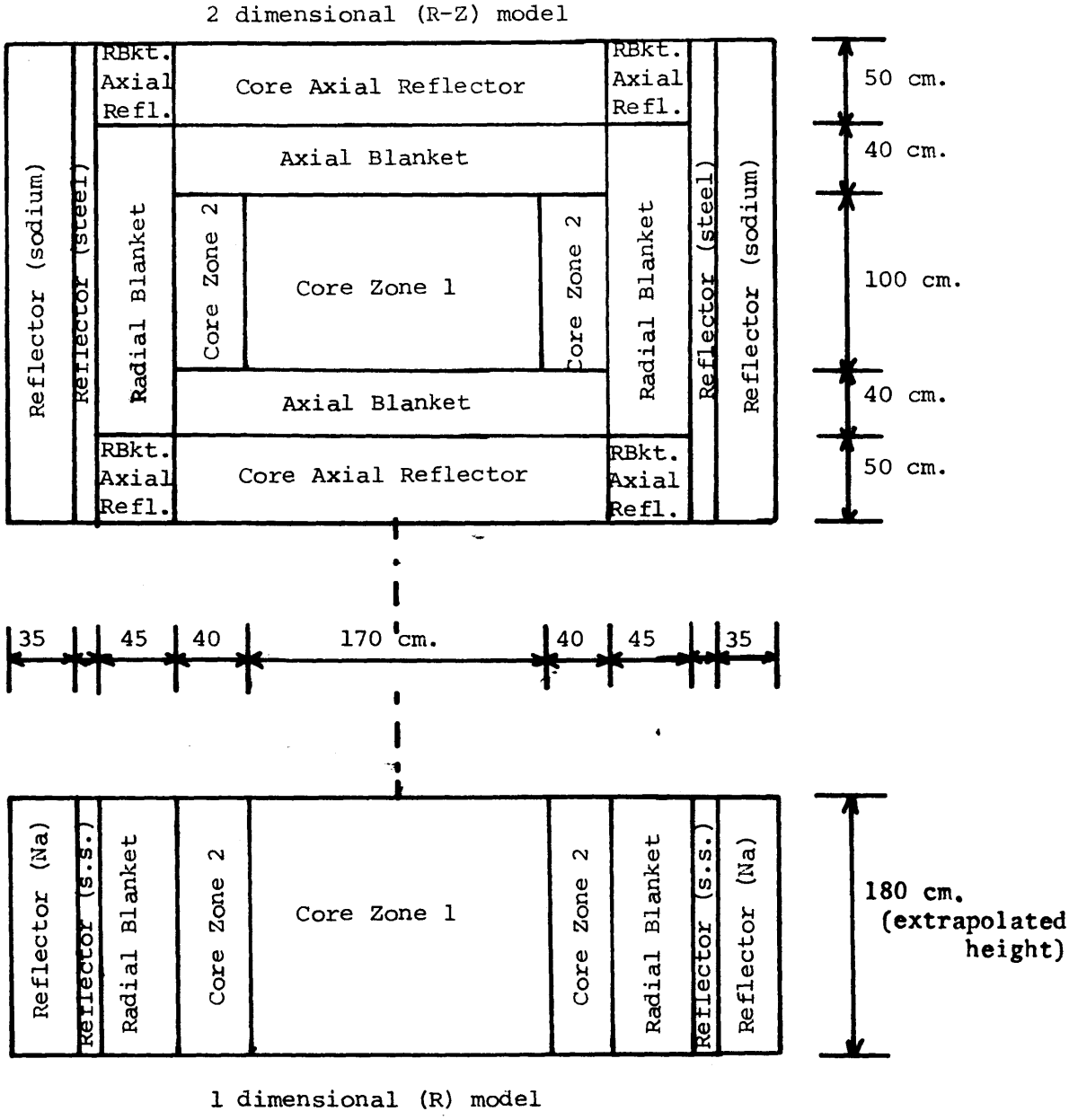

Fig. 5.1 1000MWe Reference Reactor Configurations

are two approximately equal-volume core enrichment zones, a core height-to-diameter ratio (H/D) of 0.4, a 40 cm thick axial blanket on the top and bottom of the core, and of particular concern to this study, the "base-case" blanket-reflector configuration consisting of a 3-row (45 cm thick) radial blanket surrounded by a steel reflector. Table 5.1 summarizes the pertinent data for this reference configuration which closely resembles the reference LMFBR used for the original MIT Blanket Test Facility design calculations (F-3) and other 1000 MW_e LMFBR blanket studies (B-3, W-5).

For this study the ranking of the alternative configurations was according to economic criteria determined by evaluating the levelized fuel cycle cost contribution of the radial blanket region, taking into account not only the usual burnup economic parameters (including fissile revenue and fabrication, reprocessing and carrying charges) but also the economic penalty associated with blanket overcooling due to the steep power gradient across the blanket region.

Batch blanket management was selected for this study due to its simplicity of implementation (i.e., blanket elements see only one position in the reactor, minimizing reactor down time devoted to blanket refueling and/or repositioning) and due to the fact that approximately the same amount of plutonium is bred from an equivalent number of blanket elements regardless of management scheme (e.g., out-in or in-out management) over the same time interval (e.g., see Ref. B-2, W-3 or W-5).

The best overall configuration identified in this evaluation was a 2-row blanket, fueled with depleted uranium (i.e., no blanket seeding), surrounded by a 1-row graphite reflector, incorporating individual (row-by-row) orificing. Relative to the base case configuration a savings of over 0.20 mills/kW-hr (equivalent to approximately $\$ 1.4 \times 10^6$ per year) can thereby be achieved.

TABLE 5.1 Reference Reactor Parameters

	Ht. (cm)	Rad. Thick. (cm)	No. of Equiv. Assems.[b]	Percent by Volume		
				Fuel[c]	Coolant[d]	Structure[e]
Core						
Zone 1	100	85	127	30 (85% t.d.)	50	20
Zone 2	100	40	118	30 (85% t.d.)	50	20
Axial Blanket[a]	80	125	245	30 (85% t.d.)	50	20
Radial Blanket						
Row 1	180	15	63	50 (95% t.d.)	30	20
Row 2	180	15	70	50 (95% t.d.)	30	20
Row 3	180	15	77	50 (95% t.d.)	30	20
Axial Reflector[a]						
For axial blanket	50	125	245	–	50	50
For radial blanket	50	45	210	–	30	70
Radial Reflector						
Inner	140	15	84	–	20	80
Outer	140	35	222	–	100	–

[a]Axial blanket and reflector heights refer to thickness above or below core.

[b]Assumes hexagonal assemblies 15 cm across the flats.

[c]Fuel consists of mixed uranium and plutonium dioxide in the core and uranium dioxide in the blanket. The 100 v/o, 100% t.d. molecular density is taken as 0.02447 atoms/barn-cm. Plutonium is assumed to be typical light water reactor discharge Pu at 30,000 MWD/T: 63% Pu-239/22% Pu-240/12% Pu-241/3% Pu-242 (B-9).

[d]Coolant is sodium at ~900°F having a (100 v/o) density = 0.0220 atoms/barn-cm.

[e]Structure is stainless steel with 17.7% chromium/8.3% nickel/74.0% iron having a (100 v/o) density = 0.0850 atoms/barn-cm.

5.2 Blanket Heating Analysis

A detailed blanket-heating analysis is necessary in order to determine blanket radial power profiles. The analysis is complicated by the fact that the energy deposited at a given point in the blanket is not only due to local fission events (including capture) but also due to the absorption of core-leakage gamma rays and neutrons. The analysis is further complicated by the fact that the relative effect of core-leakage gamma rays and neutrons compared to the local fission heating rate changes with time. It was found, however, that adequate estimates of the radial power distribution can be simply obtained by superposition of local and leakage effects for each of the major contributions, namely:

a) fission heating rate

b) gamma ray heating rate

c) neutron heating rate.

5.2.1 Method of Analysis

The methods of analysis employed in determining the power distributions for the three contributions to the heating rates are all similar. A criticality calculation was made with the ANISN transport code (E-4), S-8 option, (which was shown sufficient by Leung (L-2)). This yielded multigroup fluxes of both neutrons and gamma rays which were then used to calculate the volumetric energy deposition rates, E, for the various heating contributions in the blanket by application of the following equation:

$$E(r) = \sum_{i,j} N_j(r)\, \sigma_{ij}^{E} \phi_i(r), \qquad (5.1)$$

where

$N_j(r)$ is the j^{th} material number density $\left(\frac{\text{atoms}}{\text{barn-cm}}\right)$ at a particular radius, r (cm);

σ_{ij}^{E} is the microscopic energy absorption cross section for material j, energy group i (Mev-barns);

$\phi_i(r)$ is the radial flux in energy group i, at a particular radius, r (particles/cm^2-sec).

Two multigroup cross-section sets were employed to analyze the three contributions to the total heating rate. A 26-group neutron cross-section set developed from the so-called "Russian" or "ABBN" set (A-6) was utilized to acquire fission heating rates and neutron heating rates. A 40-group coupled neutron (22 groups)-gamma (18 groups) cross-section set developed at ORNL (M-2) was used for determining the gamma heating rates.

5.2.2 Fission Heating Analysis

There are approximately 200 million electron volts of recoverable energy released per fission reaction. Table 5.2 summarizes the energy contributions from fission fragments, beta rays, gamma rays, and neutrons. For the fission heating analysis it was assumed that all the energy is deposited locally, yielding "conventional" heating rates. Thus the microscopic fission energy absorption cross section is given simply by the microscopic fission cross section times the energy released per fission, 200 Mev.

Figure 5.2 shows the relative fission power density as a function of

TABLE 5.2 Distribution of Energy Released in Fission

Type	Recoverable Energy (Mev)
Fission Fragments	167
Fission Product Decay	
β rays	7
γ rays	7
(neutrinos)	(11; not recoverable)
Prompt γ rays	7
Fission Neutrons (including inelastic scatter γ's)	5
Capture γ rays	7 (varies with reactor composition)
TOTAL	200

radius for the base case, 3-row depleted uranium radial blanket. Analysis of the fission power distribution with respect to fertile (U-238) and fissile (U-235) fissions yields the interesting result that fast fissions in the fertile isotope dominate the total fission rate in the first half of the blanket, whereas the fissile fissions dominate in the latter half of the blanket. This result indicates the importance of considering the presence of U-235 even in the very small quantities occurring in depleted uranium (0.2 $^{w}/_{o}$), and the importance of fast fissions in the fertile isotope.

The relative effect of fast fission decreases with distance into the blanket and with increasing fissile enrichment, as indicated by Fig. 5.3. The ordinate in Fig. 5.3 is labelled the "U-235 equivalent enrichment

Fig. 5.2 Fission Density in a Three-Row Depleted-U Blanket at Beginning of Life

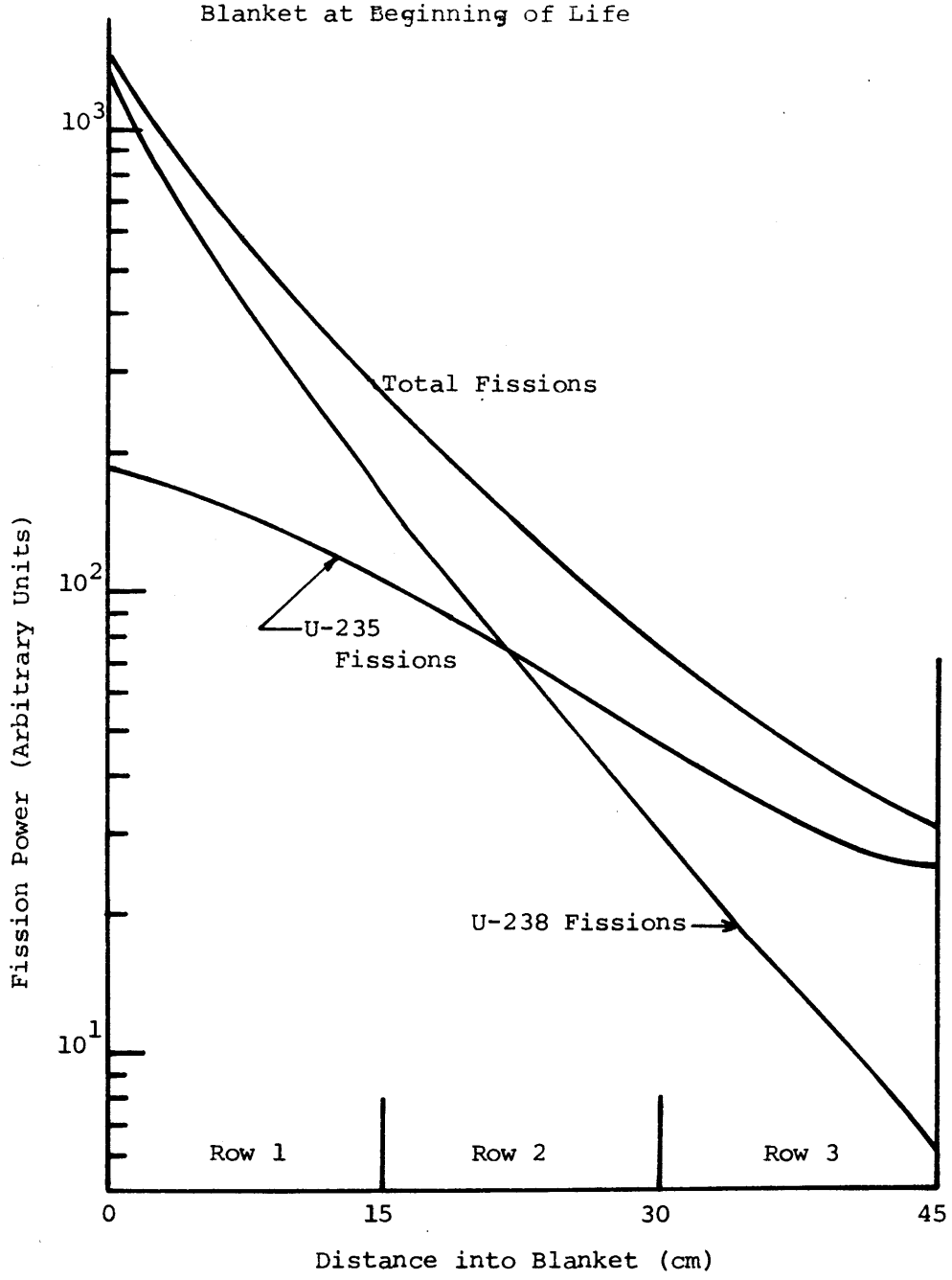

Fig. 5.3 U-235 Equivalent Enrichment of U-238 as a Function of Position in a Radial Blanket

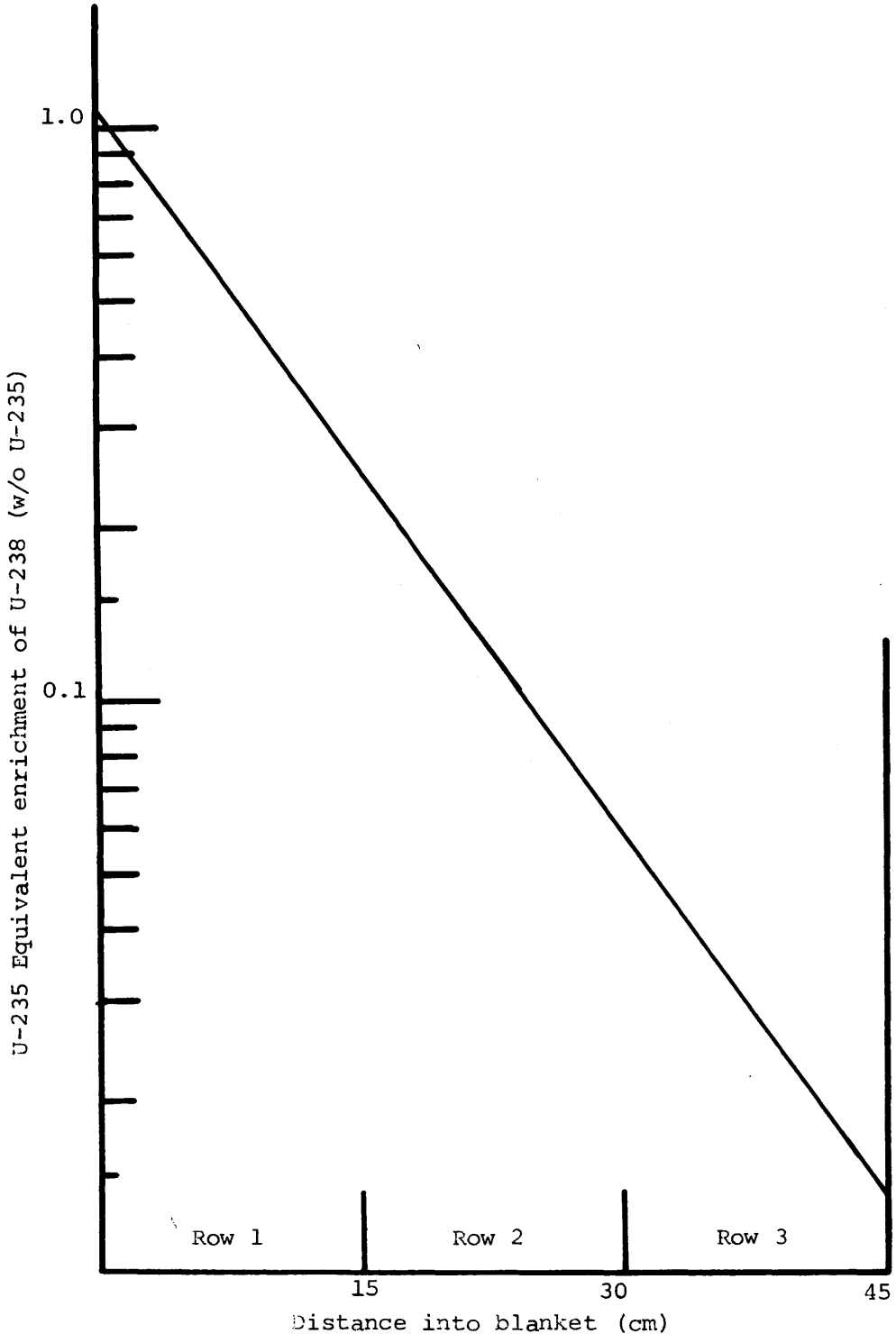

of U-238" and is determined by extrapolating fission rate data from variously enriched blankets (ranging from 0.2 $^{w}/_{o}$ to 2.5 $^{w}/_{o}$) to zero fission rate. Since there are fissions due to U-238, even at zero fissile enrichment, an effective enrichment for the U-238 could be determined. This effective enrichment decreases exponentially with radial distance into the blanket (the abscissa of Fig. 5.3). This relationship can be explained by noting that the fast flux also falls off exponentially in the blanket, as shown by the U-238 fission rate in Fig. 5.2.

5.2.3 Gamma Heating Analysis

For this analysis a 40-group coupled neutron (22 groups)-gamma (18 groups) cross-section set was employed (M-2). With this cross-section set the production of gamma rays is treated by appropriate down-scatter from the upper 22 neutron groups into the lower 18 gamma groups; and one multigroup S_n solution suffices for both neutron and gamma ray distributions. Gamma rays are produced by:

1. Nuclear fission
2. Fission product decay
3. Neutron capture product decay
4. Inelastic scatter of neutrons
5. Annihilation of positrons.

Microscopic gamma energy absorption cross sections in units of Mev-barns were conveniently included in the cross-section set so that the calculation of the volumetric energy deposition rate (Eq. 5.1) could be straightforwardly performed. Gamma rays lose energy by:

1. Pair production

2. Compton scattering

3. Photoelectric effect,

which covers the range of important gamma interactions (E-5).

Figure 5.4 shows the total gamma energy deposition in the blanket due to both local fission events and core leakage. Seven different cases of various blanket enrichments were analyzed ranging from 0.2 $^{w}/_{o}$ to 2.5 $^{w}/_{o}$ U-235, including two cases with different fissile enrichments ($^{w}/_{o}$) in each blanket row (0.71/1.2/2.0 and 2.0/1.2/0.71). These cases cover a wide range of available enrichments as might be considered for blanket seeding. Furthermore these fissile uranium enrichments (especially the mixed enrichment cases) roughly simulate the fissile plutonium enrichment that might be experienced in a radial blanket after irradiation or after out-in or in-out fuel management.

For clarity only the 0.2 $^{w}/_{o}$, 1.2 $^{w}/_{o}$, and 2.5 $^{w}/_{o}$ enriched blankets are plotted in Fig. 5.4. All the other cases are similar to, and within the bounds of, the 0.2 $^{w}/_{o}$ and 2.5 $^{w}/_{o}$ blankets. A few pertinent observations can be made. Most noticeable is the characteristic exponential attenuation of the gamma deposited energy for all enrichments, giving an e-folding distance between 13 and 15 cm. Other general features are the nonlinearity of the curves at both extremes of the blanket, which is attributed to the discontinuities in material composition at the core-blanket and blanket-reflector interfaces.

To evaluate the effect of core gamma rays leaking into the blanket, the effect of blanket-fission-produced gammas was decoupled from the total production of gamma rays. This was achieved by making the assumption that gamma rays produced by fission events were absorbed locally,

Fig. 5.4 Gamma Energy Deposition Traverses for Variously Enriched Blankets

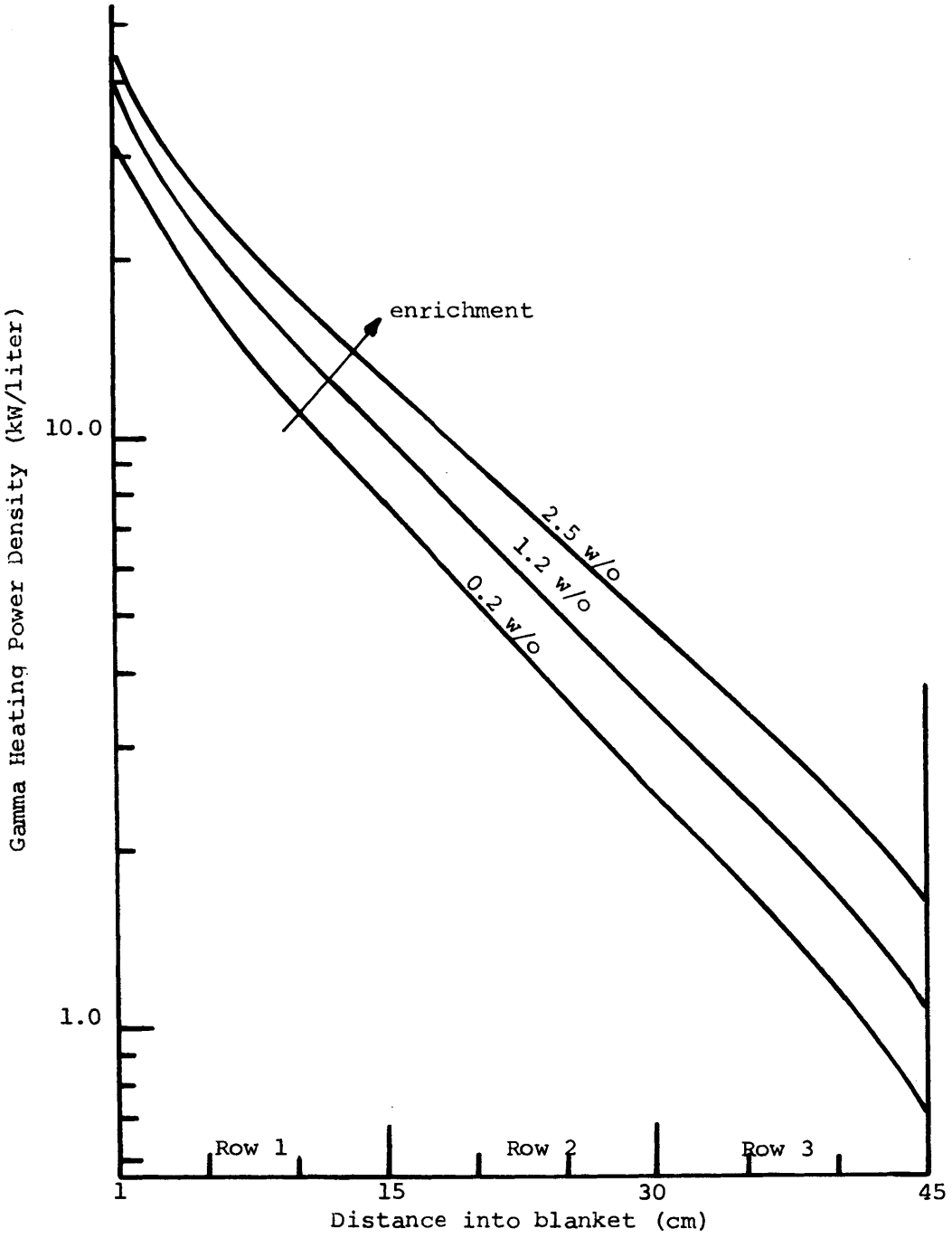

the usual "infinite medium" assumption made when calculating energy deposition rates from fission rates in reactors (L-3). Thus 25 Mev, the sum of the gamma ray energy released per local fission (including 4 Mev of inelastic scatter gammas) as given in Table 5.2, was subtracted from the calculated local gamma energy deposition, leaving the excess gamma energy, i.e., that gamma energy not attributable to local fissions, but rather due to leakage of core gamma rays. Figure 5.5 shows the excess gamma energy as a function of enrichment and distance into the blanket.

The major consequence of Fig. 5.5 follows from the closeness of the curves for the different enrichments. This figure implies that the excess gamma heating is essentially independent of enrichment, and therefore independent of blanket fission rate. This result is important since it permits inclusion of gamma rays in the heating analysis by simply adding a component, independent of the local fission rate, to the local fission heating rate. This component, $E_\gamma(kw/\ell)$, is a function only of distance from the core, x_{cm}, and can be represented by the following equation:

$$E_\gamma = P(0.864)\, e^{-0.0715x}, \qquad (5.2)$$

where P is the reactor power in units of 100 MW_T; in this case, P = 25. Table 5.3 lists the maximum percent deviation between the gamma heating results presented in Fig. 5.5 and those predicted by Eq. 5.2. Figure 5.6 shows the ratio of excess gamma energy, predicted by Eq. 5.2, to the local fission heating rate, and indicates the importance of including gamma heating in a heating analysis of the blanket. As can be seen, the ratio decreases with enrichment. Except for the depleted blanket which

Fig. 5.5 Excess Gamma Energy Deposition in the Blanket

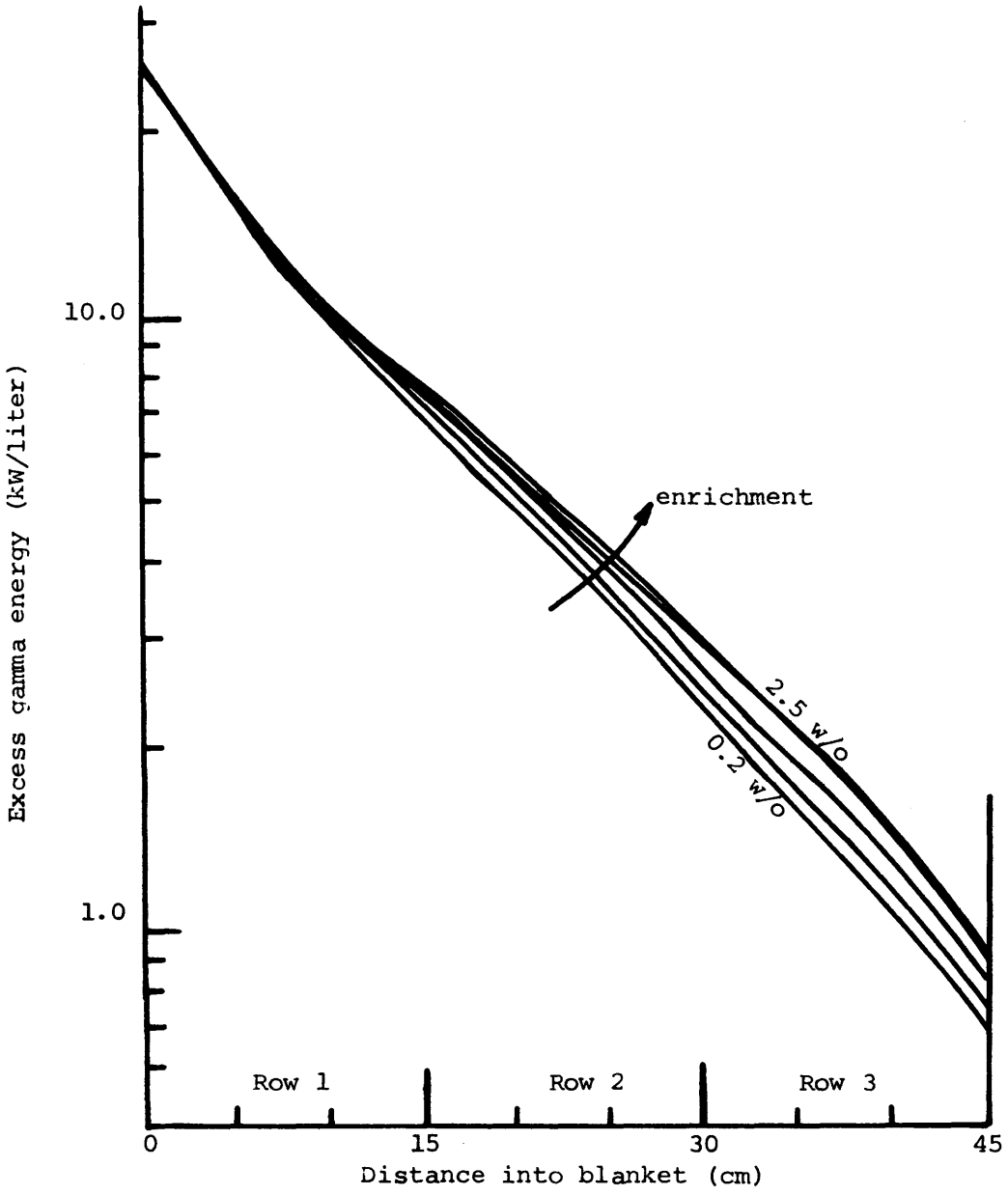

Fig. 5.6 Ratio of Excess Gamma Energy to Fission Energy Deposition in the Blanket

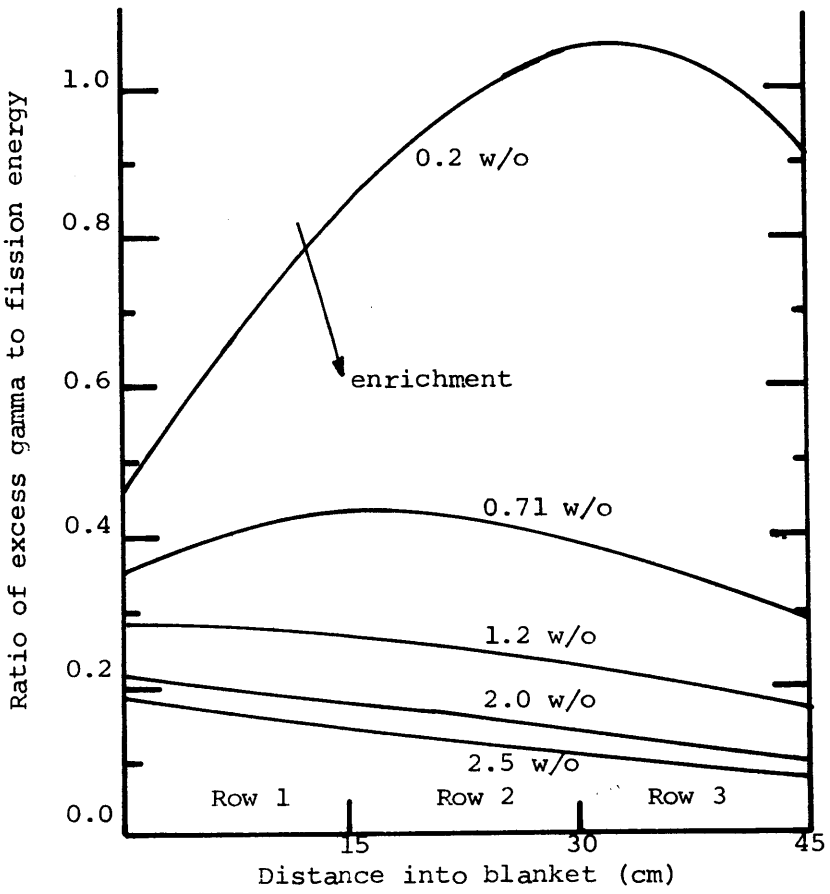

TABLE 5.3 Excess Gamma Energy Deposition

Depth into Blanket (cm)	Excess γ Energy (Eq. 5.2) (kW/liter)	Maximum Deviation* (%)
2.5	18.06	+12.8
7.5	12.64	+8.96
12.5	8.837	-5.94
17.5	6.181	+10.7
22.5	4.323	+10.9
27.5	3.024	-11.8
32.5	2.115	-16.5
37.5	1.479	+18.9
42.5	1.044	-17.9

*Percent difference between excess gamma energy predicted by Eq. 5.2 and the excess gamma energy plotted in Fig. 5.5.

has a ratio of about 1.0, the ratio is less than 0.5, decreasing to about 0.08. Thus considering that Eq. 5.2 correlates the data presented in Fig. 5.6 to within better than a 20 percent discrepancy, errors less than 10 percent would be expected in predicting the total heating rate.

5.2.4 Neutron Heating Analysis

Three different events were considered to contribute to the neutron heating rate:

1. neutron elastic scattering;
2. neutron inelastic scattering;
3. neutron capture.

Actually these three events are similar in the sense that the energy

associated with each is a recoil energy determined by the law of conservation of momentum. Thus the microscopic energy absorption cross section for event x, material j, energy group i, ${}_x\sigma^E_{ij}$, defined for use in Eq. 5.1, is determined by simply multiplying the mean energy loss per event ($\overline{\Delta E}_{ij}$) by the microscopic cross section for event x, ${}_x\sigma_{ij}$, given by the 26-group cross-section set (A-6),

$$ {}_x\sigma^E_{ij} = ({}_x\sigma_{ij})(\overline{\Delta E}_{ij}). \tag{5.3} $$

Table 5.4 gives the appropriate expressions for the terms in Eq. 5.3 for the three types of neutron heating events listed above. A detailed derivation of these relationships can be found in reference W-5.

The results of the neutron heating analysis for the variously enriched blankets are shown in Fig. 5.7, where the variation with fissile enrichment is emphasized. In order to determine the effect of the core on the total neutron heating rate, the contribution to the neutron heating rate due to neutrons produced by fissions in the blanket was determined by extrapolating the lines in Fig. 5.7 to the appropriate (negative) effective enrichment where the fission rate is zero, as determined in Fig. 5.3. The portion of the neutron heating due to neutrons originating in the core, or excess neutron heating, was found to be independent of enrichment, depending only on the distance from the core, as shown in Fig. 5.8.

This general result, isolating the excess neutron heating (due to core neutrons) parallels the previous result which isolated the excess gamma heating in the blanket caused by gammas leaking from the core. Equation 5.4 correlates the excess neutron heating, $E_n(kw/\ell)$:

TABLE 5.4 Summary of Microscopic Energy Absorption Cross Sections for Evaluation of Neutron Heating

Mechanism	Energy per Event ($\Delta \overline{E}_{ij}$)	Microscopic Cross Section ($_x\sigma_{ij}$)
Elastic Scattering	$\overline{E}_i(1 - e^{-\xi})$	$_{el}\sigma_{i,j}$
Inelastic Scattering Recoil		
due to incident neutron, $\overline{E}_i$	$\left(\frac{1}{A+1}\right)\overline{E}_i$	$_{in}\sigma_{i,j}$
due to re-emitted neutron, $\overline{E}_n$	$\left(\frac{1}{A}\right)\overline{E}_n$	$_{in}\sigma_{i\rightarrow n,j}$
due to de-excitation gamma, E_γ	$\frac{1}{A}\left(\frac{E_\gamma^2}{2m_oc^2}\right)$	$_{in}\sigma_{i\rightarrow n,j}$
Neutron Capture Recoil		
due to incident neutron, $\overline{E}_i$	$\left(\frac{1}{A+1}\right)\overline{E}_i$	$_{c}\sigma_{i,j}$
due to gamma, E_γ	$\frac{1}{A}\left(\frac{E_\gamma^2}{2m_oc^2}\right)$	$_{c}\sigma_{i,j}$

Total microscopic energy absorption cross section for neutron heating:

$$\sigma_{ij}^{E} = \overline{E}_i(1 - e^{-\xi})(_{el}\sigma_{i,j}) + \left(\frac{\overline{E}_i}{A+1}\right)(_{in}\sigma_{i,j}) + \left(\frac{\overline{E}_n}{A} + \frac{E_\gamma^2}{2m_oc^2A}\right)(_{in}\sigma_{i\rightarrow n,j}) + \left(\frac{\overline{E}_i}{A+1} + \frac{E_\gamma^2}{2m_oc^2A}\right)(_{c}\sigma_{i,j}).$$

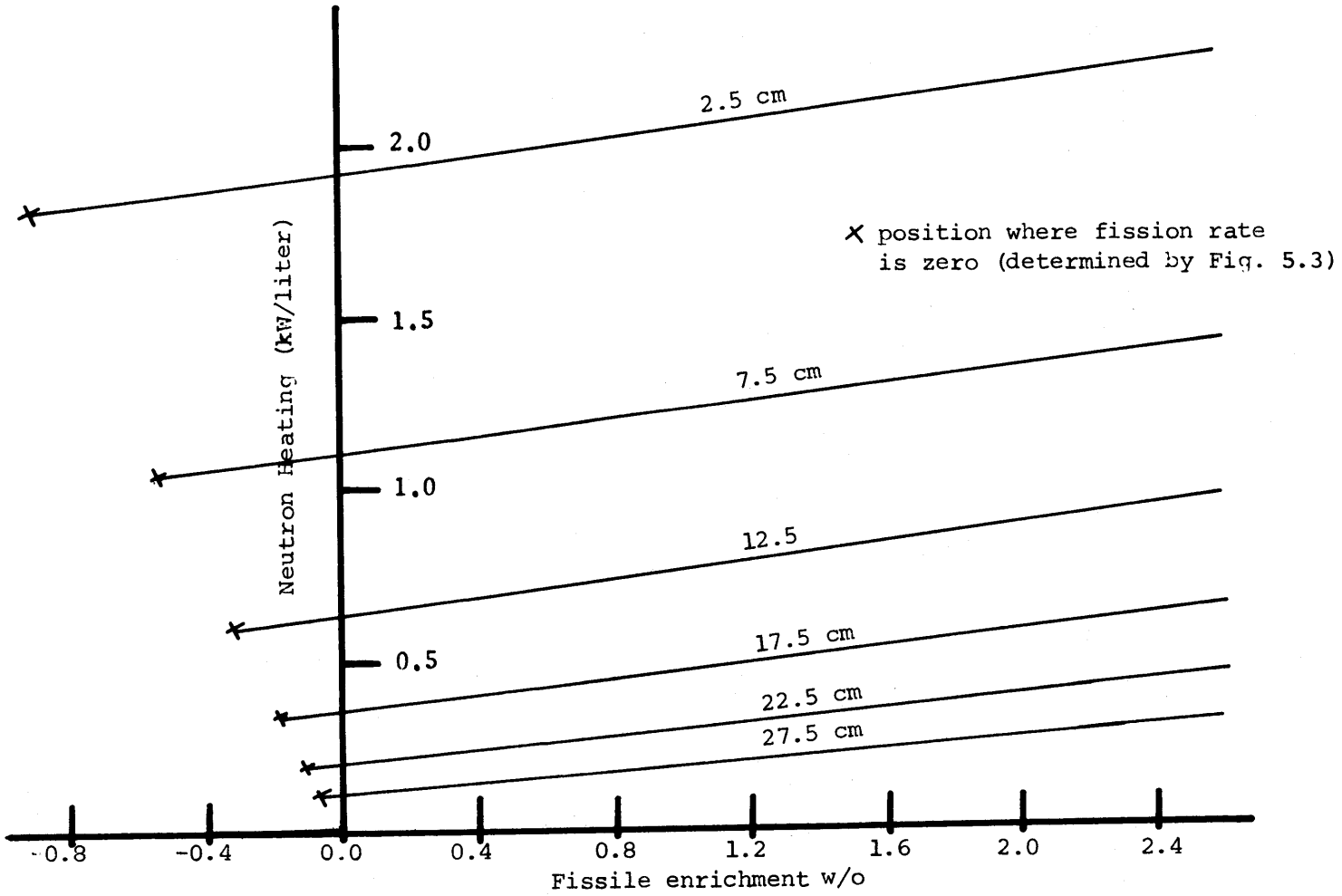

Fig. 5.7 Effect of Enrichment on Neutron Heating

Fig. 5.8 Contribution of the Excess Neutron Heating to the Total Neutron Heating Rate in the Blanket

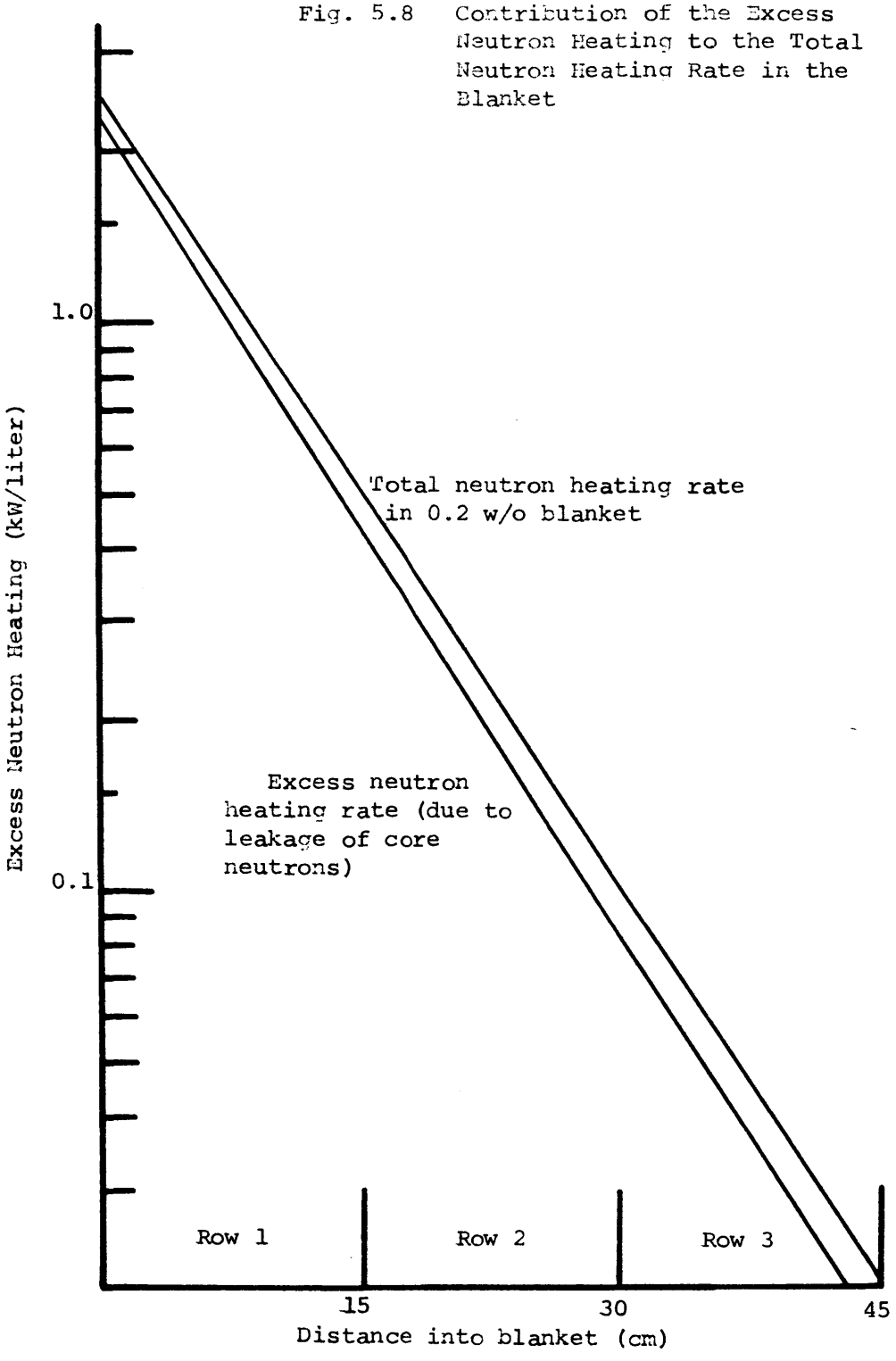

$$E_n = P(0.096)\, e^{-0.1098x}, \tag{5.4}$$

where P is the reactor power in units of 100 MW_T; in this case, P = 25.

Comparison of Eq. 5.4 to Eq. 5.2 indicates that the excess neutron heating is almost an order of magnitude less than the excess gamma heating, and decreases more rapidly with distance into the blanket.

5.2.5 Summary of Heating Analysis

Careful analysis of the three main contributions to the total blanket heating rate, fission heating, gamma heating, and neutron heating, has led to the development of equations to determine the total blanket heating rate in a manner which separates in-leakage from the core from local contributions. The total blanket heating rate (BHR) was approximated as the sum of the fission heating rate (FHR), treated as a local source at 200 Mev/fission, plus the gamma heating rate (GHR) (given by Eq. 5.2) and the neutron heating rate (NHR) (given by Eq. 5.4) given here in combined form as the shield heating rate (SHR):

$$BHR = FHR + SHR, \tag{5.5}$$

and

$$SHR = GHR + NHR = P[0.864\, e^{-0.0715x} + 0.096\, e^{-0.1098x}], \tag{5.6}$$

where P is the reactor power in units of 100 MW_T; in this case, P = 25; x is the distance into the blanket in centimeters; and the heating rates are in units of kilowatts per liter.

Figure 5.9 shows the contributions to the total heating rate for the

Fig. 5.9 Contributions to the Total Blanket Heating Rate

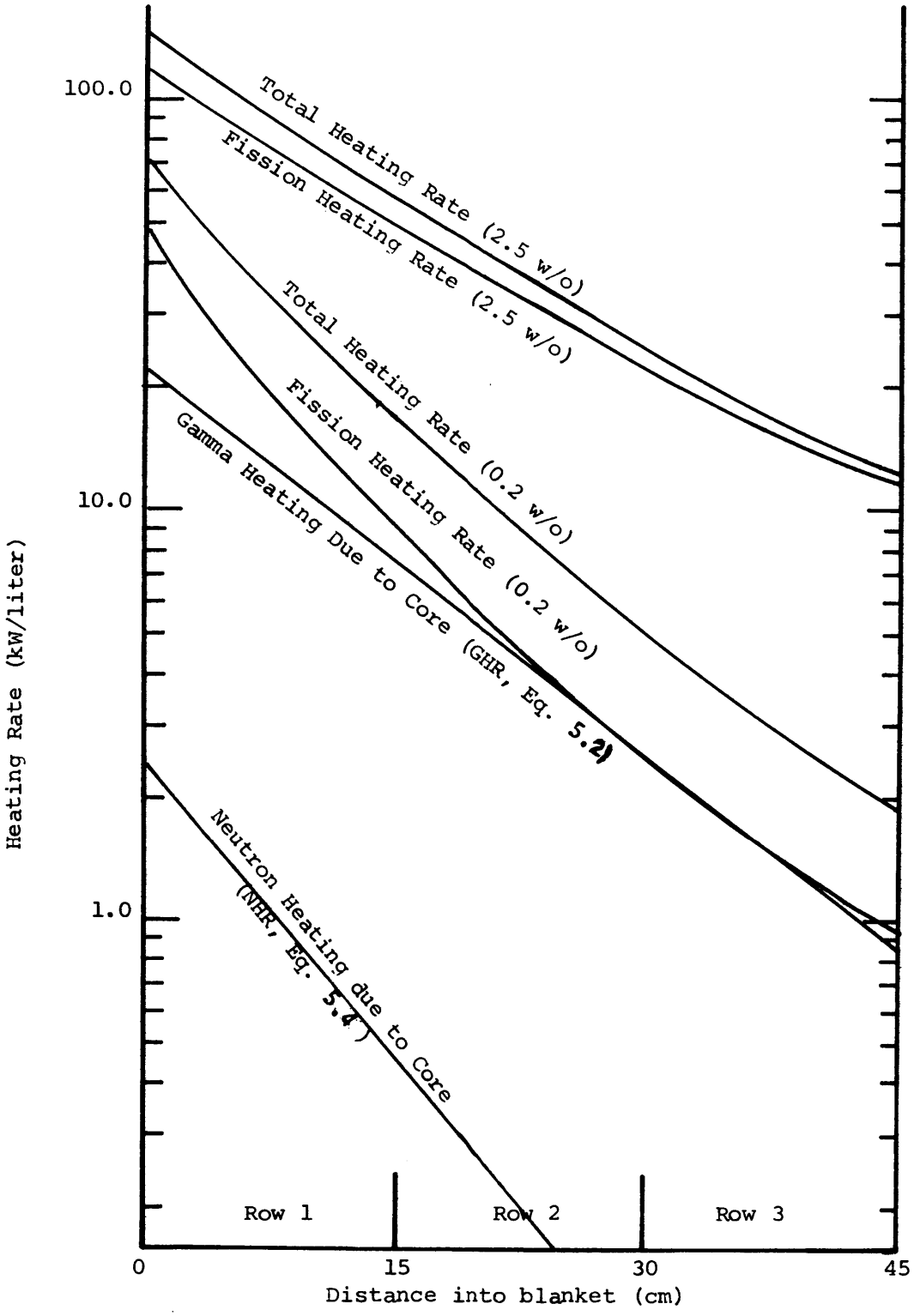

0.2 $^{w}/_{o}$ and 2.5 $^{w}/_{o}$ U-235 enriched blankets. It is clear that neglecting the contribution of the shield heating rate can lead to substantial underprediction of the total blanket heating rate. In the 0.2 $^{w}/_{o}$ blanket, the BHR would be underpredicted by 50 to 100 percent, whereas in the 2.5 $^{w}/_{o}$ blanket the BHR would be underpredicted by about 10 percent. The smaller underprediction of the more highly enriched blanket would be expected since the FHR is higher and the SHR becomes correspondingly less important than for a lower enrichment blanket.

5.3 Evaluation of Blanket Configurations

The objective of the work summarized in this section was the evaluation of the relative economic performance of various blanket configurations considering both blanket burnup and thermal-hydraulic contributions to the total power cost. The method of burnup is discussed in Section 5.3.1. The burnup economic determination follows conventional analysis (e.g., see reference B-5), and is reviewed in Section 5.3.2. A model to treat thermal-hydraulic-economic considerations has been developed and is summarized in Section 5.3.3. Section 5.3.4 summarizes the results obtained by applying these economic methods to a variety of blanket-reflector configurations which differed in initial enrichment, thickness and reflector composition.

5.3.1 Method of Burnup

Studies of various blanket-reflector configurations were carried out using the representative two-zone core, 1000 MW_e LMFBR depicted in Fig. 5.1. The primary calculational tool used in comparing the neutronic

performance of the cases studied was the two-dimensional diffusion theory burnup code 2DB (L-4). A 4-group region-wide cross-section set was employed. This set was prepared by collapsing the 26-group ABBN cross-section set (A-6) over spectra appropriate to the various reactor regions using the one-dimensional transport theory code ANISN (E-4). Region-wide 4-group cross sections have been shown here and elsewhere (H-3) to compare favorably to multigroup calculations, especially in the inner regions of the blanket which contribute most of the blanket plutonium production.

Since long burnups (up to six years) were performed in studying the blanket burnup behavior, an "equilibrium" core and axial blanket were defined which remained fixed in time. Constant core and axial blanket material concentrations (including poison concentration) at the time-average values expected in these regions were used, obviating the need to fuel-manage the core. It should be noted that although considerable care was taken to define a realistic core and axial blanket composition around which the radial blanket was irradiated, other investigators (B-5, H-4, W-5) have looked into the effect of different core-management methods on radial blanket economics, and have concluded that there is an insignificant effect on the results. Furthermore, since the same core treatment is used for all cases studied, any systematic bias (however small) should cancel out so long as relative comparisons are emphasized.

5.3.2 Burnup-Economic Model

The burnup-economic analysis was performed utilizing the cash flow method contained in the computer code BRECON developed by Brewer

(B-5), and modified by Wood (W-5) to permit direct use of 2DB burnup results as input. This method capitalizes, and consequently depreciates for tax purposes, the material purchases and fabrication charges; whereas reprocessing charges and material credit are treated as an expensed cost and taxable revenue, respectively.

The economic results generated by BRECON are the local levelized fuel component of the energy cost (mills/kW-hr) which can be applied to an entire region (e.g., radial blanket) or subregion (e.g., radial blanket row). This facilitates the determination of the minimum fuel cycle cost contribution (i.e., optimum irradiation time) for a blanket row or for the entire blanket.

Table 5.5 lists the basic economic parameters used in this study of radial blanket burnup fuel economics. These conditions (except for fissile U-235) are the same as those presented by Brewer (B-5) and Wood (W-5) and are within the range projected for the mature U.S. nuclear fuel cycle economy (W-6). The range of values for fissile U-235 is based on $38.50 per kilogram of separative work (F-6).

5.3.3 Thermal-hydraulic Economic Model

An economic model has been developed to treat the effects of power gradients in the radial blanket. Two effects were analyzed: the decrease in thermal efficiency and the increase in pumping power attributable to blanket overcooling. The results of this analysis are embodied in the following expressions:

TABLE 5.5 Economic Environment

Financial Parameters	
Income Tax Rate, τ	0.5
Capital Structure	
Bond (debt) fraction, f_b	0.5
Stock (equity) fraction, f_s	0.5
Rates of Return	
Bonds, r_b	0.07
Stocks, r_s	0.125
Discount Rate, x	0.08
Unit Blanket Fuel Processing Costs ($/kg HM)	
Fabrication, C_{fab}	69
Reprocessing, C_{repr}	50
Isotopic Market Value ($/kg)	
Pu-239, C_{Pu}	10,000
Pu-241, C_{Pu}	10,000
Pu-240	0
Pu-242	0
U-238	0
U-235 (F-6), C_U	
0.2 $^{w}/_{o}$	1,500
0.711	3,300
1.00	5,140
1.50	7,130
2.00	8,360
3.00	9,190
98.00	15,190

Thermal efficiency effect:

$$\frac{e_2 - e_1}{e_1} = \frac{f - \eta_2}{\eta_2} \left(\frac{W_2}{1 + W_2}\right) \left(\frac{1}{1 + \frac{T_i}{\Delta T_{r'}}}\right) \left(\frac{F_{b_2} - F_{b_1}}{F_{b_2}}\right) \qquad (5.7)$$

Pumping power effect (generally much smaller):

$$\frac{e_2 - e_1}{e_1} = \frac{p_P}{p_E} (1 - \eta_1) \left(\frac{W_2}{1 + W_2}\right) \left(\frac{F_{b_2} - F_{b_1}}{F_{b_2}}\right) \qquad (5.8)$$

The subscripts 1 and 2 refer to any two cases being analyzed. The parameters appearing in Eqs. 5.7 and 5.8 are defined in Table 5.6.

TABLE 5.6 Definition of Parameters in the Thermal-Hydraulic Economic Model

Parameter	Definition	Typical or Reference Value
e	Cost of electricity	10 mills/kW-hr
η	Thermal efficiency	0.4
f	Ratio of actual to Carnot efficiency	0.62
T_i	Reactor inlet temperature	1210°R (750°F)
ΔT_r	Mean reactor temperature rise	300°R (300°F)
p_P	Reactor pumping power	10.5 MW
p_E	Reactor electric output	1000 MW
W	Ratio of blanket to core coolant flow rate	0.44 (3-row radial blanket)
F	Ratio of peak to average power density	3.4 (3-row radial blanket)

It should be emphasized that Eqs. 5.7 and 5.8 reflect the economic penalty due to spatial gradients in the blanket. Another power gradient, the temporal gradient, exists in the radial blanket, and it also contributes to the total overcooling of the blanket. The temporal gradient, R, is defined as the end-of-life power divided by the beginning-of-life power. This gradient is due to the buildup with time of the fissile plutonium and consequently the fission rate. The spatial gradient is due to the radial power distribution, and it occurs throughout the blanket irradiation lifetime.

Figure 5.10 shows how the spatial gradient, F, and the temporal gradient, R, act in concert in creating blanket overcooling. The figure is roughly to scale for the base-case 3-row blanket, where it has been shown that R varies very nearly linearly with time and F is roughly constant. The cross-hatched triangular area represents the degree of overcooling in the blanket attributable to the temporal effect. The upper rectangular area bounded by the horizontal lines at P_{EOL}^{max} and P_{EOL} is a measure of the degree of overcooling due to the spatial gradient. The contribution of spatial overcooling relative to temporal overcooling is the ratio of the rectangular area to the cross-hatched triangular area:

$$\frac{\text{Spatial overcooling}}{\text{Temporal overcooling}} = \frac{2(F-1)\,R}{R-1} \,. \qquad (5.9)$$

It should be emphasized that F is the power gradient that exists in the blanket at the end of its irradiation lifetime, and R is the ratio of the blanket power produced at this time to the blanket power produced at the beginning of blanket irradiation. For both factors, the effects of the

Fig. 5.10 Overcooling Due to Temporal and Spatial Gradients

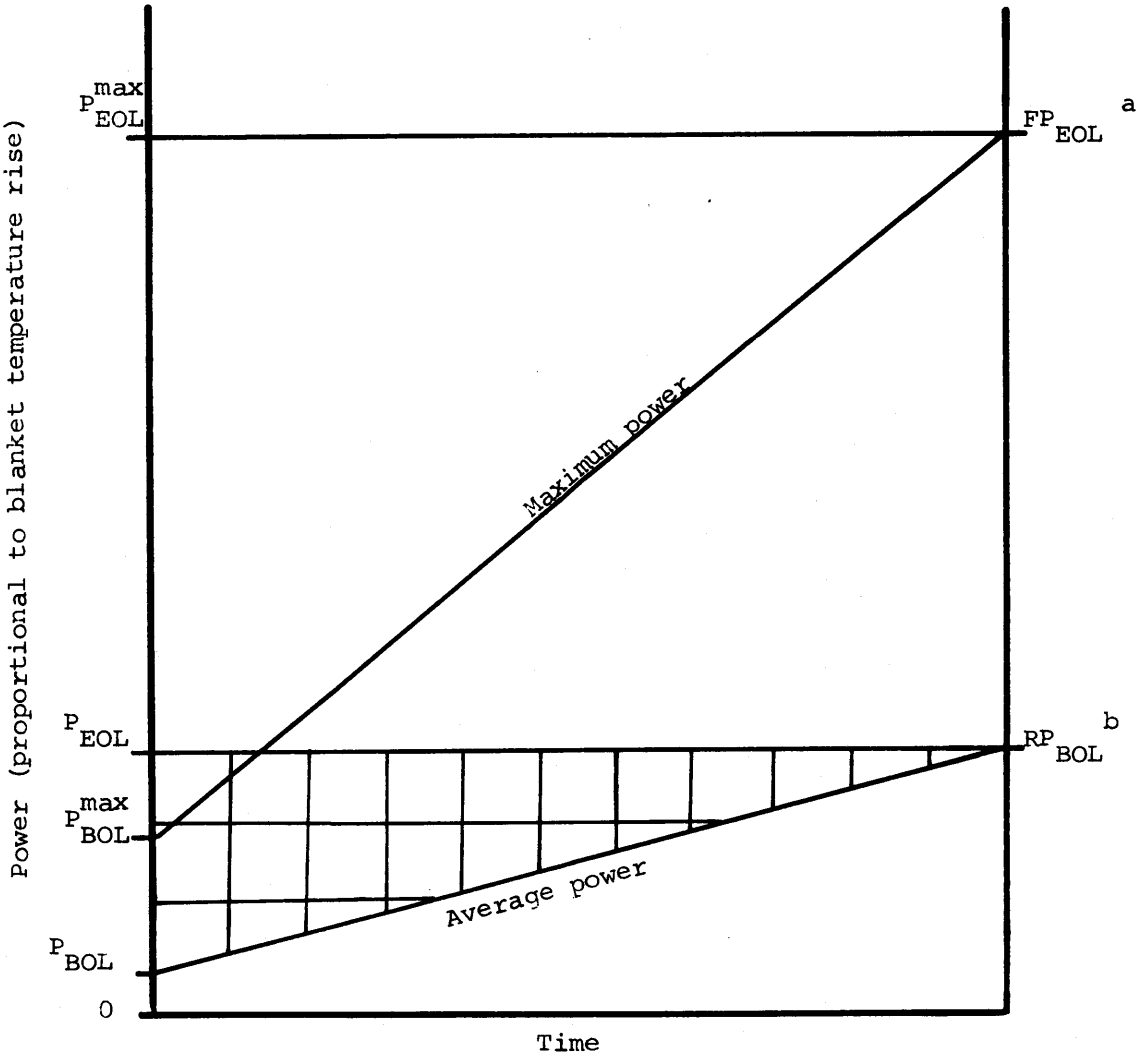

[a]$_F$: Spatial peak-to-**average** radial power gradient

[b]$_R$: Temporal power gradient, end-of-life average power divided by beginning-of-life power

shield heating rate (Eq. 5.6) must be included, being most important in determining R, since a substantial amount of blanket power at the beginning of life is due to this effect (see Fig. 5.9).

5.3.4 Results

Table 5.7 presents the results of the burnup and thermal-hydraulic analyses of the various blanket-reflector configurations. These configurations were determined by varying three design variables: blanket thickness, initial blanket enrichment, and reflector composition; with the constraint that the new reflector fit within the 45 cm thick annulus taken up by the 3-row reference blanket (see Fig. 5.1), and that only whole rows (15 cm) could be manipulated.

The first column in Table 5.7 designates the particular blanket-reflector configuration studied. The first digit designates the number of blanket rows (1, 2 or 3) and the following two letters designate the initial enrichment of the blanket fuel, and the reflector material, respectively. The uranium enrichments studied were depleted, 0.2 $^{w}/_{o}$ U-235 (D), natural, 0.71 $^{w}/_{o}$ (N), 2.5 $^{w}/_{o}$ enriched (E), and a 2-row mixed case having a depleted inner row and a natural outer row (M). The reflector compositions were either steel (S) or graphite (C).

The next column, E_{opt}, summarizes the burnup-economic analysis. E_{opt} is the absolute difference in dollars per year between the base case burnup economics and the particular case of interest. Column 3, E_{oc}, summarizes the thermal-hydraulic analysis taking into account both spatial and temporal effects. E_{oc} represents the absolute difference in dollars per year between the base case and the particular case of

TABLE 5.7 Relative Savings Realized by Various Advanced Blanket Configurations (10^5 \$/yr)[a]

Case Number[b]	Burnup E_{opt}[c]	Thermal-Hydraulic E_{oc}[c]	Total E_{net}[c]
3DS	–	– (-8.22)[d]	– (-8.22)[d]
2DS	-1.14	-7.56 (-11.78)	-8.70 (-12.92)
2NS	-0.84	-8.05 (-12.27)	-8.89 (-13.11)
2MS	-1.06	-7.71 (-11.93)	-8.77 (-12.99)
2ES	+6.44	-10.57 (-14.79)	-4.13 (-8.35)
2DC	-1.36	-8.61 (-12.83)	-9.97 (-14.19)
1DS	-0.23	-7.91 (-7.91)	-8.14 (-8.14)
1DC	-0.93	-3.36 (-3.36)	-4.29 (-4.29)

[a] 10^5 \$/yr ~ 0.014 mills/kW-hr (assuming 7×10^9 kW-hr/yr).

[b] Key: 3DS
- 3 — Number of rows.
- D — Fuel: depleted (D), natural (N), enriched (E) or mixed (M).
- S — Reflector composition: steel (S) or graphite (C).

[c] Relative economic difference: base case (3DS) minus particular case of interest. E_{opt} = fuel cycle costs; E_{oc} = cost of blanket overcooling; $E_{net} = E_{opt} + E_{oc}$.

[d] Values in parenthesis are for individually row-by-row orificed blankets relative to the uniformly orificed base case.

interest. It should be noted that for this analysis all blanket rows were assumed to be uniformly orificed, determined by the innermost row's peak power density. The values given in parenthesis indicate the relative savings that could be achieved by going to individually row-by-row orificed blankets. The last column, E_{net}, is the sum of the previous two columns and represents the total economic difference between the base case and the particular case of interest taking into account both burnup and thermal-hydraulic considerations. Note that in all cases a minus sign indicates a cost savings in going to an advanced blanket-reflector configuration.

From an analysis of the work summarized in this section the following conclusions have been drawn:

1. An optimum blanket-reflector configuration can only be selected by considering both the burnup performance and the thermal-hydraulic performance.

2. Initial blanket enrichment is undesirable due to the added cost of fissile U-235, which outweighs the improved thermal-hydraulic performance.

3. Graphite reflectors are to be preferred to steel reflectors for 2-row blankets, the difference amounting to ~$\$ 10^5$ per year.

4. Individual row orificing offers improved thermal-hydraulic performance, representing a potential present worth savings on the order of $\$4.0 \times 10^6$ over the blanket lifetime of the base case configuration; and perfect local flow-to-power matching, both spatially and temporally, can represent a present worth savings of over $\$1.1 \times 10^7$.

5. Two-row blankets are preferable, since even the improved

burnup-economic performance of a graphite-reflected 1-row blanket can not compensate for the lost revenue due to the removal of blanket row 2.

The results presented in Table 5.7 indicate that case 2DC, a 2-row, individually orificed, depleted-uranium fueled, graphite-reflected blanket, offers the largest potential savings (~1.4 million $/year) relative to the base case configuration.

5.4 Experimental Studies

The work summarized in the previous section has indicated an economic advantage for graphite-reflected blanket configurations, a result which suggested experimental confirmation, since it was not clear that methods and cross-section sets previously proven adequate for core calculations would suffice, particularly in view of the severe spectral changes in the blanket-reflector regions, here accentuated by the presence of graphite.

5.4.1 Description of the Experiment

A blanket-reflector mockup (Number 3) was irradiated using the Blanket Test Facility (BTF) at the M.I.T. Research Reactor. A detailed description of the design and construction of the BTF is presented in Reference (F-3). For present purposes the only point requiring reiteration is that the BTF converter assembly provides neutrons closely simulating the leakage spectrum from a 1000 MW_e LMFBR core, which can be used to drive blanket mockups.

Blanket-reflector mockup No. 3 had an axial thickness of 105 cm (corresponding to the radial thickness in a cylindrical configuration)

consisting of two rows of blanket subassemblies (totalling 30 cm), 30 cm of graphite and 45 cm of steel. The overall dimensions of this parallelepiped was approximately 132 cm high, 152 cm wide by 105 cm thick. The blanket subassemblies were identical to those used in previous irradiations (L-2). They consist of 5/16 inch carbon steel-clad (clad o.d.), uranium metal fuel rods arranged in a square lattice with a pitch of 0.511 inches, surrounded by anhydrous sodium chromate. The material concentrations were chosen to provide a realistic homogenized blanket composition simulating 37 $^{v}/_{o}$ depleted UO_2 (at 90% t.d.), 20.7 $^{v}/_{o}$ Type 316 stainless steel 32 $^{v}/_{o}$ sodium and 10.3 $^{v}/_{o}$ void.

Figure 5.11 shows an overhead view of blanket mockup No. 3 indicating the location of the forty-three foil tubes which provide for the irradiation of various foils in the blanket and graphite reflector in the axial and transverse directions.

The primary task in the present experiments was to obtain the necessary data to evaluate the transverse buckling and axial reaction rates for various foil materials. The foil materials employed are listed in Table 5.8 along with the reaction of interest.

5.4.2 Analysis of Experimental Results

Although the axial experiments were the most important for checking the analytic methods, the transverse experiments were needed to confirm the fact that spectral equilibrium in the central region of the reflector was achieved. This was shown to be true and also, that the transverse buckling traverses in the blanket and reflector conformed to cosine distributions having the same extrapolated dimensions found in the analysis of

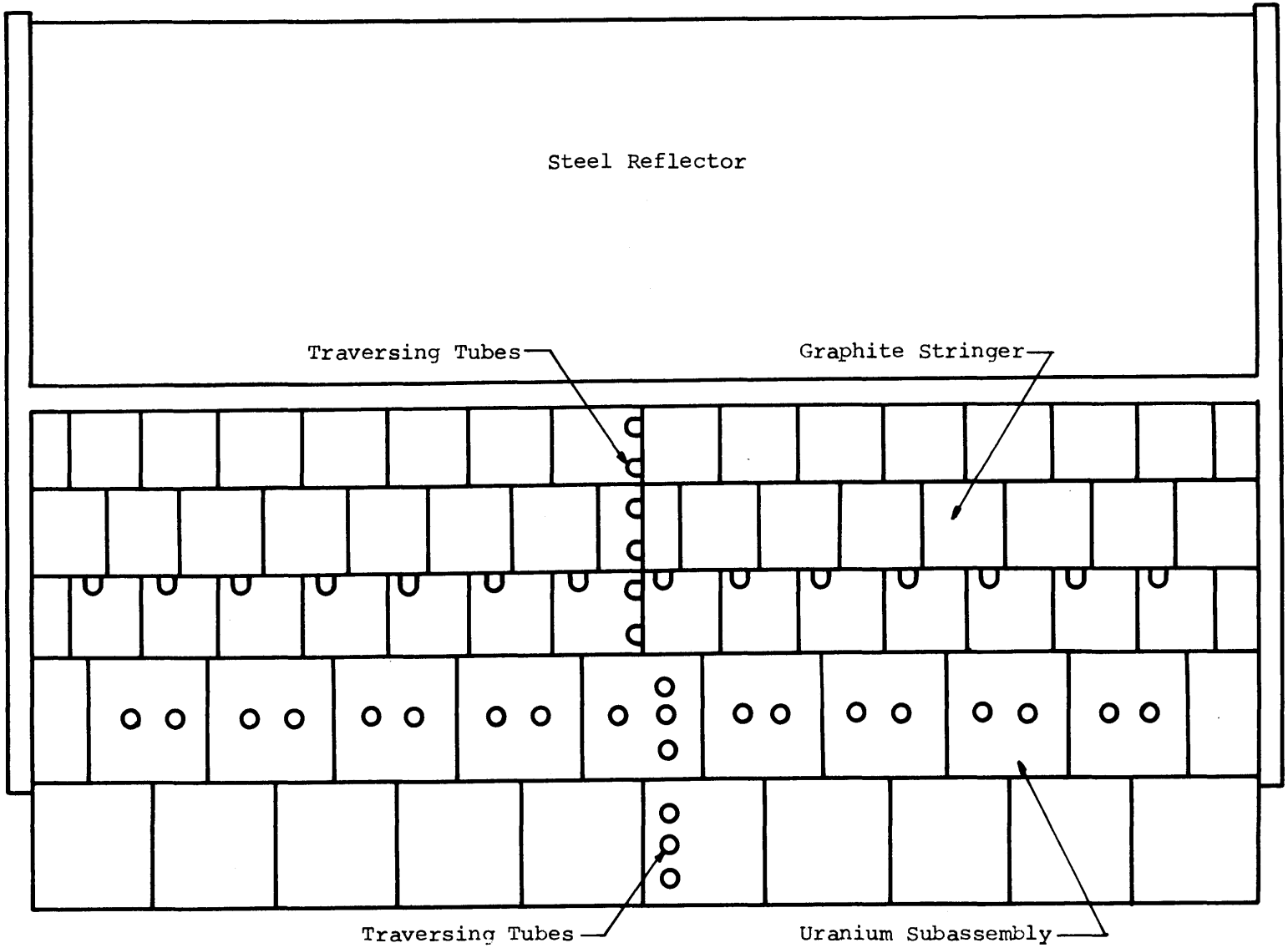

Fig. 5.11 Overhead View of Blanket Mock-Up No. 3

TABLE 5.8

Activation Foils Used in BTF Blanket Mock-Up No. 3

Foil	Reaction	Remarks
Gold	$Au^{197}(n,\gamma)\,Au^{198}$	Measures entire energy spectrum (A, B)*
Molybdenum	$Mo^{98}(n,\gamma)Mo^{99}$	Emphasizes keV range (A, B)
Indium	$In^{115}(n,n')\,In^{115m}$	Threshold reaction E > 0.2 MeV (A, B)
Manganese†	$Mn^{55}(n,\gamma)Mn^{56}$	Emphasizes keV range (A)
Sodium	$Na^{23}(n,\gamma)Na^{24}$	Typical LMFBR material (A)
Chromium	$Cr^{50}(n,\gamma)Cr^{51}$	Typical LMFBR material (A)
Uranium	–	Typical LMFBR material
-238 in-rod	$U^{238}(n,\gamma)$	(A)
-238 ex-rod	$U^{238}(n,\gamma)$	(A, B)
-238 in-rod	$U^{238}(n,f)$	Threshold reaction E > 1.0 MeV (A)
-238 ex-rod	$U^{238}(n,f)$	(A, B)
-235	$U^{235}(n,f)$	(A)
Plutonium-239	$Pu^{239}(n,f)$	Typical LMFBR material (A)
Thorium†	$Th^{232}(n,f)$	Threshold reaction E > 1.75 MeV (A, B)
Neptunium†	$Np^{237}(n,f)$	Threshold reaction E > 0.75 MeV (A)

*A indicates foil used for axial activation traverse.
B indicates foil used for transverse activation traverse (i.e., buckling determination).

†New materials, not used in BTF No. 2.

Blanket No. 2 (L-2). This confirmed the applicability of one-dimensional calculations for blanket analysis.

Axial traverses were made in the blanket and graphite reflector assemblies, simulating traverses in the radial direction in cylindrical geometry. These experimental traverses were compared with analytical axial reaction rates which were computed by means of the one-dimensional transport theory code, ANISN (E-4) in the S-8 option, using the 26-group ABBN cross-section set (A-6) for all materials except for the Au-197 capture, In-115 (n, n') and Np-237 fission cross sections, which were developed from the SAND II Library (M-4). It should be noted that the cross-section data used to evaluate the foil activities were not self-shielded, except for in-rod U-238 captures.

The general conclusion that can be drawn from this effort is that the analytical methods adequately describe the neutronic behavior of the graphite-reflected blanket for present purposes, and at least as well as they do conventional, steel-reflected blankets. In particular, the important U-238 capture event is adequately calculated, in agreement with similar observations reported by Leung (L-2) and Wood (W-5) in their studies of Blanket No. 2 and Blanket No. 4, respectively. Figure 5.12 displays plots of the measured in-rod and ex-rod U-238 capture data. As expected, the ex-rod foils are more active, being shielded only by neighboring fuel and not by the host fuel rod. Also shown are the calculated in-rod traverses (normalized to the experimental data) and a comparable traverse calculated using infinitely-dilute U-238 cross sections (solid line at top of graph) correctly normalized relative to the in-rod traverse. The same traverse is also shown renormalized to the ex-rod

Fig. 5.12 U-238 (n-γ) Axial Traverse in Blanket

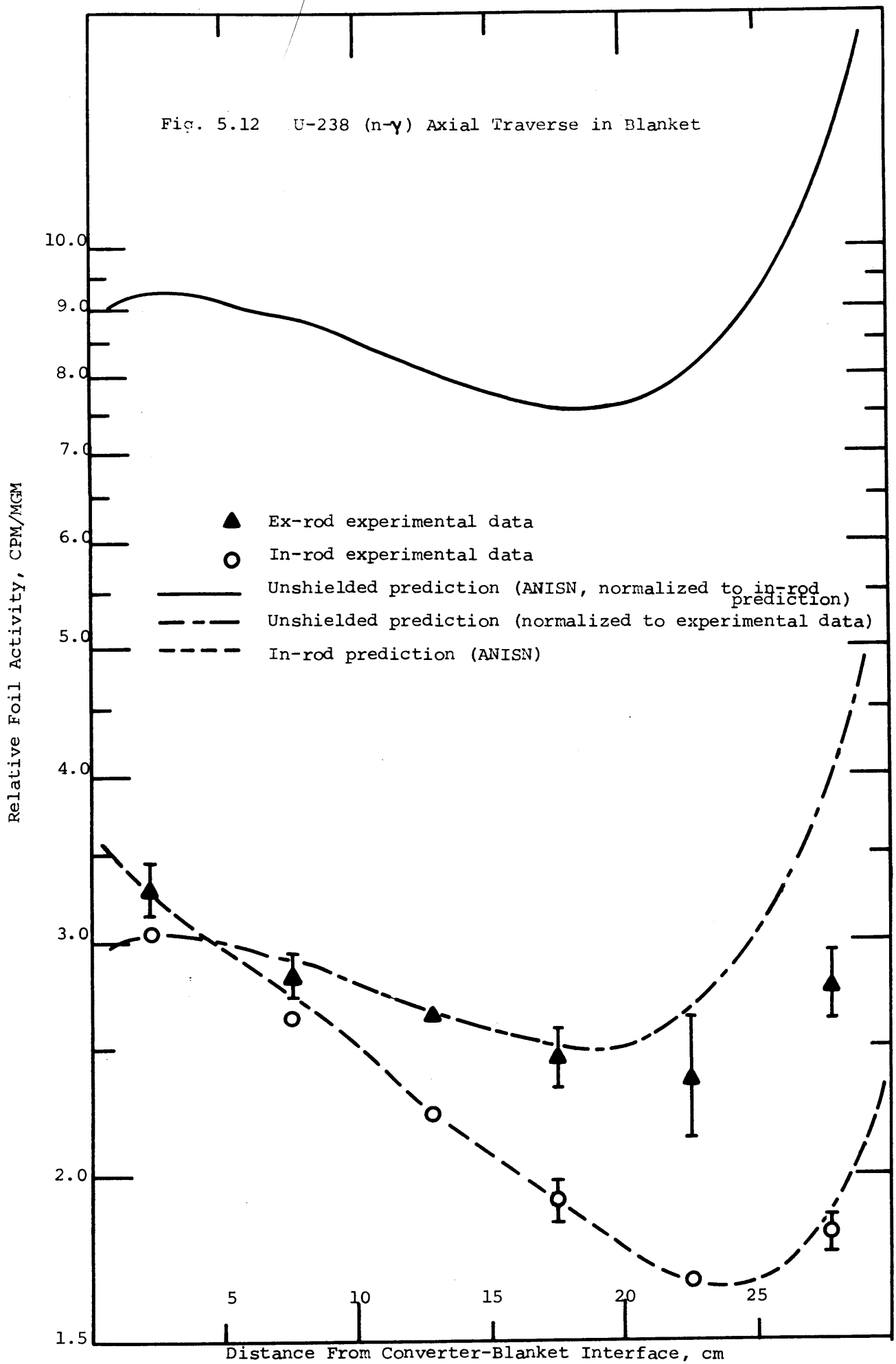

data (dot-dash line). While it is clear that the ex-rod activities are less shielded than those in-rod, they are far from being in an infinitely dilute environment. Even so, the shape of the infinitely dilute calculated traverse is in fair agreement with that of the ex-rod measurements. The results of Fig. 5.12 also display the expected effects of spectral softening near the graphite reflector: the in-rod flux depression is enhanced and the spread between the in-rod and ex-rod traverses widens, and both the in-rod and ex-rod capture rates are enhanced near the graphite reflector.

Although the experimental data agree quite well with the predictions in the blanket region, the threshold-detector activations in the graphite reflector do not. Uranium-238 fission and indium (n-n') data deep in the reflector are an order of magnitude higher than calculated. It should be noted that this same problem was observed in the steel reflector of Blankets No. 2 and No. 4. Choong (C-2) has examined this problem in some detail and concluded that the anomalous results are due to a variety of causes, such as subthreshold fission in U-238, and probably do not, therefore, indicate excessive fast neutron penetration, which would indicate a significant shielding problem. In late 1974, Blanket No. 5, with a special steel reflector designed to permit more detailed, and more precise measurements, is scheduled for irradiation, so that further experimental information can be acquired to aid in the resolution of this problem.

5.5 Conclusions and Recommendations

The objectives of the present work have been met, resulting in the

selection of a 2-row, depleted-uranium fueled, graphite-reflected blanket as the advanced blanket configuration offering the largest potential savings (~1.4 million $/year) relative to the base case 3-row, depleted uranium fueled steel-reflected blanket. Also, experimental verification of the neutronic behavior of a graphite-reflected blanket was satisfactorily accomplished, indicating that nuclear design can be accomplished at least as well as that for conventional steel-reflected blankets.

Special attention was given to a complete analysis of the blanket heating rates where it was confirmed that fission heating (heating proportional to the local fission rate) is not the only contribution to the heating rate, but rather gamma and neutron heating, empirically attributable to core-leakage gamma rays and neutrons, form a significant fraction of the total heating rate (up to 50% at the beginning-of-life of a depleted-uranium fueled blanket). An expression has been developed (Eq. 5.6) which treats this "shield heating rate" independently of the local fission rate.

Also, an economic model to deal with the thermal-hydraulic performance of the blanket was developed (Eqs. 5.7 and 5.8) and used in conjunction with a conventional burnup economic model to identify the best blanket-reflector configuration previously mentioned. The thermal-hydraulic model was also utilized to determine that the maximum economic potential of a perfectly orificed blanket, both spatially and temporally, was about $\$1.1 \times 10^7$ present worthed over the six-year lifetime of the batch-managed base-case blanket-reflector configuration: about $\$5 \times 10^4$ per subassembly.

In meeting the goals of the present work certain items have been

identified that merit further analysis. These include:

1. a detailed mechanical and thermal-hydraulic design of a graphite-reflector assembly and a fabrication cost comparison with a standard steel assembly. The cost advantage of graphite cited previously considers only fuel cycle and overcooling costs and amounts to a present worth savings over the plant lifetime of about $ 15,000 per reflector subassembly, a margin which is much greater than the fabrication cost differential (even a blanket assembly costs only ~$ 15,000).

2. a more thorough evaluation of the effect of blanket fuel-management schemes on the thermal-hydraulic performance of the blanket;

3. a more detailed study of blanket-orificing schemes, with particular attention to ways of decreasing the spatial gradient (e.g., via mixing) and the temporal gradient (e.g., via time-varying orifices);

4. an investigation of the applicability of graphite reflectors to thorium-fueled blankets. Steel-reflected thorium blankets were shown by Wood (W-5) to offer improved burnup economic performance over uranium-fueled blankets;

5. an evaluation of the applicability of graphite reflectors for use in a gas-cooled fast reactor;

6. analysis of the applicability of graphite reflectors for use in large, commercially competetive (2000+ MW_e), breeder reactors. This would appear attractive since the reduced radial blanket breeding contribution in large reactors would favor thinner (e.g., 1-row) blankets whose performance would be significantly improved by the use of a graphite reflector.

7. further evaluation of the discrepancy between calculations and

measurements of the fast neutron penetration deep in the reflector region. Blanket No. 5, which will be irradiated at the M.I.T. Research Reactor in the near future, will help resolve this item.

8. the empirical method applied in this investigation of separating gamma and neutron heating contributions into local and core-leakage components, as it appears to have potential for eliminating complicated coupled neutron/gamma calculations in the determination of blanket heating rates.

In conclusion, the 2-row, depleted-uranium fueled graphite-reflected blanket offers sufficient prospects for improved fast breeder reactor performance and economic savings to merit its consideration as the reference design for future fast breeder reactors.

REFERENCES

A-1 Argonne National Laboratory, "Proceedings of the International Conference on Fast Reactors (Critical Experiment)," ANL-7320, October, 1966.

A-2 Argonne National Laboratory, Evaluation Report: 1000 MWe LMFBR Follow-On Study, Volume I – Summary, Volume II – Plant Design Part I (Draft), January 16, 1970.

A-3 Almenas, K., et al., "Properties of H_2 Reflectors of Fast Critical Assemblies," Trans. Am. Nucl. Soc., 7, 2, November 1964.

A-4 Avery, R., et al., "Coupled Fast-Thermal Power Breeder Critical Experiments," Vol. 12, Second ICPUAE, Geneva, 1958.

A-5 Argonne National Laboratory, "Proceedings of the International Conference on Sodium Technology and Large Fast Reactor Design," ANL-7510, November 1968.

A-6 Abagyan, L. P., et al., Group Constants for Nuclear Reactor Calculations, I. I. Bondarenko (Ed.), Consultants Bureau, N.Y., 1964.

A-7 Aalto, E., et al., "Measured and Predicted Variations in Fast Neutron Spectrum in Massive Shields of Water and Concrete," AE-197, 1965.

A-8 Atomic Power Development Associates, "Fast Reactor Core Design Parameters Study," APDA-133, Detroit, Michigan, March 1960.

B-1 Benedict, M., "The Fast Reactor – Its Promise and Its Problems," Trans. Am. Nucl. Soc., 15, 2, November 1972.

B-2 Barthold, W. P., "Fuel Shuffling in LMFBR Blankets," Applied Physics Division, Argonne National Laboratory, FRA-TM-40, August 1972.

B-3 Brewer, S. T., et al., "The Economics of Fuel Depletion in Fast Breeder Reactor Blankets," COO-3060-4, MITNE-123, November 1972.

B-4 Brewer, S. T., et al., "On the Economic Potential of FBR Blankets," Trans. Am. Nucl. Soc. 14, 1, June 1971.

B-5 Barthold, W. P., "Utilization and Economic Potential of Different Uraniums in LMFBR's," Applied Physics Division, Argonne National Laboratory, FRA-TM-50, February 1973.

B-6 Billaux, M., et al., "Physics Studies Associated with the Blanket Management of the SNR Reactor," The British Nuclear Engineering Society Conference on the Physics of Fast Reactor Operation, Paper 2.4, London, England, June 1969.

B-7 Brown, W. K., et al., "Fission Cross Sections of ^{237}Np from Pommard," Los Alamos Scientific Laboratory, LA-4372, January 1970.

B-8 Benedict, M., "Economics of Nuclear Power," M. I. T. Course 22.27, Spring 1970.

B-9 Benedict, M., "Principles and Methods of Nuclear Fuels and Power Management," M. I. T. Course 22.98s, Summer 1972.

B-10 Brown, G. J., "A Study of High Albedo Reflectors for LMFBR's," Nucl. E./S. M. Thesis, Nuclear Engineering Department, M. I. T., March 1972.

C-1 Cohen, K. P. and G. L. O'Neill, "Safety and Economic Characteristics of a 1000 MWe Fast Sodium Cooled Reactor Design," Advan. Nucl. Sci. Technol., Vol. 4, 1968.

C-2 Choong, T., "Fast Neutron Spectrometry in an LMFBR Blanket Reflector," M. S. Thesis, Nuclear Engineering Department, M. I. T., August 1973.

C-3 Clegg, Richard, Personal Communication, American Steel and Aluminum Company, Norwood, Mass., March 20, 1974.

D-1 Doerner, R. C. and W. G. Knapp (ANL), "Studies in Fast Cores with Light Metal and Oxide Reflectors," Trans. Am. Nucl. Soc., 9, 1, June 1966.

D-2 Driscoll, M. J., "Fast Reactor Physics Notes," M. I. T. Course 22.94S, Summer 1970.

D-3 Driscoll, M. J., Quarterly Progress Report (January 1 - March 31) M. I. T. Blanket Research Project, AT(11-1)-2250, April 23, 1973.

E-1 Elias, D., "Blanket Fuel Management Optimization of an LMFBR in a Dynamic Environment," Ph. D. Thesis, Nuclear Engineering Department, University of Maryland, 1970.

E-2 Elias, D. and F. J. Munno, "Reactor Fuel Management Optimization in a Dynamic Environment," Nuclear Technology, Vol. 12, September 1971.

E-3 Enge, Harold, Introduction to Nuclear Physics, Addison-Wesley Publishing Company, Inc., Reading, Mass., 1966.

E-4 Engle, W. W., "A User's Manual for ANISN," L-1693, March 1967.

E-5 Engel, F. C. and R. A. Markley (WARD), "Design Considerations Unique to LMFBR Radial Blanket Assemblies," Trans. Am. Nucl. Soc. 16, 1, June 1973

E-6 El-Wakil, M. M., Nuclear Heat Transport, International Text Book Co., Scranton, Pa., 1971.

E-7 Etherington, H., editor, Nuclear Engineering Handbook, McGraw-Hill, New York, 1958.

E-8 Markets, Engineering and Mining Journal, 25, 1 January 1974.

F-1 Froelich, R., "Optional Radial Blanket Fuel Management for an LMFBR," Trans. Am. Nucl. Soc. 14, 1, Boston, Mass. June 1971.

F-2 Forbes, I. A., et al., editors, "LMFBR Blanket Physics Project Progress Report No. 1," MITNE-116, MIT-4105-3, June 30, 1970.

F-3 Forbes, I. A., et al., "Design Construction, and Evaluation of a Facility for the Simulation of Fast Reactor Blankets," MITNE-110, MIT-4105-2, February 1970.

F-4 Forbes, I. A., et al., (editors), "LMFBR Blanket Physics Report No. 2," COO-3060-5, MITNE-131, June 30, 1971.

F-5 Fuller, E. L., "Reactivity Effects of Core Slumping in Fast Reactors: A Case Study," Argonne National Laboratory, FRA-TM-35, 1972.

F-6 Federal Register, Vol. 38, No. 30, February 19, 1973, page 4432.

G-1 Goldschmidt, P., "Optimal Fuel Enrichment Distribution in Fast Reactors," Nucl. Sci. Eng. 50, 2, February 1973.

G-2 Golubev, V. I., et al., "The Effects of Reflectors made of Various Materials on the Increase in the Number of Neutron Captures in the Uranium Blanket of a Fast Reactor," Soviet Atomic Energy, Vol. 15, No. 4, October 1963.

G-3 Gavrilov, K. A., et al., "The Cross Section for Fission of Np-237 by Slow Neutrons," Soviet Atomic Energy, pp. 469-467, Volume 28, No. 4, 1970.

H-1 Hasnain, S. A. and D. Okrent, "On the Design and Management of Fast Reactor Blankets," Nuclear Science and Engineering, Vol. 9, pp. 314-322, 1901.

H-2 Harde, R. and K. W. Stohr, "A Sodium-Cooled Power Reactor Experiment Employing Zirconium-Hydride Moderator," Vol. 6, Third ICPUAE, Geneva, 1965.

H-3 Hoover J. and D. A. Menley, "Alternative Neutron Energy Group Collapsing Schemes Applied to Fuel Cycle Calculations," ANL-7710 (January 1971).

H-4 Hirons, T. J. and R. D. O'Dell, "Calculational Modelling Effects on Fast Breeder Fuel Cycle Analysis," LA-4187, September 1969.

J-1 CEMA Symposium on Atomic Power Stations with Fast Reactors (Volume II), USSR, JPRS 48331, Reproduced by CLEARING HOUSE for Federal Scientific and Technical Information, July 1, 1969.

K-1 Kang, C. S., et al., "Use of Gamma Spectroscopy for Neutronic Analysis of LMFBR Blanket," COO-3060-2, MITNE-130, November 1971.

L-1 Larimore, J., "Short Course in Breeder Reactor Design," Nuclear Engineering, I. A. P. Course, M. I. T., January 22, 1973.

L-2 Leung, T. C., et al., "Neutronics of an LMFBR Blanket MOCK-UP," COO-3060-1, MITNE-127, January 1972.

L-3 Lamarsh, J. R., Introduction to Nuclear Reactor Theory, Addison-Wesley Publishing Company, Inc., Reading, Mass., 1966.

L-4 Little, W. W., Jr., and R. W. Hardie, "2DB Users Manual-Revision I," BNWL-831 Rev 1, August 1969.

M-1 Mayer, L., "Studies on the Optimum Design of the Radial Blanket on the Basis of a Steam-Cooled Fast Breeder," EURFNR 377, PSB NO. 263/67, May 18, 1967.

M-2 Morrison, G. W., et al., "A Coupled Neutron and Gamma Ray Multigroup Cross Section Library for Use in Shielding Calculations," Radiation Shielding Information Center ORNL-4464, Oak Ridge, Tenn., December 1969.

M-3 2D-Gamma: Two Dimensional Gamma Heating Code for Fast Reactors, Mitsubishi Atomic Power Inductries, Inc., Omiya, Japan, United States - Japan Fast Reactor Exchange Program, JAPFNR-97, March 1972.

M-4 McElroy, W. N., "A Computer-Automated Iterative Method for Neutron Flux Spectra Determination by Foil Activation," AFWL-TR-67-41, August 1967.

M-5 Mickley, Harold S., et al., Applied Mathematics in Chemical Engineering, McGraw-Hill Book Co., 1957.

M-6 M. I. T. Summer Program, "Fuel Management Summer Course," M. I. T. Course 22.98S, July 1972.

N-1 News from Correspondents, "Virginia," Nuclear News, Vol. 10, No. 9, July 1973, p. 77.

O-1 Ortiz, N. R., et al., "Instrumental Methods for Neutron Spectroscopy in the MIT Blanket Test Facility," COO-3060-3, MITNE-129, May 1972.

P-1 Pellaud, B., "The Physics Design of the Gas-Cooled Fast Breeder Reactor Demonstration Plant," GA 10509, Gulf General Atomic, San Diego, California, August 29, 1971.

P-2 Pluta, P., (G. E.), "LMFBR Primary System Design Overview," Nuclear Engineering I. A. P. Course, M. I. T., January 22, 1973.

P-3 Phenix, Prototype Fast-Neutron Nuclear Power Station, AEC-tr-7130, February 1970.

R-1 Rohan, P. E., "Comparisons of Transport and Diffusion Theory Calculations of Performance Characteristics for Large Fast Reactors," Ph. D. Thesis, Nuclear Engineering Program, University of Illinois, 1970.

S-1 Smith, D. C. G., et al., "Some Physics Studies in Support of PFR Design," in Fast Breeder Reactors, Proceedings of 1966 British Nuclear Energy Society London Conference, P. V. Evans ed., Pergamon Press, New York, 1967.

T-1 Tzanos, C. P., et al., "Optimization of Material Distributions in Fast Breeder Reactors," MITNE-128, MIT-4105-6, August 1971.

T-2 Taylor, J. J. and N. A. Petrick, "LMFBR Keys to Industrial Success," Nuclear News, January 1973.

V-1 Vendryes, G. A., et al., "Fuel Management and Economics," Trans. Am. Nucl. Soc. 15, 2, November 1972.

W-1 "LMFBR Program Plan, Vol. 6, Core Design," WASH-1106, August 1968.

W-2 Westinghouse Advanced Reactor Development, "Design Analysis of the LMFBR Radial Blanket," WARD 3045T2B-9, March 1973.

W-3 Westinghouse Advanced Reactor Development, "Radial Blanket Design and Development," Quarterly Progress Report, WARD 3045T2B-6, August 1972.

W-4 Weiss, E., et al., "Open Duct Cooling Concept for the Radial Blanket Region of a Fast Breeder Reactor," Nuclear Engineering and Design, Vol. 16, July 1971.

W-5 Wood, P. J. and M. J. Driscoll, "Assessment of Thorium Blankets for Fast Breeder Reactors," MITNE 148, COO-2250-2, July 1973.

W-6 "Reactor Fuel Cycle Costs for Nuclear Power Evaluation," WASH-1099, 1971.

W-7 Wilsey, Harvey, Ultra Carbon Corp., Bay City, Michigan, Personal Communication, March 20, 1974.

Y-1 Yevick, J. G. (editor), Fast Reactor Technology: Plant Design, M. I. T., Press, Cambridge, Mass., 1966.